1997

Grain growth and continuous cooling transformation behaviour of austenite in Ti-Nb-Mn-Mo microalloyed steels

Priyadarshan Manohar
University of Wollongong

GRAIN GROWTH AND CONTINUOUS COOLING TRANSFORMATION

BEHAVIOUR OF AUSTENITE IN Ti-Nb-Mn-Mo MICROALLOYED STEELS

A thesis submitted in (partial) fulfilment of the

requirements for the award of the degree

DOCTOR OF PHILOSOPHY

from

THE UNIVERSITY OF WOLLONGONG

by

PRIYADARSHAN MANOHAR

B. E. (Met.) MIEAust CPEng

DEPARTMENT OF MATERIALS ENGINEERING

1997

CANDIDATE'S CERTIFICATE

This is to certify that the work presented in this thesis is original and was carried out by the candidate in the Department of Materials Engineering, the University of Wollongong and has not been submitted to any other university or institution for a higher degree.

<div align="right">

....

PRIYADARSHAN MANOHAR

</div>

Table of Contents

Chapter 2:   Literature Review: Thermomechanical Processing

(TMP) of Austenite in Microalloyed Steels

Preface

The work presented in this thesis is based on a project sponsored by the Australian Research Council in collaboration with the BHP Steel Company - Flat Products Division, Port Kembla, Australia to investigate the grain growth and continuous cooling transformation behaviour of austenite in Ti-Nb-Mn-Mo microalloyed steels. The initial work consists of experimental determination, physical conceptualisation and mathematical modelling of grain growth of austenite during reheating in microalloyed steels whilst the experimental work of characterisation and simulation of the TMP in laboratory using quench and deformation dilatometry is included in the later part of this thesis. The latter part reports the results of the investigation in to the continuous cooling transformation behaviour of undeformed and thermomechanically processed austenite. The work was carried out entirely within the laboratories of the Department of Materials Engineering, University of Wollongong between April 1994 to August 1997 under the guidance of A/Prof. T. Chandra.

Synopsis

Experiments were carried out to study the grain growth during reheating and phase transformation behaviour during continuous cooling of austenite in five microalloyed steels. Two of these steels were supplied in as-cast slab as well as in controlled rolled plate conditions. These steels contained similar levels of C ($\sim$ 0.07%), Ti ($\sim$ 0.013%) and Mo ($\sim$ 0.2%) but had different levels of Mn (1.1 to 1.7 %) and Nb (0.03% to 0.06%) contents. The principal aim of this work was to simulate as closely as possible the controlled rolling schedule used in industry for the production of plates in laboratory. Laboratory process simulation was carried out using quench and deformation dilatometry. Continuous cooling transformation behaviour of the undeformed as well as thermomechanically processed austenite was investigated from the dilatometric data, quantitative optical metallography and microhardness tests. Continuous cooling transformation (CCT) diagrams of the undeformed and thermomechanically processed steels were constructed. Effects of thermomechanical processing (TMP), accelerated cooling and Mn and Nb contents on austenite transformation critical temperature (Ar_3), phase transformation kinetics, CCT diagrams, grain size and hardness were investigated.

The experimental work on the grain growth of austenite during reheating involved mainly the determination of Grain Coarsening Temperatures (GCT) for various microalloyed steels. It was found that the conventional method of detecting the GCT from the mean grain size v/s reheating temperature plot was inadequate in locating the abnormal grain growth in some microalloyed steels. An alternative quantitative metallographic method which consists of plotting the mean size of the largest grain as a function of reheating temperature was therefore developed. The new method was found

to be more effective and sensitive in detecting the abnormal grain growth in all microalloyed steels studied. The factors in addition to precipitate dissolution and coarsening which influence the GCT of microalloyed steels were investigated. It was found that a high heterogeneity ratio (Z) present in the initial austenite grain structure (prior to coarsening) can result in lowering the GCT significantly. The reasons why different steels exhibit different values of heterogeneity ratios were also investigated. It was found that microstructural features before reheating influences the $\alpha \rightarrow \gamma$ transformation which results in different values of Z in different steels. In slab steels, a microstructure containing coarse ferrite grains and a small volume fraction of acicular ferrite + pearlite resulted in a high value of Z. In case of plate steels, microstructure consisting of heterogeneous distribution of ferrite grain sizes and a non-uniform distribution of pearlite (banded microstructure) led to the generation of high Z in austenite grain sizes. Grain growth behaviour of plate steels was found to be significantly different than that of slab steels of the same composition. Plate steels exhibited two stages of accelerated grain growth compared to only one stage of accelerated grain growth found in slab steels. Also, abnormal grain growth in plate steels was found to be not as significant as that in slab steels.

Empirical mathematical models to predict the grain growth of austenite were critically reviewed. It was found that, for the same starting conditions, predictions from these models differ from one other considerably. Furthermore, none of the models could adequately describe the grain growth behaviour, particularly at higher temperatures, of as-cast slabs. Basic principles of grain growth were therefore revisited in an attempt to develop a mathematical model which can account for abnormal grain growth. A model was developed which also accounts for the effect of initial grain size on the process of

grain growth. Supporting mathematical models for the prediction of particle coarsening and dissolution as a function time, temperature and composition were developed. It was found that predictions based on this model were in close agreement with the experimental grain growth data.

In the second part, an effort was made to characterise the TMP used in the industry for the production of controlled rolled plates and then to simulate this process as closely as possible in the laboratory using quench and deformation dilatometry. Effects of TMP, accelerated cooling and alloying elements (Nb and Mn) on Ar_3 temperature, phase transformation kinetics, grain size, CCT diagrams and microhardness were investigated. It was found that the TMP accelerated the onset of γ/α transformation (γ transformation start temperature, Ar_3, was raised). However, the progress of γ/α transformation was retarded considerably in the deformed samples. TMP lowered the hardenability of austenite considerably, thus lowering the hardness of the deformed samples. TMP had pronounced effects on the CCT diagrams which include:

1. γ/α transformation was raised to higher temperatures,

2. γ/α transformation nose was shifted towards faster cooling rates; and

3. γ/α transformation occurred over a wider temperature range.

TMP also refined the ferrite grain size significantly.

Increase in cooling rate lowered the Ar_3 significantly and also accelerated the progress of γ transformation. Increased cooling rate allowed the transformation of γ to non-equilibrium phases such as bainite and martensite and thus increased the hardness of undeformed as well as deformed samples. Increased cooling rate was found to have marginal effect on the refinement of ferrite grain size.

For similar levels of other alloying elements, an increase in Nb content was found to lower the Ar_3 of undeformed samples at a rate of about 10 °C/ 0.01% dissolved Nb. However, in deformed samples, increase in Nb content actually raised the Ar_3 temperature. This effect was considered to be due to two main reasons: firstly, the strain induced precipitation of Nb in austenite which would act as nucleation sites for phase transformation and secondly, due to the scavenging of Nb during precipitation which decreases the hardenability of austenite. Higher Nb content retarded the progress of γ transformation of undeformed as well as deformed austenite. Increase in Nb content increased the hardness of undeformed as well as deformed samples and refined ferrite grain size marginally. Nb had no significant influence on the location of phase transformation noses in the CCT diagrams.

For similar levels of other alloying elements, an increase in Mn content was found to lower the Ar_3 of undeformed samples. In contrast with Nb, increased Mn content lowered the Ar_3 of deformed samples as well, suggesting that Mn is not scavenged during the strain induced precipitation of Nb and remains dissolved in the austenite which increases its hardenability. Increase in Mn content retarded the progress of transformation of undeformed as well as deformed samples. Increased Mn content increased the hardness of both undeformed and deformed samples significantly. Mn also refined ferrite grain size. B_s temperature was significantly lowered due to a higher Mn content. Increase in Mn content pushed the polygonal ferrite nose in CCT diagrams to slower cooling rates which indicates increased hardenability of austenite and thus counters the effect of TMP which decreases the hardenability.

Acknowledgements

The research work reported in this thesis was carried out under the supervision of A/Professor Tara Chandra. I express my appreciation for his constant support, guidance and encouragement during the course of this work.

I acknowledge the support extended by Prof. Druce Dunne who supervised my work for a period of seven months when A/Prof. Chandra was away on his sabbatical leave in 1994-95.

I express my gratitude to the Australian Research Council and BHP Steel Company - Flat Products Division, Port Kembla for providing the financial and material support. I also acknowledge the staff at Central Research Lab., BHP Steel for providing me with the steel slab and plate samples along with the analysis of chemical composition.

I thank Mr. Chris Killmore, Mr. David Langley and Mr. Paul Kelly (BHP Steel - Central Research Lab. - Product Development Group) for their guidance. It is because of their input that this work has retained its industrial relevance. Their experience and the data collected by them over a number of years have been a great help to me in reaching my goal of simulating the complex industrial controlled hot rolling process in the laboratory.

I thank Mr. Greg Tillman for his assistance in optical microscopy, Mr. Graham Hamilton for providing me with the furnaces and other equipment that I needed, Mr. Ron Kinnell and Mr. Jose Gonzalez for making high quality dilatometry samples on

Chapter 1: Literature Review: Grain Growth of Austenite in Microalloyed Steels

1.1 Introduction: Grain Growth in Metals and Alloys

Grain growth is a process by which the average crystal (grain) size increases and the total grain boundary area decreases when a polycrystalline material is annealed. The driving pressure for this process results from the decrease in free energy which accompanies reduction in total grain boundary area. Grain size influences physical properties as well as service performance properties of materials. For example, a decrease in grain size increases yield strength [1, 2], increases notch (fracture) toughness [3], increases formability [4], decreases hardenability [5], increases creep resistance, but decreases creep strength [6], increases resistance to stress corrosion [7], increases resistance to temper embrittlement [8, 9], increases fatigue strength [10], increases hysteresis and eddy current loss [11] and also affects optical transmission and critical current in superconductors [12]. Understanding the process of grain growth and grain size control is not only of intrinsic interest but also has a great technological significance.

Burke and Turnbull [13] summarised the principal points of the process of grain growth as given below:

- Grain growth occurs by the migration of the grain boundaries and not by the coalescence of neighbouring grains.

- The process of grain boundary migration is discontinuous (jerky) i.e., the rate of grain boundary migration of any particular boundary is not constant and also the direction of migration may change from time to time.

- A given grain may grow into a neighbouring grain, on one side, while simultaneously being consumed by a different neighbour on another side.

- Rate of consumption of a grain frequently becomes more rapid just as the grain is about to disappear.

- A curved boundary usually migrates towards its centre of curvature.

- Grains included by angles < 120° will be consumed while the grains included by angles > 120° will grow until the stable angles of 120° are achieved.

1.1.1 Normal Grain Growth

Grain growth occurs by two mechanisms: Normal and Abnormal grain growth. Normal grain growth consists of uniform and monotonous motion of all grains in grain size - time space and tends to achieve a quasi-steady state distribution of grain sizes [14]. Kurtz and Carpay [15] have noted four main attributes that distinguish normal grain growth:

- Uniformity - The grains fall into a narrow range of sizes which gives the microstructure a uniform appearance throughout the process of grain growth.

- Scaling - A change in scale (magnification) is sufficient to make the grain structures at various times appear geometrically similar, i.e. the form of grain size distribution is time-invariant.

- Stability - Perturbations in the grain growth process do not affect the asymptotic (late-stage) structure and dynamics, which are also insensitive to initial conditions.

- Log-normality - Distributions of both shape and linear size parameters can be well fitted by log-normal distributions.

1.1.2 Inhibition of Normal Grain Growth

Harker and Parker [16] first proposed the two conditions for internal equilibrium (end of normal grain growth) during the process of normal grain growth: a) grain boundaries should be straight and b) the grain boundary tensions should be balanced (the dihedral angles equal 120°). They proposed that grain shape and not the grain size determines the ability of grains to grow and that the grain growth should stop when face-junction angles of 120° are achieved. However, Miller [17] showed that the normal grain growth is not inhibited after the attainment of 120° dihedral angles. Normal grain growth is thus expected to continue until, in the limit, the microstructure consists of a single crystal. In reality, this goal is rarely achieved. The main reasons for this are that the process of grain boundary migration may be impeded and/or normal grain growth may reach a stage of stagnation where from no further normal grain growth is possible. Normal grain growth may be inhibited due to several factors which include:

a) Grain size distribution in the sample is too narrow - Hillert [18], Gladman [19],

b) Mean grain size in the sample approaches the limiting grain size determined by the size and the volume fraction of the second phase particles - Zener [20],

c) Normal grain growth may be inhibited in metals which have particularly pronounced preferred orientation texture - Dunn and Koh [21],

d) Solute atoms cause drag on the grain boundary resulting in impediment to grain boundary migration and thus cause the inhibition of normal grain growth - Higgins [22],

e) Free (external) surfaces cause inhibition to normal grain growth as observed in thin films - Beck et al. [23], Palmer et al. [24]; and

f) Certain combinations of temperature and low deformation cause strain induced grain

    boundary migration and promote abnormal grain growth - Tanaka et al. [25], Cuddy

    [26].

1.1.3 Abnormal Grain Growth

When normal grain growth is inhibited due to any of the above mentioned factors, grain

growth may proceed via an alternative mechanism known as abnormal grain growth (also

variously known as secondary recrystallization, anomalous grain growth, elephant grain

growth, discontinuous grain growth, grain coarsening, exaggerated grain growth and

non-uniform grain growth). Abnormal grain growth consists of growth of only a few

grains in the material while the remainder are virtually unaltered until they are consumed.

Abnormal grain growth continues until all of the smaller grains are consumed and the

microstructure consists of larger grains (usually of millimetre size) only. Further growth

of the large grains is inhibited at the last stage of abnormal grain growth due to

impingement and the grain growth process then returns to the normal mode. During the

process of abnormal grain growth, the microstructure exhibits a large variation in grain

sizes, see Fig. 1.1.
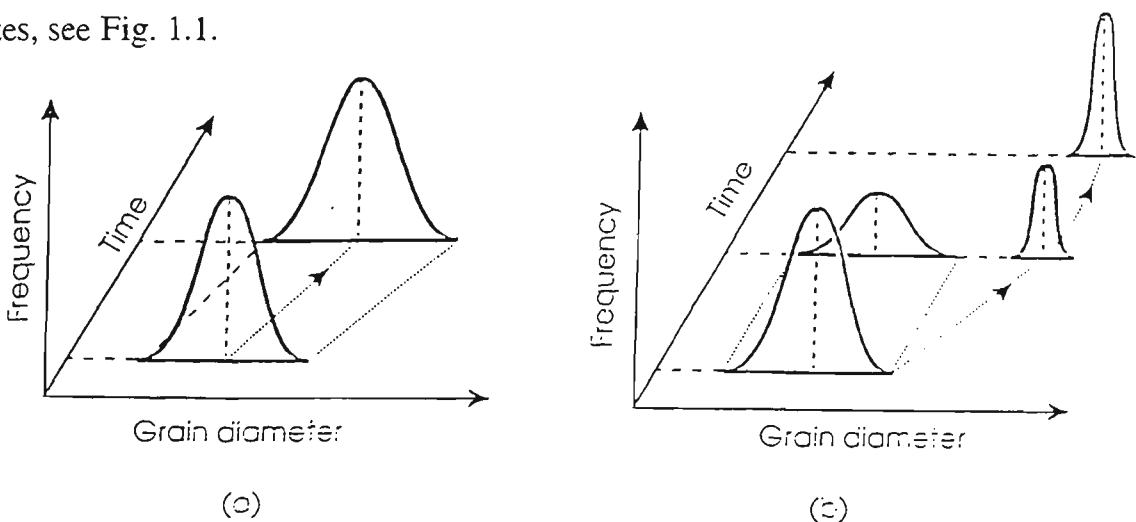
Figure 1.1: Schematic representation of the change in grain size distribution during
        (a) normal grain growth and (b) abnormal grain growth. {After [27]}.

Such a microstructure is usually referred to as 'mixed' or 'duplex' microstructure which means a mixture of very coarse and fine grains. Occurrence of duplex microstructure is considered to be a transient state in the process of grain growth. Abnormal grain growth was first demonstrated by Jeffries [28] during annealing of thoriated tungsten and has since been observed in a variety of materials as reviewed by Dunn and Walter [29]. Cahn and Haasen [30] summarised the experimental observations of abnormal grain growth and suggested the following characteristics of abnormal grain growth:

- The large grains which are developed during abnormal grain growth are not freshly nucleated: They are particular grains of the initial structure which then coarsen.

- There exists is a significant incubation period for the onset of abnormal grain growth. Abnormal grain growth is controlled by nucleation and growth and can be described by Avrami type reaction kinetics [29, 31]. The rate of growth of abnormal grains is independent of time [13] in contrast with normal grain growth where rate of grain growth decreases as the grain size increases.

- The grains which are to grow abnormally are appreciably larger than the average grain size and they usually have significantly different orientations from those within the initial preferred orientation if such a texture exists. However, the factors which determine the selection of the preferred grains which are to grow are yet unclear.

- The preferred orientation texture at the end of abnormal grain growth is usually different than any major texture which may have been present prior to the start of abnormal grain growth.

- Abnormal grain growth is initiated only when normal grain growth is inhibited.

- For any particular metal there is usually a well-defined minimum temperature which must be exceeded for abnormal grain growth to occur. This is referred to as the "grain coarsening temperature".

- The driving pressure for abnormal grain growth is basically same as that for normal grain growth viz. the reduction of the total grain boundary area and the energy associated with it. However, under certain circumstances, such as in thin films, the surface energy of the metal may also have a role in determining the abnormal grain growth behaviour.

Rosi et al. [32] found that a grain has to be at least twice the mean grain size in order to grow abnormally. Hillert's theory [18] suggested that abnormal grain growth would occur in a material if the initial grain distribution contains some grains with size larger than 1.8 times the mean grain size. However, it has been shown [33, 34] that this is incorrect and the large grains must have some advantage <u>other than size</u> over their neighbours in order to grow abnormally. Gladman [35] suggests that following three conditions must be met simultaneously for abnormal grain growth to occur:

- Size of the largest grain must be greater than 1.5 times the mean grain size,

- Grains with mean size must be stagnated or pinned; and

- Initial log-normal distribution of grain sizes should be wider.

Recently, Novikov [36] has attempted to clarify the nucleation stage of the abnormal grain growth using computer simulation. He suggests that if the numbers of the large grains (with high-mobility boundaries) are small, they are more likely to be surrounded by stagnated (low-mobility) grains and therefore, these grains can grow to larger sizes.

1.1.4 Grain Coarsening Temperature

The temperature above which abnormal grain growth becomes predominant is known as the 'grain coarsening temperature (GCT)'. The knowledge of GCT for a given

microalloyed steel grade is extremely important in designing the hot rolling schedule for that steel because the GCT is related to the very first step in hot rolling process of the steel, namely, the reheating temperature. The reheating temperature controls the amount of microalloying elements in solution in austenite and the austenite grain size at the start of the hot rolling schedule. These two factors significantly influence the metallurgical phenomena during TMP such as recrystallization, precipitation, phase transformation and final grain size which in turn control final structure and properties of the steel product. If the reheating temperature is too low compared to the GCT, then microalloy precipitates remain undissolved in austenite. This means that the microalloying elements are not available for precipitation hardening and/or hardenability control during further processing. If the reheating temperature is equal to the GCT, then it leads to mixed initial austenite grain structure which is not eliminated even after repeated deformation, recrystallization and phase transformation [25, 26]. Such a mixed structure is found have inferior mechanical properties [25]. If the reheating temperature is much higher than the GCT, then it leads to very coarse austenite grains due to lack of inhibition to grain growth. This leads to an increase in the critical amount of deformation which is needed to complete the recrystallization and the coarse grain size may make it almost impossible to achieve sufficient deformation per pass to complete the recrystallization. This leads to non-uniform distribution of deformation bands and causes mixed grains to form. Thus, the reheating temperature should be selected in reference to the GCT such that sufficient amount of microalloying elements are dissolved, but the austenite grain size is kept desirably small and uniform.

The GCT of microalloyed steels is usually determined experimentally by heating a series of samples in the temperature range of 900 - 1350 °C in steps of 50 or 100 °C for a

period of 30 or 60 minutes and then quenching the samples immediately in water or iced

brine solution to achieve a fully martensitic microstructure. An alternative method is to

allow the samples to cool to just below the Ar_3 temperature and then quenching the

samples. In this method, ferrite forms on the prior austenite grain boundaries and thus

allows the measurement of austenite grain size as a function of temperature. In the

former method, prior austenite grain size has to be revealed by metallographic

techniques. Several techniques are available to reveal the prior austenite grain size in

steels [37 - 40]. Hot picric acid method [8, 39 - 42] is the most commonly used method

to reveal the prior austenite grain size in microalloyed steels. This method will be

described in detail in Chapter 3. Sometimes the samples are tempered prior to etching to

improve the grain contrast [37, 40, 43]. Mean austenite grain size is then measured

using appropriate quantitative metallographic technique [37] and plotted as a function of

temperature. It was found in this work that this method of analysing the mean grain size

v/s temperature is inadequate to locate the GCT in plate steels. Alternative methods

were therefore developed in the current work which are sensitive and effective in

detecting the abnormal grain growth and the GCT in both slab as well as plate steels [44

- 45]. Another method to locate the GCT is to find the temperature above which mixed

microstructure is observed. A mathematical model to predict the GCT was proposed by

Gladman and Pickering [46]. More recently, a relative rate model [47] has been

proposed which achieves this goal to some extent. Relative rate model will be discussed

in more detail in # 1.3.4. An alternative approach is to correlate the GCT with the

precipitate dissolution temperature for various microalloy precipitate species found in

microalloyed steel [46, 48].

Since the pioneering work of Jeffries's [28] on the abnormal grain growth of particle containing material (ThO_2 impregnated tungsten), the concept of GCT has been intimately coupled with the concepts of inhibition of normal grain growth by second phase particles and the subsequent unpinning of the grains due to progressive dissolution and coarsening of the particles as the reheating temperature is increased. The influence of precipitates on the GCT of microalloyed steels has received a great deal of attention. Several papers have been published which describe the effect of stability of precipitates such as AlN [46, 49], Nb and Ti based carbides and nitrides [48, 50, 51], Nb carbonitrides [52], Ti oxide [35], V carbides and nitrides [53 - 55] on the GCT of microalloyed steels. In general, the GCT of microalloyed steels is influenced by the austenite grain size and distribution as well as the size, distribution, volume fraction and stability of pinning particles [18, 20, 46, 56]. There is some evidence in C-Mn steels that a higher heating rate through the $\alpha \rightarrow \gamma$ transformation range causes heterogeneity in austenite grain sizes which results in a higher probability of abnormal grain growth [57]. This effect, however, has not been verified in microalloyed steels. Webster and Allen [55] found that VC particles can inhibit normal grain growth, however their influence can be dependent on heating rate: Slow heating led to the coalescence and/or dissolution of VC, which then led to the onset of abnormal grain growth, whereas rapid heating led to structures having much finer dispersions and for which both normal and abnormal forms of grain growth were inhibited. Gladman [35] found that addition of Nb or V to Ti containing steels results in anomalous particle coarsening and reduces the GCT of Ti steels. Palmiere et al. [48] found that the GCT of Nb steels increases as the Nb content is increased and that the value of GCT equals dissolution temperature of NbC minus 125 °C. Tamehiro and Nakasugi [58] found that microstructure before reheating influences the GCT in Ti-treated high hardenability (Mn+Mo) microalloyed steels. They

suggest that austenitization from an initially bainitic region is difficult when the heating rate is low (<10 °C/min.) resulting in duplex austenite grain structure after $\alpha \rightarrow \gamma$ transformation which leads to the lowering of GCT.

1.1.5 Dissolution Temperature for Microalloy Precipitates

It is clear from the foregoing discussion that inhibition of normal grain growth is an essential condition for abnormal grain growth to occur and that precipitate particles inhibit normal grain growth most effectively. Therefore, it is pertinent to examine the stability of various particles in austenite as a function of temperature. Stability of the particles is usually expressed as their solubility in austenite which is represented by a general equation of the type given below:

$$\text{Log } [M]^x [C]^y = A - B/T \qquad (1.1)$$

where, M_xC_y is the stoichiometric formula of the precipitate, M stands for the microalloying element (Ti, Nb, V etc.), C stands for the interstitial element (C or N), A and B are constants and T is the temperature (K). A number of equations are available in the literature which are derived empirically (multiple regression analysis), semi-empirically or by using thermodynamic considerations to find the values of A and B in Eq. 1.1 for different precipitates of Nb and Ti in microalloyed steels. Some of these equations are summarised in Table 1.1 given below:

Table 1.1: Summary of equations describing solubility of microalloy precipitates

Type of Ppt.	A	B	Reference	Remark
TiC	2.75	7000	59	
	5.33	10475	60	
NbN	2.80	8500	60	
	3.82	9940	61	
	4.04	10230	62	
NbC	2.06	6700	48	
	3.42	7900	60	
	2.96	7510	62	
	3.40	7920	63	$LHS=Log[Nb][C]^{0.87}$
NbCN	2.26	6770	59	$=Log[Nb][C+0.86N]$
	2.15	6770	64	$=Log\{[Nb][C+0.86N]-0.248[Mn]\}$
TiN	0.322	8000	65	
	5.90	14400	66	
	4.94	14400	67	
	5.19	15490	68	
	4.42	15400	69	

Slightly more complicated equations to describe the solubility of NbC and NbCN are given Akben et al. [70] and Rios [71] respectively.

It is clear from Table 1.1 that the equations describing the precipitate dissolution differ from each other considerably. Eq. 1.1 incorporates the influence of the most predominant variables such as temperature and composition on precipitate dissolution. However, there are a number of other factors which affect the precipitate dissolution process which are not fully accounted for during the derivation of equations given in Table 1.1. These factors are:

- Thermochemistry of phase changes - depends on the free energy of formation of phases, chemical activities of the species and temperature.

- Reaction (Dissolution and Precipitation) kinetics - depends on diffusivity, degree of supersaturation, interfacial energies, density on nucleation sites, time and temperature.

- Austenite grain size - which is a measure of diffusion distance involved. Dutta and Sellars [72] have suggested that in the absence of strain-induced deformation sites (dislocations, deformations bands), austenite grain boundaries are the only predominant sites for precipitate nucleation. As a result, rate of precipitation is significantly retarded and hence more of microalloying elements are held in solution rather than precipitated when grain size is large, even when reheating temperatures are considerably lower than the solubility temperatures calculated from the equations.

- Effect of (hot) deformation - which affects density of nucleation sites.

- Size of particles - smaller particles are more soluble than the larger ones [73].

- Synergistic effects of elements such as Mn, Mo, Si etc. on particle dissolution: Hansen et al. [74] have found that an increase in Mn content (from 1.3 % up to 2.0 %) in low carbon, Nb containing steels has no significant influence on NbCN precipitation and γ recrystallization. On the other hand, Xiuqiu and Wenxuan [75] and Koyama [76] have shown that an increase in Mn content (from 0.92 % up to 2.18%) in similar steels increases the solubility of NbC in austenite which causes retardation on NbC precipitation in γ and hence a significant acceleration of recrystallization of γ. Koyama [76] has also shown that Si, a graphite and ferrite stabiliser, increases activity coefficient of C in γ which leads to a decrease of solubility of NbC in γ. Bacroix et al. [77] And Oakwood et al. [78] have shown that an addition of 0.3 % Mo in Nb-bearing steel decreases activity coefficient of C and

N and consequently increases the solubility of NbCN and retards their precipitation in γ.

- Exact stoichiometry of microalloy precipitates is unclear - several researchers [79 - 81] have shown that Ti combines with Nb to form a range of mixed precipitates of the type Ti, Nb (C,N) whose dissolution temperature depends on the amount of Ti in the precipitates. Stoichiometry of carbides has been suggested to be varying between $TiC_{0.61}$ - $TiC_{1.0}$ and $NbC_{0.77}$ - $NbC_{0.99}$ [82].

A comprehensive equation which is able consider the effect of all of these variables on particle dissolution is currently lacking. Therefore, correlation of calculated particle dissolution temperature with the GCT has enjoyed only a partial success. Furthermore, as will be shown in this work that (Chapter 4) several other factors such as particle coalescence, microstructure before reheating and heterogeneity in the austenite grain size distribution exert a significant influence on the GCT of microalloyed steels. Hence, precipitate dissolution temperature can not decide the GCT by itself, but may provide a useful pointer for finding the GCT.

1.2 Kinetics of Grain Growth in Absence of Particles

1.2.1 Theories of Normal Grain Growth

C. S. Smith [83] emphasised that normal grain growth results from the interaction between the topological requirements of space filling and the geometrical needs of surface tension equilibrium. Most of the grain growth theories can be considered to originate from these two concepts. The theories usually also keep in hand with the kinetics of grain boundary migration developed by Burke and Turnbull [13] embodied in

the form of isothermal grain growth law. Theories of grain growth attempt to mathematically describe such parameters as the growth of mean grain size and grain size distribution as a function of time and the time independent grain growth rate at a given, fixed temperature and for a given composition. Several theories of grain growth have been developed over last five decades. These theories are classified according to the classification system suggested by Hunderi and Ryum [84] and Atkinson [85] as shown in Figure 1.2.

The theories can be classified in to two main categories: mean field theories and computer simulation models. Mean field theories are based on the assumption that the behaviour of the whole grain assembly can be calculated by generalising the behaviour of a small part of the microstructure. Computer simulation models, on the other hand, attempt to calculate the growth and shrinkage of every grain in the assembly. Foundation of the mean field theories was laid by Burke and Turnbull [13] and the theory was later developed by Peltham [86] and Hillert [18]. Peltham and Hillert theories are sometimes called as drift models because their theory assumes that during the process of grain growth larger grains grow while the smaller grains shrink under the action of the driving force which causes a drift in the mean grain size. Peltham started with a assumed log-normal distribution while Hillert predicted a grain size distribution which is peaked at $Log\ (R/\overline{R}) = 0$. Louat [87] argued that boundary motion is a random process and that the diffusion concept, not the drift velocity concept, which is important. Louat's diffusion model was able to predict a Rayleigh distribution which is very close to log-normal distribution. It should be noted that all of the above theories [13, 86, 18, 87] predict a parabolic grain growth law. None of them take in to consideration topological equations.

Grain Growth Theories

Mean Field (Statistical) Theories
Calculate behaviour of a small part of microstructure (such as one grain) and then generalising it to the whole grain assembly.

Computer Simulation
Calculates the growth or shrinkage of every grain in the assembly.

Drift Models -
Peltham [86], Hillert [18].

Diffusion Model -
Louat [87].

Topological Models -
Rhines and Craig[88], Kurtz and Carpay [15], Lucke et al. [89].

Direct Simulation
A boundary network is constructed which is operated on by the computer program which considers topology.

Statistical
Assumes a probable collection of grains and then solves equations so as to find the behaviour of a typical numbers of typical types of grains with no topological constraints. Novikov [90].

Deterministic
Each subsequent configuration of the boundary network arises from one particular previous network.

Probabilistic
Considers probabilities of events on a microscopic scale.

Equation of motion for boundary velocity, e.g. $v \propto P_g \propto 1/\rho$ - Ceppi and Nasello [91].

Direct computer procedure for evolving the grain structure - Weaire and Kermode [92].

Monte Carlo Anderson et al. [93].

Non-Monte Carlo Telley et al. [94].

Figure 1.2: Classification of grain growth theories. {After [84, 85]}.

Topology was taken in to account by Rhines and Craig [88]. They suggested that when a grain shrinks and disappears, then not only must this volume be shared out between neighbouring grains, but because the topological attributes (shape, faces, edges and vertices) of the neighbours also alter, this will in turn influence grains which are further away. One of the most surprising outcomes of this approach is that the theory predicts a grain growth exponent of value **3**! Rhines and Craig suggested that this could be because of their serial-sectioning technique of measuring the grain size in three dimensions rather than the conventional technique of measuring the grain size in two dimensions on the one plane of polish. Rhines and Craig analysis was continued later by Kurtz and Carpay [15] where they allowed a log-normal distribution of not only sizes but also of shapes of the grains. Kurtz and Carpay predicted a parabolic grain growth law (n = 2) for the overall mean grain size as well as the mean grain size of the individual shape class of the grains. Lucke et al. [89] considered the topological effects in two dimensions and also arrived at the parabolic grain growth law.

Computer simulation models have not been covered in this review, but some key features and literature [90 - 94] are included in Figure 1.2. The general conclusion is that most of the theories (mean field and computer simulation) predict a parabolic grain growth law and the grain size distribution to be either log-normal or very close to it (Fig. 1.3). Parabolic grain growth law is, therefore, discussed in the following section.
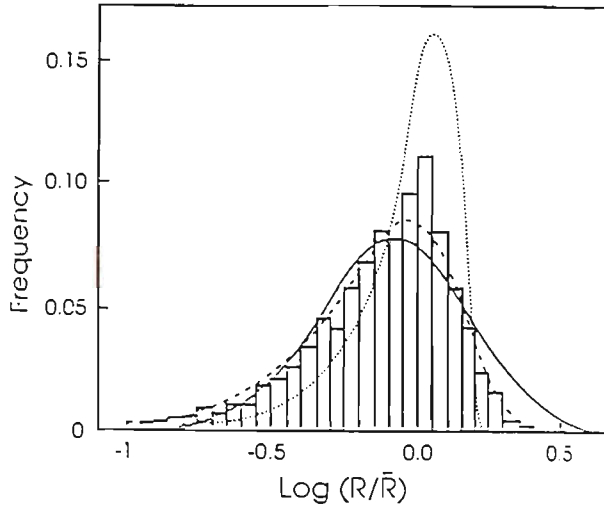
Figure 1.3: Comparison of grain size distributions: Histogram - Monte-Carlo
simulations by Anderson et al. [93], Continuous line - log-normal
distribution assumed by Peltham [86]. Dotted line - distribution
predicted by Hillert [18]; and Dashed line - Louat (Rayleigh)
distribution [87]. {After [95]}.

1.2.2 Parabolic Grain Growth Law

Beck et al. [23] showed that the experimentally determined values of grain sizes under

isothermal annealing conditions fitted a power relation such as:

$$D^n - D_o^n = Ct \qquad (1.2)$$

where D is the final grain diameter, D_o is the initial grain diameter, t is annealing time and

n and C are constants which depend on alloy composition and annealing temperature. but

are independent of the grain size. Eq. (1.2) is known as the **isothermal grain growth**

law while n is called as the **grain growth exponent**.

Eq. (1.2) can be mathematically derived by assuming that the instantaneous rate of grain

growth (dD/dt) is proportional to the grain boundary energy per unit volume of the

material, which in turn is proportional to the inverse of the instantaneous grain diameter

(D).

Thus:

$$dD/dt = k (1/D)$$

$$\therefore \int_0^D D\,dD = k \int_0^t dt$$

$$\therefore D^2/2 - D_o^2/2 = kt$$

Putting $C = 2k$,

$$D^2 - D_o^2 = Ct \qquad\qquad\qquad (1.3)$$

Eq. (1.3) is known as the **parabolic grain growth law**. The general form of Eq. (1.3) is

Eq. (1.2).

If D_o is neglected in comparison with D, rearranging Eq. (1.2) and taking logarithms on

both sides yields:

$$Log\,D = 1/\mathbf{n}\,Log\,C + 1/\mathbf{n}\,Log\,t$$

Thus a plot of Log D *v/s* Log t gives the value of the constant C (in terms of 1/**n** Log C)

as intersection of the Log D axis, while the slope of the curve gives the value of **n** (in

terms of 1/**n**). This technique of plotting the grain growth data on the double log scale to

find the values of C and **n** was first demonstrated by Beck et al. [23].

1.2.3 Grain Growth Exponent "n"

The theoretical value of **n** was expected to be 2, as given in Eq. (1.3). However, in real

materials, **n** was found to be much higher than the theoretical value. For example, the

value of **n** in high purity Al was found to be 3.1 - 11 [23], in α-brasses 2 - 5 [96], in

high purity metals 2 - 4 [93], in plain carbon and low alloy steels 4.4 - 20 [17] and in

various other materials as summarised by Higgins [22] and Humphreys and Hatherly

[97]. It is interesting to note that the experimentally determined value of **n** was rarely

found to be 2 in all of these materials.

The reasons why the value of experimentally determined grain growth exponent is

higher than its theoretical value of 2 has also been discussed by Burke and Turnbull [13]

and more recently by Humphreys and Hatherly [98]. The main reasons suggested for **n**

to be higher than two are: (i) the assumption that the grain growth rate is independent of

time is incorrect because grain growth rate decreases as grains coarsen and also under

conditions approaching inhibition to normal grain growth (see # 1.1.2), (ii) the rate of

grain growth may not be proportional to the driving force due to solute drag effect, (iii)

neglecting D_o may be incorrect, because if D_o is not negligible, the slope of the log D *v/s*

log t curve will be lowered, and (iv) initial grain size distribution or changes in grain

size distribution during grain growth can affect the measured grain growth kinetics.

1.2.4 Interpretation of the Constant "C"

Interpretation of the constant C (m^2/s) is rather more complex because of two reasons:

firstly because this so-called constant depends on a number of variables and secondly

because the parabolic grain growth law can be derived by several ways. This problem

has been dealt with in detail elsewhere [99] however, a summary of this paper is given

below:

Turnbull [100] considered the atomic mobility under the influence of potential gradient across the grain boundary to derive the parabolic grain growth law which gives following expression for C:

$$C = 4K"K\sigma V_m$$

where $K" = 1/K'$, K' is defined through $\rho = K'D$, ρ is the curvature of the grain boundary (m), D is the grain diameter (m), $K = D_g/\lambda RT$, D_g is the diffusion coefficient for matter transport during grain boundary migration (m^2/s), λ is the thickness of grain boundary (m), R is the universal gas constant (J/molK), T is temperature (K), σ is grain boundary energy (J/m^2) and V_m is the molar volume (m^3/mol).

Burke and Turnbull [13] applied the reaction rate theory developed by Mott [101] to derive the parabolic grain growth law according to which:

$$C = 4K"K_3\sigma V_m$$

$$K_3 = K_2 \exp(-Q_g/RT)$$

$$K_2 = 2.72 (kT/h) (\lambda/RT) \exp(\Delta S/R)$$

where the meaning of $K"$, σ, V_m, R, T and λ is as given above, Q_g is the activation energy for grain growth (J/mol), k is the Boltzmann's constant (= 1.38×10^{-23} J/K), h is the Planck's constant (= 6.6256×10^{-34} Js) and ΔS is the difference in the entropy of the atom in its activated state and in its lattice position within the shrinking grain.

Parabolic grain growth law can also be derived according to the mobility theory which yields the relation:

$$C = 4K"\sigma M$$

where M is the grain boundary mobility (m^4/Js) given by:

$$M = M_o \exp(-Q/RT)$$

where M_o is the pre-exponential constant (m^4/Js) and Q is activation energy for grain growth (J/mol).

Nishizawa [102] and Yoshie et al. [103] have given the mathematical equation describing C based on the above ideas. Their grain growth model can be represented by:

$$d^2 - d_o^2 = Ct$$

$$C = \sigma V_m D_{gb} / \lambda RT$$

$$D_{gb} = D^o_{gb} \exp. (-Q_{gb}/RT)$$

where, D_{gb} is the diffusion constant at the grain boundary for austenite, D^o_{gb} is the diffusion coefficient, Q_{gb} is the activation energy for grain boundary self diffusion of austenite and the rest of the terms have the same meaning as given before.

Bjorklund and Hillert [104] describe their interpretation of C as follows:

$$d^2 - d_o^2 = (0.5\alpha\sigma M) t$$

where α is a constant of the order unity and M is a rate controlling parameter, interpreted as the grain boundary mobility for the system under consideration.

Sellars and Whiteman [105] analysed previously published grain growth data on low carbon - manganese steels and arrived at the following general expression for evaluating the constant C as given below:

$$d^n - d_o^n = \{A \exp. (-Q_{gg}/RT)\} t$$

where A is a constant which depends on material composition and temperature and Q_{gg} is the apparent activation energy for grain growth.

Mechanism of grain boundary migration is considered to be dependent on diffusion and therefore the activation energy for grain growth should be relatable to the activation energy for grain boundary self diffusion in metals. This is found to be the case for high purity metals, especially for the migration of low angle grain boundaries [106], but not in commercial alloys and the migration of high angle grain boundaries: See Table 1.2

Table 1.2: Reported data on M_0, Q_{gg} and Q_{gb}

Material	M_0 (m^4/Js)	Q_{gg} (kJ/mol)	Q_{gb} (kJ/mol)	Reference
Aluminium	4.6×10^{15} *	364	84	[23]
α-Brass (commercial purity)	16.7 - 167 *	251	-	[107]
0.08 - 0.8 % C, low alloy steels	-	377 - 473	159^+	[17]
Ferritic irons	-	460	174^+	[13]
Ti-microalloyed steels Nb-microalloyed steels and Cr-Mo low alloy steels	71.8×10^{-4} 34.5×10^{-4}	224 224	- -	[109]
Nb-microalloyed steels	$\cong 10^{-12}$ (0.06 Nb), 10^{-11} (0.03 Nb), 10^{-10} (0.01 Nb)	200	-	[55]

* See Annexure I for calculation procedure

+ Data from [108] included for comparison

It can be seen from Table 1.2 that the reported values of Q_{gg} are found to be much higher than Q_{gb} values. The possible reasons are: 1) Changes in grain boundary structure can occur at high temperature from ordered to disordered and therefore boundaries may lose their mobility. 2) Effect of solute atoms in reducing the mobility (solute drag effect).

It is clear from the foregoing discussion that the parameter C thus incorporates complex

influences of diffusion reaction, temperature, composition and grain boundary mobility

on the grain growth law. It is felt that the experimental data of grain boundary mobilities

in metals are very scarce and systematic experimentation is needed to advance the

understanding of the concept of grain boundary mobility and consequently the parameter

C.

1.2.5 Hillert's Theory of Normal Grain Growth

In his landmark paper, Hillert [18] applied the principles of particle coarsening

developed earlier by Lifshitz and Slyozov [110] to the problem of normal and abnormal

grain growth in metals. Some of the important results of Hillert's theory concerning

normal grain growth in absence of particles are presented in this section while results

related to grain growth in presence of particles are given later in #1.3.2.

Hillert's analysis is based on the following assumptions:

- The grain boundary migration rate is proportional to the "curvature" of the grain

  boundary and hence proportional to the inverse of its "radius of curvature" {smaller

  the radius of curvature (smaller the grain size) $\Rightarrow$ higher the curvature $\Rightarrow$ higher the

  rate of g. b. migration; and higher the radius of curvature (larger the grain size) $\Rightarrow$

  lower the curvature $\Rightarrow$ lower the rate of g. b. migration}.

- The rate of grain growth is proportional to the rate of grain boundary migration.

- There is a critical size for grain growth to occur such that grains larger than this size

  will grow and grains smaller than this size will be eliminated.

- Grain shape is assumed to be circular in two dimensional analysis and spherical in

  three dimensional analysis.

Based on these assumptions, Hillert arrived at the following equation which describes the rate of grain growth as a function of the grain size:

$$dR/dt = \alpha M\sigma \ (1/R_{cr} - 1/R) \qquad (1.4)$$

where R is the grain radius, R_{cr} is the **critical minimum** radius for grain **growth**, α is a geometric constant (= 0.5 for two dimensions and 1 for three dimensions), M is the mobility of the grain boundary and σ is the grain boundary energy.

It is clear from Eq. (1.4) that for R = R_{cr}, dR/dt = 0; for R > R_{cr}, dR/dt has a positive value which indicates <u>grain growth</u> and for R < R_{cr}, dR/dt has a negative value which indicates <u>grain shrinkage</u>. Hillert then demonstrated that, in fact, the mean grain radius of the population, $\overline{R}$, approaches R_{cr} in two dimensional analysis and $\overline{R}$ = 8/9 R_{cr} in three dimensional analysis. In other words, a grain must be at least as big as the mean size to be able to grow in two dimensions while it has to be at least 1.125 times bigger that the mean size to be able to grow in three dimensions.

Hillert derived an expression for time-invariant growth rate of mean grain size according to which:

$$d\overline{R}^2/dt = 0.5\alpha M\sigma \qquad (1.5)$$

Integrating this expression –

$$\overline{R}^2 - \overline{R}_o^2 = 0.5\alpha M\sigma t \qquad (1.6)$$

Hillert thus obtained the parabolic grain growth kinetics.

Finally, Hillert's theory gives the time-invariant grain size distribution according to:

$$f(u) = \{(2e)^\beta \ \beta u/(2-u)^{2+\beta}\} \ \exp. \ [-2\beta/(2-u)] \qquad (1.7)$$

where β has a value of 2 for two dimensions and 3 for three dimensions and u is the relative size (= $R/\bar{R}$). This distribution function predicts the maximum size of the grain as $R_{max} = 1.8\,\bar{R}$ for three dimensions and $R_{max} = 1.7\,\bar{R}$ for two dimensions during the process of grain growth. This means that if a given microstructure already contains grains larger than $\cong 1.8\,\bar{R}$, then these grains will grow abnormally. Abnormal grain growth is expected to end when the grain size distribution approaches that given by Eq. (7). As has been mentioned in #1.1.3, this result is considered incorrect and experimental results of this work will also show that grains larger than $1.8\,\bar{R}$ do not always grow abnormally in the microalloyed steels studied.

1.3. Kinetics of Grain Growth in Presence of Particles

1.3.1 The Zener Limit

1.3.1.1 Background

It has been pointed out in sections 1.1.2 and 1.1.3 that the presence of precipitate particles can inhibit the normal grain growth quite effectively. Zener [20] first proposed that the driving pressure for grain growth arising due to the curvature of the grain boundary would be counteracted by the pinning (drag) pressure exerted by the particles on the grain boundary. As a consequence, the normal grain growth would be completely inhibited when the grain size reaches a critical **maximum** grain size (R_c) given by:

$$R_c = 4r/3f \tag{1.8}$$

where R_c is called the Zener limit, r is the radius of the pinning particles and f is the volume fraction of particles. Eq. (1.8) is known as the Zener Equation. The general form of the Zener equation can be given as:

$$R_c = K \, r/f^m \qquad\qquad (1.9)$$

where K is a dimensionless constant and m is the index for volume fraction of precipitates.

It should be pointed out at the outset that the Zener equation is **not** a theory of grain growth in particle containing materials. As has been given in #1.2.1, any theory of grain growth must describe at least three parameters: mean grain size and grain size distribution as a function of time and the time-invariant grain growth rate. In this context, the Zener limit is simply the "critical" grain size which neither grows nor shrinks due to the balance of driving and pinning pressures. The Zener equation thus does not give information about the actual process of grain growth nor does it indicate the growth rate or the size distribution of grains in a material.

However, Eq. (1.8) is of great significance because this is the first equation which demonstrated qualitatively as well as quantitatively that in a material with high volume fraction of fine precipitates, grain size will be limited to a smaller value. Thus, Eq. (1.8) is a key to achieve fine grain size in materials, particularly in microalloyed steels. Further, the Zener equation has played a pivotal role in the subsequent development of grain growth theories in particle containing materials (these theories will be treated separately in #1.3.2, #1.3.3 and #1.3.4). Mathematical model developed in this work (Chapter 5) is also based on Eq. (1.8).

Derivation of Eq. (1.8) involved several assumptions which limited the applicability of Eq. (1.8) in describing the grain growth situations in real materials. Therefore, the subsequent research efforts were directed at accounting for these assumptions and modifying Eq. (1.8) such that the equation becomes more realistic. Mathematical derivation of the Zener equation is given in #1.3.1.2, the assumptions made in the derivation of Eq. (1.8) and the consequent modifications of Eq. (1.8) are detailed in # 1.3.1.3 while the applications of the Zener equation are summarised in #1.3.1.4.

1.3.1.2 Derivation of the Zener Equation

Zener did not give any diagram for particle-grain boundary interaction geometry, however, based on the description given by Smith [20] a schematic illustration has been prepared by Reed-Hill [111] as given Fig. 1.4.
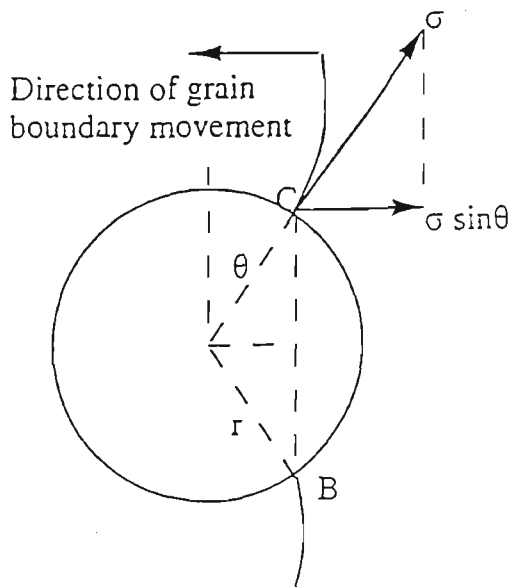
Line of contact in two dimensions = BC
∴ (BC/2) / r = Cosθ
∴BC = 2rcosθ
Total length of line of contact in three dimensions = π (BC) = 2πrcosθ

Figure 1.4: Schematic illustration of the particle - grain boundary interaction geometry assumed in Zener analysis. {After [111]}.

In reference to Fig. 1.4, the Zener derivation can be divided into five steps as given below:

STEP 1: Calculation of maximum pinning (drag) force (F_z) exerted by **one** particle on the grain boundary:

Pull on the g. b. due to one particle = (Total line of contact in three dimensions)x(Component of surface tension in the direction opposite to the direction of movement of the g. b.)

$$= 2\pi r\sigma \sin\theta\cos\theta$$

For maximum pull, $\theta = 45°$.

$$\therefore \text{Maximum pinning force per particle } (F_z) = \pi r\sigma \qquad (1.10)$$

F_z is also called the Zener pinning (drag) force.

STEP 2: Calculation of the surface density of particles (n_s) on the g. b.:

$$n_s = \{\text{number of particles per unit volume } (n_v)\}x(r)$$

No explanation was given for this postulate. However, Nes et al. [112] suggested that this equation accounts for the number of particles within a distance r in front of the grain boundary. They reasoned further that n_v should be multiplied by, in fact, 2r to calculate n_s because all the particles within a distance $\pm$ r of the grain boundary (in front of as well as behind the g. b.) would interact with the grain boundary. In any case, following the **original** logic,

$$n_s = \{\text{volume fraction of precipitates (f)/volume of one spherical precipitate}\}x(r)$$

$$= 3f/4\pi r^2 \qquad (1.11)$$

STEP 3: Calculation of maximum pinning pressure due to all particles (P_z) on the grain boundary:

$$P_z = F_z\, n_s$$

$$= 3f\sigma/4r \qquad \{\text{from Eq.s (1.10) and (1.11)}\} \qquad (1.12)$$

If the suggestion by Nes et al. [112] was considered, then the P_z is given by:

$$P_z = 3f\sigma/2r \qquad (1.12a)$$

Equation 1.12 can also be written as:

$$P_z = \sigma \, \mathbf{z} \qquad (1.13)$$

where $\mathbf{z}$ (= $3f/4r$) is called the **Zener factor**. However, according to Nes et al. [112] the Zener factor is given by:

$$\mathbf{z} = 3f/2r \qquad (1.13a)$$

STEP 4: Calculation of driving pressure (P_g) for grain growth:

Smith states "the driving force for grain growth is provided by the surface tension and is quantitatively equal to σ/ρ_{net} .... to a first approximation, one can anticipate a definite relation between curvature of the boundary (virtually equal to grain size)...."

From these statements, one has to construct an equation for P_g.

$$P_g = \sigma/\rho_{net} \qquad (1.14a)$$

where, $1/\rho_{net} = 1/\rho_1 + 1/\rho_2$, where ρ_1 and ρ_2 are the principal radii of curvature of the grain boundary. For a spherical grain, $\rho_1 = \rho_2 = \rho$ which leads to $\rho_{net} = \rho/2$, substituting this in Eq. (1.14a) yields:

$$P_g = 2\sigma/\rho \qquad (1.14b)$$

Now, the next problem is the relation between ρ and 'grain size'. It is not clear whether Smith was referring to "ρ_{net}" or "ρ" as the grain size. Further, it is also not clear if he was referring to "R (grain radius)" or "D (grain diameter)" as the "grain size". We thus have four possibilities:

$$\rho_{net} = R \qquad\qquad P1$$

$$\rho_{net} = D \qquad\qquad P2$$

$$\rho = R \qquad\qquad\qquad P3$$

$$\rho = D \qquad\qquad\qquad P4$$

Substituting possibilities P1 and P2 in Eq. (1.14a) gives the results:

$$P_g = \sigma/R \qquad\qquad\qquad (1.14c)$$

$$P_g = \sigma/D = \sigma/2R \qquad\qquad\qquad (1.14d)$$

Substituting possibilities P3 and P4 in to Eq. (1.14b) yields:

$$P_g = 2\sigma/R \qquad\qquad\qquad (1.14e)$$

$$P_g = 2\sigma/D = 2\sigma/2R = \sigma/R \qquad\qquad (1.14f) = (1.14c)$$

We thus have three distinct expressions for P_g namely $\sigma/2R$, σ/R and $2\sigma/R$.

STEP 5: Equilibrium when $P_z = P_g$; $R = R_c$:

We have three possible equations for P_g {Eq. s (1.14c, 1.14d and 1.14e)} and two

possible equations for P_z {Eq. s (1.12 and 1.12a)}. This will lead to six possible

equations for R_c as given below:

Eq. (1.14c) = Eq.(1.12)	Eq. (1.14c) =Eq.(1.12a)	Eq. (1.14d) =Eq. (1.12)	Eq. (1.14d) =Eq.(1.12a)	Eq. (1.14e) = Eq. (1.12)	Eq. (1.14e) =Eq.(1.12a)
σ/R_c = 3fσ/4r	σ/R_c = 3fσ/2r	$\sigma/2R_c$ = 3fσ/4r	$\sigma/2R_c$ = 3fσ/2r	$2\sigma/R_c$ = 3fσ/4r	$2\sigma/R_c$ = 3fσ/2r
R_c = 4r/3f	R_c = 2r/3f	R_c = 2r/3f	R_c = r/3f	R_c = 8r/3f	R_c = 4r/3f
OK	Possible	Possible	No	No	OK

In view of the final result given by Zener - Smith (R_c = 4r/3f), it appears that $P_g = \sigma/R_c$

($\rho = D$) in combination with $P_z = 3\sigma f/4r$; and $P_g = 2\sigma/R_c$ ($\rho = R$) in combination with P_z

$= 3\sigma f/2r$ gives the same final result.

1.3.1.3 Modifications of the Zener Equation

Several assumptions were made during the derivation of the Zener equation. These

assumptions have been classified and a summary of the modifications to account for

these assumptions is given in the following sections.

Assumptions regarding geometry of particle-grain boundary interaction:

- Shape of the particle-grain boundary interface is not clearly defined.

- Grains and particles are assumed to be spherical.

- Particles are treated as incoherent.

- Surface tension between the grains (σ) is considered, however, interface tension between the grains and the particle is ignored.

Gladman [19] analysed the particle-grain boundary interface geometry and concluded that the grain boundary can not remain planar (flat) near the particle and the g. b. will be pulled towards the particle causing the grain boundary to be curved. Based on this modification, he arrived at $F_z = 3.96r\sigma$, which is slightly higher than that due to Zener {Eq. (1.10)}.

Ashby et al. [113] considered the interaction of "coherent" particles with the g. b. and arrived at the expression for $F_z = 2\pi r\sigma$, which is twice the value given by Zener {Eq. (1.10)}.

Doherty [114] accounted for the experimentally observed fact that small coherent particles can be dissolved (a process like the inverse of precipitation) by a moving g. b. and gave a relation for F_z similar to that given by Ashby et al. [113].

Ryum et al. [115] considered the effect of 'shape' (ellipse) of the particles and their orientation with respect to the g. b. to calculate F_z according to:

$$F_z = F_z^s/\pi\{(1+2.14\varepsilon)/\varepsilon^{0.33}\} \text{ for } \varepsilon \geq 1, \text{ and long axis perpendicular to the g. b.}$$

$$= F_z^s \, \varepsilon^{0.47} \text{ for } \varepsilon \leq 1, \text{ and long axis perpendicular to the g. b.}$$

$= F_z^s \{2/(1+\varepsilon) \varepsilon^{0.33}\}$ when long axis is parallel to the g. b.

where ε is the eccentricity of the ellipse given by the ratio of the lengths of the short and long axis and F_z^s is the maximum pinning force due to spherical particle. They have shown that in Al-Mn alloy, the drag force could be two to four times higher ($\varepsilon = 0.1$ to 0.5) in the direction normal to the rolling direction which leads to very elongated grains after the recrystallization of the alloy.

Analysis by Ringer et al. [116] gives the result that 'cubic' shaped particles of certain orientations lead to approximately double the maximum pinning force offered by the spherical particles. They have also demonstrated the effect of not neglecting the surface tension between particles and the grains which leads to significantly lower value of K in Eq. 1.9 (more effective pinning) than the value of 1.33 given by Zener.

Haroun and Budworth [117] considered the effect of 'shape of the grains' (truncated octahedron) on the P_g and gave the result that $\rho = 18R$ and not $\rho = 2R$ as assumed in Zener - Smith analysis. This modification leads to significantly lower value of K (= 0.074) in Eq. 1.9.

Considerations of the distribution of particles in a material:

Some of the assumptions made in the derivation of the Zener equation in relation to the distribution of particles in a material were as follows:

- Particles are randomly distributed.

- Details of the interaction of the grain boundary with the distribution of particles are not given at all.

- All particles are of equal size.

Fullman [118] accounted for the distribution of particle sizes by introducing a "dirt factor (I)" given by $I = \Sigma\ f(r)/r$ where $f(r)$ is the volume fraction of spherical particles of size r. The pinning pressure is then given by:

$$P_z = 3I\sigma/4$$

Wold and Chambers [119] included the fact that the particles tend to form more at the grain boundaries than the interior of the grains so that particles are <u>not</u> randomly distributed. With this approach they suggested the following equation for P_z:

$$P_z = 3k\sigma f/4r$$

where K is a factor greater than unity (1~2) which expresses the greater likelihood of finding particles in the g. b. than in the bulk of the metal. They also investigated the effect of disc and needle shaped particles on P_z.

Hazzledine et al. [120] considered the effect of pulling of the g. b. (flexible grain boundary) by many particles which cause "dimples" on the inside and outside surface of the g. b. s. Using this logic, they arrived at:

$$P_z = 1.1 - 1.37\ \sigma f/r$$

which is close to the modified Zener estimate of $1.5\sigma f/r$ {Eq. (1.12a)}. A similar result was obtained by Nes et al. [112] whereby:

$$P_z = 1.3\sigma f^{0.92}/r \cong 1.3\sigma f/r.$$

However, Hunderi et al. [121] considered the Louat effect [122] {particles ahead of the moving g. b. would pull the g. b. towards them, thus in fact, tend to assist the movement of the g. b.} to arrive at:

$$P_z = 0.33 \sigma f^{0.87}/r \text{ for } f < 0.03.$$

In addition to the particle-assisted g. b. motion, Louat [122] also considered the effect of

particles which trail the boundary at distances exceeding r and arrived at:

$$R_c = 4r/3f\{16/\ln(Re^2/2r)\}$$

which indicates that for large R, the R_c would be smaller than Zener (higher restraint)

and for small R, the R_c would be larger than Zener (lesser restraint).

Chan and Humphreys [123] suggested that the grain boundaries migrate by means of

ledges or steps sweeping across the boundary and arrived at:

$$P_z = 1.38 \sigma f^{0.5}/r,$$

giving almost an order of magnitude larger pinning pressure than the modified Zener

{Eq. (1.12a)}.

Hellman and Hillert [124] reported the effect of grain size on P_z. They suggested that

when the grain size is large, the grain boundary is able to stay in contact with larger

numbers of the particles and therefore the pinning effect increases in proportion to ρ/r

where ρ is the macroscopic curvature of the grain boundary (spherical grain) given by ρ

= 6R. They found that:

$$R_c = 4r/9\beta f, \quad \beta = 0.125 \ln(8\rho/r) \text{ or } \beta = 0.125 \ln(40\rho/r)$$

It is clear from the above equation that the ratio ρ/r controls the value of R_c. For

example, considering $\beta = 0.125 \ln(8\rho/r)$, for $\rho/r = 10$, $R_c = 0.81r/f$ while for $\rho/r = 10000$,

$R_c = 0.32r/f$. This result is in qualitative agreement with the Louat [122] analysis

although completely different logic is used in each case.

Assumptions regarding the relation between grain boundary curvature (ρ) and the grain radius (R):

- Driving pressure (P_g) is given equal to σ/ρ_{net} where $\rho_{net} = \rho/2$, where ρ is the macroscopic curvature of the spherical grain, resulting in $P_g = 2\sigma/\rho$. Further, ρ = "grain size" = (possibly) D where D is the grain diameter = 2R where R is the grain radius, so that $P_g = \sigma/R$.

Feltham [86] analysed the relation between the radius of curvature and the 'shape' of the grain in two dimensions and arrived at:

$$R/\rho = f(n/n^*)$$

where,

$$f(n/n^*) = \sin[\pi/6(1-n^*/n)]/\sin[\pi/6(n^*/n)]$$

where n is the number of sides of a grain and n* is the most probable number of sides of a grain to be expected in a truly planar arrangement (= 6). When a grain has sides < 6, then it has convex boundaries and such a grain will shrink. On the other hand when a grain has sides > 6, then it has concave boundaries and it will grow. For example, for a grain with n = 4, the value of $f(n/n^*) = R/\rho = -0.33$ ($\Rightarrow\rho = -3R$) with "-" sign indicating convex boundary and for a grain with n = 8, the value of $f(n/n^*) = R/\rho = +0.33$ ($\Rightarrow\rho = +3R$) with "+" sign indicating the concave boundaries.

Haroun and Budworth [117] suggest the relation as $\rho = 18R$ as mentioned before. Patterson and Liu [125] have introduced the mean linear intercept λ and suggest the relation $\lambda = 0.31\rho$ for a three dimensional structure. λ can be measured on the metallographic sample. Using the relation $\lambda = 1.33R$ reported by Han and Kim [126] for

spherical grains, the value of ρ thus becomes $\rho = 4.3\ R$. However, Hellman and Hillert [124] have suggested the relation $\rho = 6R$ as mentioned before.

Assumptions regarding the effect of initial grain size distribution on the driving pressure (P_g) for grain growth:

Original derivation of the Zener equation does not involve detailed consideration of the effect of initial grain size distribution on the driving pressure for grain growth (P_g). Hillert [18] analysed the effect of grain size distribution together with the pinning effect of particles on grain growth and suggested two limits in the process of grain growth given by:

a) $R_{c1} = 0.44r/f$ which is the limit for normal grain growth, however abnormal grain growth can continue; and

b) $R_{c2} = 0.67r/f$ which is the limit for total grain growth inhibition.

A more detailed account of the Hillert's theory will be given in the section 1.3.2.

Gladman [19] considered that the distribution of grain size would affect the driving pressure according to:

$$R_c = [\pi(0.25-0.33/Z)]r/f \qquad\qquad (1.15)$$

where Z is the ratio of growing grains to matrix grains and which represents the heterogeneity of grain size distribution in the sample. Equation (1.15) indicates that the higher the value of Z, the higher is the tendency for grains to coarsen i.e. larger R_c.

Wold and Chambers [119] incorporate Gladman's theory with their k factor ($\sim 1 - 2$) and reported that the value of R_c can be:

$$R_c = 2r/3kf[(3Z-4)/2Z]$$

Elst et al. [127] attempted to combine the concepts of Zener [20], Hellman-Hillert [124], Gladman [19] and Ryum et al. [115] to explain experimental results of grain growth obtained by them in a particle containing β-Copper-based shape memory alloy and found a good correlation between the experimental results and theoretical predictions of grain growth.

Based on the themes outlined above, modifications were made to make the Zener equation more realistic. Such modifications are summarised in Table 1.3. This list of modifications covers all major modifications however it is not exhaustive as some minor modifications and some of the computer simulation results are not included.

A few general observations can be made regarding the modifications listed in Table 1.3. The most striking observation that can be made is the variation in the value of 'K' - the value of K is found to be significantly lower in all modifications and in the extreme case, K is found to be as low as 0.05 {Patterson and Liu [125]}, which is about 27 times lower than the value of 1.33 as given by Zener. Secondly, in comparison with Zener analysis, researchers have found F_z for incoherent particles to be lower than Zener, n_s higher than Zener, P_z much higher than Zener and P_g lower than Zener, the total effect being a much finer predicted R_c than Zener.

Table 1.3: Modifications of the Zener Equation

(Arranged chronologically)

r is the particle radius, f is the volume fraction of particles and ρ is the radius of curvature of the grain boundary, σ is the grain boundary energy, z is the Zener factor (= 3f/4r), Z is the Gladman's heterogeneity factor (= R_{max}/R_{mean}), R is the grain radius, R_c critical grain radius at inhibition of normal grain growth, P_g is the driving pressure for grain growth, P_z is the maximum pinning pressure due to all particles, F_z is the maximum pinning force due to one particle and n_s is the surface density of particles on the grain boundary.

* Equations are derived after equating the P_z given by the authors with the appropriate expression for P_g as given under 'comments' column.

Reference	Equation, $R_c =$	Comments
C. Zener [C. S. Smith]: Trans. AIME, 175, (1948), 15 [20]	1.33r/f	Original equation. ($P_g = 2\sigma/\rho$, $\rho = D$, $\therefore P_g = \sigma/R$)
R. L. Fullman: Metal Interfaces, ASM, (1952), 179 [118]	1.33/I $I=\Sigma f(r)/r$	I is the dirt factor which accounts for a range of particles, f(r) is the volume fraction of spherical particles of radius r. ($P_g = 2\sigma/\rho$, $\rho = D$, $\therefore P_g = \sigma/R$)
M. Hillert: Acta. Metall., 13, (1965), 227 [18]	0.44r/f 0.67r/f	Lower limit for normal g.g. inhibition. Upper limit for total g.g. inhibition. Considered the effect of g.s. distribution on g. g., driving force for g.g. proportional to ($1/R_{cr}$- $1/R \pm$ z)
T. Gladman and F. B. Pickering: JISI, 205, (1967), 653 [46]	$[\pi(1/4-1/3Z)]r/f \cong$ 0.05 - 0.26 r/f	Driving force is considered a function of grain size distribution and $\therefore$ proportional to Z and $\therefore$ R_c depends on the value of Z (typically, Z = 1.41 and 2). Z is the heterogeneity factor. Z $\geq$ 4/3 for g. g. to occur.
N. A. Haroun and D. W. Budworth: J. Mater. Sci., 3, (1968), 326 [117]	0.074 r/f 1.03r/(f)$^{0.5}$	After considering ρ=18R, and not ρ=2R as assumed by Zener. Modified Zener eqt. under condition that there exists at least one particle on each grain boundary. Both eqt.s derived for truncated octahedron grain shape and yield similar results for f = 0.5%.
K. G. Wold and F. M. Chambers: J. Aust. Inst. of Metals, 13, (1968), 79 [119]	2r/3kf[(3Z_{max} -4)/(2Z_{max})]	k>1 after considering that particles would be present more on the g. b. than in the bulk. Also combined Gladman's approach.
M. F. Ashby, J. Harper and J. Lewis: Trans. Met. Soc. AIME, 245, (1969) 413 [113]	0.33r/f *	$F_z = 2\pi\sigma r$ - twice the value given by Zener. Considered the effect of coherency of particles on the max. pinning force. ($n_s = 3f/2\pi r^2$ and $P_g = \sigma/R$)

Reference	Equation, $R_c =$	Comments
P. Hellman and M. Hillert: Scand. J. Metals, 4, (1975), 211 [124]	$4r/9\beta f \cong 0.81 - 0.31\ r/f$ $\beta = 0.125 \ln (8\rho/r)$	Depending on the value of the ratio ρ/r, which can be between 10 - 10000. β is expected to decrease as the volume fraction increases. Also gave $\rho = 6R$
L. Anand and J. Gurland: Metall. Trans., 6A, (1975), 928 [129]	$1.18 r/(f)^{0.5}$ *	$\lambda = 1.63 r/(f)^{0.5}$. Considered that λ (mean linear intercept)/1.38 = mean grain radius of a truncated octahedron.
P.M.Hazzledine, P.B.Hirsch and N. Louat: Proc. 1st Riso Int. Symp, ed. by N. Hansen et al., Denmark, (1980), 159 [120]	$0.91 - 0.73 \ r/f$ *	Considered the effect of pulling of the g. b. s by the particles causing "dimples" on the inside as well as outside surface of the g. b. s. ($P_z = 1.1 - 1.37\sigma f/r$; $P_g = 2\sigma/R$)
O. Hunderi and N. Ryum: Acta Metall., 30, (1982), 739 [256]	$0.67\ r/f$ or $0.33\ r/f$	$R_c = 1/2z$, $z = 3f/4r$ or $3f/2r$ is not clarified in the paper.
N. Louat: Acta Metall., 30, (1982), 1291 [122]	$4r/3f\{16/(\ln[Re^2/2r])\}$	Considered effects of: a) particles at distances > r from g. b. and b) some particles would assist the motion of the g. b. s.
R. D. Doherty: Metal Sci. J., 16, (1982), 1 [114]	$0.17 r/f$ *	Considered the effect of coherent particles and arrived at $F_z = 2\pi\sigma r$, twice that by Zener (similar to Ashby et al. [113]), and $P_z = 6\sigma f/r$, 8 times that by Zener, $P_g = \sigma/R$
N. Ryum, O. Hunderi and E. Nes: Scripta Met., 17, (1983), 1281 [115]	see text for eqt. describing F_z	Considered effect of ellipsoidal particles and their orientation w.r.t. g. b. s on F_z.
H. M. Chan and F. J. Humphreys: Acta Metall., 32, (1984), 235 [123]	$1.45 r/f^{0.5}$ *	Considered the effect of ledge mechanism of g. b. migration to arrive at eqt. for P_z.($P_g = 2\sigma/R$)
E. Nes, N. Ryum and O. Hunderi: Acta Metall., 33, (1985), 11 [112]	$1.54 r/(f)^{0.92}$*	Correction of original Zener's equation, also considered the effect of initial distribution of g.s. on R_c. Dimple model. $P_z = 1.3\sigma f^{0.92}/r$; $P_g = 2\sigma/R$
P. R. Rios: Acta Metall., 35, (1987), 2805 [257]	$0.17 r/f$	Considered energy dissipation approach, rather than pinning pressure when a g. b. moves through a dispersion of particles.
R. D. Doherty, D. J. Srolovitz, A. D. Rollet and M. P. Anderson: Scripta Metall., 21, (1987), 675 [258]	$1.7 r/(f)^{0.5}$	Result of the two dimensional computer simulation considering non-random particle distribution.
M. Hillert: Acta Metall., 36, (1988), 3177 [259]	$0.22 r/(f)^{0.93}$ $1.8\ r/(f)^{0.33}$ $1.7 r/(f)^{0.5}$	3 Dimensions, f < 0.1 3 Dimensions, f > 0.1 2 Dimensions, Attempted to explain computer simulation results by using mean field theory.

Reference	Equation, $R_c =$	Comments
R. Elst, J. Von Humbeeck and L. Delaey: Acta Metall., 36, (1988), 1723 [127]	$2/3\beta(3/2 - 2/Z)r/f$ $\cong 0.075 - 0.45\ r/f$	Combined approaches of Zener [20], Ryum et al. [112], Gladman [19] and Hellman-Hillert [120]. Also calculated R_c for elongated ppt.s / bimodal distribution / g.b. ppt.s.
S. P. Ringer, W. B. Li and K. E. Easterling: Acta Metall., 37, (1989), 831 [116]	$1/2K(r/f)$	K depends on interaction geometry of the g. b. with particle. (Assuming incoherent particles and $\rho = 2.15D$, $R_c = 0.16r/f$ for spherical and $R_c = 0.06 / 0.08 / 0.12\ r/f$ for cubic particles of different orientations with respect to the g. b.)
O. Hunderi, E. Nes and N. Ryum: Acta Metall., 37, (1989), 129 [121]	$6.1r/f^{0.87}$ * for f < 0.03	Considered Louat effect [122] viz. some particles tend to assist the g. b. movement. ($P_g = 2\sigma/R$)
B. R. Patterson and Y. Liu: Metall. Trans., 23A, (1992), 2481 [125]	Theoretical: $0.31r/f$ Experimental: $0.051 - 0.155\ r/f$	considered relationship between λ (Mean Linear Intercept) and the grain boundary curvature: $\rho = \lambda/0.31$, with $\lambda = 1.33R$, $\rho = 4.3R$. Experimentally determined values of K lower than theoretical due to non-random intersection of pores with the g. b. s. Data for $Al-Al_2O_3$ system by C. J. Tweed, N. Hansen and B. Ralph: (Met. Trans. ASM, 14A, 1983, 2235 [260]) found fitting well with the prediction from proposed equation.
Y. Liu and B. R. Patterson: Scripta Met., 27, (1992), 539 [261]	$0.051 - 0.155r/f$	Experimentally determined expression.
P. A. Manohar, D. P. Dunne and T. Chandra: ISIJ Int., 36, (1996), 194 [262]	$0.17r/f$	Prediction from the equation correlates well with the experimental data for g.g. of mean γ g.s. during reheating of MA steel slabs.
P. R. Rios: Scripta Mater., 34, (1996), 1185 [263]	$0.33r/f$	Proposed equation derived based on three different approaches.

1.3.1.4 Applications of the Zener Equation

Despite the several limitations mentioned above, the Zener equation has been utilised to describe the grain growth phenomenon in a wide variety of materials including steels and the correlation between experimental results and predictions based on Eq. (1.9) has been found to be encouraging. Gladman and Pickering [46] obtained a good correlation between the experimentally determined and calculated GCT of Al- and Nb- treated grain refined steels. Hellman and Hillert [124] explained the grain growth of ferrite in presence of cementite particles in 0.2, 0.4 and 0.8 % C, plain carbon steels. Anand and Gurland [129] obtained a good relation between the sub-grain size and the size of the spheroidized cementite particles in a range of plain carbon steels containing 0.4 to 1.24 % C in quenched and tempered condition. L'Ecuyer and L'Esperance [130] found that particle pinning delayed the dynamic recrystallization in a Mo-bearing HSLA steel. Sinha et al. [131] explained abnormal grain growth observed in maraging steel (18Ni-8Co-5Mo-0.4Ti) in terms of Zener pinning. Palma et al. [132] found Eq. (1.9) useful in predicting grain size in sintered high speed tool steel. Hannerz and de Kazinczy [133] utilised Zener approach to calculate grain growth in C-Mn and Nb/V/Ti-treated C-Mn steels. Yoshie et al. [103] included Eq. (1.9) to predict reheated austenite grain size of a series of steels containing 0.1% C and 1.4 % Mn as base composition with 0.03 % Al, 0.03 % Al + 0.035 % Nb, 0.03 % Al + 0.01 % Ti steels in their global mathematical model to predict microstructural evolution and mechanical properties of steel plates. Monte-Carlo simulation of grain growth in particle containing materials by Saito and Enomoto [134] has resulted in an equation which is a variation of Eq. (1.9). Liu and Jonas [135] found experimentally a value of $K = 0.1$ and $m = 1$ in Eq. (1.9) for a series of Ti-steels containing 0.07 % C, 1.5 % Mn as base composition with 0.05, 0.11, 0.18

and 0.25 % Ti additions. Recently, Gladman [136] has used a variation of Eq. (1.9) to explain principles of grain size control in Al-treated steels. Eq. (1.9) has also been used in non-ferrous metals - for example, in Al-Cu and Al-Co alloys by Ashby et al. [113], Al containing Al_2O_3 by Tweed et al. [128], Al-Si alloys by Chan and Humphreys [123], β-copper-based shape memory alloy by Elst et al. [127] and two-phase Ti alloys by Grewal and Ankem [137]. Eq. (1.9) has been used in a number of ceramic materials which has been summarised by Worner and Hazzledine [138].

1.3.2 Hillert's Theory

Hillert [18] extended the logic used to describe the normal grain growth in particle-free materials to explain the grain growth behaviour of particle-containing materials by incorporating the Zener factor. The rate of grain growth in particle-containing materials, according to Hillert, is given by:

$$dR/dt = \alpha M\sigma \ (1/R_{cr} - 1/R \pm z/\alpha) \tag{1.16}$$

where $z = 3f/4r$. Thus the pinning pressure "σz" acts in such a way as to always oppose the movement of the grain boundary.

For small values of R, the term $-1/R$ dominates the right hand side of the Eq. (1.16) and negative growth rates are obtained. The z term will be positive in this case. According to Eq. (1.16), such grains can shrink if they are small enough to satisfy the condition:

$$1/R_{small} > 1/R_{cr} + z$$

For large values of R, the term -1/R will be small, and a positive growth rate can be obtained. However, the z term will be negative in this case. Large grains can grow if they are large enough to satisfy the condition:

$$1/R_{large} < 1/R_{cr} - z$$

Between these two limits, $R_{small} < R < R_{large}$, the value of z term is such that zero growth rate is obtained. These grains neither grow nor shrink. Hillert then argued that if all the grains in the material are larger than R_{small} and if all the large grains are pinned by particles, then the structure is in equilibrium. He found the value of R_{cr} at which this can occur according to:

$$R_{cr1} = 1/3z = 0.44 \, r/f$$

If $R = R_{cr1} = \overline{R} = 0.44r/f$, then inhibition of normal grain growth occurs. If there are some grains already coarser than R_{cr1}, they can grow abnormally until they grow to a size given by:

$$R_{cr2} = 1/2z = 0.67r/f$$

In this case, if $R = R_{cr2} = \overline{R} = 0.67r/f$, then even abnormal grain growth has to cease and the structure is in equilibrium. However, if there exist any grains which are already coarser than R_{cr2}, then abnormal grain growth can continue without limit.

Hillert proposed the rate of growth of the mean grain size according to:

$$d\overline{R}^2/dt = 0.5\alpha M\sigma(1-z\overline{R}/\alpha)^2 \qquad (1.17)$$

Comparison of Eq. s (4) and (1.16) shows that the rate of grain growth is retarded by second phase particles. Comparison of Eq. s (5) and (1.17) shows that the maximum mean grain size that can be obtained in particle-containing materials is determined by the values of r and f and is equal to R_{cr2}.

1.3.3 Gladman's Approach

Prior to Gladman's work, it had been widely acknowledged that the driving force for grain growth is derived from the reduction in grain boundary energy as the grain size is increased. The mechanism by which a grain grows had been suggested to be curvature driven growth [13, 18] where the boundaries migrate towards their centre of curvature; and the angle driven growth [83, 86] where the triple points move to make 120° angles between the interfaces of the three grains concerned. Gladman considered the change in 'energy' accompanying the growth of tetrakaidecahedral shaped grains filling space in three dimensions to arrive at:

$$dE/dR = \sigma\,(2/R - 3/2R_o) \tag{1.18}$$

where dE/dR is the rate of change of energy with respect to the radius 'R' of the growing grain and R_o is the radius of the matrix grains. Equation (1.18) indicates that the grain growth is possible only when $R > 4/3R_o$ so that dE/dR has a negative value. This means that when a grain is larger than 1.33 times its neighbours, the growth of such a grain would decrease the energy of the system.

Gladman also considered the relation between coarsening of the particles and grain growth. He argued that when a grain is unpinned from the particles, it contributes to an increase in the energy of the system. The energy released due to unpinning has to be balanced by the decrease in energy due to grain growth which leads to the following condition:

$$r_{crit} = 6R_o f/\pi\,(3/2 - 2/Z)^{-1} \tag{1.19}$$

Equation (1.19) shows that when particles coarsen to a size given by "r_{crit}", they are no longer able to pin the grains and the grain growth can then proceed. r_{crit} can be seen to

increase with increasing matrix grain size (R_o), and volume fraction of particles (f) and with decreasing Z. This means that with higher heterogeneity in the material (higher Z) even the smaller particles would be relatively ineffective in pinning of the grains because r_{crit} decreases with increasing Z. Increase in r_{crit} increases the GCT because the particles must grow up to r_{crit} before grain growth can commence. Thus Gladman's theory suggests that to have a higher GCT (i. e. higher r_{crit}) a material must have a relatively coarser matrix or mean grain size (higher R_o), a high volume fraction of precipitates and a lower heterogeneity in the grain size distribution (low Z).

Gladman [35] has considered the effect of particles distributed preferentially at the grain boundaries (non-random particle distribution) which could influence r_{crit} and can be given by:

$$r_{crit} = 2R_o f^{0.5} (3/2 - 2/Z)^{-1}$$

Equation (1.19) can be rewritten in the following form to obtain the size of the critical grain at unpinning according to:

$$R_c = \pi (1/4 - 1/3Z) r/f \qquad (1.20)$$

When $Z \leq 4/3$, inhibition to grain growth occurs. When Z is inordinately large, the criterion for grain coarsening becomes unsatisfactory because in this case we start with a duplex structure. Gladman found that Z values between 1.41 and 2 give excellent agreement with experimental results. Inserting these values of Z in to Eq. (1.20), Gladman's criterion for grain coarsening can be written as:

$$R_c = 0.05 \sim 0.26 \ r/f \qquad (1.21)$$

1.3.4 Relative Rate Model

1.3.4.1 Introduction

Rios [47] proposed a relative rate model (RR model) for predicting abnormal grain growth in the presence of coarsening particles. Relative rate model has been derived based on the fundamental equation given by Hillert [18] and its solution by Hunderi and Ryum [14]. The conditions of grain growth under which the RR model is thought to be applicable are quite similar to those experienced during reheating of microalloyed steels. Relative rate model attempts to find the growth rate of the large grain relative to the growth rate of the critical grain and can be represented by the following equation:

$$dU_a/dU_c = \varepsilon [1/2 - 1/U_a - U_a/(U_c\varepsilon)] \qquad (1.22)$$

where, $U_a = R_a/R_c$, $U_c = R_c/R^o_c$, R_a is radius of the large grain, R_c is the instantaneous critical grain radius for normal grain growth, R^o_c is the initial critical grain radius, ε is a dimensionless parameter. R_c and R^o_c are given by:

$$R_c = br/f$$

$$R^o_c = br^o/f^o$$

where, b is a constant {= 0.083 [139]}, r is the particle radius, r^o is the initial particle radius, f^o is the initial volume fraction of precipitates.

The parameter ε can be evaluated according to the following equation:

$$\varepsilon = 3(r^o f^2/b^2)K_g/K_p \qquad (1.23)$$

The parameter K_g incorporates the grain boundary mobility and can be described by the following equation:

$$K_g = \alpha \sigma M \qquad\qquad (1.24)$$

where, α is a geometric constant (= 1 for three dimensional grain growth), σ is the grain boundary energy and M is the grain boundary mobility.

The parameter K_p describes the particle coarsening and the value of K_p can be found through the following equation:

$$K_p = 8D\sigma V_m C^s/9RT \qquad\qquad (1.25)$$

where, D is the diffusivity of solute atoms in the matrix, V_m is the molar volume of the precipitate, and C^s is the concentration of solute dissolved in the matrix at temperature T (K).

The value of dU_a/dU_c determines the nature of grain growth and therefore, a discussion on the possible values of dU_a/dU_c is presented in the following section.

1.3.4.2 Interpretation of the model

In general, dU_a/dU_c can have a value higher than, equal to or less than zero. Each of these possibilities represent a set of definite circumstances of grain growth. It is necessary to understand the physical implications of these possible values of dU_a/dU_c in order to interpret the results obtained by using RR model.

Case 1: Grain growth when $dU_a/dU_c > 0$:

Positive value of dU_a/dU_c indicates that the rate of growth of the large grain is faster than the rate of growth of the limiting grain for normal grain growth. This means that the large grains are able to grow even larger as compared to the limiting size. This condition is analogous to abnormal grain growth. Smaller grains (R < Rc) are pinned by

second phase particles and get consumed by the growth of large grains. The value of dU_a remains > 0, indicating generation of greater heterogeneity in the grain size distribution due to the process of abnormal grain growth.

Case 2: Grain growth when $dU_a/dU_c = 0$:

When large grains grow in exact proportion to the growth of the limiting size, the relative rate of growth of the large grains with respect to the growth rate of limiting size equals zero. This condition thus represents steady state grain growth. In order to achieve the steady state, it is necessary from Eq. (1.22) that :

$$\varepsilon \left[1/2 - 1/U_a - U_a/U_c\varepsilon \right] = 0$$

The only condition when ε can be zero is when $f = 0$, because all other terms which determine the value of ε can not be zero in real systems {see Eq. (1.23)}. It has been reported in Ti-microalloyed steels that it is not feasible to dissolve all types of precipitates in austenite [140] and it is likely that f will not become zero. This suggests that steady state grain growth is achieved only when :

$$1/2 - \left[1/U_a + U_a/U_c\varepsilon \right] = 0$$

$$\therefore 2U_a^2 - (U_c\varepsilon)U_a + 2U_c\varepsilon = 0$$

For a given composition and for a given condition of temperature and time, the above equation can be treated as a second degree equation in the variable U_a. The steady state solutions for U_a are :

$$U_a = \left[U_c\varepsilon \pm \{ (-U_c\varepsilon)^2 - 16U_c\varepsilon \}^{0.5} \right] / 4 \qquad (1.26)$$

In order that these solutions be real, it is necessary that :

$$U_c\varepsilon \geq 16$$

Thus, the RR model predicts that steady state grain growth is achieved if $U_c\varepsilon \geq 16$ and when the values of U_a are equal to those given by Eq. (1.26).
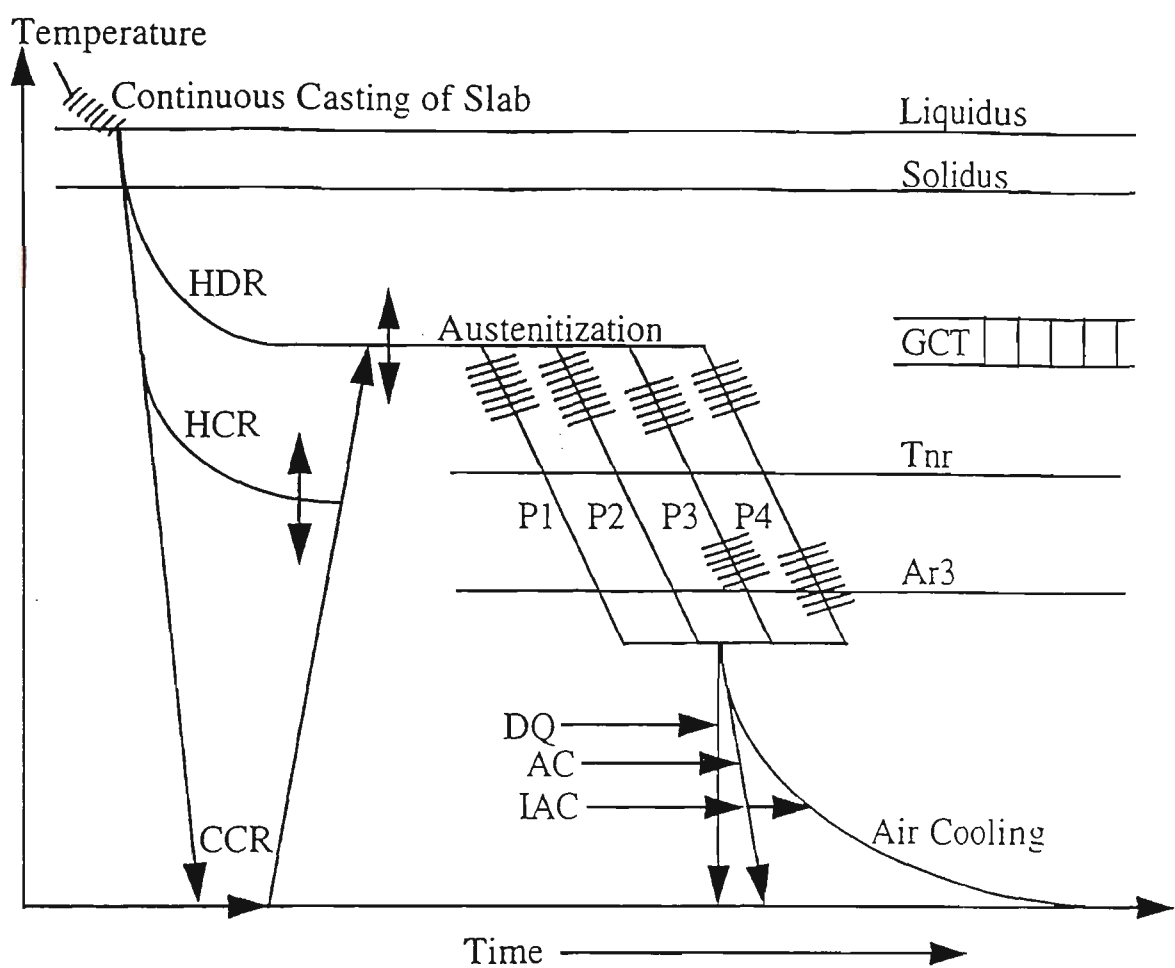
Case 3: Grain growth when $dU_a/dU_c < 0$:

The mathematical possibility that $dU_a/dU_c < 0$ indicates that the large grain grows at a rate which is slower than the critical grain. This means that the growth rate of the mean grains is faster than that of the large grains and therefore, this process will tend to reduce the heterogeneity in grain size distribution in the microstructure. This is consistent with Hillert's theory of grain growth which assumes existence of a quasi-steady state grain size distribution which is stable for a given condition of time and temperature. This condition can arise in microalloyed steels when the process of abnormal grain growth leads to the total consumption of the smaller grains and the final microstructure consists of larger grains only. In this condition, second phase particles have either been dissolved or coarsened to such an extent that they are ineffective in controlling the grain growth process. Now, the large grains can not attain further abnormally larger sizes because of the occurrence of impingement with its already coarsened neighbouring grains. Such a condition must result in a relatively homogeneous grain size distribution. Therefore, the negative value of dU_a/dU_c may be taken as a certain indication of the end of abnormal grain growth. In other words, negative value of dU_a/dU_c is an indication of beginning of normal grain growth tending to achieve a steady state distribution of grain sizes.

Chapter 2: Literature Review: Thermomechanical Processing (TMP) of Austenite in Microalloyed Steels

2.1 Introduction

Thermomechanical processing (TMP) is defined as a hot deformation schedule (rolling, forging, extrusion etc.) designed for the purpose of achieving a predetermined microstructure in austenite prior to transformation [DeArdo/141]. The microstructure of austenite can be described by parameters such as grain size, composition, presence or absence of microalloy precipitates, degree of recrystallization and texture. Comparison of conventional and TMP techniques for hot rolling of steel is shown schematically in Fig. 2.1. Conventional hot rolling (CHR) consists of reheating the continuously cast slab to austenitization, soaking, continuous rolling of the slab to the desired thickness and subsequent air cooling to room temperature. In conventional controlled rolling (CCR), the first two stages (reheating and soaking) are similar to CHR, however rolling involves <u>two</u> stages in CCR, see Fig. 2.2. In the first stage, which is called 'roughing', deformation is carried out <u>above</u> a certain critical temperature known as "No-Recrystallization Temperature (T_{nr})". Roughing deformation results in austenite grain refinement due to repeated recrystallization cycles after each rolling pass. In the second stage, called 'finishing', deformation is carried out below T_{nr}. There is significant time delay between the roughing and finishing deformations to let the temperature of the rolling stock to fall below T_{nr}. Finishing deformation below T_{nr} results in deformation and flattening of the austenite grains because the austenite is unable to recrystallize at this stage.

Temperature

Continuous Casting of Slab   Liquidus

Solidus

HDR

Austenitization   GCT

HCR   Tnr

P1 P2 P3 P4

Ar3

DQ

AC

IAC   Air Cooling

CCR

Time

Legend:
HDR = Hot Direct Rolling
HCR = Hot Charge Rolling
CCR = Cold Charge (Conventional Controlled) Rolling
P1   = Conventional Hot Rolling (CHR)
P2   = Recrystallization Controlled Rolling (RCR)
P3   = Conventional Controlled Rolling (CCR)
P4   = Ferrite Rolling (a variation of CCR)
DQ   = Direct Quenching
AC   = Accelerated Cooling
IAC = Interrupted Accelerated Cooling
GCT = Grain Coarsening Temperature
Tnr   = No-Recrystallization Temperature
Ar3 = Austenite Transformation Start Temperature

Figure 2.1: Schematic illustration of comparison of conventional
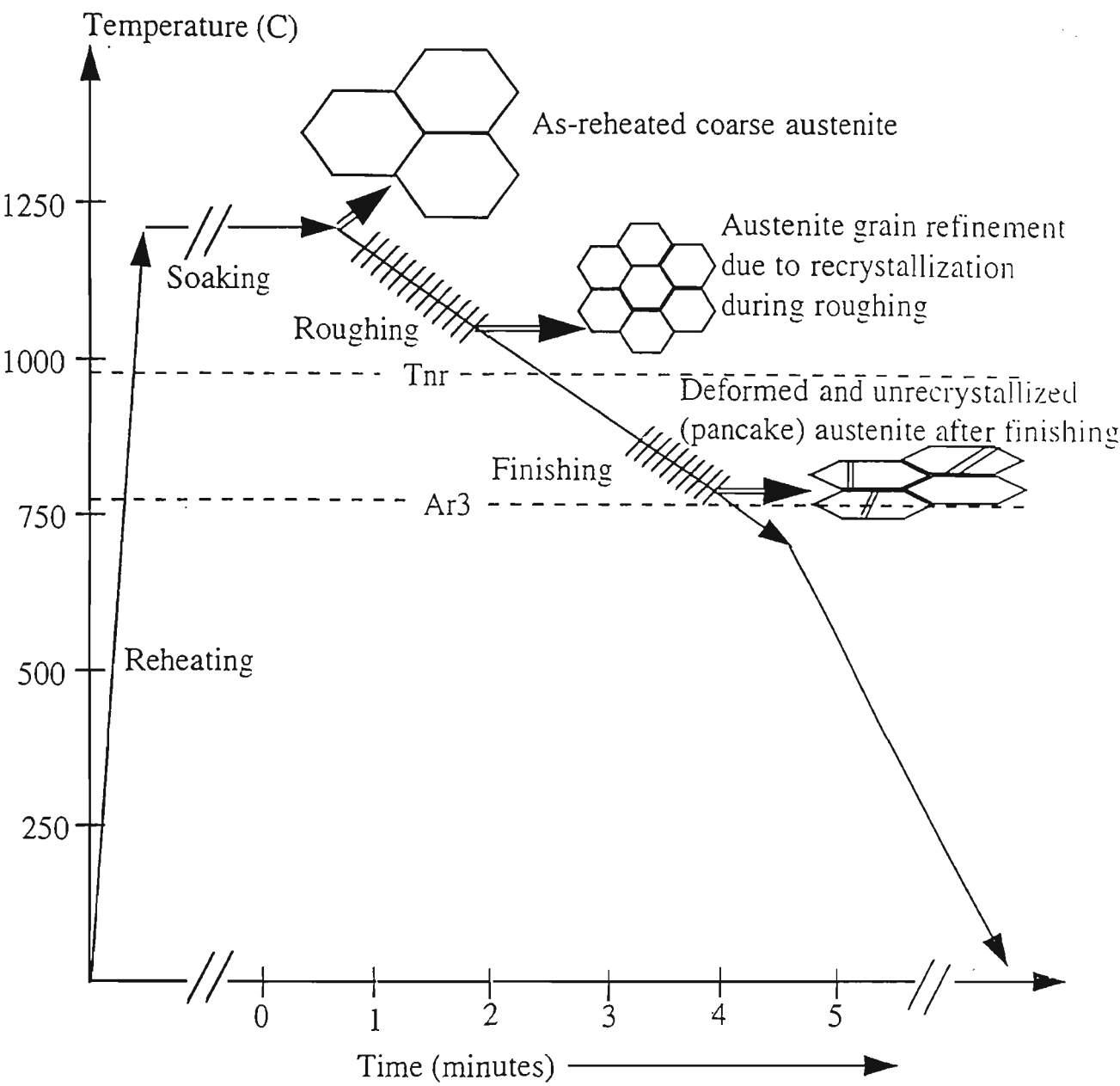and TMP techniques for hot rolling of steels.

Figure 2.2: Schematic time - temperature profile for conventional controlled rolling (CCR) of plates. {After [142]}.

The flattened and deformed austenite microstructure is called as 'pancake' structure.

Pancake austenite grains also contain deformation bands and twins. The combination of

fine austenite grain size after roughing and flattening and deformation of austenite grains

after finishing results in to an increase in "surface area per unit volume (S_v)" of austenite. This parameter - surface area per unit volume (S_v) of austenite was first proposed by Underwood [143] and later adopted by Kozasu et al. [144] to explain the underlying physical metallurgical principles of TMP of microalloyed steels. S_v can also be maximised by an alternative TMP technique called as "Recrystallization Controlled Rolling (RCR)". In RCR, the reheated austenite grain size before roughing is kept as small as possible and subsequently the grain size is refined further by repeated recrystallization cycles in roughing above T_{nr}, as shown in Fig. 2.1. The effectiveness of the TMP techniques in increasing the value of S_v is shown in Fig. 2.3.
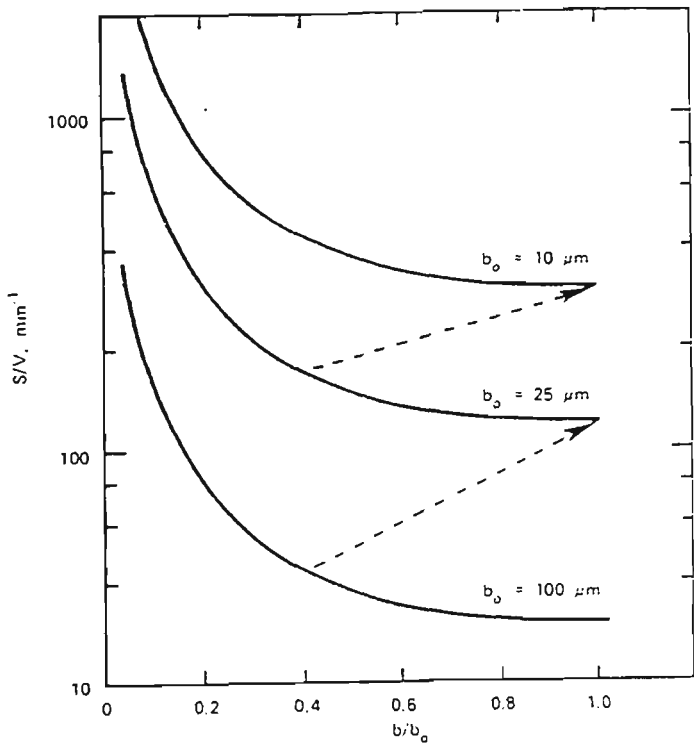

Figure 2.3: Effect of original grain diameter (b_o) and reduction in height (b/b_o) on grain boundary area per unit volume (S_v) of austenite. {After [145]}. See text for explanation.

Fig. 2.3 shows the effect of three initial grain sizes (100, 25 and 10 µm) when deformed from original sphere radius b_o to a pancake height of b (i. e. as b/b_o decreases) on S_v. If during rolling, the flattened grain recrystallizes to a smaller equiaxed grain (i. e. jumps to a smaller b_o curve), a further increase in S_v can be realised. By following a path (indicated as dotted lines in Fig. 2.3) of repeated flattening and recrystallization (such as in RCR)

and final flattening below T_{nr} (such as in CCR), S_v can be maximised by almost two

orders of magnitude as shown in Fig. 2.3. The more the surface area of austenite (i. e.

the higher the value of S_v), the higher are the sites for nucleation of transformation of

austenite during cooling, which directly results into very fine grained ferrite after the

transformation. Effect of S_v on the refinement of ferrite grain size after transformation is
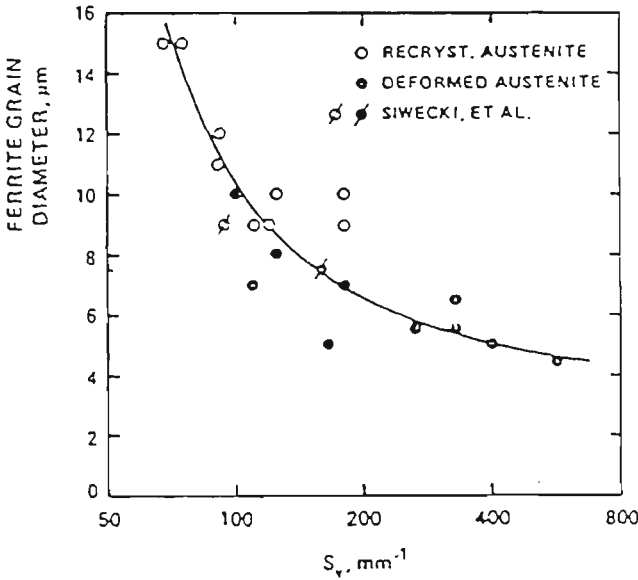
shown in Fig. 2.4.

Figure 2.4: Effect of S_v on ferrite grain size obtained from the transformation
of recrystallized and unrecrystallized austenite. {After [141]}.

In addition, it has been reported that S_v increases fracture toughness of steels as shown in

Fig. 2.5. S_v is believed to provide a set of powerful barriers to the propagation of

cleavage cracks during low temperature Charpy V-Notch impact testing, thus raising the
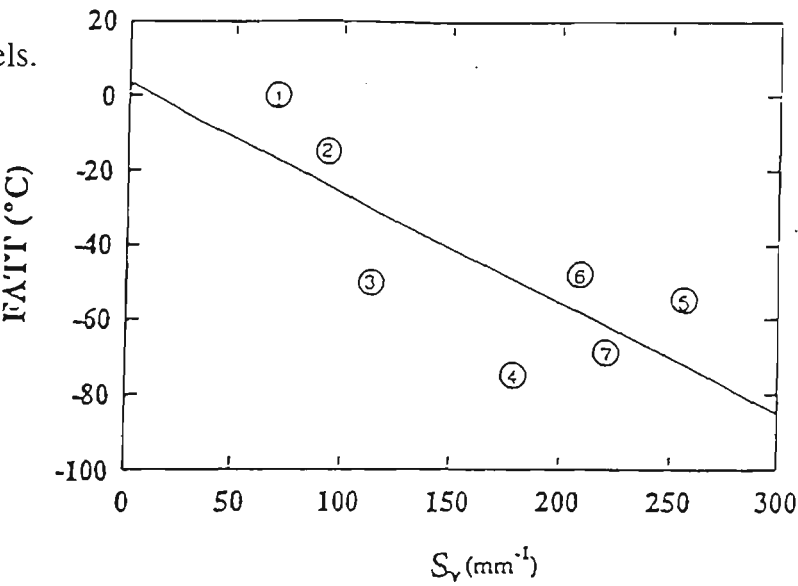
FATT of steels.

Figure 2.5: Influence of S_v on FATT. {After [146]}.

The main advantage of RCR over CCR is that in RCR, all of the deformation passes are

carried out at much higher temperature (> 1000 °C, for example) which requires lower
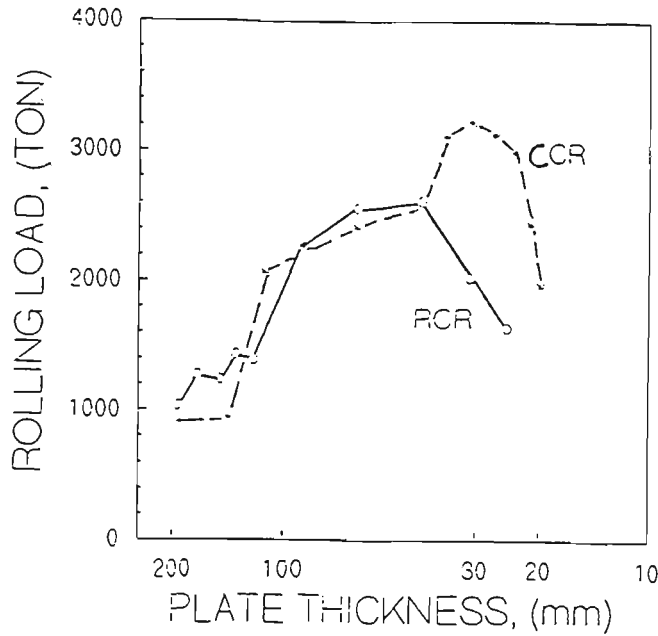
rolling loads see Fig. 2.6.

Figure 2.6: Comparison of observed rolling loads during RCR
and CCR of Ti-V-N microalloyed steels. {After [147]}.

Conventional Controlled Rolling (CCR), on the other hand, involves low temperature

deformation (at ~ 800 °C) of unrecrystallized austenite and hence requires much higher

rolling loads for finishing deformations to take place. Therefore CCR is not suitable for

those mills which are limited by the rolling load capacity. Alloy composition must be

designed such that it suits the particular TMP to be used. For example. in RCR. T_{nr}

should be <u>as low as</u> possible so that a larger processing window between the reheat

temperature and the finishing temperature is available for the processing to be finished.

In contrast, the alloy composition for CCR should be such that T_{nr} is raised <u>as high as</u>

possible so that there is sufficient gap between T_{nr} and austenite transformation start

temperature (Ar_3) without the requirement of too high rolling loads. Alloying elements

such as Mn and Mo which lower the Ar_3 also facilitate the CCR. Effect of alloy

composition and TMP variables on T_{nr} is discussed separately in # 2.5.3.

Some newer technologies in TMP have been developed such as hot direct rolling (HDR) and hot charge rolling (HCR) which are also shown in Fig. 2.1. HDR and HCR technologies offer several advantages which include significant reduction in energy consumption, efficient furnace utilisation, reductions in mill scale loss, improved delivery performance, reduced slab handling and surface and internal quality improvements [82].

Another area of on going research is the different cooling techniques subsequent to the TMP. As shown in Fig. 2.1, essentially four different options can be used: air cooling, accelerated cooling, interrupted accelerated cooling and direct quenching. Interrupted accelerated cooling of 0.06 C, 1.4 Mn, 0.08 Nb and 0.04 Ti containing steel is found to have significant effect on the type of microstructure (ferrite or bainite) and ferrite precipitation strengthening, where it was found that interruption of accelerated cooling between 700 - 640 °C gave maximum ferrite strengthening [148]. Effect of accelerated cooling variables on the metallurgical structure evolution and steel product properties is given separately in # 2.6.3.

TMP has also been used to improve the properties of conventional C-Mn steels. Matsumura and Yada [149] refined ferrite grain size up to 2 ~ 5 μm by using large reductions ($\varepsilon \sim 0.7$) just above Ar$_3$. In multi-pass deformation of 0.1 C, 1.1 Mn steel, very short interpass times (~ 2s) led to accumulation of strain, promoting deformation induced $\gamma \rightarrow \alpha$ transformation and the subsequent dynamic recrystallization of transformed ferrite, resulting in ferrite grain refinement. Another area of TMP of industrial interest involved the use of lower slab reheat temperatures, see Fig. 2.7.
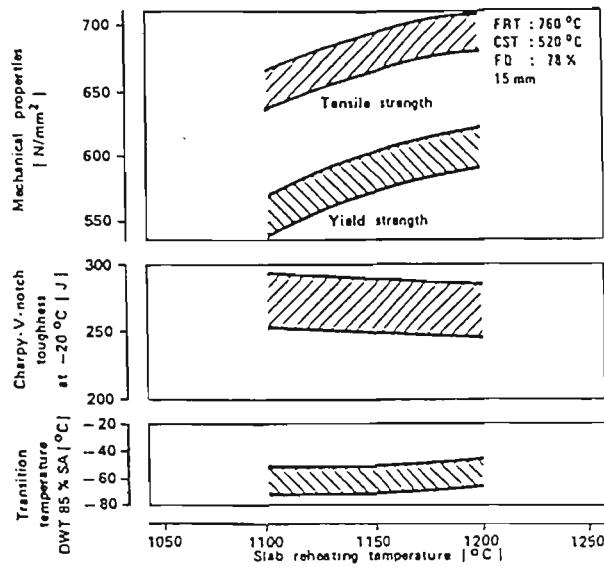
Figure 2.7: Influence of slab reheating temperature on mechanical properties
of a TM treated and AC Mn-Ti-Nb steel. {After [150]}.
Legend: FRT = Finish Rolling Temperature, CST = Cooling Stop
Temperature, FD = Finish Deformation.
Steel Composition: 0.08 C, 1.85 Mn, 0.04 Nb, 0.02 Ti. Ti:N = 5

Lower slab reheating temperatures control the austenite grain growth during soaking.

However, as can be seen from Fig. 2.7 that, in Nb containing microalloyed steels. high

reheat temperatures are found to be more effective compared to lower temperatures as

the high reheat temperatures increase the yield and tensile strengths. without any

significant decrease in the notch toughness.

2.2 Microalloyed Steels

2.2.1 Background

Microalloyed steels contain microalloying elements (MAE) of the order of 0.001% -

0.1% which significantly modify properties (yield strength, tensile strength, toughness,

formability etc.) of the base steel. Typical base composition may contain 0.06 - 0.12 % C

and 1.0 - 2.0 % Mn with optional additions of Mo (up to 1 %) , Ni (up to 3 %) and Cr

(up to 1 %). Microalloying elements include Nb (0.03 - 0.1 %), Ti (0.01 - 0.05 %). B (

0.0018 - 0.006 %), V (0.06 - 0.15 %) and Al (0.03 - 0.08 %). Copper-treated steels are

a part of High Strength Low Alloy (HSLA) steels, however they can not be termed as

microalloyed steels as the usual level of Copper addition (up to 1.25 %) is much higher

than the level of microalloy addition. Much higher levels of microalloying element

(MAE) addition (Nb up to 0.5%, Ti up to 0.3 %) have been tried out on the

experimental basis, however such high levels of addition are not common in commercial

steels. Microalloying elements (MAE) may be added either singly or in combination.

Chronological development of the use of MAE in steels is shown in Fig. 2.8.
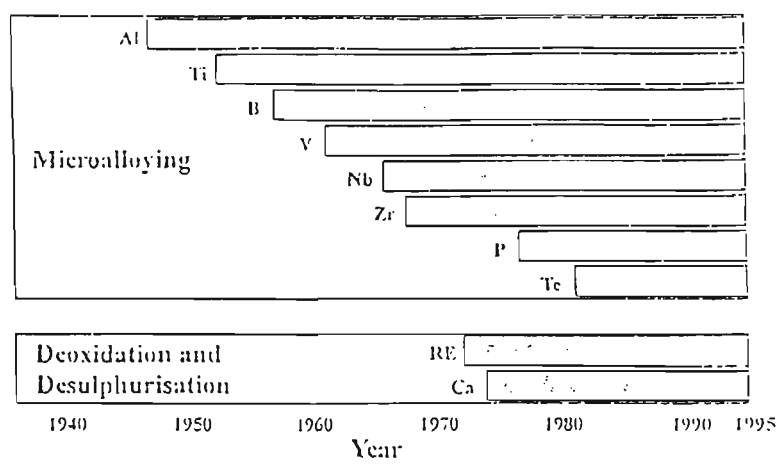
Figure 2.8: Chronological development of the use of MAE in steels. {After [151]}.

Microalloyed steels have found diverse applications over last four decades in areas such

as pipes for oil and gas pipe lines (including arctic conditions and sour-gas

environments), ship building (tanks and vessels), offshore drilling platforms, mining

equipment, structural engineering (including earthquake resistant ductile RCC

constructions) and automotive parts (long members, wheels and axles).

The advantages of microalloyed steels over conventional C-Mn steels include superior

mechanical properties, good strength/toughness ratio, excellent weldability and cold

formability, higher toughness and low transition temperature, flexibility of heat treatment

(can be used in as-rolled, normalised, accelerated cooled or in quenched and tempered

conditions) and cost-effectiveness.

Fig. 2.9 demonstrates the strength and toughness advantage of microalloyed steels and

TMP over the conventional C-Mn steels.
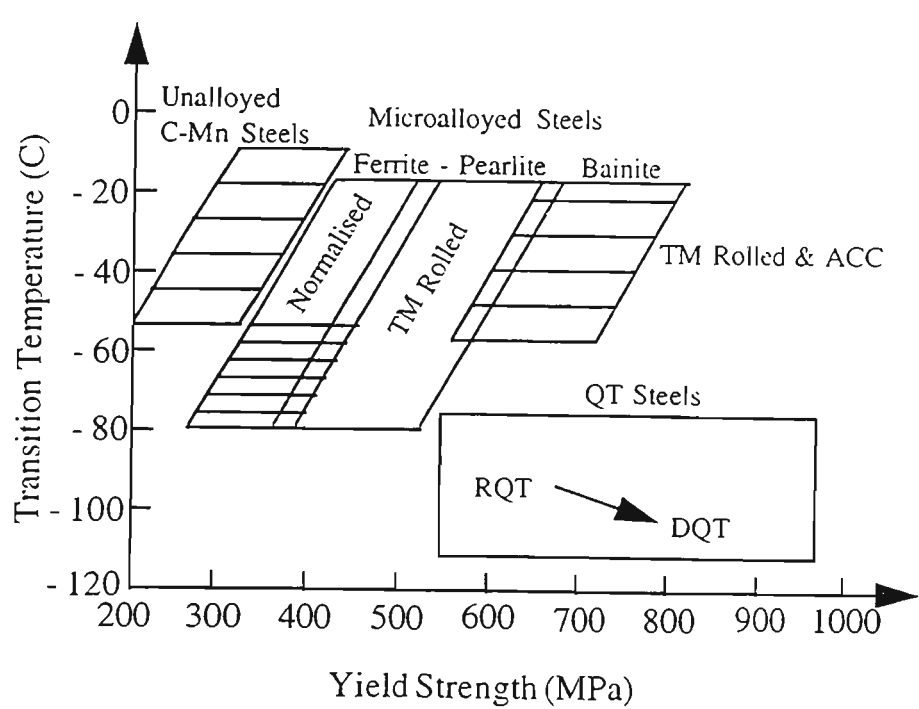
Figure 2.9: Comparison of properties of conventional C- Mn
steels and TM processed microalloyed steels. {After [151]}.
Legend: ACC = Accelerated Cooled, QT = Quenched and
Tempered, RQT = Reheated, Quenched and Tempered, DQT =
Direct Quenched and Tempered.

It can be seen from Fig. 2.9 that the combination of microalloying, TMP and accelerated

cooling can increase the strength of the base C-Mn steel almost four folds without

sacrificing toughness. Such a dramatic improvement in mechanical properties of TM

processed microalloyed steels is achieved through several metallurgical phenomena such as grain refinement, precipitation hardening, dislocation strengthening, solid solution hardening, control of microstructure through TMP and accelerated cooling (AC) and the generation of favourable textures. Fig. 2.10 gives a qualitative assessment of the individual phenomena contributing to the increase in yield strength of TM rolled and AC (bainitic) hot strip. Effects of addition of individual alloying and microalloying elements on metallurgical structure and mechanical properties of steels is presented in the following section.
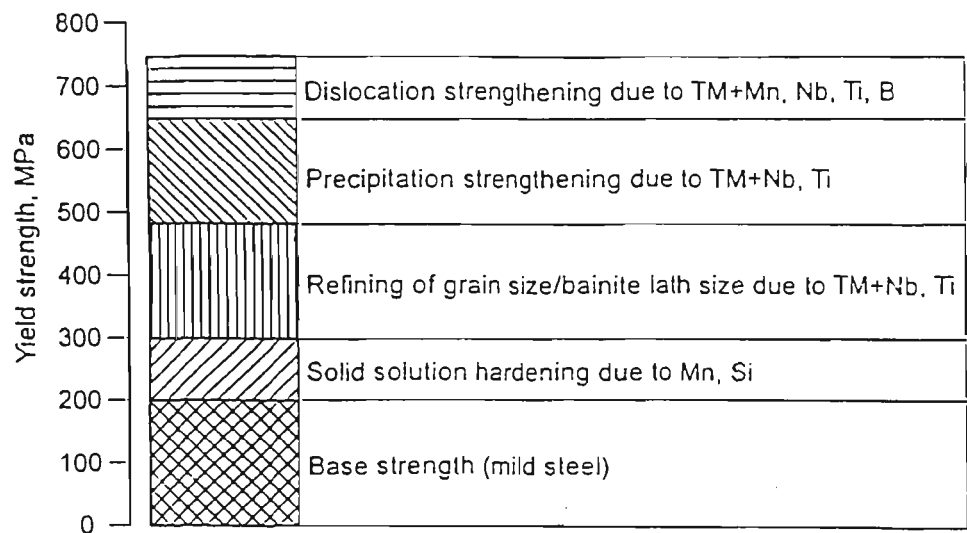
Figure 2.10: Contributions to yield strength due to alloying, MAE and TMP of a TM rolled bainitic hot strip. {After [151]}.

2.2.2 Effects of Alloying and Microalloying on Metallurgical Structure Parameters

The interaction of alloying, microalloying and TMP variables exerts a strong influence on metallurgical structure parameters such grain size and shape, precipitates of various sizes and their stability, microstructure type (ferrite, bainite, martensite etc.), dislocation

density, texture and size, shape and distribution of non-metallic inclusions. These parameters in turn control the properties of the final steel product. The MAE differ from one another in their physical and chemical features and have different effects on precipitation (through reaction with C and N), recrystallization, phase transformation and inclusion control (through reaction with S and O). Effects of individual alloying and microalloying elements on the metallurgical phenomena are briefly described in the following sections.

Niobium:

Strain induced precipitation of NbCN retards recrystallization most effectively while Nb in solution also retards the recrystallization to some extent. Kwon and DeArdo [152] found that Nb suppresses recrystallization by one order of magnitude when in solution (at T > 1000 °C) and by 2.9 orders of magnitude when precipitated (at T < 950 °C). Zadeh and Dunne [153] found that Nb in solution and as strain induced precipitates increases not only the incubation time but also the time for completion of recrystallization. The retarding effect of strain induced NbC on the progress of recrystallization was much more marked than that of solute Nb. As a consequence, addition of Nb significantly increases the T_{nr}. Dissolved Nb increases hardenability and contributes to microstructure control in conjunction with AC. It has been reported that the addition of Nb increases yield strength, tensile strength and toughness through refinement of ferrite grain size and an increase of volume fraction of bainite [154]. Precipitation of Nb in ferrite increases strength of ferrite even further through precipitation hardening.

Titanium:

Ti reacts preferentially with N to form stable TiN precipitates which control grain growth behaviour of austenite. Dissolved or precipitated Ti has a similar effect of

retarding austenite recrystallization as Nb, although Ti is not as effective as Nb in retarding austenite recrystallization. Ti also has an affinity for S to form hard carbosulfides and thus prevent the undesirable effects exerted by elongated MnS particles. Ti raises T_{nr}. Precipitation of Ti in ferrite leads to precipitation strengthening. It has been reported that an increase in Ti content from 0% up to 0.15% increases the tensile strength, yield strength, toughness and refines ferrite grain size [154]. Effect of Nb, Ti and other MAE on properties of steels is shown qualitatively in Table 2.1.

Table 2.1: Effects of MAE on metallurgical parameters and mechanical properties of steels. {After [155]}.

MAE	Effect on hot formability of concast slabs	Increase of rolling loads	Retardation of Rx	Effect on γ→α transformation rate	Grain refinement	Ppt. strengthening	Texture development	Resistance to ageing	Cold formability (Sulphide shape control)	Ability to form IF steels
Nb	-	+	+ +	-...+ (*)	+ +	+ +	+	+		+
Ti	+	+	+ +	-...+ (*)	+	+ +	+	+	+	+
V			(+)	-	(+)	+		+		
Zr	+							+	+	
B	+			- -				(+)		

Notes:

+ ⇒ positive effect, - ⇒ negative effect, open ⇒ no significant effect, (*) ⇒ effect depends on thermal history

Nitrogen:

Most optimum properties in Ti-bearing steels are achieved when Ti:N ratio is ≤ 3.42. Effect of Ti:N ratio on austenite grain size at fusion line of C-Mn-Nb steels is shown in Fig. 2.11.
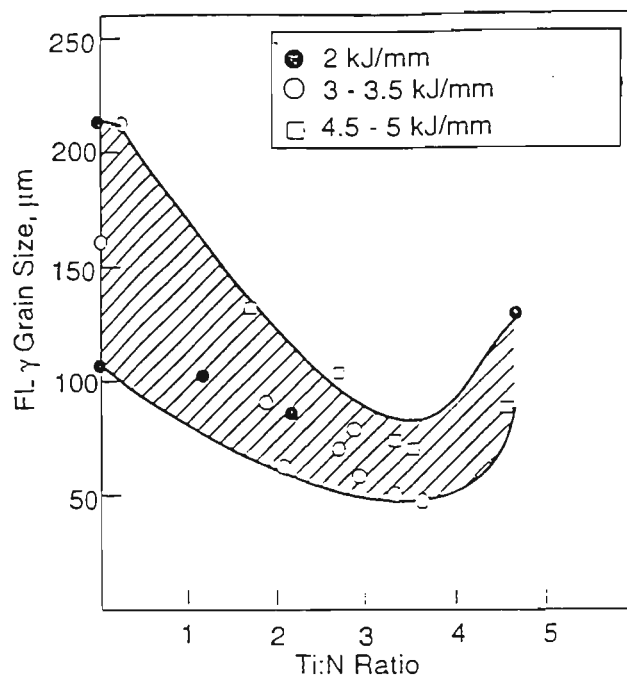
Figure 2.11: Effect of Ti:N ratio on austenite grain size at
fusion line in C-Mn-Nb steels. {After [156]}.

Excessive addition of N content (> 80 ppm) in Nb steel was found to have deleterious

effect on mechanical properties because large (~1.3 μm), cuboidal NbN particles formed

in the steel melt which could not be dissolved even up to 1300 °C during reheating and

thus this Nb was lost and not available for precipitation during further processing or for

grain refining [Albarran et al., 157]. For RCR processing, N content should be ≤ 40 ppm

to reduce the formation of NbCN precipitates which inhibits recrystallization strongly

[147]. Higher N content in Ti-V steels however, has been found to improve the

transformation ratio ($\gamma_{g.s.}$ / $\alpha_{g.s.}$) [147]. In Ti-treated steels, N content in excess of

stoichiometry can be tolerated without seriously affecting Ti:N dispersion [142, 158].

Silicon:

Addition of Si has been found to increase the yield and tensile strengths without affecting

either % elongation or yield ratio [159]. Silicon is a ferrite stabiliser and when added in

excess of 1 % leads to enrichment of austenite in C during transformation which

promotes bainitic or martensitic transformation of the enriched austenite. In dual phase

steels (ferrite + martensite microstructure), the martensitic transformation causes internal stresses in ferrite due to volume expansion during martensitic transformation, which has a favourable effect of eliminating the yield point and results in continuous yielding behaviour of dual phase steels. However, small changes in Silicon content (0.1 ~ 0.35 % Si) are found to have effect on HAZ toughness of Ti-killed steels [160]. Higher addition of Si scavenges O from melt and forces Ti to form TiN instead of TiO. TiN refines grain size leading to a decrease in hardenability, which reduces the amount of acicular ferrite and promotes the formation of grain boundary allotriomorphic and Widmanstatten ferrite thus reducing the toughness of the HAZ. TiO is considered to be most effective in nucleating acicular ferrite which has a higher toughness than allotriomorphic or Widmanstatten ferrite.

Molybdenum:

It has been found that the addition of Mo increases yield and tensile strengths of steel which is attributed to the increase in acicularity of ferrite [161]. However, when Mo contents exceed ~ 0.4 %, a sharp drop in toughness is observed which is caused by martensitic transformation.

Manganese:

Effect of Mn content on mechanical properties of Nb bearing microalloyed steels is shown in Fig. 2.12. Addition of Mn increases yield strength of steels. Appropriate combination of Mn and Mo reduces the precipitation of NbCN in austenite by decreasing the diffusivity of Nb in austenite [163], offsets Bauschinger effect and generates acicular ferrite structure which exhibits continuous yielding behaviour [77, 78]. These characteristics have been found to be of great importance in the manufacture of high strength, ERW linepipe [164].
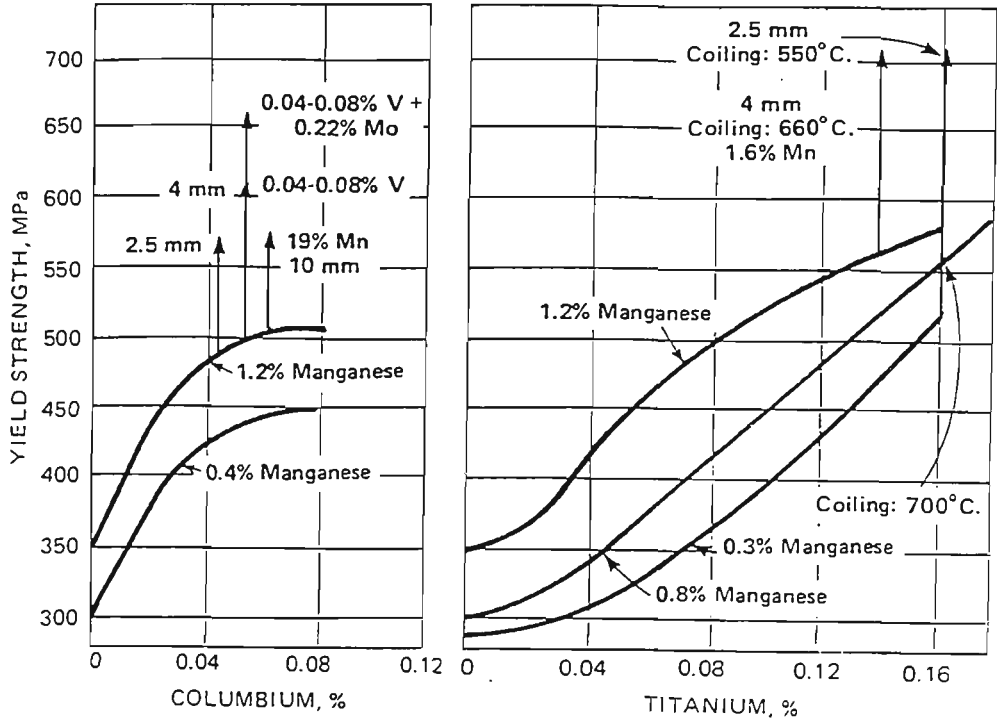
Figure 2.12: Effect of Mn content on the yield strength of hot rolled strip. {After [162]}. The base composition averaged 0.08 C and 0.3 Si and the strip thickness was 8 mm. The effect of thinner gages, lower coiling temperatures or additional alloying is shown by arrows.

2.3 Recrystallization Behaviour of Microalloyed Austenite

2.3.1 Background

Thermomechanical processing of microalloyed steels following reheating and soaking begins by high temperature deformation of austenite usually referred to as "roughing" deformation. The objective of roughing deformation is to achieve as fine and uniform austenite grain size as possible along with thickness reduction of the rolling stock through repeated recrystallization. Consider for example following practical values of the process parameters during controlled rolling of a Ti-Nb microalloyed steel:

Table 2.2: Typical practical values of the process parameters used during conventional controlled rolling of Ti-Nb Microalloyed steels.

Reheating Temperature = 1250 °C

	Rolling Start Temp. (°C)	Initial Thickness (mm)	Number of Passes	Amount of Defor. Per Pass	Strain Rate (s^{-1})	Rolling Finish Temp. (°C)	Final Thickness (mm)
Roughing	1100	250	10-15	5-15 %	2-10	1000	40-50
Finishing	900	40-50	5-10	5-15%	10-20	750-800	15-20

The values of process parameters given in Table 2.2 may change depending on the particular composition to be processed and also on the type of TMP to be used. For example, in Recrystallization Controlled Rolling (RCR), the values of the amount of deformation per pass in roughing may be substantially higher as compared to the values for Conventional Controlled Rolling (CCR) given in Table 2.2. Following the deformation of austenite, several softening processes such as, dynamic, metadynamic and static recovery and recrystallization, may operate in the austenite structure. When the strains during roughing are high, the deformed austenite may immediately begin to recover while in the roll-gap, a process known as dynamic recovery. At strains higher than a critical value, the austenite recrystallizes as soon as it is deformed, a process known as dynamic recrystallization. In dynamic recrystallization, the rate of work hardening of austenite is balanced by the rate of softening. Dynamic recrystallization occurs while the deformation is taking place within the roll gap. At pass strains much lower than the critical strain for dynamic recrystallization, austenite may soften during the interpass time following the pass deformation by processes called as static recovery and static recrystallization. In conventional controlled rolling, it is the static recrystallization which is most common and therefore the information presented in the following sections pertains to static recrystallization. Subsequent reference to recrystallization in this review refers to static recrystallization.

In microalloyed steels, the static recrystallization kinetics are considerably delayed as compared to the C-Mn steels so that sufficient amount of deformation must be given during each roughing pass to ensure that static recrystallization is completed before the next pass begins. Light reductions during roughing deformations may result in partially recrystallized austenite or may trigger abnormal grain growth [25] instead of grain refinement.

2.3.2 Influence of Compositional and Process Parameters on the Static Recrystallization of Microalloyed Austenite

Medina and Mancilla [165] suggest that refinement of initial austenite grain size increases the nucleation sites for recrystallization by increasing the surface area per unit volume (S_v) of austenite and thus contributes to the acceleration of recrystallization. Increase in pass strain has been found to accelerate recrystallization strongly through increased nucleation due to increased dislocation density of austenite and also through greater driving force for recrystallization [165 - 167]. Increase in strain rate allows less time for deformation which leads to less restored and more highly work-hardened austenite which increases the driving force for recrystallization. However, the accelerating effect of strain rate has been found to be a less dominant effect on recrystallization kinetics [167]. Lowered temperature of deformation has been shown to retard recrystallization because the thermal activation needed to rearrange dislocation arrays as a pre-cursor to recrystallization is decreased at low temperatures [166, 168].

Increase in microalloy content (Ti, Nb) retards recrystallization through solute drag effect at high temperatures and retards recrystallization very strongly at low

temperatures through precipitate pinning. Addition of B to Nb microalloyed steels has been found to retard the recrystallization due to the segregation of B to dislocations and the subsequent formation of Nb-B complexes [169]. Increase in C content has been reported to retard recrystallization in microalloyed steels [166]. Increase in Mn content increases the solubility of Nb [163] and delays its precipitation in austenite which may promote recrystallization [75, 170]. Increase in Nb content has been found to be the most effective in delaying austenite recrystallization as compared to Ti addition [171] because it increases the activation energy for recrystallization most effectively [172]. Other alloying elements such as Mn, Si, Mo also retard recrystallization [172, 173] which has been attributed to the increase of activation energy for recrystallization [172].

Recrystallization kinetics of Nb-containing microalloyed steels can be given according to the equation due to Dutta and Sellars [72] as follows:

$$t_{0.05x} = 6.75 \times 10^{-20} x d_o^2 x \varepsilon^{-4} x exp. (300000/RT) x exp. \{[(2.75 \times 10^5/T) - 185][Nb]\}$$

$$t_{0.95x} = 7.64 x t_{0.05x} \{after [167]\}$$

where $t_{0.05x}$ and $t_{0.95x}$ represent the time required for 5% and 95% recrystallization respectively and rest of the symbols have their usual meaning.

Recrystallization kinetics are significantly influenced by the precipitation of microalloy carbonitrides during thermomechanical processing and hence some background on the precipitation of microalloy carbonitrides is given in following section.

2.4 Precipitation Phenomena in Microalloyed Steels

2.4.1 Introduction

Role of microalloy precipitation during the entire sequence of thermomechanical processing is of critical importance in achieving superior mechanical properties in microalloyed steels. For instance, thermal stability of the precipitates influences the grain coarsening behaviour during reheating and soaking, strain induced precipitation during deformation significantly affects the recrystallization kinetics, precipitation during phase transformation influences the phase transformation kinetics while precipitation in ferrite after transformation contributes to increased strength of ferrite through precipitation hardening. Final properties of the microalloyed steels are dependent on the size distribution and volume fraction of precipitates at each stage during the TMP.

Typical physical properties of the precipitates found in Ti-Nb microalloyed steels are given in the Table 2.3 as follows.

Table 2.3: Physical properties of precipitates found in Ti-Nb microalloyed steels. {Data from [174]}.

Precipitate Type	Molecular Weight (gm)	Density (gm/cc)	Lattice Type	Lattice Parameter $(10^{-10}m)$	Molar Volume (cc/mol)
NbC	104.92	7.81	NaCl - B1 (Cubic)	4.4691	13.43
NbN	106.92	8.06	As Above	4.3880	12.81
TiC	59.91	4.92	As Above	4.3290	12.18
TiN	61.91	4.73	As Above	4.2460	11.53

Besides the type of precipitates listed in the above table, several "mixed" precipitates of the type Ti, Nb (C, N) have been observed in industrially produced steels [79 - 81, 148].

Liu and Jonas [140] have categorised TiCN precipitates observed in Ti-treated microalloyed steels as:

Type I Precipitates

These precipitates form prior to, during and immediately after solidification of the steel. Such precipitates are deposited in the liquid phase, on the solid-liquid interface and in δ iron. Precipitates of this type are typically coarse (0.5 - 10 μm) and very stable and do not dissolve in austenite during reheating. These precipitates are usually too coarse and widely dispersed to have any significant influence on either grain growth or recrystallization of austenite [135, 140, 175].

Type II Precipitates

Type II precipitates form following reheating and during the hot deformation involved in TMP. These precipitates are strain induced and typically fine ($\sim$ 5 nm for NbCN precipitates [176]). Such precipitates have been found to be the most effective in retarding austenite recrystallization and promoting ferrite grain refinement [140, 152, 176 - 179].

Type III Precipitates

These precipitates form after the decomposition of austenite. This category may be further subdivided [177, 180, 181] in to two groups. Firstly those which form on the travelling $\gamma \rightarrow \alpha$ transformation front and which are termed interphase precipitates. Secondly, those which form within the ferrite matrix following transformation. In both cases, the precipitates are very fine and may contribute significantly to overall steel strength through precipitation hardening [182].

2.4.2 Strain Induced Precipitation

As indicated previously, it is the fine strain induced precipitates which are of most importance in the control of grain growth and recrystallization of austenite during TMP. Precipitation reaction depends on the driving force for the nucleation and the subsequent growth of precipitate nuclei. Driving force for precipitation increases with increased undercooling and high solute supersaturation. Growth rate is considered proportional to the product of solute supersaturation and the square root of the diffusion coefficient [183]. As diffusion coefficient decreases with increased undercooling due to decreased atomic mobility at lower temperatures, growth rate decreases as transformation (precipitation) temperature is lowered. The combination of nucleation and growth kinetics of precipitation thus yields the well-known "C-curve" associated with any phase transformation. An example of C curves for microalloy precipitation is shown in Fig. 2.13
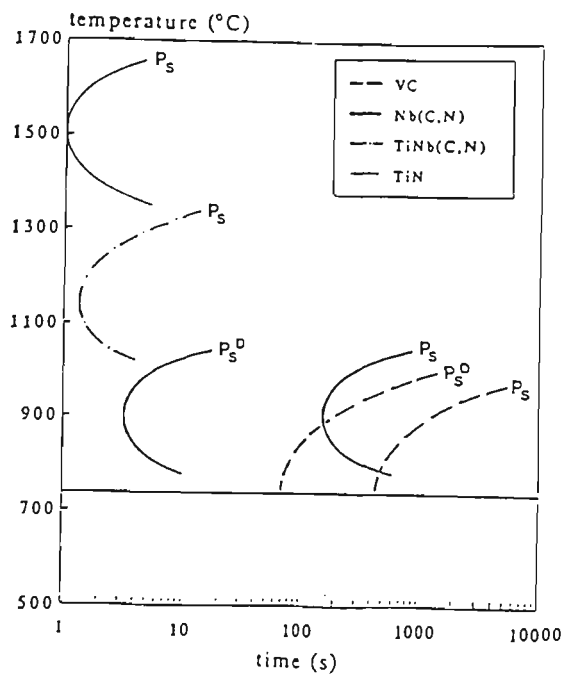

Figure 2.13: Precipitation - Time - Temperature (PTT) diagram of some carbides and nitrides in deformed and undeformed austenite. {After [183]}.

Fig. 2.13 represents the Precipitation - Temperature - Time (PTT) diagram for VC, NbCN, TiNb(C, N) and TiN in both deformed and undeformed microalloyed steel austenite. In Fig. 2.13 the start of precipitation in undeformed austenite is denoted P_s and the start of precipitation in deformed austenite is denoted P_s^D The location of the C-curve is very important in regards to processing since: (1) precipitates will only form when the processing temperature - time profile passes through the C-curve, and (2) the amount and distribution of precipitates directly depends on the C-curve. All conditions being similar, the nose of the C-curve will be displaced to higher temperatures as the thermodynamic stability of the precipitates increases. Hence, the relative location of the C-curve is related directly to the solubility of a given precipitate in austenite and/or in ferrite.

Several processing and compositional variables influence precipitation reaction. Increase in strain accelerates precipitation, but not strongly [165 - 167]. Lowered temperature of deformation accelerates precipitation because of increased supersaturation, which also results in a finer dispersion of precipitates [166, 168]. Increase in microalloy content accelerates precipitation strongly [172]. Simultaneous addition of Ti and Nb accelerates precipitation because complex precipitates have much larger driving force for precipitation than binary precipitates [184, 185]. Increase in C content accelerates precipitation due to higher supersaturation [166]. Addition of B to Nb-microalloyed steels accelerates precipitation of NbCN up to 40 ppm B content [169].

Kinetics of strain induced precipitation of NbCN can be described by the equations given by Dutta and Sellars [72] as follows:

$$t_{0.05p} = 3 \times 10^{-6} \times [Nb]^{-1} \times \varepsilon^{-1} \times Z^{0.5} \times exp. \ (270000/RT) \ exp. \ \{(2.5 \times 10^{10}/[T^3 (lnK_s)^2\}$$

where,

$$Z = \dot{\varepsilon} \ \text{x exp. (400000/RT) and}$$

$$K_s = \{[Nb] \ [C+(12/14N)]\}_{\text{in solution}} \ / \ \{10^{(2.26 - 6770/T)}\}$$

where $t_{0.05p}$ is time for 5% precipitation, Z is the Zener - Hollomon parameter. K_s is the supersaturation ratio while other symbols have their usual meaning. Roucoules et al. [186] and Liu and Jonas [187] have recently proposed the precipitation kinetics of TiCN based on the thermodynamics of nucleation and growth of precipitates. Interaction of recrystallization and strain induced precipitation is given in the following section.

2.5 Interaction of Recrystallization and Precipitation During TMP

2.5.1 Introduction

The complex interaction of recrystallization and precipitation during TMP of microalloyed steels can be understood by using a generalised Recrystallization - Precipitation - Temperature - Time (RPTT) diagram, initially proposed by Hansen et al. [74]. Consider a RPTT diagram proposed by Kwon and DeArdo [188] shown in Fig. 2.14.
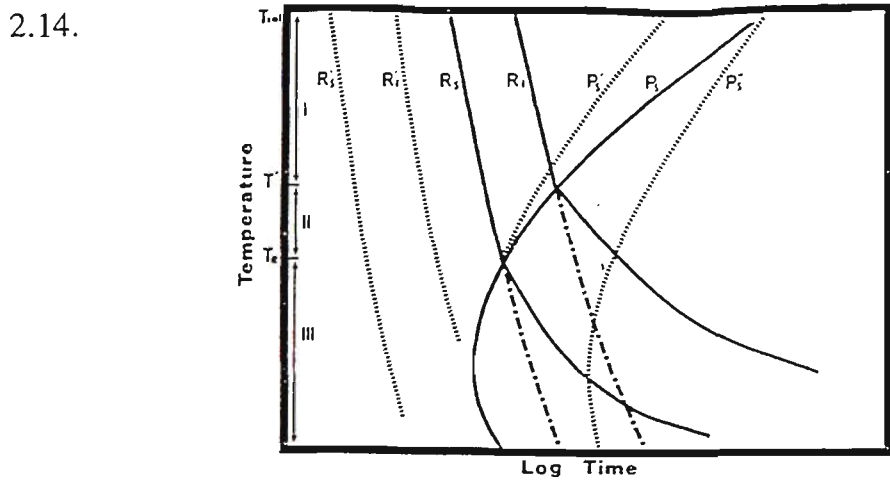

Figure 2.14: Recrystallization - Precipitation - Time - Temperature (RPTT) diagram showing the interaction between precipitation and recrystallization. {After [188]}. R_s and R_f refer to the start and finish of recrystallization, respectively, in microalloyed steels; and R_s' and R_f' refer to the start and finish of recrystallization, respectively, in plain carbon steels. P_s' and P_s" refer to the hypothetical precipitation start times in deformed and undeformed austenite, respectively. P_s is the actual precipitation start time.

In Fig. 2.14, T_{sol} corresponds to the solution temperature above which Nb-rich precipitates are completely dissolved in austenite. T' is the temperature below which recrystallization and precipitation compete and T_R is the temperature below which precipitation occurs prior to recrystallization. Fig. 2.14 exhibits three distinct regimes which are described below.

Regime I in Fig. 2.14 corresponds to when the steel is initially austenitized above T_{sol}, followed by deformation and holding between T_{sol} and T'. In this regime, recrystallization is completed (R_f) before the actual start of precipitation (P_s). This regime corresponds to the roughing deformation during the TMP.

In regime II, precipitation occurs after partial recrystallization (i.e. during the time interval between R_s and R_f). Hence an acceleration of the precipitation kinetics is observed during this regime due to the presence of inhomogeneities in the partially recrystallized austenite. Deformations which occur within this regime should be avoided due to the undesirable properties associated with duplex microstructure [145, 189 - 191]. This regime should thus correspond to the "delay" period in the TMP schedule.

In regime III, precipitation commences prior to recrystallization. Under these conditions, the resulting precipitate pinning force is considered large enough to impede the progress of recrystallization which eventually suppresses the recrystallization such that no recrystallization takes place after the deformation [183]. This regime therefore corresponds to the finishing deformation during the TMP.

Obviously, the knowledge of the temperature below which no recrystallization can take place is of critical importance in designing a TMP schedule for any microalloyed steel. Methods of estimating this critical "no-recrystallization temperature" are therefore summarised in the following sections.

2.5.2 No-Recrystallization Temperature (T_{nr})

The key feature that differentiates controlled rolling from conventional rolling is the second stage of rolling below the no-recrystallization temperature (T_{nr}). The temperature below which austenite remains unrecrystallized after deformation is called the no-recrystallization temperature. Several compositional and processing variables influence the T_{nr}. In general, the factors that assist austenite recrystallization lower the T_{nr} while the factors that retard or delay the austenite recrystallization raise the T_{nr}. Effects of some of the variables on T_{nr} are summarised in Table 2.4 below:

Table 2.4: Effects of compositional and process variables on T_{nr}.

Parameter	Effect on T_{nr}	Reference
Austenite grain size	Small grain size lowers T_{nr}	[165]
Strain	High strain lowers T_{nr}	[165 - 167]
Strain Rate	High $\dot{\varepsilon}$ lowers T_{nr}, more effective when strain is also large	[167]
Interpass Time	t < 12s $\Rightarrow$ Lowers T_{nr}, t = 12 ~15s $\Rightarrow$ Raises T_{nr} strongly, t >> 15s $\Rightarrow$ Lowers T_{nr}	[192, 193]
Temperature of deformation	Lower temperature of deformation raises T_{nr}	[166, 168]
Addition of alloying and MAE	High MAE raises T_{nr} strongly. Alloying elements such as Mn and Mo also raise T_{nr}	[172]
Addition of B to Nb steels	Raises T_{nr} (B ≤ 40 ppm), Lowers T_{nr} (B > 40 ppm)	[169]
Simultaneous addition of Ti and Nb	Raises T_{nr}	[184, 185]
Increase in carbon content	Raises T_{nr}	[166]

Effect of microalloying elements (MAE) on T_{nr} is shown in Fig. 2.15.
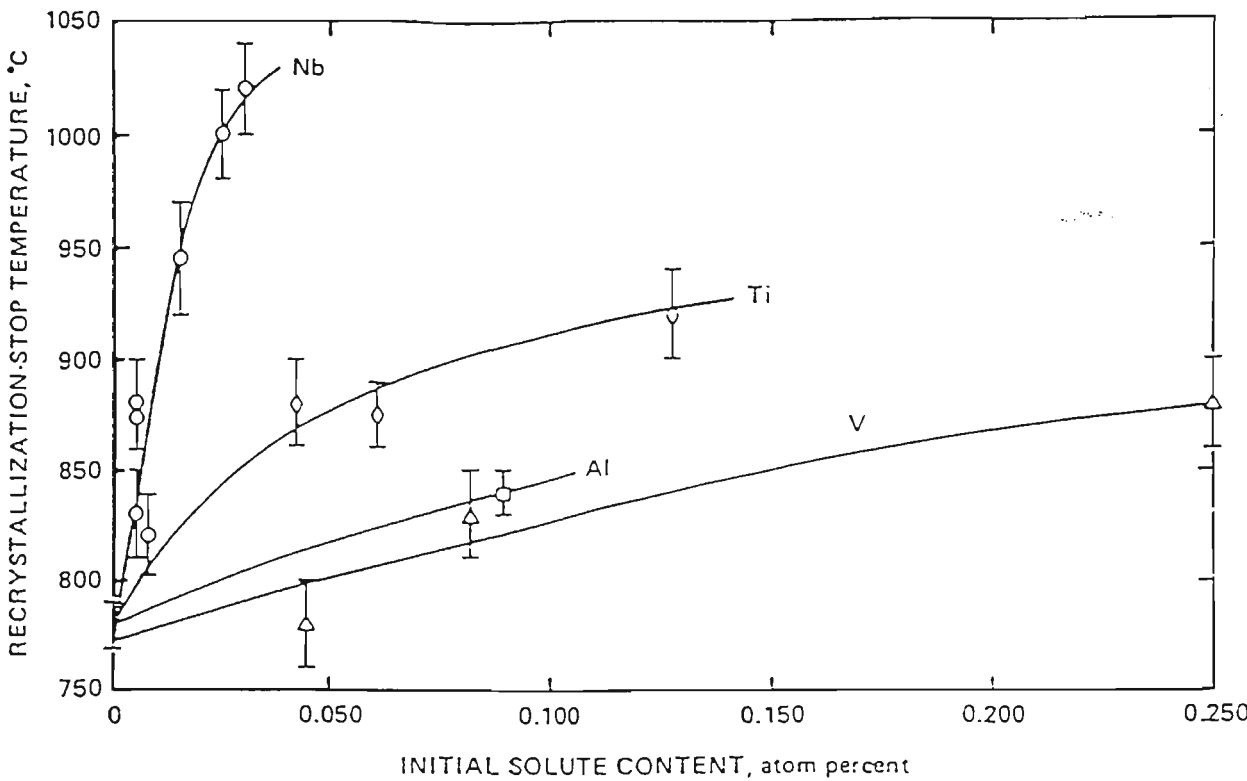

Figure 2.15: Effect of MAE addition on T_{nr} of a
0.07 C, 1.4 Mn, 0.25 Si steel. {After 189]}.

It can be seen from Fig. 2.15 that MAE exert a significant influence on T_{nr} and that addition of Nb is the most effective in raising the T_{nr}. The reasons why MAE raise the T_{nr} have been investigated. Some authors [70, 176, 194] have suggested that the dissolved MAE cause solute drag effect on austenite grain boundaries which leads to the retardation of recrystallization. However, there is a strong evidence now which suggests that strain induced precipitation of MAE causes retardation and eventual total suppression of austenite recrystallization thus raising the T_{nr} [171, 188, 195]. Some mathematical models to calculate T_{nr} are given in the following sections.

2.5.3 Calculation of T_{nr} Based on Composition

Barbosa et al. [196] used multi-pass torsion testing to determine experimentally T_{nr} of 17 steels containing different levels of Nb, V, Ti and Al. T_{nr} of other 20 steels reported in literature was added to this data and then regression analysis was used to arrive at the following relation between T_{nr} and the composition:

$$T_{nr} (^{\circ}C) = 887 + 464\ C + (6445\ Nb - 644\ \sqrt{Nb}) + (732\ V - 230\ \sqrt{V}) + 890\ Ti +$$

$$363\ Al - 357\ Si$$

Maccagno et al. [197] have recently found this equation to be satisfactory in calculating the T_{nr} of Cu-bearing (0.4% Cu) Nb and Nb-V steels. They compared the experimentally determined T_{nr} and T_{nr} based on the analysis of data from rolling mill logs with predicted T_{nr} based on the above equation and found a good quantitative agreement between T_{nr} values.

2.5.4 Calculation of T_{nr} based on Recrystallization and Precipitation Kinetics

It was realised that no-recrystallization temperature can not be a sharp, well defined temperature below which recrystallization stops suddenly. Instead, in multi-pass rolling schedule, the amount of recrystallization between passes was seen to reduce gradually as the temperature of deformation was lowered, until austenite remained essentially unrecrystallized between the passes. Thus, in fact, two critical temperatures were needed: first critical temperature when the inhibition to recrystallization was just experienced (95% recrystallized, 5% unrecrystallized austenite) and second critical temperature below which austenite remained essentially unrecrystallized (95% unrecrystallized and 5% recrystallized austenite). Dutta and Sellars [72] were first to

distinguish between these two critical temperatures. They called the first critical temperature as the "Recrystallization Limit Temperature (RLT)" which was defined as the lowest possible temperature at which complete recrystallization can take place. The second critical temperature was called as "Recrystallization Stop Temperature (RST)" which was defined as the highest possible temperature at which recrystallization was completely absent. The RLT and RST was estimated by considering the recrystallization and precipitation kinetics. The authors postulated that RLT can be obtained as an intersection between $t_{0.05p}$ (time for 5% precipitation) and $t_{0.95x}$ (time for 95% recrystallization) curves. Similarly RST can be obtained by intersection of $t_{0.05p}$ and $t_{0.05x}$ (time for 5% recrystallization) curves. $t_{0.05p}$ and $t_{0.05x}$ was calculated for NbCN precipitation according to following equations given earlier. Roucoules et al. [186] and Liu and Jonas [187] have recently proposed the precipitation kinetics of TiCN which can be used to estimate RLT and RST in Ti-containing steels.

It has been shown by Bai et al. [192] that T_{nr} corresponds metallographically to 75 - 85 % recrystallized austenite and that T_{nr} lies between RLT and RST, see Fig. 2.16.
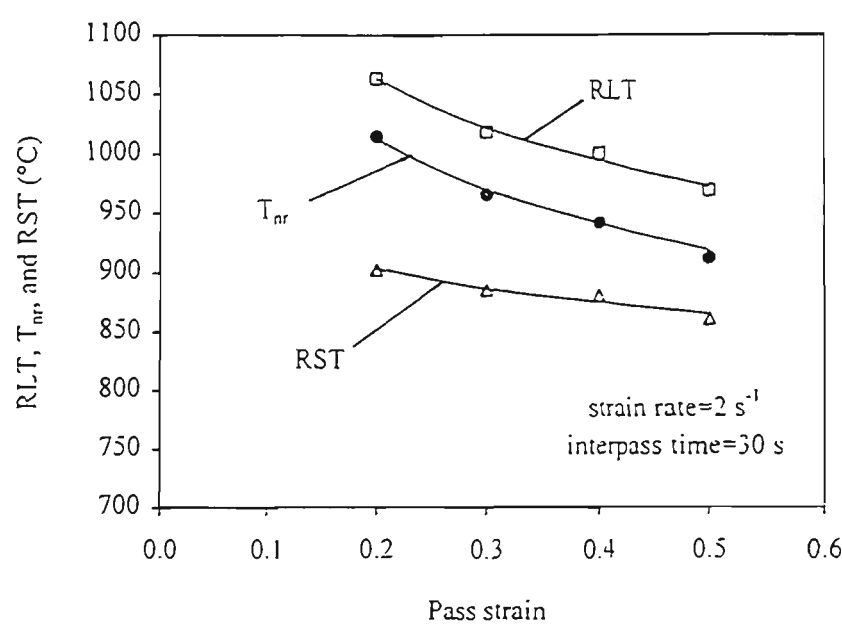

Figure 2.16: Calculated values of RLT and RST for a 0.07 Nb steel compared with the experimentally determined T_{nr} s. {After [192]}.

The authors have proposed following equations to predict T_{nr} based on the deformation conditions:

$$T_{nr} = (A \log[Nb]_{eq.} + B) \, \varepsilon^{-0.12} \, (\dot{\varepsilon})^{-0.01} \, t^{-0.1} \text{ for } t < 12s$$

where,

$A = 88.1 \, ^{\circ}C$ per wt. % $[Nb]_{eq.}$ $B = 1156 \, ^{\circ}C$ and $[Nb]_{eq.} = [Nb + 0.31 \, Ti + 0.15 \, Al]$

Medina [195] has used similar analysis to arrive at "Static Recrystallization Critical Temperature (SRCT)" which represents a temperature at which precipitation hinders recrystallization eventually leading to total suppression of recrystallization. SRCT is considered approximately equal to T_{nr}. SRCT for 0.1 C, 1.23 Mn steel is given according to:

$$SRCT \, (K) = A - 600 \, d_o^{-0.27} \varepsilon^{0.5}$$

where A = 1376 for 0.042 Nb and A = 1410 for 0.093 Nb. From these equations it is clear that an increase in Nb content increases T_{nr} while increase in strain and a decrease in grain size decreases it.

Majta et al. [198] have proposed the following equation to predict the RST:

$$RST = 990 \exp. (-0.2\varepsilon)$$

Effect of strain pass and grain size on RST has been investigated by Majta et al. [198]. They found that an increase in austenite grain size increases the RST. Bai et al. [167] have used these concepts to calculate T_{nr} based on the interaction of precipitation and recrystallization reaction kinetics, see Fig. 2.17. Fig. 2.17 shows that as the pass strain is increased, recrystallization is accelerated considerably and precipitation is also accelerated to some extent. For $\varepsilon < 0.27$, $t_{0.05p} < t_{0.05x}$, i. e. the precipitation is initiated before recrystallization begins which will inhibit any further recrystallization. On the

other hand, for $\varepsilon > 0.43$, $t_{0.05p} > t_{0.95x}$, i. e. precipitation is initiated only when 95% recrystallization is already complete.
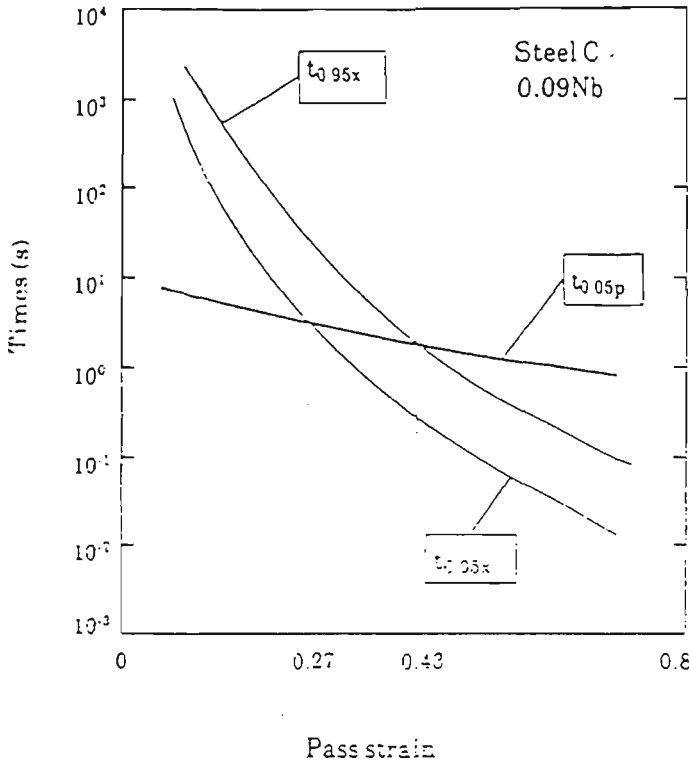

Figure 2.17: Influence of pass strain on $t_{0.05p}$, $t_{0.05x}$ and $t_{0.95x}$ at 960 °C for a 0.04 C, 1.5 Mn, 0.14 Mo and 0.09 Nb steel. {After [167]}.

2.5.5 Prediction of T_{nr} Based on Precipitate Dissolution Temperatures

Medina and Mancilla [199] have proposed calculation of SRCT ($\cong T_{nr}$) based on dissolution temperature for NbCN, TiC and TiN precipitates. Their model can be represented as follows:

For Nb Steels:

$$SRCT\ (K) = T_s - 1.05 \times 10^3 \times d_0^{-0.35} \times \varepsilon^{0.5}$$

$$T_s \Rightarrow \log\ [Nb]\ [N] = 2.8 - 8500/T_s \text{ for Nb : N} < 8; \text{ and}$$

$$T_s \Rightarrow \log\ [Nb]\ [N] = 3.42 - 7900/T_s \text{ for Nb : N} > 8$$

For Ti Steels:

$$SRCT\ (K) = T_s - 1.05 \times 10^3 \times d_0^{-0.35} \times \varepsilon^{0.2}$$

$$T_s \Rightarrow 1360\ K\ for\ Ti : N < 3.42;\ and$$

$$T_s \Rightarrow log\ [Ti]\ [C] = 5.33 - 10475/T_s\ for\ Ti : N > 3.42$$

2.5.6 Prediction of T_{nr} based on Force Equilibrium Approach

Arieta and Sellars [200] and Palmiere et al. [201] suggest that inhibition to recrystallization would occur when pinning force offered by precipitate particles on austenite grain boundaries exceeds the driving force for recrystallization. The equations to calculate the pinning and driving forces are given below:

$$F_{PIN} = 4r\sigma N_s;\ and$$

$$F_{RXN} = \mu b^2 \Delta\rho/2$$

where F_{PIN} is the pinning force opposing recrystallization, F_{RXN} is the driving force for recrystallization, r is the precipitate particle radius, σ is the grain boundary energy (0.7 J/m^2), N_s is the surface density of particles, μ is the shear modulus of austenite (4x10^4 MPa), b is the Burger's vector ($\sim$ 0.25 nm) and $\Delta\rho$ is the change in dislocation density associated with the migration of recrystallization front into the deformed region. The value of N_s depends on the assumptions made and can be calculated according to $3f/2\pi r^2$ [19] or $3f^{2/3}/4\pi r^2$ [189] or $3fl/8\pi r^3$ [74] where f is the volume fraction of particles and l is the average subgrain boundary intercept distance. This approach, however, needs further refinement in order to be used practically to predict the T_{nr} of microalloyed steels.

2.6 Phase Transformation Behaviour of Thermomechanically Processed Microalloyed Austenite

2.6.1 Decomposition of Austenite During Cooling

Decomposition of austenite during cooling is intimately related to several factors such as the amount of deformation below T_{nr}, composition of austenite prior to transformation, presence / absence of precipitates and cooling conditions. Austenite stabilisers such as Ni, Mn, Co, Cu, C and N lower austenite transformation temperature - Ar_3 and retard transformation kinetics through solute drag effect on phase boundaries. Ferrite forming elements such as Cr, Si, P, Al, V, Mo, Ti, Nb, Zr raise Ar_3, but retard the progress of transformation. This effect is considered to take place by a strong reduction of the diffusivity of carbon in austenite and by the partitioning of the elements within the product phases offering a strong diffusive drag on phase transformations [202].

Microalloying elements can cause retardation of phase transformation if they are still in solid solution in austenite prior to transformation. It has been suggested that segregation of microalloying elements at austenite grain boundaries reduces the surface energy of austenite grain boundaries (up to 0.3 J/m^2 from 0.7 J/m^2), thus decreasing their effectiveness as nucleation sites [203 - 205]. An alternative explanation is the decrease in the nucleation rate due to solute drag effect on phase boundaries [202, 206]. Enomoto et al. [207] consider the effect of Nb and Ti addition on $\gamma \rightarrow \alpha$ transformation. They suggest that the addition of Ti and Nb retards the $\gamma \rightarrow \alpha$ transformation due to following reasons: (1) reduction of grain boundary energy of austenite due to grain boundary segregation of Ti and Nb causes reduced nucleation rate, (2) deceleration of carbon

diffusion and the formation of solute atom clusters or fine coherent precipitates at potential ferrite nucleation sites; and (3) retardation of growth rate due to the decrease of carbon activity in front of interphase boundary due to segregation (solute drag effect) and the suppression of ledge nucleation. Exact mechanism of retarding effect of microalloying elements (either in solution or as precipitates formed during TMP) on phase transformation kinetics is still being debated and is not yet well understood [208].

Deformation below T_{nr} has been found to increase Ar_3 and promote $\gamma \rightarrow \alpha$ transformation through increased nucleation. Accelerated cooling increases intragranular ferrite nucleation sites and refines transformed ferrite grain size further [209]. Sellars [210] suggests that increasing strain below T_{nr} not only increases the density of grain boundary nucleation sites on grain surfaces but also increases the effectiveness of pre-existing intragranular nucleation sites such as inclusions or undissolved coarse carbo-nitride particles, and introduces new intragranular nucleation sites such as deformation bands or locally deformed annealing twin boundaries.

Kwon et al. [205] considered the effects of steel composition, austenite grain size, Ar_3 temperature, austenite grain morphology, degree of supercooling, and retained strain in deformed austenite after finish rolling on $\gamma \rightarrow \alpha$ transformation kinetics in their development of a mathematical transformation model based on Kolmogorov/ Johnson - Mehl / Avarami (KJMA) equation. Tamura et al. [28] accounted for the effect of austenite grain size in their modified Johnson - Mehl equation for decomposition kinetics during isothermal transformation of austenite according to the equation given below:

$$X = 1 - \{exp. (-K(T) \, t^n/d_\gamma^m)\}$$

where X is the fraction transformed, K(T) is the rate constant which depends on transformation temperature, t is the isothermal holding time, d_γ is austenite grain size and n and m are constants which depend on both the mechanism of transformation and the types of nucleation sites. The transformation mechanism could either be "nucleation and growth" type where the transformation progresses with nucleation and growth over entire range of transformation; or "site saturation" type where all nuclei are nucleated at an early stage during transformation and the progress of transformation is then mostly controlled by growth rate of nuclei in the later stages. Viable nucleation sites could be grain edge, corner or surface as shown schematically in Fig. 2.18.
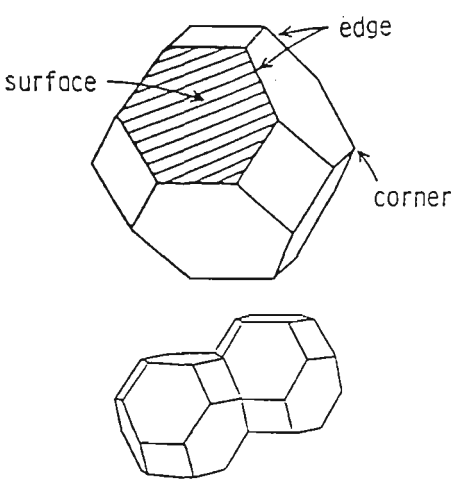

Figure 2.18: Schematic diagram of austenite grain as a tetrakaidecahedra and showing three types of ferrite nucleation sites. {After [211]}.

For different types of transformations, the value of n and m in the above equation are as given in the Table 2.5

Table 2.5: The values of n and m for various transformation modes. {After [211]}.

Transformation Type	n	m	Transformation Mechanism	Predominant Nucleation Site
Pearlite	4	2	Nucleation and Growth	Grain Edge
Ferrite	1	1	Site Saturation	Grain Surface
Bainite	4	0.6	Nucleation and Growth	Grain Boundary and Intragranular

Umemoto et al. [212] have shown that the ferrite grain size after transformation depends on the type of nucleation sites. They propose the dependence of d_α on d_γ to be proportional to $d_\gamma^{0.33}$ for grain surface nucleation, $d_\gamma^{0.67}$ for grain edge nucleation and d_γ for grain corner nucleation. Several types on nucleation sites may act simultaneously during actual transformation, however, grain surface has been found to be the predominant nucleation site during $\gamma \rightarrow \alpha$ transformation [213].

Another parameter which influences the transformation behaviour of austenite is the austenite transformation critical temperature - Ar_3. Factors such as austenite conditioning, composition and cooling rate determine the Ar_3. Austenite stabilising elements (such as Ni, Mn etc.), microalloying elements (Ti, Nb) and increase in cooling rate lower Ar_3 while small austenite grain size and deformation below T_{nr} raises it. The lower the Ar_3, the following microstructural changes are observed: (a) grain size refinement of transformed product, (b) increases in dislocation density, (c) finer dispersion of precipitates, and (d) increased tendency to retain solute in solution, thus contributing to increases in strength by solid solution and/or precipitation hardening [214].

Depending on composition of steel, thermomechanical processing conditions (austenite conditioning and precipitation reactions) austenite may transform to a variety of ferritic, bainitic or martensitic phases or indeed to any combination of these phases depending on the cooling rate. A review of the phases found in low carbon, microalloyed steels is presented in the following section.

2.6.2 Microstructures in Thermomechanically Processed Low Carbon Microalloyed Steels

The types of microstructures observed in microalloyed steels are quite varied and complex and therefore a clear understanding of phase identification, classification and nomenclature is of great importance. Particularly, bainitic microstructures in low carbon microalloyed steels differ in variety and form as compared to the classical bainitic microstructures [215]. Aaronson and Lee have proposed three general definitions of bainites [216] as follows:

Microstructure Definition

Bainite is the product of a non-lamellar, non co-operative mode of eutectoid decomposition. Product phases form by diffusional nucleation and growth. Second phase may form within or at the interphase boundaries of the first product phase. Phases may have any morphology.

Reaction Kinetics Definition

Bainite has its own C-curve on the Time - Temperature - Transformation (TTT) diagram. No bainite can form above the highest temperature of this curve, which termed B_s. Transformation finishes at B_f which may be close to M_f.

Surface Relief Definition

Bainite is formed by precipitate plates formed by shear at rates well above those allowed by diffusional processes at temperatures above M_s.

Six possible morphologies of ferrite and cementite based on above definitions were recognised as bainite [217] as shown schematically in Fig. 2.19.
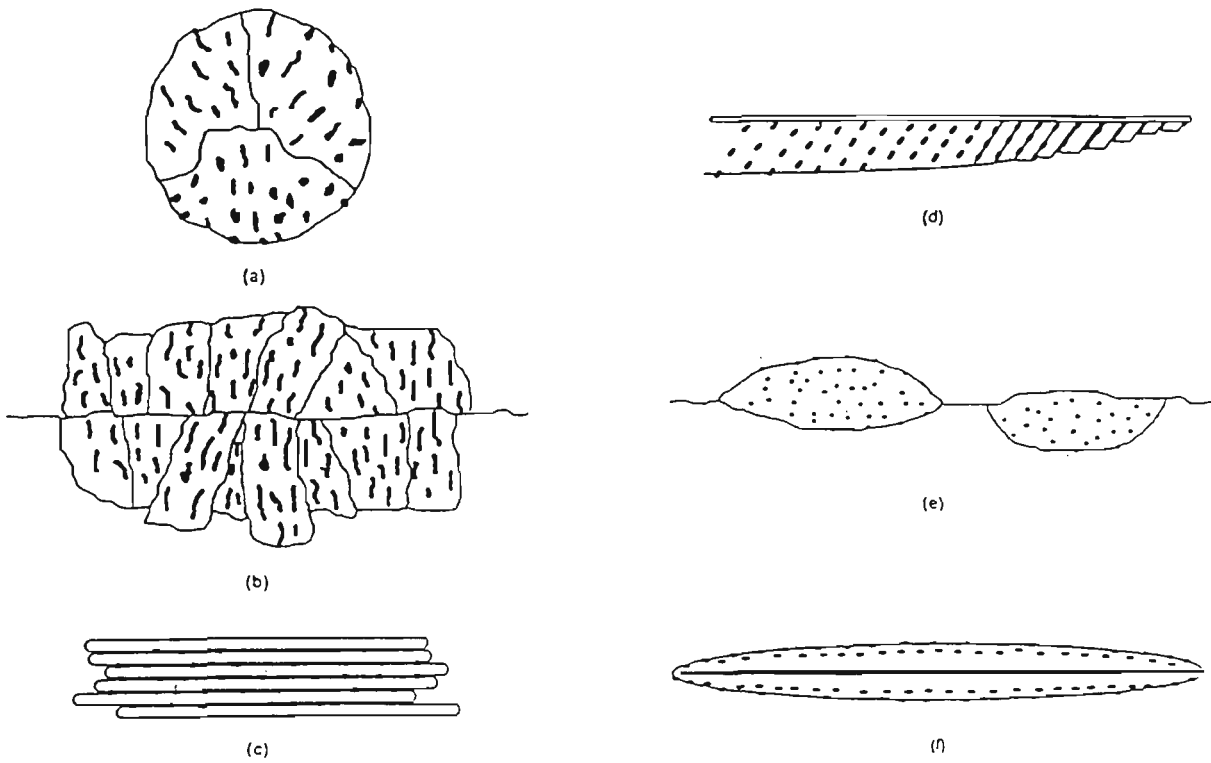
Figure 2.19: Schematic illustrations of various ferrite (white) and cementite (dark) morphologies: (a) nodular bainite, (b) columnar bainite, (c) upper bainite, (d) lower bainite, (e) grain boundary allotriomorphic bainite. and (f) inverse bainite. {After [217]}.
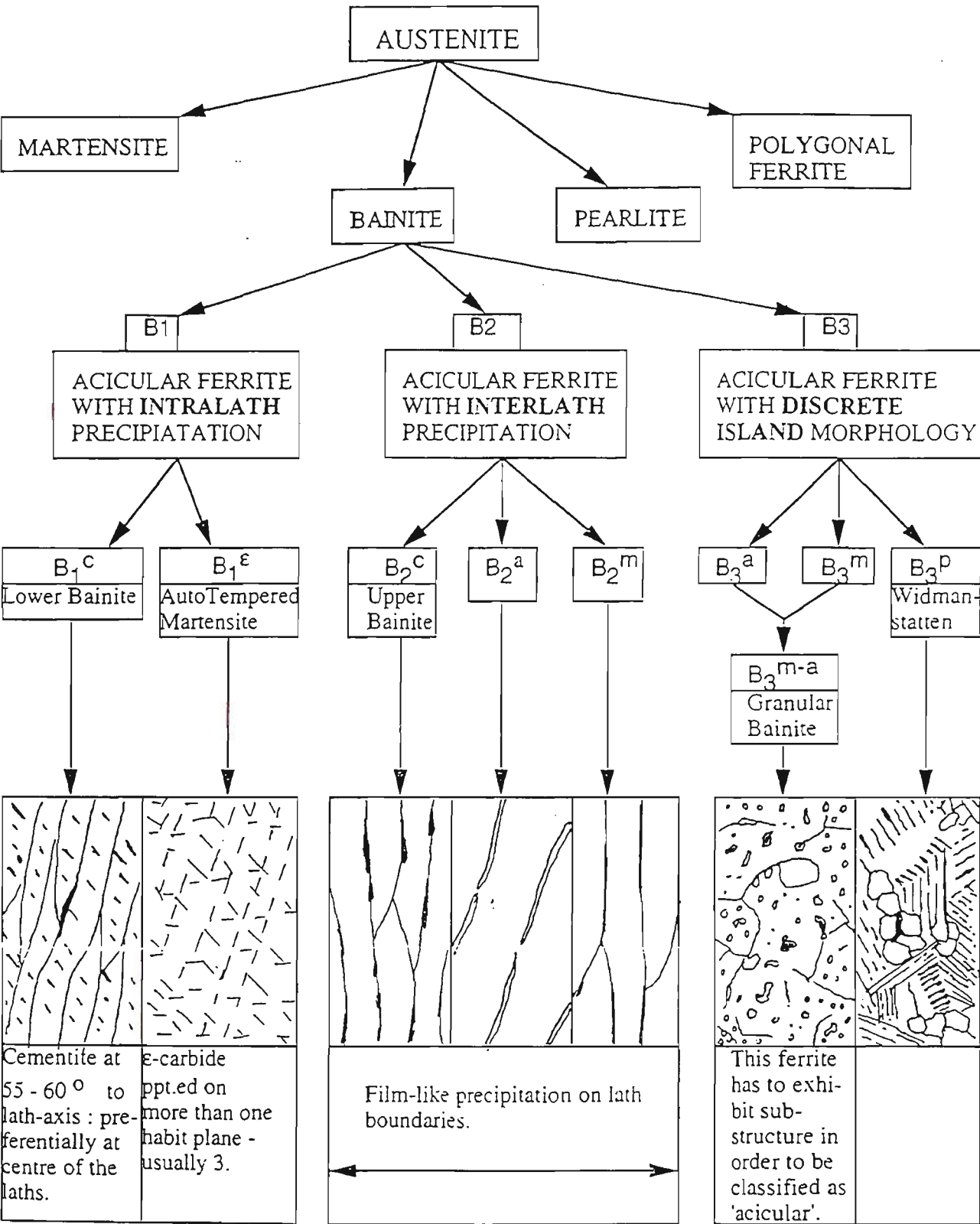
However, it has been found that in low carbon microalloyed steels some bainitic microstructures are observed which do not fit any of the above definitions of bainite. Such microstructures are characterised by the total absence of carbides and consists of isolated regions austenite and martensite between crystals of ferrite which may or may not have a lath or plate morphology [218, 219].

Extensive work carried out by the Bainite Research Committee of ISIJ [220, 221] dealt with this problem and arrived at the classification of bainites observed in low carbon microalloyed steels as given in Table 2.6.

Table 2.6: Classification of bainitic microstructures in low carbon microalloyed steels according to ISIJ Bainite Committee. {After [220, 221]}.

Symbol	Nomenclature	Comment
I_o Major Matrix Phase		
α_p	Polygonal Ferrite	Equiaxed, fully recovered or recrystallized, formed at high temperature across prior γ grain boundaries
α_q	Quasi-polygonal (Idiomorphic / Massive) Ferrite	Irregular shaped, recovered, formed across prior γ grain boundaries, usually observed in rapidly cooled very low and ultra low carbon steels
α_w	Widmanstatten Ferrite	Plate-like, recovered, formed within prior γ grains, rare in low carbon steels
α_b	(Granular) Bainitic Ferrite	Fairly recovered, featureless, formed at slow cooling rates
α^o_b	(Acicular) Bainitic Ferrite	Sheaf-like, without cementite, but with carbon-enriched γ films, contains high dislocation density
α'_m	Dislocated Cubic Martensite	Low carbon martensite, lath type massive shaped
II_o Minor Secondary Phases		
γ_r	Retained Austenite	Usually enriched in carbon
MA	Martensite - Austenite Constituent	Usually "island" morphology
α'_M	Martensite	High carbon martensite
aTM	Auto-Tempered Martensite	
B	$BII/B_2/B_U$ - Upper Bainite B_L - Lower Bainite	
P'	Degenerated Pearlite	
P	Pearlite	
θ	Cementite Particle	
Z_w	Granular Intermediate Ferritic Phases	Mixture of α_b and/or α^o_b / α_q

Another system of classification of bainites in microalloyed steels was proposed by Bramfitt and Speer [218]. Their system of bainite classification is presented in Fig. 2.20.

AUSTENITE

MARTENSITE   BAINITE   PEARLITE   POLYGONAL FERRITE

B1 — ACICULAR FERRITE WITH **INTRALATH** PRECIPIATATION

B2 — ACICULAR FERRITE WITH **INTERLATH** PRECIPITATION

B3 — ACICULAR FERRITE WITH **DISCRETE** ISLAND MORPHOLOGY

B_1^c Lower Bainite B_1^ε AutoTempered Martensite

B_2^c Upper Bainite B_2^a B_2^m

B_3^a B_3^m B_3^p Widmanstatten

$B_3^{m\text{-}a}$ Granular Bainite

Cementite at 55 - 60° to lath-axis : preferentially at centre of the laths.

ε-carbide ppt.ed on more than one habit plane - usually 3.

Film-like precipitation on lath boundaries.

This ferrite has to exhibit substructure in order to be classified as 'acicular'.

p = pearlite, m = martensite, a = austenite and c. ε = carbide

Figure 2.20: Bramfitt and Speer classification of microstructures. {After [218]}.
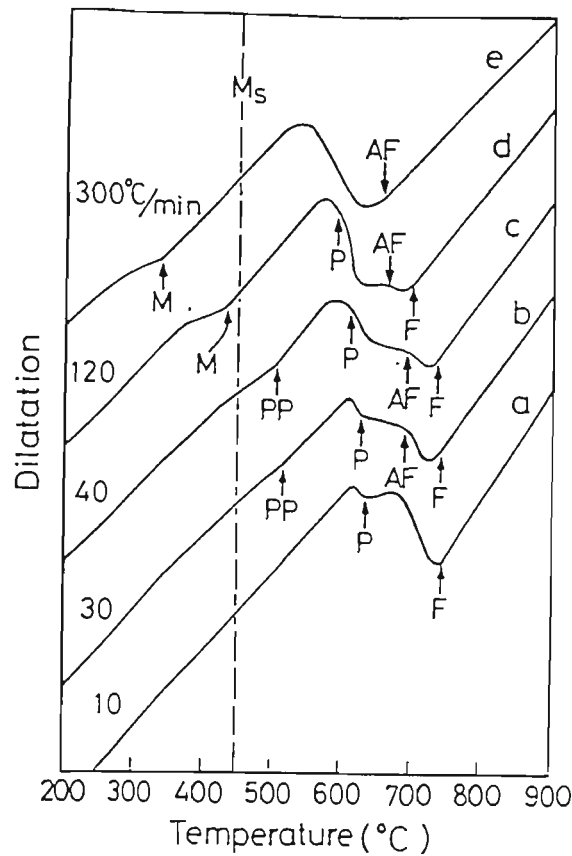
Figure 2.21: Schematic diagram illustrating dilatation curves for different phase
transformations. Arrows show the transformation start temperatures
of polygonal ferrite (F), acicular ferrite (AF), pearlite (P),
pseudo-pearlite (PP) and martensite microphases (M). M_s represents
the martensitic transformation start temperature. {After [222]}.

While the effect of deformation on $\gamma \rightarrow \alpha$ transformation kinetics has been extensively

investigated, effect of deformation on bainitic transformation has received relatively less

attention. Bhadeshia et al. [224, 225] have investigated the effect of deformation on

bainitic transformation in a 0.45 C- 2.08 Si - 2.69 Mn - Fe alloy. Their results indicate

that bainitic transformation can be mechanically stabilised due to deformation. The

mechanism of stabilisation appears to be that the growth of bainite is retarded by the high

dislocation density. Heterogeneous nucleation may become more frequent as the defects

are introduced in to austenite, but the growth of nuclei is retarded as the motion of

transformation interface is impeded by dislocation structure. Deformed austenite

therefore transforms to a smaller quantity of bainite than undeformed austenite. and any

bainite that forms is more refined. The formation of pearlite was found to be accelerated by straining the austenite. They suggest that the retardation of bainite transformation may be compensated by enhanced nucleation when the strain is high.

Fujiwara et al. [226] suggest that transformation from a heavily deformed austenite refines bainite due to the formation of dislocation cell structure within austenite grains prior to transformation. This leads not only to the nucleation of bainite at the cell boundaries but also termination of growth on the cell structure boundaries. Yamamoto et al. [227] studied a 0.04 C, 2.95 Mn, 0.03 Nb, 0.023 Ti and 0.0002 B steel and found that prior austenite grain size does not significantly influence either the B_s or the bainite morphology. However, deformation below T_{nr} was found to increase the nucleation rate of bainite, raise B_s temperature and lower the hardness of bainite. Liu and Zhang [228] found (in a 0.43 C - 3.0 Mn - 2.12 Si - Fe alloy) that Mn segregates to prior austenite grain boundaries which produces a restraining effect on the nucleation of bainitic ferrite which shifts the TTT curve to right (i.e. delays bainitic transformation). Increased Mn level was also found to promote intragranular nucleation of bainitic ferrite. Si was found to inhibit Fe_3C precipitation and also enhance grain boundary segregation of Mn, thus contributing indirectly to the retardation of bainitic transformation. Similar observations were made in Fe - C - Ti alloys where TiC precipitation was inhibited due to the additions of Si, Mn or Si + Mn [229]. Umemoto et al. [230] found that the rate of bainitic transformation is not significantly influenced by the deformation of austenite in contrast with ferrite or pearlite transformations where deformation has a large influence on the transformation kinetics.

2.6.3 Effect of Accelerated Cooling on Phase Transformations

Accelerated cooling (AC) technique was first developed in 1965 with an initial modest objective of achieving a low coiling temperature (~ 600 °C) in a hot strip mill to eliminate the differences in strength among the samples taken from front, centre and end of a coil [231]. Subsequent to this effort, several advantages of AC were realised in the production of strip as well as plate steels. One major advantage of AC when used in conjunction with TMP is the ferrite grain refinement, see Fig. 2.22.
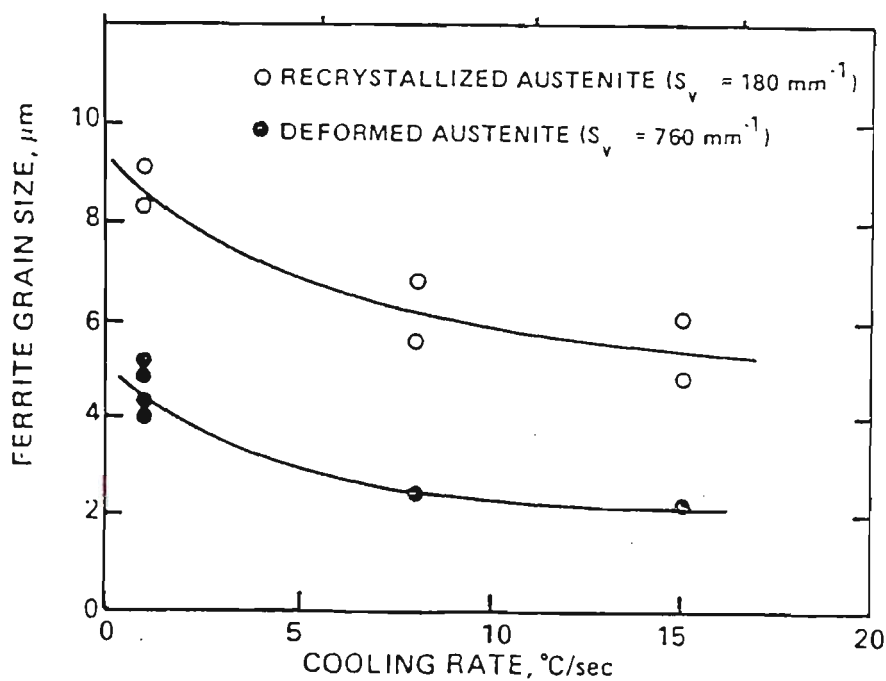
Figure 2.22: Effect of AC on ferrite grain size formed from the transformation of recrystallized and unrecrystallized austenite. {After [232]}.

AC was also found to improve yield and tensile strengths and the low temperature Charpy impact energy, without seriously affecting fracture appearance transition temperature [154]. Main reasons for improvement in mechanical properties due to AC was attributed to the refinement of ferrite grain size and the formation of acicular ferritic. bainitic or martensite - austenite constituent microstructures, see Fig. 2.23.
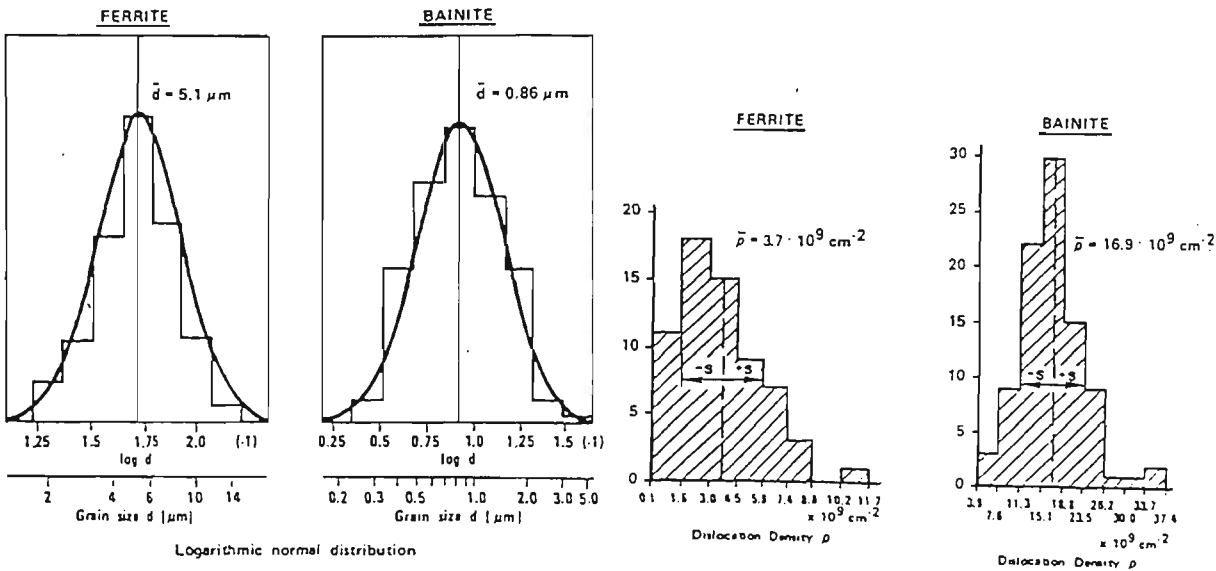
Figure 2.23: Frequency distribution of grain sizes and dislocation
densities in ferrite and lath type bainite of TM
treated Mn-Nb microalloyed steels. {After [150]}.

Fig. 2.23 indicates that the TM processed Mn - Nb microalloyed steels contain extremely fine grained bainite which also has a higher dislocation density as compared to ferrite which contributes to the increased strength of AC steels. As a consequence of increased strength of AC steels, a reduction of carbon content became possible which led to the superior notch toughness and weldability of AC steels. The gap between properties of quenched and tempered steels and AC microalloyed steels was thus reduced. This fact was used to eliminate completely the separate heat treatment process after rolling of low alloy steels making the AC process cost-effective. Fatigue resistance of precipitation strengthened microstructure (which is developed after TMP and AC of microalloyed steels) was also found to be much superior to that of quenched and tempered steels [231]. Interrupted accelerated cooling (IAC) was also found to influence significantly the ultimate tensile strength of Nb and Nb - Ti microalloyed steel plates (lower IAC temperatures resulted in higher tensile strengths) [233]. Tamehiro et al. [154] found that microstructures developed by the AC process offered higher resistance to fracture in sour-gas environments and exhibited a better HIC resistance.

Chapter 3:   Experimental

3.1 Materials

The chemical composition of the steels studied is given Table 3.1.

Table 3.1: Chemical composition of the steels studied.

Wt. % Element	Grade 1	Grade 1A	Grade 4	Grade 5
C	0.07	0.085	0.075	0.07
P	0.018	0.014	0.013	0.014
Mn	1.66	1.55	1.07	1.08
Si	0.32	0.41	0.28	0.09
S	0.001	0.011	0.005	0.004
Mo	0.22	0.18	0.25	0.19
Al (Total)	0.029	0.027	0.037	0.032
Nb	0.054	0.031	0.047	0.040
Ti	0.013	0.013	0.016	0.014
N	0.0065	0.0044	0.0086	0.0036
Ti : N	2.0	2.96	1.86	3.89
Initial Condition	Slab and Plate	Slab and Plate	Slab	Slab
Initial Size	225 mm thick slab and 20 mm thick plate	225 mm thick slab and 20 mm thick plate	225 mm thick slab	225 mm thick slab

Grade 1 contains high levels of Mn and Nb and is an established steel grade at BHP

Steel Co. which is used to manufacture API X80 grade line pipe for oil and gas

transmission. Grade 1A is an cost-effective alternative to Grade 1 because it has a lower

Nb content as compared to Grade 1 while maintaining the similar level of Mn addition.

On the other hand, Grade 4 contains lower level of Mn content, but similar level of Nb

addition as compared to Grade 1 which contributes to the improved weldability of Grade

4. Grade 4 is used to manufacture API X65 and X70 grade small diameter line pipe.

Grade 5 is a leaner version of Grade 4 in terms of the microalloy content and it also has

a reduced level of Si content to improve the weldability even further. Reduced level of

Si content in Grade 5 also contributes to reduced scaling during rolling and therefore contributes to better paintability of the steel surface. Grade 5 is used to manufacture automotive wheels and axles. The steels were supplied in 220 mm thick as-cast slab and/or 20 mm thick controlled rolled plate form as given in Table 3.1.

The steel compositions have several features in common such as effective utilisation of TiN technology by keeping the Ti content between 0.010% and 0.016% and Ti : N ratio below or very close to the stoichiometric value of 3.42. The steels contain Mo for ferrite strengthening through precipitation hardening and/or enhanced hardenability. Grades 1 and 1A contain an appropriate combination of Mn and Mo for reducing the precipitation of Nb in austenite, to offset Bauschinger effect and to achieve continuous yielding behaviour. These steels are used in the manufacture of high strength ERW linepipe because of their ability to generate satisfactory combination of strength, ductility and weldability after controlled rolling. In addition, these compositions offer greater flexibility for microstructure control through controlled cooling subsequent to the thermomechanical processing.

Comparison of the results obtained after TMP of Grades 1 and 4 (both in slab condition) enables to study the role of Mn addition while comparison of Grades 1 and 1A (both in plate form) permits the study of effect of Nb on Ar_3 temperature, phase transformation behaviour and transformation kinetics during continuous cooling and CCT diagrams for these steels.

3.2 Experimental Procedure for Grain Growth Studies

3.2.1 Outline of Grain Growth Experiments

Cubic samples (10x10x10 mm) samples were cut from the steels and heated at temperatures between 900 °C to 1250 °C in steps of 50 °C for a period of 30 minutes at each temperature. The samples were heated in argon (inert) atmosphere and quenched immediately in water after the specified heat treatments were carried out. A thermocouple was inserted in the sample to ensure that correct austenitizing temperature was maintained during each reheating. Quenched samples were tempered at 500 °C for 2 hours to improve the response of the grain boundaries to etching. Tempered samples were sectioned and prepared for metallographic examination.

3.2.2 Metallographic Techniques

The samples were etched in saturated aqueous picric acid solution containing 10 ~ 15 drops of concentrated HCl and 10 ~ 14 drops of undiluted liquid detergent (Teepol). Etching was carried out at 60 ~ 70 °C for times ranging from 3 ~ 14 minutes to reveal satisfactorily prior austenite grain size. Sometimes etching - polishing technique was used to achieve a good grain boundary etch.

The mean austenite grain size was measured using quantitative metallography in accordance with the procedure outlined in ref. [37]. A circle of 0.86 mm in diameter was superimposed on the microstructure and the number of grains (N) intersecting the

circumference was noted. At least 600 grain intersections were counted for each sample. The mean linear intercept (λ) was calculated using following formula:

$$\lambda \, (\mu m) = \pi(86L)/N$$

where L = 20 μm at 50 magnification, = 10 μm at 100 mag., = 5 μm at 200 mag. and = 2.5 μm at 400 mag. Grain diameter was considered to be equal to the mean linear intercept. Grain counting was done near centre of the sample to avoid measuring the effect of free external surface on grain growth.

As will be discussed in the Chapter 4, this conventional method of measuring the mean grain size and plotting it as a function of reheating temperature was found to be inadequate to reveal the onset and termination of abnormal grain growth in plate steels as well as in slab steels in some cases. Therefore, an alternative quantitative metallographic method was developed which seems to be more effective and sensitive in detecting the onset and termination of abnormal grain growth in microalloyed steels. The new method consists of recording the size of the largest grain in a given field of observation. This method is similar, but not identical to the methods outlined in ASTM standards E 1181 - 87 [264] and E 930 - 92 [265]. The shapes of the grains during abnormal grain growth are quite irregular and therefore, longest dimension of the largest grain was considered to be the size of the largest grain in a given field of observation. Arithmetic mean of this data was used to determine the mean size of the largest grain in every sample. A plot of the mean size of the largest grain *v/s* temperature thus provides an alternative technique of analysing the grain growth data.

3.2.3 Procedure for Studying the α→γ Transformation During Reheating of Steels

It was felt that the microstructure before reheating may influence the α→γ transformation during reheating which would have significant effect on the grain coarsening behaviour of transformed austenite. Therefore α→γ transformation behaviour was studied using quench dilatometry. 10 mm long cylindrical specimens of 5 mm outside diameter and 3.5 mm inside diameter were prepared from the steel blocks. The samples were heated in vacuum at a rate of 5 °C/s up to various temperatures between the Ac_1 (α → γ transformation start temperature) and the Ac_3 (α → γ transformation finish temperature). The samples were held at the appropriate temperature for 5 seconds and quenched immediately at a rate of ∼ 200 °C/s to room temperature using inert (Helium) gas flow. Samples were then sectioned, mounted, polished and etched using hot saturated aqueous picric acid method to reveal the martensite grain boundaries which represents the prior austenite grains during the α → γ transformation. The α → γ transformation could be mapped in each case. The experimental programs are shown in Figures 3.1 to 3.4 for Grades 1A (Slab), 4 (Slab), 1A (Plate) and 1 (Plate) respectively.
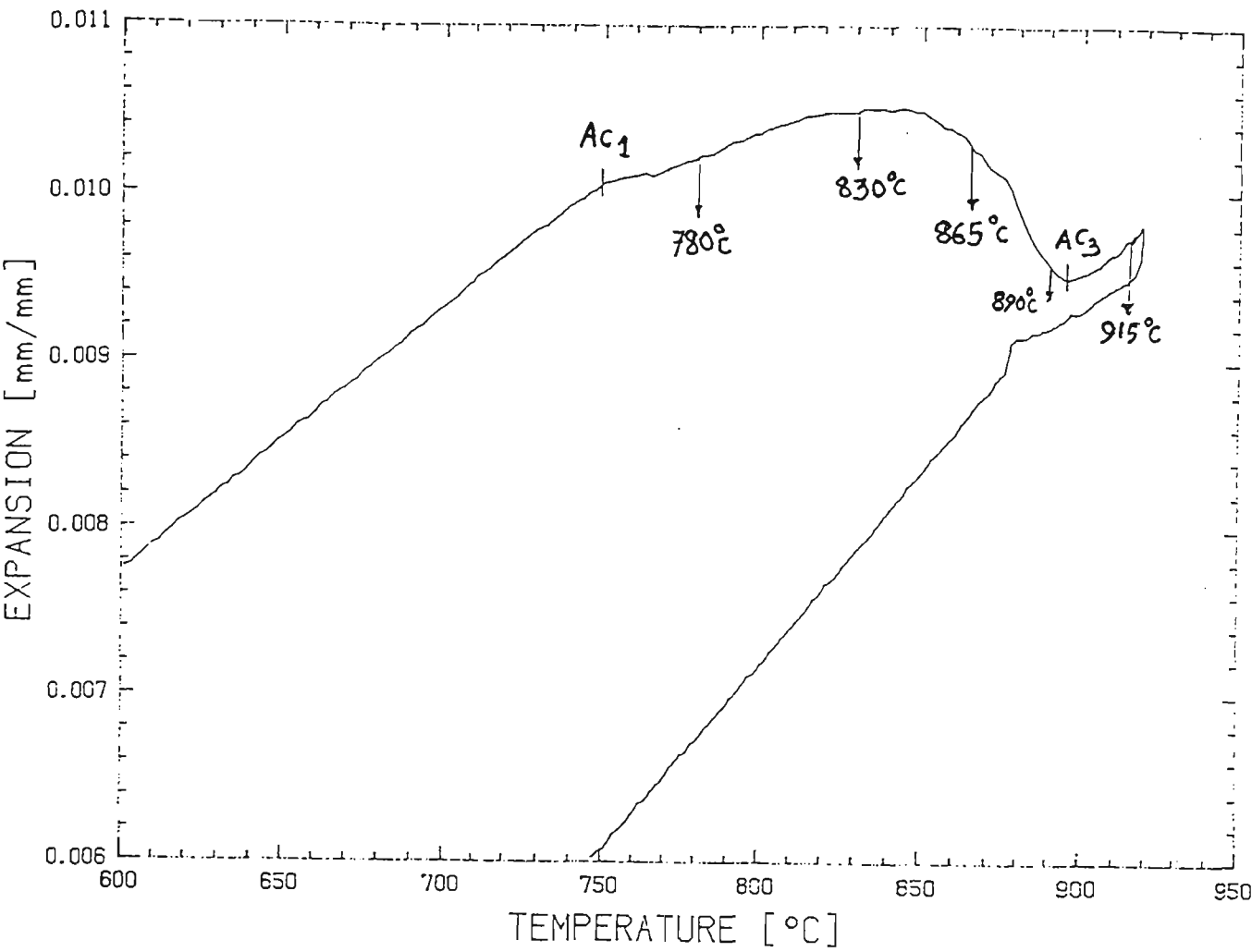
Figure 3.1: Experimental program for α→γ transformation studies in Grade 1A
(slab). α→γ transformation is mapped by observing microstructures of
the samples quenched from temperatures indicated on the figure.
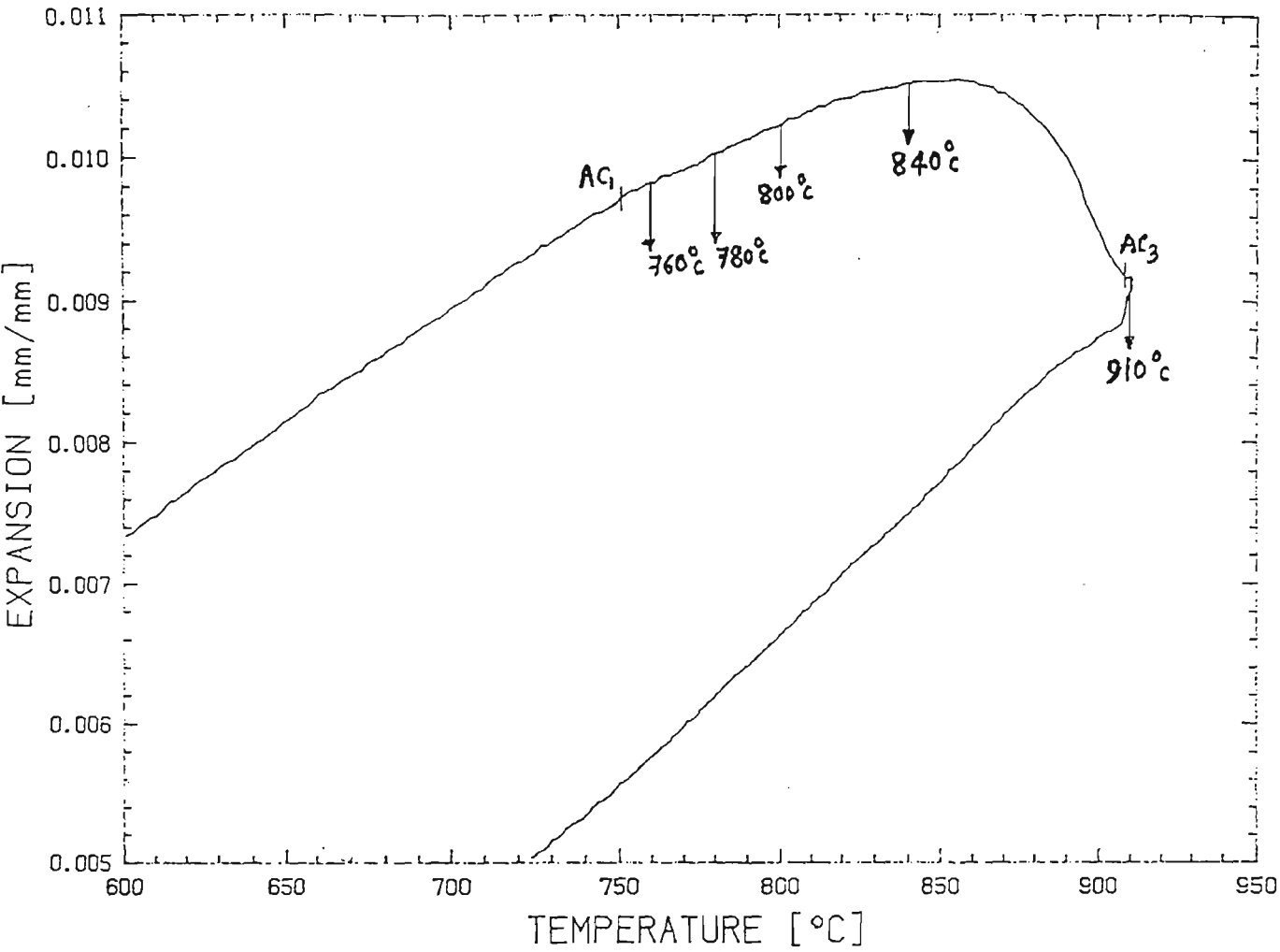
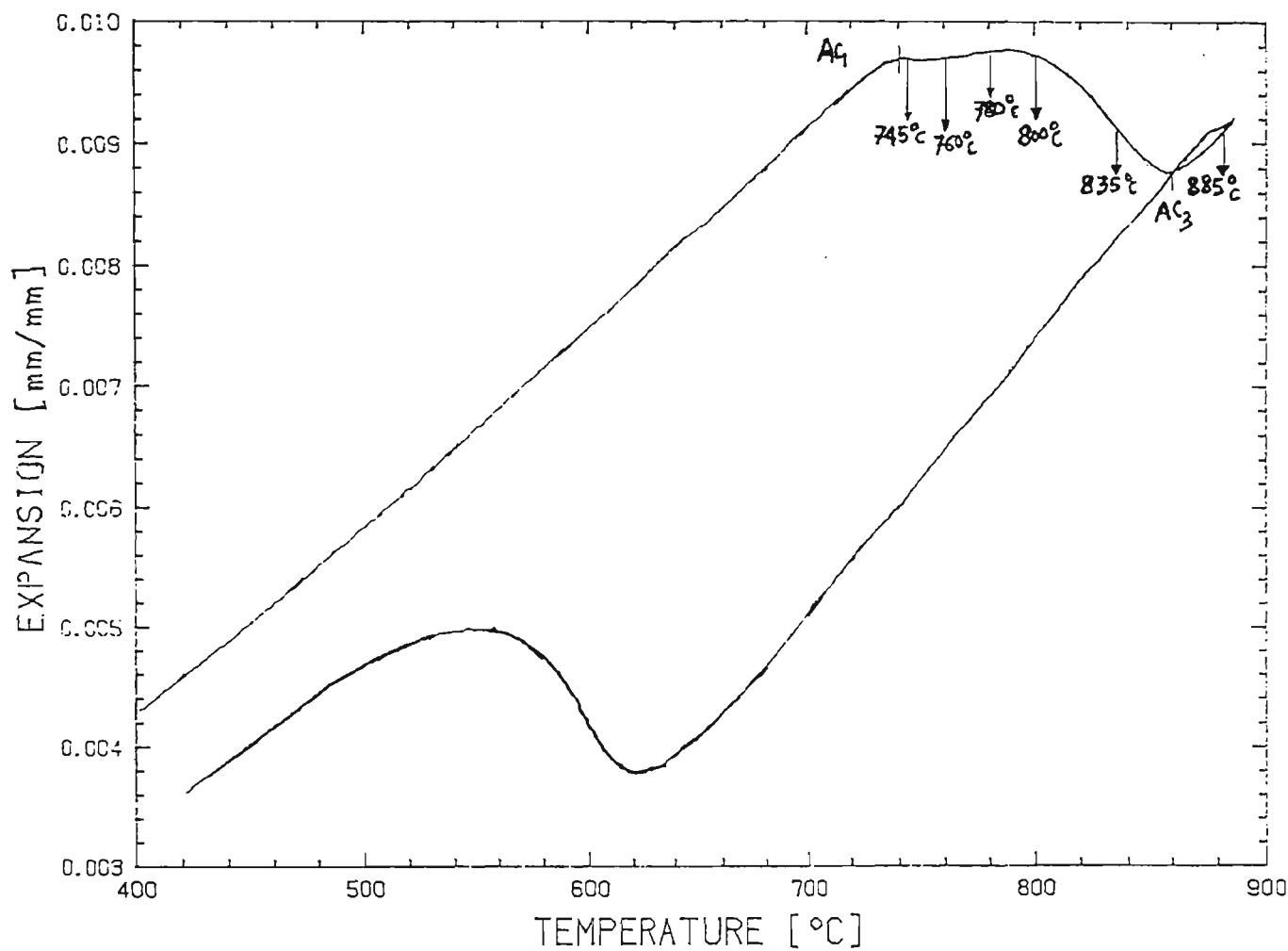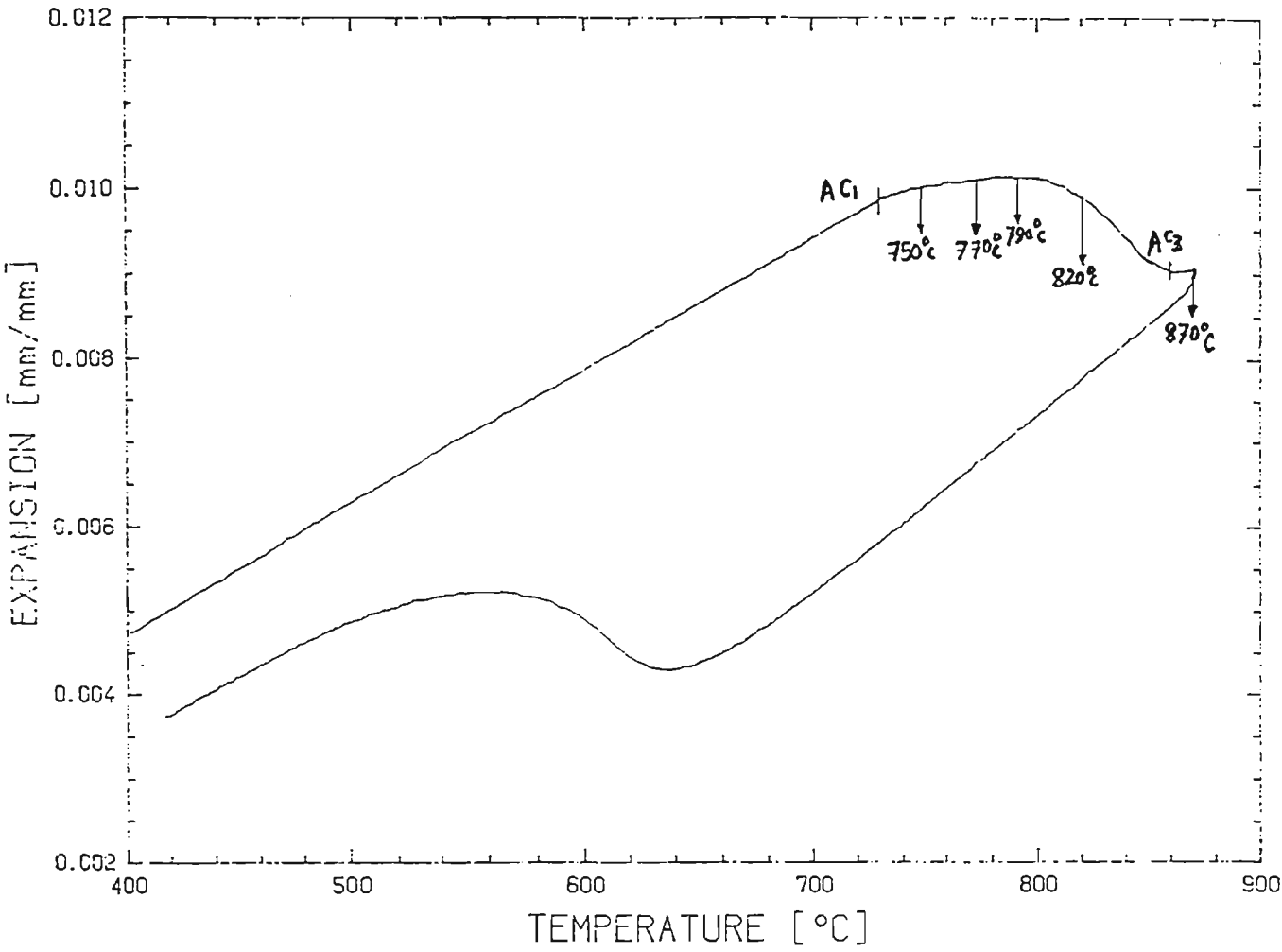Figure 3.2: Experimental program for α→γ transformation studies in Grade 4
(slab). α→γ transformation is mapped by observing microstructures of
the samples quenched from temperatures indicated on the figure.

Figure 3.3: Experimental program for α→γ transformation studies in Grade 1A (plate). α→γ transformation is mapped by observing microstructures of the samples quenched from temperatures indicated on the figure.

Figure 3.4: Experimental program for α→γ transformation studies in Grade 1
(plate). α→γ transformation is mapped by observing microstructures of
the samples quenched from temperatures indicated on the figure.

3.3 Experimental Procedure for TMP Studies Using Dilatometer

Thermomechanical processing simulation studies were carried out using *Dilatronic* Quench and Deformation Dilatometer. Set-up for quench and deformation dilatometry, sample preparation, simulation program and the techniques of dilatometer data analysis are explained in the following sections.

3.3.1 Experimental Set-up for Quench Dilatometry

Schematic diagram showing set up for quench dilatometry is shown in Fig. 3.5.
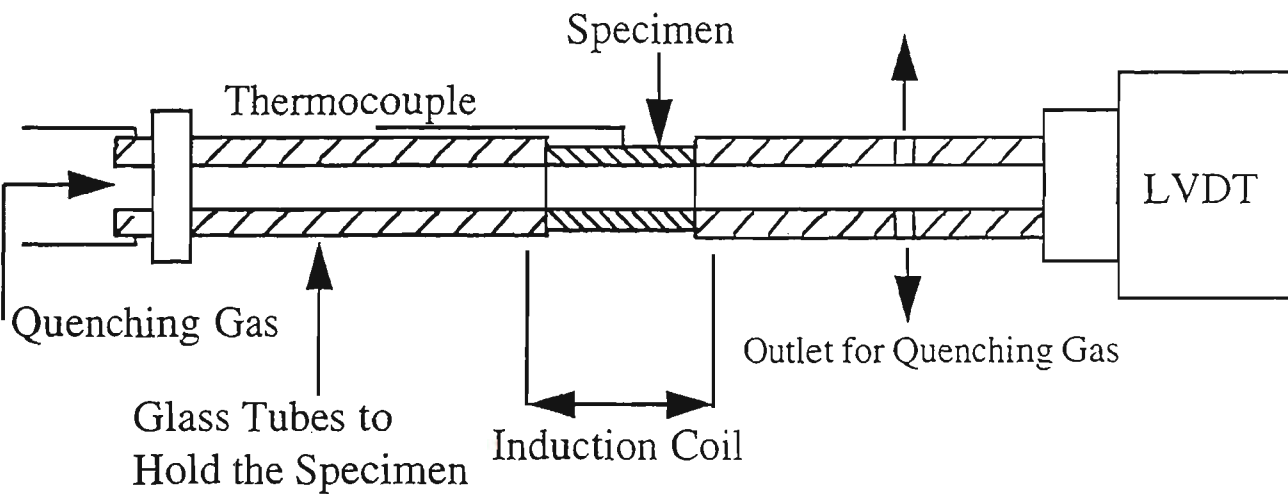
Figure 3.5: Schematic diagram showing set-up for quench dilatometry.

Specimen is held between two glass tubes. Sample is heated by water cooled induction coil in vacuum. Temperature program is controlled by the thermocouple spot welded on the surface of the sample. Changes in the dimensions of the sample during heating and cooling are sensed by the LVDT (Linearly Variable Differential Transformer) connected to one of the glass tube. Sample cooling is achieved by controlling the inert (Helium) gas flow through the glass tubes and the inside of the sample. Contact surfaces of the

tubes and the sample are kept flat and perpendicular to the longitudinal axis because only

a very small compressive pressure is used to hold the sample between the glass tubes. If

the sample is not held correctly between the glass tubes or if the contact surfaces are not

flat and parallel, then the sample may move or even slip when the quenching gas flows

through it. Slight vibrations of the sample (when not held correctly between the glass

tubes) causes noise in the dilatation curve which makes data analysis quite difficult.

3.3.2 Experimental Set-up for Deformation Dilatometry

Schematic diagram showing the set-up for deformation dilatometry is shown in Fig. 3.6.
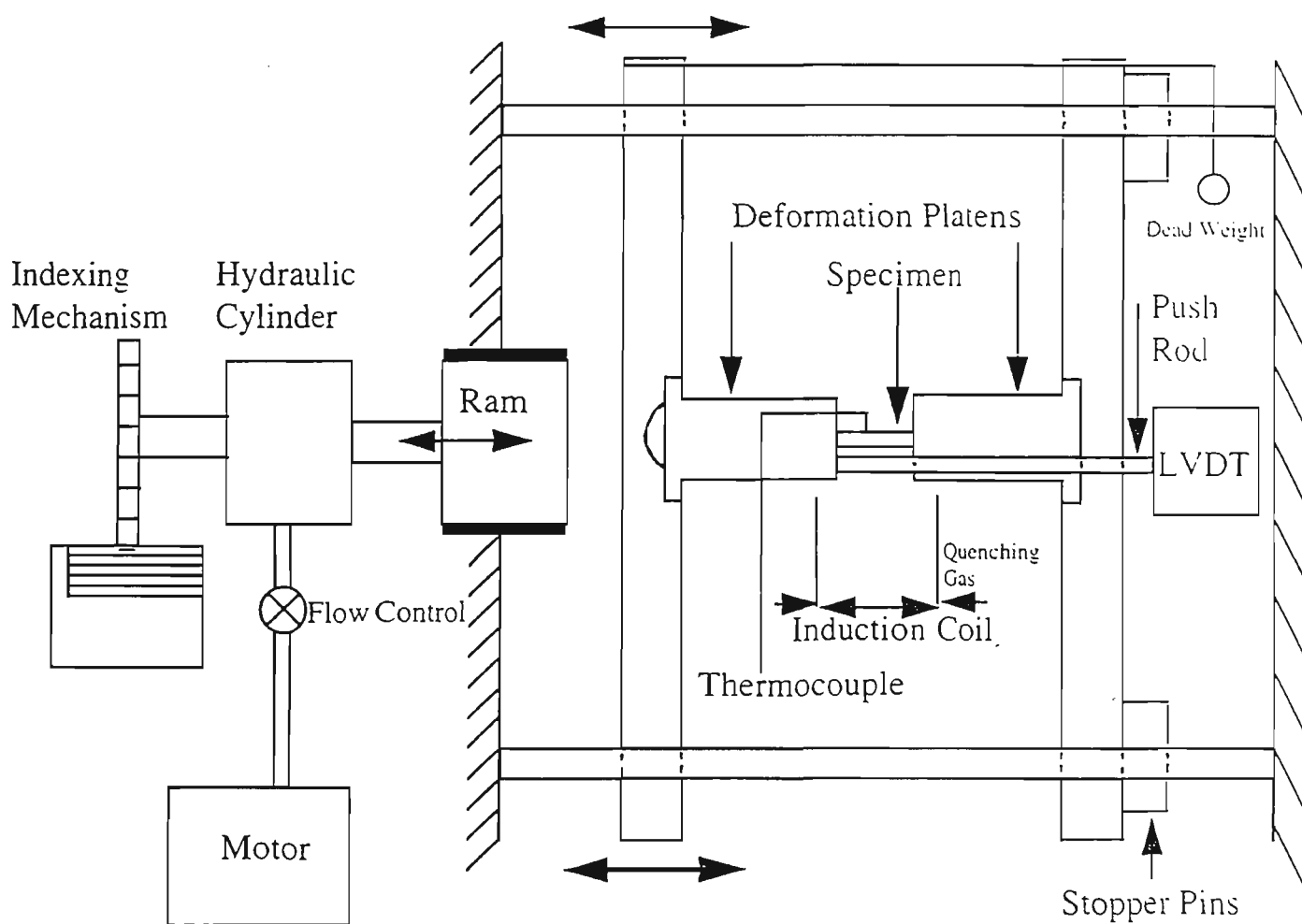
Figure 3.6: Schematic diagram showing set-up for deformation dilatometry.

The specimen is held between quartz deformation platens using a dead weight. A glass push rod is threaded through one of the deformation platens. The push rod presses against the contact surface of the opposing deformation platen on one end while the other end is connected to a LVDT. The changes in the dimensions of the sample during deformation, heating and cooling are sensed by the LVDT through the movement of the push rod. Temperature program is controlled by the thermocouple spot welded on the surface of the sample. Cooling / quenching is achieved through the inert (Helium) gas flow through the induction coil which has holes on the inside surface. The quenching gas comes out of these holes and cools the sample uniformly from all sides. Deformation program is controlled by the indexing mechanism. Rate of movement of the ram ($\equiv$ strain rate) is controlled by adjusting flow control valve situated between the motor and the hydraulic cylinder. The contact surfaces of the deformation platens and the sample are kept flat and perpendicular to the longitudinal axis. If the surfaces are not flat and parallel, then the compressive force during deformation does not remain axial and the deformation becomes non-uniform.

3.3.3 Accuracy of Deformation Control

Accuracy of deformation control is evaluated as the % error between the expected deformation and the actual deformation given by the dilatometer. The % error in deformation is calculated using following formula:

% Error   = {(Expected Defor. - Actual Defor.) / Expected Defor. } x 100

           = {($l_f^{act.} - l_f^{exp.}$) / ($l_o - l_f^{exp.}$)} x 100, where

$l_f^{act.}$ = actual final length of the sample, $l_f^{exp.}$ = expected final length of the sample. l_o = original (before deformation) length of the sample. % error in deformation as a function of test count is given in Fig. 3.7.
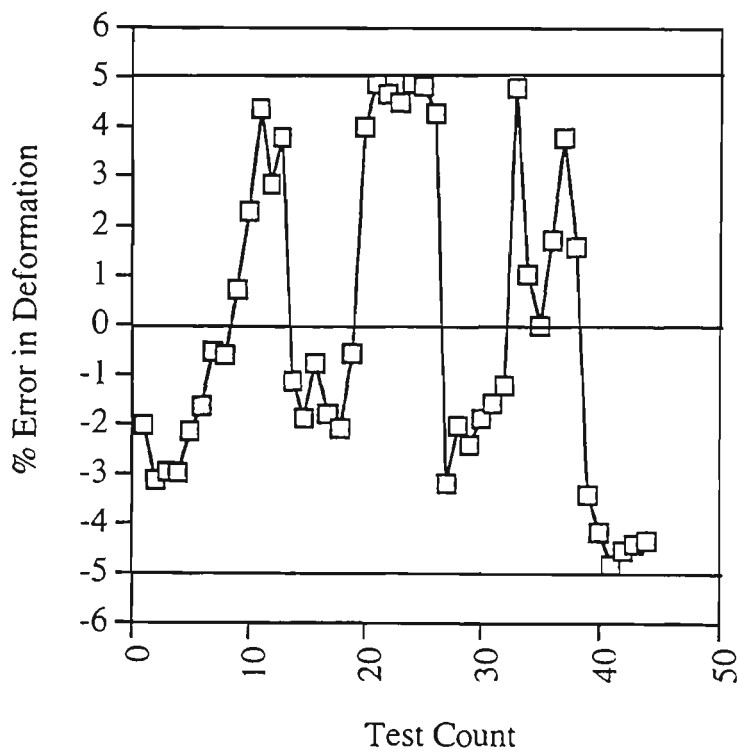
Negative sign indicates that actual deformation is more than the expected and the positive sign indicates actual deformation to be less than the expected deformation.

Figure 3.7: Estimation of the accuracy of deformation control in the dilatometer.

Fig. 3.7 indicates a systematic variation in % error as more tests are carried out. The reason for this is the wear of the contact surfaces of the deformation platens. When the deformation surfaces are freshly ground and flat, the actual deformation is slightly more than the expected. As the tests are continued, the contact surfaces wear out and start to become uneven. This leads to actual deformation being less than the expected amount. When the error became + 5%, the platens were removed and reground and made flat which again gives actual deformation to be slightly more than the expected. Accuracy of

deformation control was maintained within ± 5 % of the expected value as shown in Fig. 3.7.

3.3.4 Sample Preparation for Dilatometric Testing

Specimens used for quench dilatometry were 10 mm long cylindrical tubes with out side diameter of 5 mm and a wall thickness of 0.75 mm. Samples for deformation dilatometer were 6 mm long solid cylinders of 3.2 mm in diameter. Thermocouple was spot welded on the surface of each sample during the tests to continuously monitor sample temperature. 0.025 mm thick Tantalum foils were spot welded on the contact surface of the deformation samples. Boron nitride powder was applied on the contact surfaces of the deformation platens to minimise friction and promote homogeneous deformation. The testing was carried out in vacuum (10^{-4} torr). Samples were sectioned, mounted and prepared for metallographic examination after the dilatometric testing.

3.3.5 Procedure for Dilatometer Data Analysis

The transformation kinetics of austenite can be determined from the dilatometric data. The method for data analysis to determine the transformation kinetics of austenite is shown schematically in Fig. 3.8.

As the temperature is decreased during cooling, austenite contracts which results in a straight line in the ΔL/L v/s Temperature plot (Line AB in Fig. 3.8). The slope of line AB represents the coefficient of thermal expansion (contraction in this case) for austenite. As the temperature gets lower than Ar_3, γ begins to transform to ferrite. $\gamma \rightarrow \alpha$ transformation involves volume expansion which tends to compensate for volume

contraction due to decreasing temperature. This results into a deviation from linearity of

the cooling curve (ΔL/L v/s T plot).

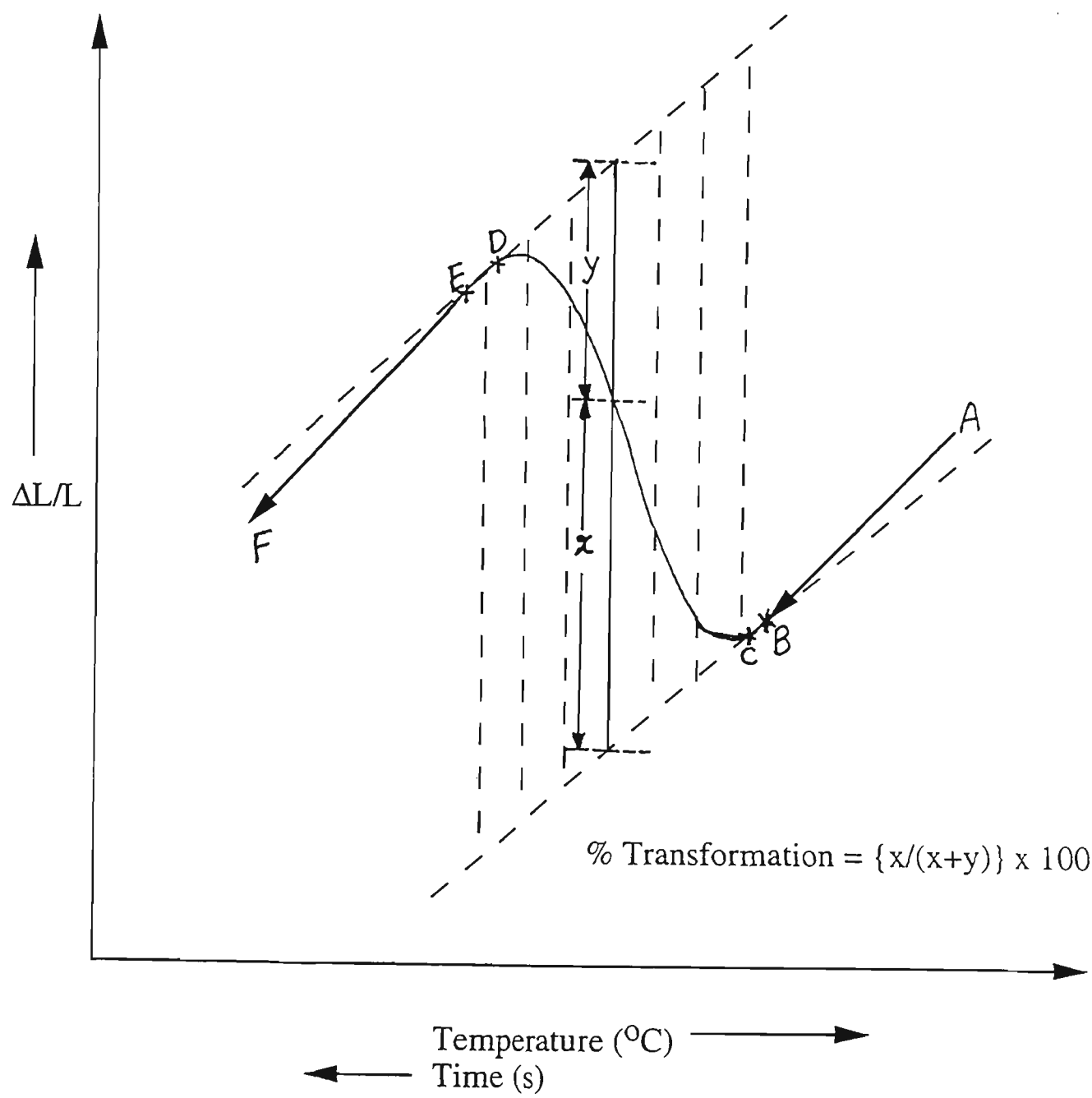% Transformation = {x/(x+y)} x 100

Figure 3.8: Determination of transformation kinetics (schematic).

As the temperature is lowered further, significant amount of $\gamma \rightarrow \alpha$ transformation takes

place and the corresponding volume expansion is so high that it overtakes the volume

contraction. This results in to a net expansion of the sample as shown by curve CD in Fig. 3.8. As $\gamma \rightarrow \alpha$ transformation reaches near completion, thermal contraction balances the volume expansion due to transformation and the cooling curve tends to flatten (line DE in Fig. 3.8). As the temperature is lowered further, $\gamma \rightarrow \alpha$ transformation is complete and the thermal contraction of ferrite again results in a straight line (line EF in Fig. 3.8). The slope of line EF is different than that of line AB and represents the coefficient of thermal expansion (contraction in this case) of ferrite.

The kinetics of $\gamma \rightarrow \alpha$ transformation can be evaluated by choosing points on the straight portions of cooling curve (points B, C, D and E in Fig. 3.8) and drawing tangents to the cooling curves through these points. Lines parallel to Y axis are drawn which intersect the curve BCDE at various positions. Fraction of transformation completed (in %) at any temperature or time can be given according to following formula and as shown in Fig. 3.8:

$$\% \text{ Transformation Completed} = \{X/(X+Y)\} \times 100$$

Thus the progress of transformation as a function of time or temperature can be evaluated by analysing the dilatometric data. The threshold for determining the onset of transformation is set at 2.5 % in the present investigation This means that the point at which the cooling curve exhibits 2.5 % deviation from the linearity is considered as the transformation start temperature (Ar_3).

The choice of points B, C, D and E is important. As a guide line, these points are chosen as close to the curved portion of the cooling curve as possible. The choice of these points can lead to a variation of 5 - 10 °C in the estimated values of transformation start and finish temperatures. Other factor which can introduce some variability in results is

the nature of cooling curve itself. If the cooling curve exhibits a sharp transition between the straight line portion and the curved portion as shown in Fig. 3.8, then the error due to the choice of points B, C, D and E is quite marginal. The problem arises when the cooling curve exhibits a basin shape between the straight line and the upward portion of the cooling curve. This is particularly important in finishing stages of the transformation where the curve may exhibit an extensive flat top before it dips down. In this case, the variation in the results due to the choice of the points B, C, D and E could be more significant (~ 20 °C). Special care was taken to choose the points as consistently as possible. When the cooling curve exhibits double or triple transformation (ferrite - pearlite, ferrite - bainite, ferrite - bainite - martensite) similar analysis is carried out for each of these transformations to determine the onset and termination of relevant transformation.

3.3.6 Metallography and Optical Microscopy

Samples for metallographic examination were sectioned and mounted in hot set resin (bakelite) using a Buehler mounting press. In case of deformed samples, section was taken parallel to the longitudinal axis through the centre of the samples. Following mounting, samples were ground and polished using conventional techniques, then etched with 2.5 % Nital for metallographic examination.

The microstructures of etched samples were examined using a Nikon optical microscope. The mean grain size of the deformed samples was measured at the centre of the samples using single circle intercept technique [37]. The volume fractions of second

phases in all samples were estimated using MD20 image analysis system which was

coupled with the optical microscope.

3.3.7 Microhardness Testing

Microhardness testing was undertaken to investigate the effect of TMP, cooling rate and

Ti/Nb contents on the hardness of samples. In these tests, a Leco microhardness testing

machine, operated at 100 gm load, was used to determine hardness. In deformed

samples, the hardness was taken at the centre of the samples. At least three hardness

readings were taken for every sample and the average of these readings was recorded as

the hardness of the sample. Care was taken to ensure that the distance between the

hardness indentations was at least three times the diagonal of the indentation.

3.3.8 Procedure for the Construction of CCT Diagrams

The cooling curves were plotted on a linear temperature scale (Y axis) and logarithmic

time scale (X axis). The temperatures of onset and termination of the transformation as

determined from the dilatometric data analysis were marked on each cooling curve. The

type of transformation was identified by metallographic examination of the dilatometer

sample. Start and finish temperatures for a given type of transformation ($\gamma \rightarrow \alpha$

transformation, for example) on different cooling curves were then joined by a smooth

curve. Cooling rates and the corresponding hardnesses of the samples were marked at

the end of cooling curves. Transformation temperatures during reheating (Ac_1 and Ac_3)

were also included in the CCT diagram for reference. In the present work, phase

identification was done based on the classification system suggested by Bramfitt and

Speer [218] which has been reproduced in Fig. 2.20. Exact locations of the phase boundaries are difficult to be determined. In such cases dotted lines have been used which represent possible locations of the phase boundaries.

3.4 Design of Thermomechanical Process Simulation Using Dilatometer

3.4.1 Experimental Program for TMP Simulation

Experimental program for deformation dilatometry is shown schematically in Fig. 3.9.
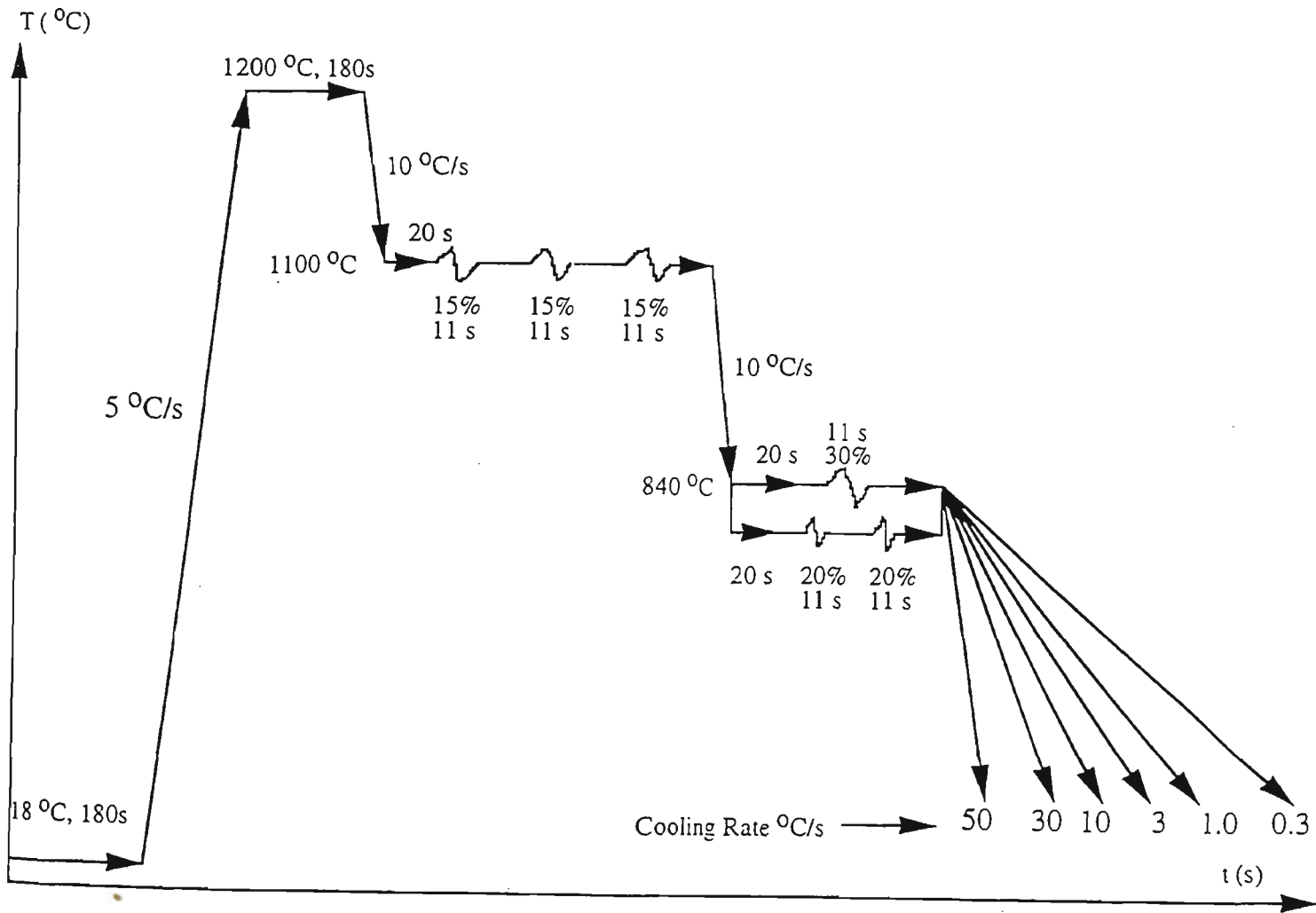

Figure 3.9: Schematic presentation of the experimental program for dilatometry.

The austenitizing temperature - time program for undeformed sample (quench dilatometry) was identical to that shown in Fig. 3.9. TMP simulation involves reheating up to 1200 °C to ensure dissolution of MAE and generation of uniform austenite grain size, roughing deformation at 1100 °C to refine austenite grain size, finishing deformation below T_{nr} to achieve unrecrystallized (pancake) austenite microstructure and subsequent cooling at different rates up to room temperature. The choice of time, temperature, deformation and cooling parameters to simulate industrial TMP in laboratory is explained in the following sections.

3.4.2 Reheating

Reheating temperature of 1200 °C was selected based on the results of grain growth studies. It will be shown in Chapter 4 that the steels studied exhibit GCT between 1050 - 1200 °C. Abnormal grain growth is found to be reaching near completion at around 1200 °C. Calculated precipitate solution temperatures for all steels also fall below 1200 °C as given in Chapter 4. Thus choice of reheating temperature of 1200 °C assured a relatively stable grain growth regime with most of MAE in solution in austenite.

Soaking time of 3 minutes at 1200 °C was determined based on some experimental trials. Sample were heated to 1200 °C for different soaking times and then quenched immediately to room temperature. Prior austenite microstructure was revealed using hot picric acid method described in # 3.2.2. The results of these trials for Grade 4 (Slab) are given below:

Soaking Time at 1200 °C	Mean γ grain size (μm)	Remark
30 sec.	157	Mixed microstructure
2 min.	115	Mixed Microstructure
3 min.	118	Uniform Microstructure
5 min.	122	Uniform Microstructure

Soaking time of 3 minutes was chosen which seems to be the minimum time required to generate a uniform austenite grain size at 1200 °C in dilatometer samples.

3.4.3 Roughing

Choice of roughing temperature of 1100 °C was based on the typical roughing temperature for rolling of similar steels in the industrial practice. Roughing deformation schedule was determined based on the experimental trials. Samples were reheated to 1200 °C for 3 minutes and cooled to 1100 °C. Various roughing deformation schedules were given at 1100 °C to achieve as fine and uniform austenite grain size as possible. The results of these trials for Grade 4 are given below:

Roughing Deformation Schedule	Recrystallized γ Grain Size (μm)
33 %	37
20 % + 20 %	35
50 %	32
25 % + 25 %	29
15 % + 15 % + 15 %	27

Recrystallized austenite grain size for the steels studied using 15 % + 15 % + 15% roughing deformation schedule at 1100 °C is given below:

Steel Grade	γ Grain Size after Roughing Deformation (μm)
Grade 1 (Slab)	26.4
Grade 4 (Slab)	27
Grade 1 (Plate)	28.8
Grade 1A (Plate)	32.4

Austenite microstructure after roughing deformation was fairly uniform for all steels. Thus, three recrystallization cycles with 15 % deformation at each pass at 1100 °C

achieved fine, uniform and comparable grain size in all steels. More deformation at this stage can achieve further grain refinement, however this can not be done on the dilatometer due to physical limitations of the small sample size. Interpass time of 11 sec. simulates typical interpass time in industrial rolling practice. Strain rate during deformation was ~ 2.5 s^{-1} which was kept constant during all deformation trials.

3.4.4 Finishing

Choice of finishing deformation temperature is important since this temperature needs to be higher than Ar_3 (to avoid deformation in the $\gamma+\alpha$ two phase field) and lower than the "No-Recrystallization Temperature - T_{nr}" (to gain the maximum advantage from the TMP). In the present study the Ar_3 temperature for the steels studied was determined experimentally using quench dilatometry at a cooling rate of 0.3 $^{\circ}C/s$. The results are given below:

Steel Grade	Ar_3 ($^{\circ}C$) (undeformed samples cooled at 0.3 $^{\circ}C/s$)
Grade 1 (Slab)	690
Grade 4 (Slab)	723
Grade 1 (Plate)	685
Grade 1A (Plate)	705

The Ar_3 of deformed samples was expected to be much higher than that of undeformed sample. Combination of roughing and finishing deformations was expected to raise the Ar_3 up to ~ 800 $^{\circ}C$. Thus finishing deformation temperature needed to be higher than 800 $^{\circ}C$ to avoid deformation in the $\gamma+\alpha$ two phase field.

No-recrystallization temperatures for the steels studied were calculated according to equations reported in the literature. Results of these calculation are given as follows:

T_{nr} (°C) for Grade 1 - Slab and Plate	T_{nr} (°C) for Grade 4 - Slab	T_{nr} (°C) for Grade 1A - Plate	Reference
986	987	988	Bai et al. [192]
942	942	942	Medina [195]
1013	1013	888	Barbosa et al. [196]
905	905	905	Majta et al. [198]

$\varepsilon = 0.45$, $\dot{\varepsilon} = 2.5\ s^{-1}$, $d_o = 30\ \mu m$

Thus, choice of 840 °C to be the finishing deformation temperature meets both requirements: higher than Ar_3 and well below T_{nr}.

Finishing deformation of either 30 % (one pass) or 40 % (two passes of 20 % reductions each) was given at 840 °C to simulate controlled rolling practice for these steels. Choice of 11 sec. interpass time simulates typical interpass time in industrial rolling.

Evolution of austenite microstructures after reheating and soaking, roughing and finishing in Grade 4 - Slab are shown in Fig. 3.10a - 3.10c, while austenite microstructures after finishing deformation for other steels are shown in Fig. 3.10d to 3.10f. It can be seen from Fig. 3.10a that austenite microstructure in Grade 4 - slab after reheating and soaking at 1200 °C for 3 minutes is coarse (~ 118 μm) and uniform, while austenite microstructure is fine (~ 27μm), uniform and fully recrystallized after roughing deformation at 1100 °C (Fig. 3.10b); and essentially unrecrystallized, pancake structure after finishing deformation below T_{nr} at 840 °C (Fig. 3.10c). It can also be seen from Figs. 3.10d to 3.10f that austenite microstructures after finishing deformation in other steels (Grade 1 - Slab, Grades 1 and 1A - Plates) are comparable to that of Grade 4 - Slab (Fig. 3.10c) at similar deformation condition.
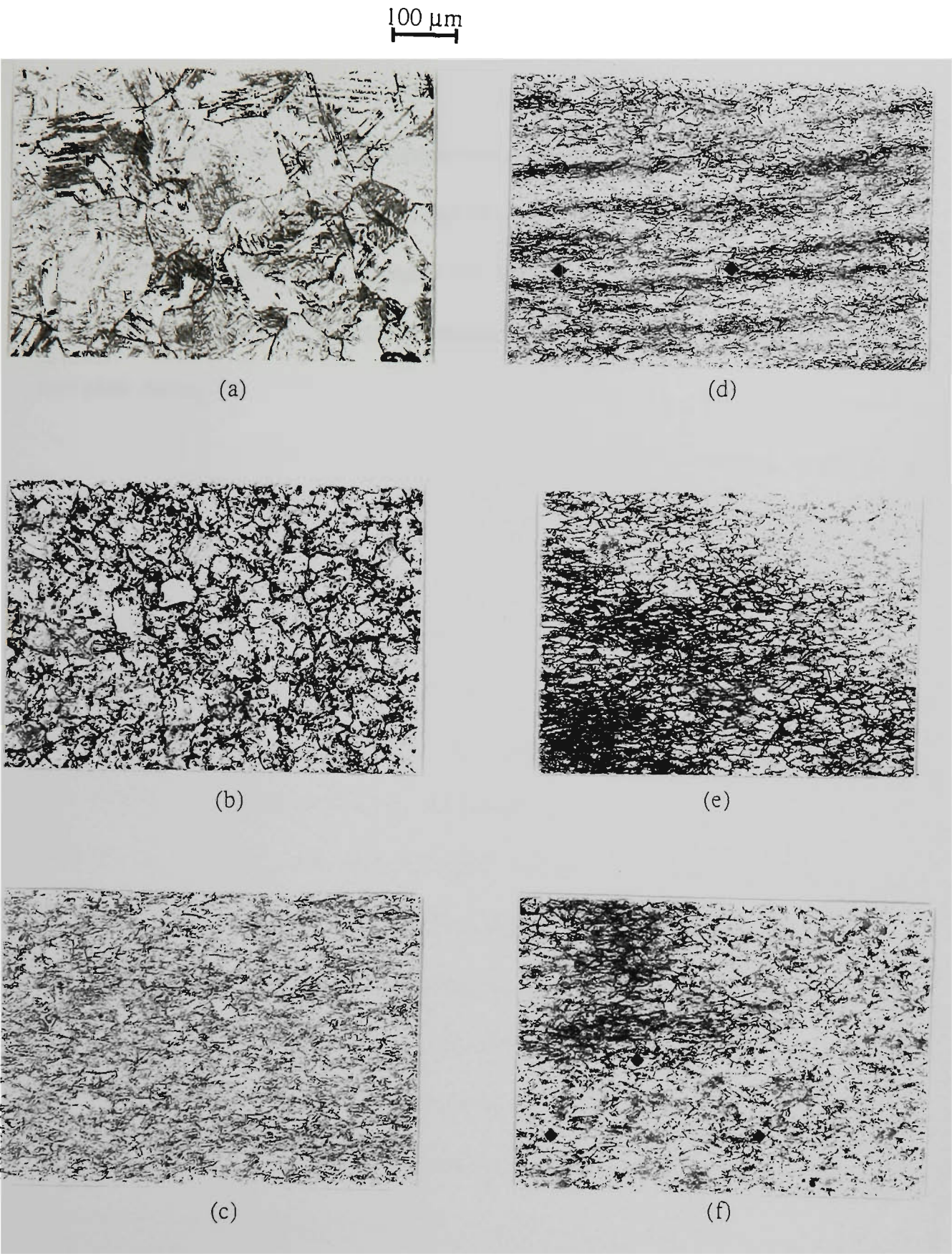
100 μm

(a)

(d)

(b)

(e)

(c)

(f)

Figure 3.10: Austenite microstructures during TMP of Grade 4 - Slab: (a) after reheating and soaking at 1200 °C for 3 minutes, (b) after roughing (3 * 15% R) at 1100 °C; and (c) to (f) after 2 * 20% finishing deformation at 840 °C in Grade 4 - Slab. Grade 1 - Slab, Grade 1 - Plate and Grade 1A - Plate. respectively. Magnification: 100 X, etching tchnique: hot saturated aqueous picric acid method.

3.4.5 Cooling

Controlled cooling from finishing temperature of 840 $^{\circ}$C up to room temperature was achieved by controlling inert (Helium) gas flow. Linear cooling rates of 0.3, 1, 3, 10, 30 and 50 $^{\circ}$C/s were employed to construct CCT diagrams. These cooling rates simulate the cooling rates which are encountered in practice during air cooling or accelerated cooling after plate rolling.

Chapter 4:   Austenite Grain Growth During Reheating in
Ti-Nb-Mn-Mo Microalloyed Steels

4.1 Introduction

It is known that particle containing materials such as microalloyed steels exhibit

abnormal grain growth during reheating. The occurrence of abnormal grain growth has

been related to the progressive dissolution and coarsening of microalloy precipitates as

the reheating temperature is increased. The temperature above which abnormal grain

growth becomes predominant is commonly termed as the 'grain coarsening temperature

(GCT)'. The knowledge of GCT for a given microalloyed steel grade is extremely

important in designing the hot rolling schedule for that steel. GCT is related to the very

first step in hot rolling process of the steel, namely, the reheating temperature. As has

been explained in detail in # 1.1.5, the reheating temperature should be selected in

reference to the GCT such that sufficient amount of microalloying elements are

dissolved, but the austenite grain size is kept desirably small and uniform. Experimental

determination of GCT usually involves heating a series of samples in the temperature

range of 900 - 1350 °C in steps of 50 or 100 °C for a period of 30 or 60 minutes,

quenching the samples immediately in water or iced brine, revealing and measuring the

prior austenite grain size by suitable techniques and then plotting the mean austenite

grain size as a function of temperature.

In the present work, the GCT of five microalloyed steels containing Ti, Mo and various

levels of Mn and Nb addition (Table 3.1) in as-cast slab and controlled rolled plate

conditions was determined experimentally. The conventional method of measuring

mean grain size as a function of temperature was found to be inadequate to determine

the GCT in some cases. Therefore, an alternative way which consists of measuring the mean size of the largest grain as a function of temperature was developed to determine the onset and termination of abnormal grain growth in slab and plate steels.

Heterogeneity in initial grain size distribution of austenite was identified as an additional factor which can influence the GCT of microalloyed steels. Generation of heterogeneity in initial austenite grain sizes in different steels has been discussed in terms of microstructural features before reheating, and their influence on the evolution of austenite during $\alpha \rightarrow \gamma$ transformation. It was also found that the grain coarsening behaviour of austenite during reheating of plate steels was markedly different than that in slab steels. Abnormal grain growth in slab steels was found to be single stage and highly pronounced. On the other hand, abnormal grain growth in plate steels was found to be not so significant and occurred in two stages. It is suggested that the two-stage coarsening behaviour of plate steels can be related to the dissolution of two different species of microalloy precipitates found in controlled rolled steels. Finally, the possibility of correlating the precipitate dissolution temperature with the GCT has been critically examined. It was found that the calculated precipitate dissolution temperature provided a useful pointer to locate the GCT of the microalloyed steels studied.

4.2 Results

4.2.1 Grain Growth in Slab Steels

The results of the mean grain size in Grade 1A - Slab (1.55% Mn. 0.03% Nb) as a
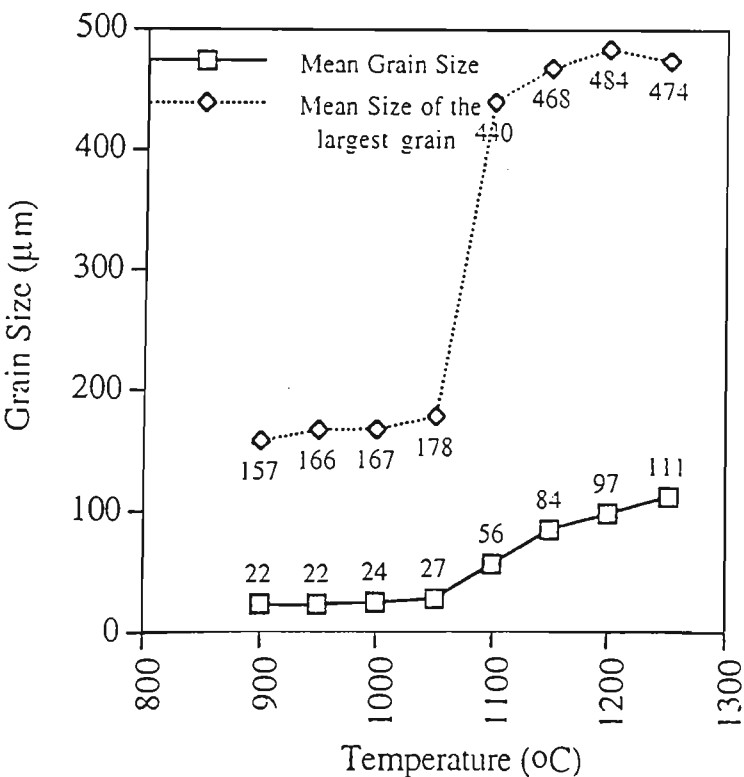
function of temperature are presented in Fig. 4.1.
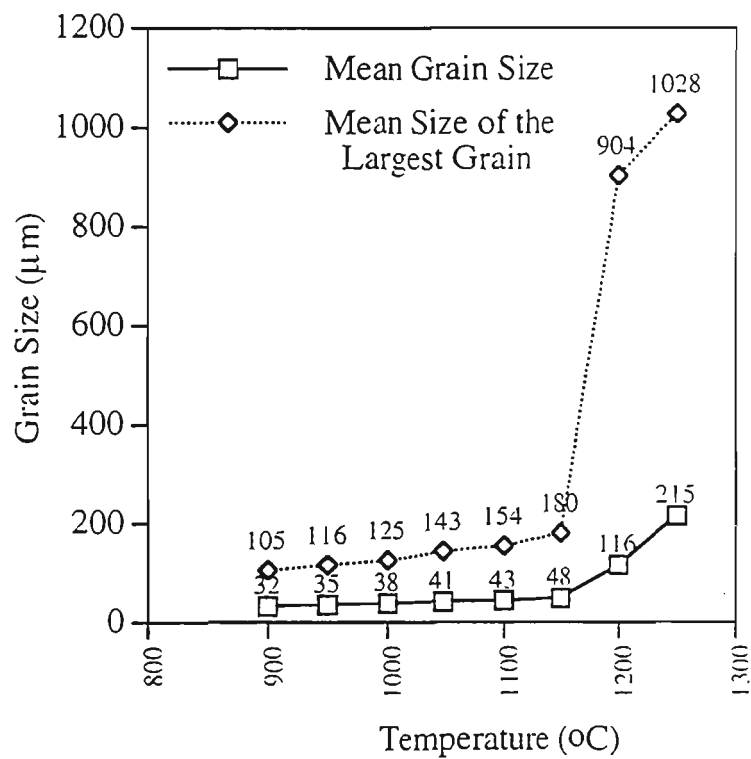
Figure 4.1: Mean grain size and the mean size of the largest grain
as a function of temperature in Grade 1A (Slab)

It can be seen that the mean grain size increases steadily from 32 μm to 48 μm when the

temperature is raised from 900 °C to 1150 °C. Furthermore, when the temperature is

raised to 1200 °C, the mean grain size increases suddenly up to 116 μm and continues to

increase rapidly at 1250 °C. The data show that the GCT for Grade 1A (Slab) seems to

be ~ 1150 °C.

The results of the mean size of the largest grain as a function of temperature for Grade

1A (Slab) are also included in Fig. 4.1. The data indicate that the mean size of the largest

grain increases gradually from 105 μm up to 180 μm when the temperature is increased

from 900 °C up to 1150 °C. Mean size of the largest grain increases abruptly up to 904

μm at 1200 °C and then increases less rapidly to 1028 μm at 1250 °C. Thus, GCT for

Grade 1A (Slab) can be seen to be 1150 °C which is in agreement with the data for

growth of the mean grain size. In addition, data for growth of the mean largest grain size

also indicate that the abnormal grain growth reaches near completion at around 1200 °C

which is hard to detect in the mean grain size curve.

The experimental results of the mean grain size in Grade 4 -Slab (1.07% Mn. 0.047%

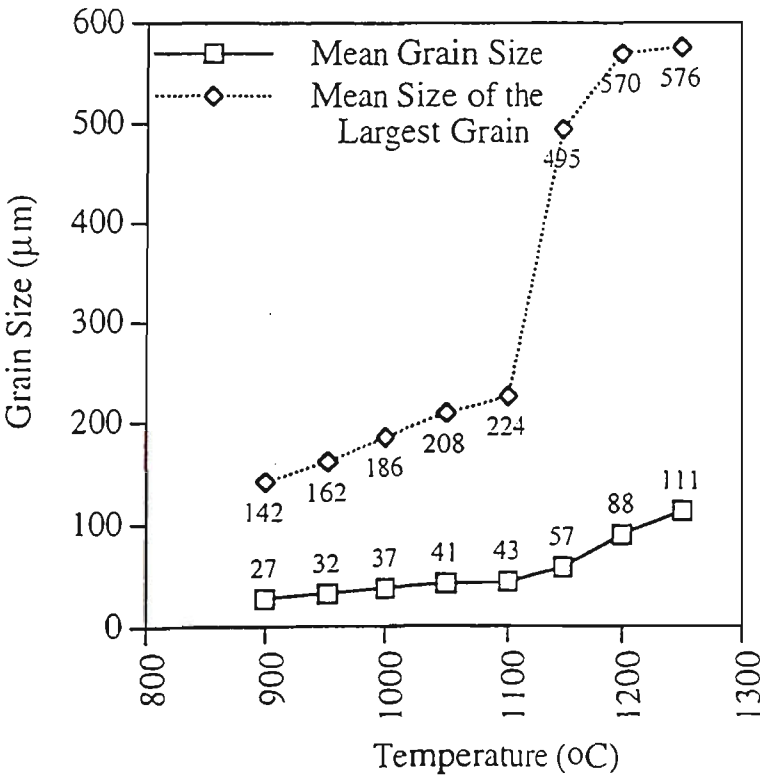Nb) as a function of temperature are presented in Fig. 4.2.

Figure 4.2: Mean grain size and the mean size of the largest grain
as a function of temperature in Grade 4 (Slab)

The data given in Fig. 4.2 indicate that the mean grain size increases steadily from 22 μm

to 27 μm when the temperature is raised from 900 °C to 1050 °C. When the temperature

is raised to 1100 °C, the mean grain size increases suddenly up to 56 μm and continues

to increase rapidly until 1150 °C. Mean grain size increases less rapidly above 1150 °C.

Thus the range of GCT for Grade 4 (Slab) appears to be 1050 °C - 1150 °C. For Grade 4

(Slab), the results of the mean size of the largest grain as a function of temperature are

included in Fig. 4.2. The data indicate that the mean size of the largest grain increases

gradually from 157 μm up to 178 μm when the temperature is increased from 900 °C up

to 1050 °C. Mean size of the largest grain increases suddenly up to 440 μm at 1100 °C

and then increases less rapidly above 1150 °C. Thus, the range of GCT for Grade 4

(Slab) is 1050 - 1150 °C, which is in agreement with the mean grain size data.

Results of the mean grain size in Grade 5 -Slab (1.07% Mn, 0.04% Nb) as a function of

temperature are presented in Fig. 4.3.

Figure 4.3: Mean grain size and the mean size of the largest grain
as a function of temperature in Grade 5 (Slab)

The data given in Fig. 4.3 indicate that the mean grain size increases steadily from 27 μm to 43 μm when the temperature is raised from 900 °C to 1100 °C. When the temperature is raised to 1150 °C, the mean grain size increases suddenly up to 57 μm and continues to increase rapidly until 1250 °C. Thus the GCT for Grade 5 (Slab) is 1100 °C.

Results of the mean size of the largest grain as a function of temperature for Grade 5 (Slab) are included in Fig. 4.3. The data indicate that the mean size of the largest grain increases gradually from 142 μm up to 224 μm when the temperature is increased from 900 °C up to 1100 °C. Mean size of the largest grain increases suddenly up to 498 μm at 1150 °C and then increases less rapidly above 1200 °C. Thus, GCT for Grade 5 (Slab) can be seen to be 1100 °C which is in agreement with the data for growth of the mean grain size. In addition, data for growth of the mean largest grain size also indicates that the abnormal grain growth reaches near completion at around 1200 °C which can not be detected in the mean grain size curve. Thus, the range of GCT for Grade 5 (Slab) is 1100 - 1200 °C.

Representative microstructures during reheating of Grade 4 at different reheating temperatures are shown in Fig. 4.4. Development of duplex microstructure and abnormal grain growth in Grade 4 - Slab is evident from the occurrence of very large, multi-sided grains with concave grain boundaries in the microstructure at 1100 °C as shown in Fig. 4.4e

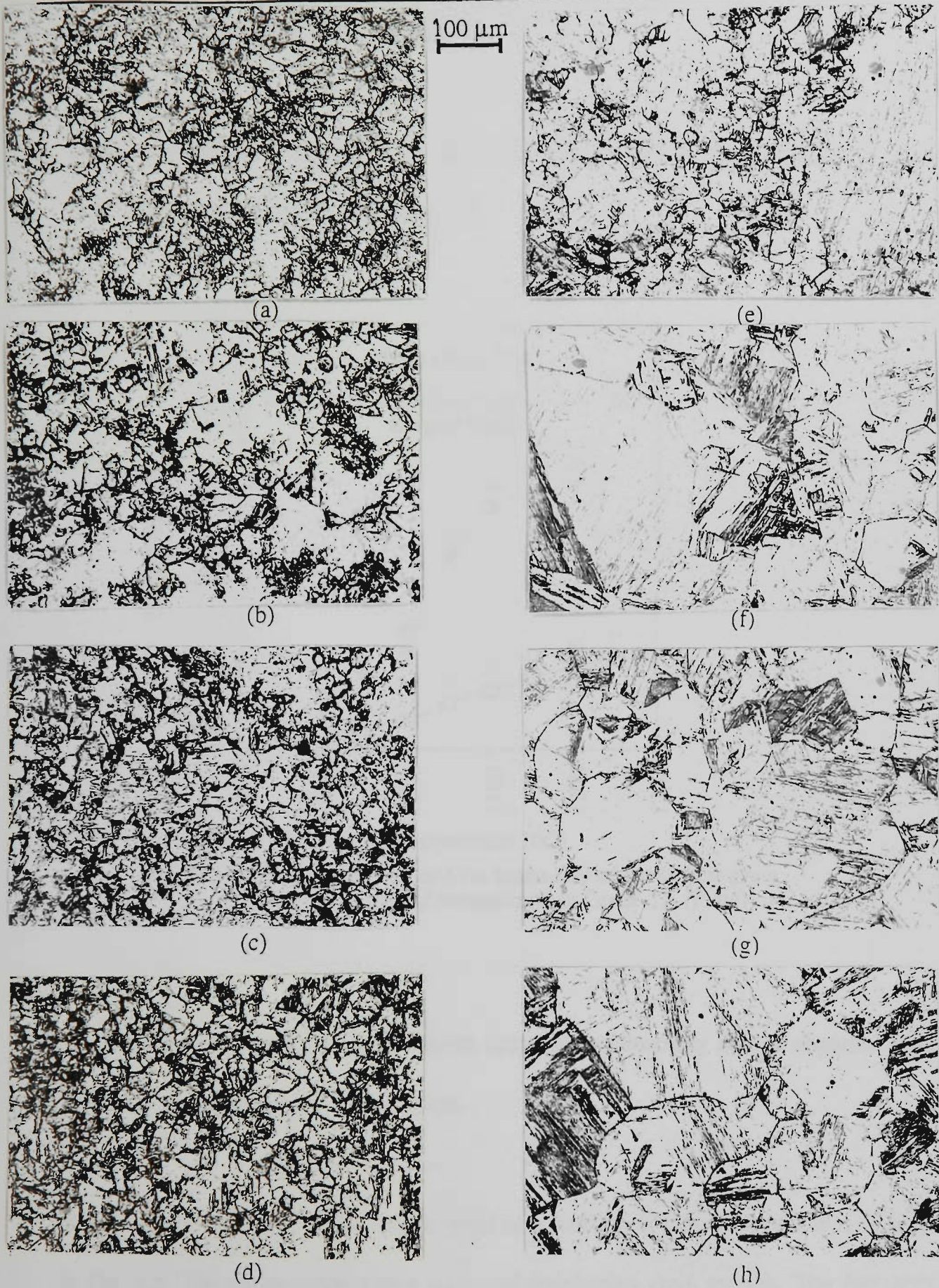Figure 4.4: Representative microstructures of austenite during reheating of Grade 4 (1.1% Mn, Ti-Nb-Mo) - Slab (t = 1800s) at: (a) 900 °C, (b) 950 °C, (c) 1000 °C. (d) 1050 °C, (e) 1100 °C, (f) 1150 °C, (g) 1200 °C and (h) 1250 °C. Note the development of duplex microstructure in (e). Magnification: 100X, etching tchnique: hot saturated aqueous picric acid method.

4.2.2 Grain Growth in Plate Steels

Effect of reheating temperature on the mean austenite grain size in Grade 1A -Plate (1.55% Mn, 0.031% Nb) is given Fig. 4.5.
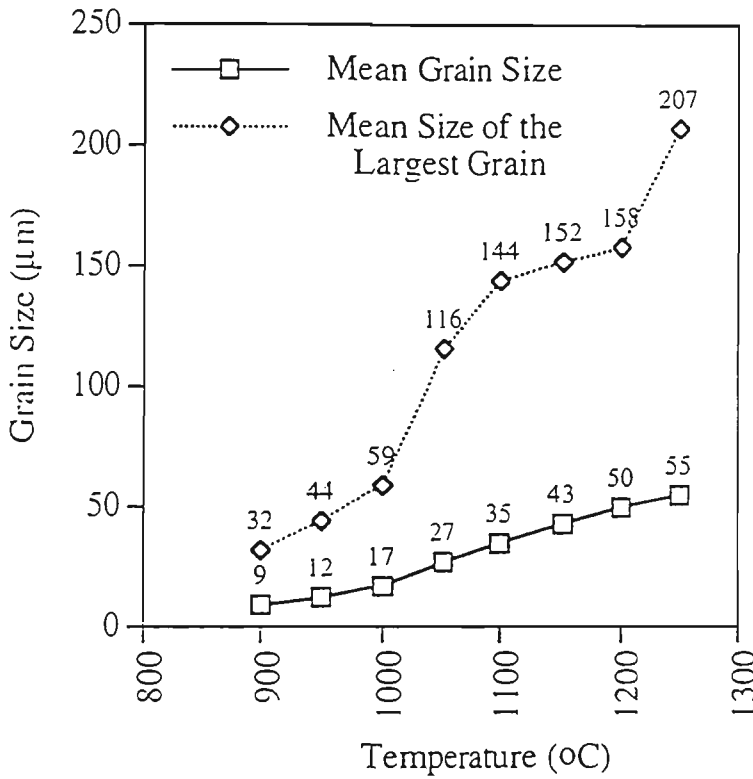
Figure 4.5: Mean grain size and the mean size of the largest grain as a function of temperature in Grade 1A (Plate)

The data indicate that the mean grain size increases continuously and no abnormal grain growth is evident at higher temperatures.

Results of the mean size of the largest grain as a function of temperature is also included in Fig. 4.5. The curve exhibits two stages of accelerated grain growth. The first stage starts at about 1000 °C and continues up to 1100 °C. As the temperature is increased further, the second stage of accelerated grain growth is reached which is above 1200 °C for Grade 1A (Plate). The two stage coarsening behaviour observed in plate steel is

unique which can not be detected in the conventional mean grain size v/s temperature curve. The GCT for Grade 1A (plate) seems to be ~ 1200 °C.

Effect of reheating temperature on the mean austenite grain size in Grade 1 -Plate (1.66% Mn, 0.054% Nb) is given Fig. 4.6.
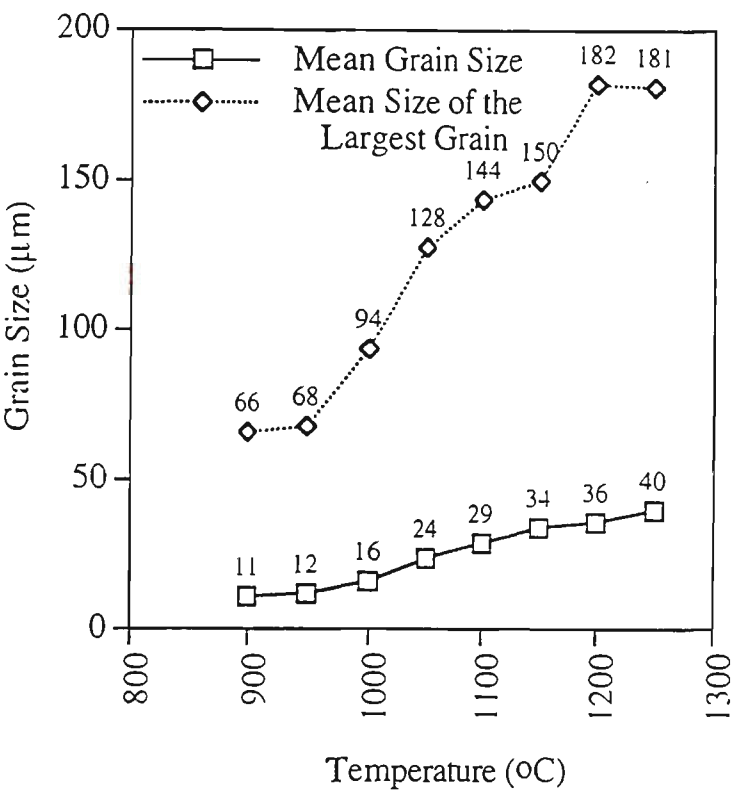

Figure 4.6: Mean grain size and the mean size of the largest grain
as a function of temperature in Grade 1 (Plate)

The data indicate that the mean grain size increases continuously and no abnormal grain growth is evident at higher temperatures.

Results of the mean size of the largest grain as a function of temperature is also included in Fig. 4.6. The curve exhibits two stages of accelerated grain growth. The first stage starts at about 950 °C and continues up to 1050 °C. As the temperature is increased further, the second stage of accelerated grain growth is reached which is above 1150 °C for Grade 1 (Plate). This two stage coarsening behaviour observed in Grade 1 - plate steel is similar to that observed in Grade 1A (Plate) and it can not be detected in the

mean grain size v/s temperature curve. The GCT for Grade 1 (plate) seems to be 1150 °C - 1200 °C. Representative microstructures during reheating of Grade 1A at different reheating temperatures are shown in Fig. 4.7.

Summary of experimentally determined grain coarsening temperatures for different steels studied is given in Table 4.1.

Table 4.1: Summary of experimentally determined GCTs.

Steel Grade	Experimentally Determined GCT (°C)
Grade 1A (Slab)	1150
Grade 4 (Slab)	1050 - 1150
Grade 5 (Slab)	1100 - 1200
Grade 1A (Plate)	1000 - 1100 and above 1200
Grade 1 (Plate)	950 - 1050 and 1150 - 1200

It is interesting to note that Grade 1A -Slab (0.031% Nb) exhibits a higher GCT, as compared to Grade 4 Slab (0.047% Nb). It should be noted that Grade 5 Slab (0.04% Nb, 0.014% Ti) contains slightly lower levels of microalloy addition as compared to Grade 4 Slab (0.047% Nb, 0.016% Ti), but it exhibits a GCT which is higher than Grade 4. Similarly, in plate steels, Grade 1 has a higher microalloy content (0.054% Nb) compared to Grade 1A (0.031% Nb) at similar levels of Mn addition, but Grade 1 plate steel exhibits a lower GCT compared to Grade 1A - Plate. These results are rather unusual in the sense that it is commonly believed that increases in microalloy content would result in an increase in the GCT. Reasons for this behaviour have been investigated in detail and are discussed in the following sections.
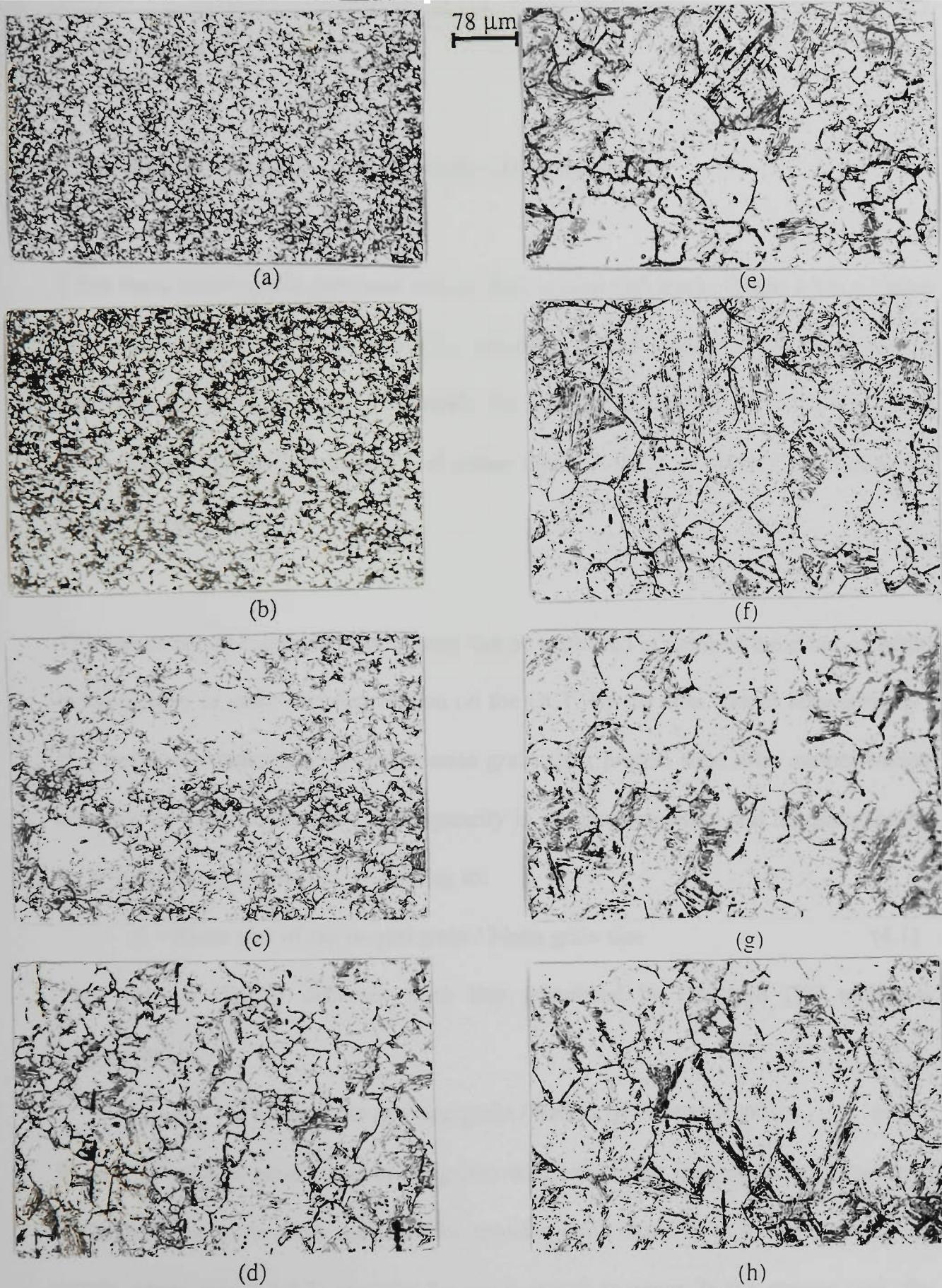
Figure 4.7: Representative microstructures during reheating for Grade 1A (0.03% Nb. Ti-Mn-Mo) - Plate (t = 1800s) at: (a) 900 °C, (b) 950 °C, (c) 1000 °C, (d) 1050 °C. (e) 1100 °C, (f) 1150 °C, (g) 1200 °C and (h) 1250 °C. Note the development of duplex microstructure in (c) and (h). Magnification: 128X, etching tchnique: hot saturated aqueous picric acid method.

4.3 Discussion

4.3.1 Effect of Grain Size Heterogeneity (Z) on the GCT

It has been shown in the previous section that, in case slab steels, Grade 4 has a higher microalloy content (0.047 Nb, 0.016 Ti) compared to both Grade 5 (0.04 Nb, 0.014 Ti) and Grade 1A (0.031 Nb, 0.013 Ti) steels, but the GCT of Grade 4 (1050 °C) was found to be lower compared to the GCT of either Grade 5 (GCT $\sim$ 1100 °C) or Grade 1A (GCT $\sim$ 1150 °C).

The reason for this apparent discrepancy can be explained in terms of the effect of initial heterogeneity in grain size distribution on the GCT. By the term 'initial heterogeneity', it is meant the heterogeneity in austenite grain sizes present soon after austenitization but prior to grain coarsening. Heterogeneity in the microstructure can be characterised by a "heterogeneity ratio (Z)" according to:

$$Z = \text{Mean size of the largest grain / Mean grain size} \tag{4.1}$$

This ratio is slightly different from that postulated by Gladman [19] which is represented by:

$$Z_{Gladman} = \text{Radius of the growing grain / Radius of the matrix grains} \tag{4.2}$$

In Eq. (4.2) matrix grains refer to the grains which are in the <u>immediate neighbourhood</u> of the growing grain. Also, radius of the growing grain has to be at least 1.33 times the matrix grains (see # 1.4.2) in order for grain growth to occur. In the present case, the largest grain based on Eq. (4.1) may or may not be in the immediate neighbourhood of the mean or matrix grains. The value of Z in the current work is determined experimentally by dividing the mean size of the largest grain by the overall mean grain

size in the microstructure. Z is simply a measure of the actual heterogeneity in grain size distribution in a given sample. The value of Z as a function of temperature for Grades 4, 5 and 1A is given in Figure 4.8.
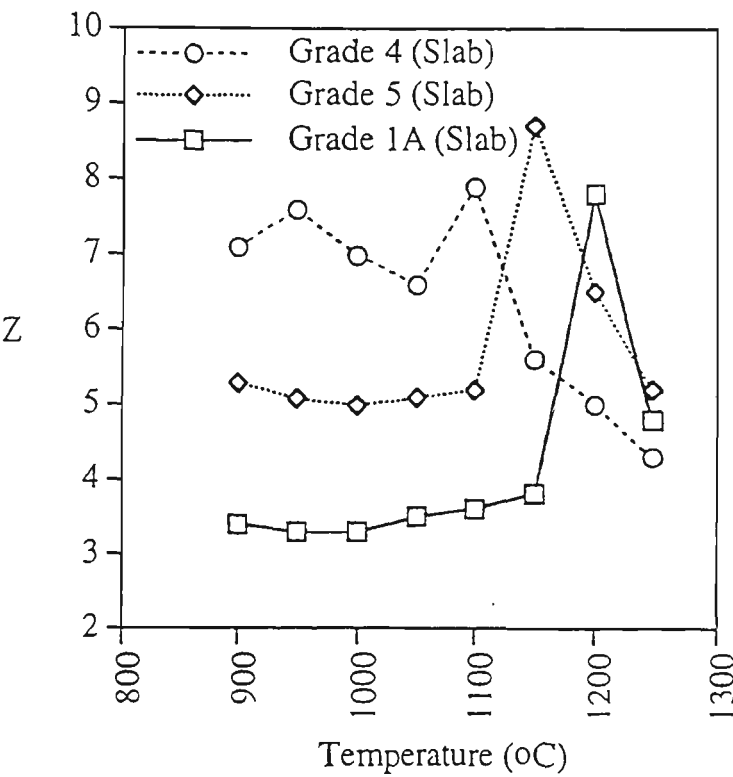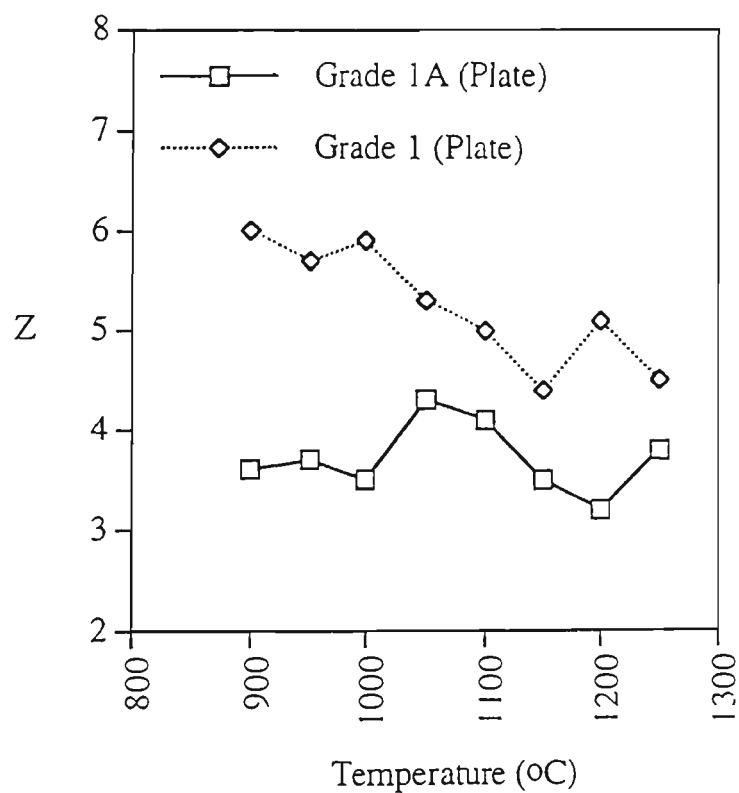

Figure 4.8: Heterogeneity ratio 'Z' as a function of temperature for slab steels

Figure 4.8 shows that Grade 1A has lower Z as compared to Grade 5 at all temperatures up to grain coarsening while the Z for Grade 4 is more than double as compared to Grade 1A and much higher than that of Grade 5. High values of Z in a material indicate presence of grains which are much larger than the mean sized grains and are potential candidates for the nucleation of abnormal grain growth. Thus high value of Z represents an increased inherent tendency for abnormal grain growth which would result in lower GCT in an isochronal experiment such as carried out in this investigation. Grade 1A has the lowest Z values (low heterogeneity) and exhibits the highest GCT despite its low microalloy content. Grade 4, on the other hand, has the highest value of Z and shows

lowest GCT despite its enriched microalloy content. The Z values for Grade 5 are in between those of Grades 1A and 4 and thus exhibits an intermediate GCT.

In case of plate steels, Grade 1 has a higher microalloy content (0.054 Nb, 0.013 Ti) than Grade 1A (0.031 Nb, 0.013 Ti), but the GCT of Grade 1 (1150 °C) is lower than that of Grade 1A (1200 °C). The reason for this apparent discrepancy can be explained in terms of the effect of initial heterogeneity in austenite grain sizes on the GCT as discussed above for the slab steels. The value of Z as a function of temperature for Grades 1 and 1A is given in Figure 4.9.

Figure 4.9: Heterogeneity ratio 'Z' as a function of temperature in plate steels

Figure 4.9 clearly shows that Grade 1A has lower values of Z as compared to Grade 1 at all temperatures up to grain coarsening. As explained before, high values of Z shows an increased inherent tendency for abnormal grain growth in a material which would lower its GCT. Grade 1A has lower values of Z (low heterogeneity) and exhibits the higher

GCT despite its low microalloy content. Grade 1, on the other hand, has the higher values of Z and shows lower GCT despite its enriched microalloy content.

The comparison of microstructures shown in Figs. 4.4 and 4.7 and the analysis for slab and plate steels presented in Figs. 4.8 and 4.9 indicates that the abnormal grain growth in plate steels is not as extensive as in slab steels. The Z value in plate steels does not show a very large increase during the abnormal grain growth period. The reason for this is not clear, however, it is believed that finer starting grain size in plate steels may have an effect on the size of the largest grain that can be developed during abnormal grain growth thus limiting the extent of Z values.

The reasons why different steels exhibit different Z values were investigated and are discussed in the following section.

4.3.2 Effect of Initial Microstructure on Z

It has been shown in the above section that the presence of higher heterogeneity in austenite grain structure (high value of Z) can lower the GCT of microalloyed steels quite significantly in slab as well as plate steels. There could be two main reasons as to why different steels exhibit different values of Z. Firstly, the presence of heterogeneity in microstructure before reheating and secondly the type of microconstituents present in the initial microstructure which could influence the $\alpha \rightarrow \gamma$ transformation resulting in different values of Z in γ region. In order to investigate these possibilities, experiments were carried out to follow the $\alpha \rightarrow \gamma$ transformation in some of the steels using quench dilatometry. Grade 1A (Z = 3.4 at 900 °C) and Grade 4 (Z = 7.1 at 900 °C) were selected

in slab condition because these two steels exhibited the largest difference in the Z values while Grade 1A (Z = 3.6 at 900 °C) and Grade 1 (Z = 6.0 at 900 °C) were used in plate condition. The experimental technique used for this study has been described in # 3.2.3. The resultant microstructures are shown in Figs. 4.10 - 4.13 and details of the microstructure during $\alpha \rightarrow \gamma$ transformation is discussed as follows:

4.3.2.1 $\alpha \rightarrow \gamma$ Transformation in Slab Steels

Microstructure before reheating in Grade 4 (Fig. 4.11a) shows coarse α grains with some (12%) acicular α + pearlite grains. The acicular α - pearlite aggregate transforms first in to fine γ grains (Fig. 4.11 - b, c and d). When austenitization temperature approaches Ac_3, the remaining coarse α grains transform in to relatively coarse γ grains (Fig. 4.11e), thus generating a high value of Z soon after the $\alpha \rightarrow \gamma$ transformation is complete (Fig. 4.11f).

On the other hand, microstructure before reheating in Grade 1A (slab) {Fig. 4.10a} exhibits relatively fine α grains and a higher proportion (23%) of acicular α + pearlite grains. As the austenitization temperature is increased, acicular α - pearlite aggregate transforms in to fine γ grains (Fig. 4.10 b, c and d). Because the volume fraction of acicular α - pearlite is higher in this steel, a larger proportion of material transforms to fine γ. As the temperature approaches Ac_3, the remainder of the α grains, which are also fine in this steel, transform to relatively fine γ grains (Fig. 4.10e). Such a situation results in lower Z value soon after the $\alpha \rightarrow \gamma$ transformation is complete in Grade 1A (Slab) {Fig. 4.10f}.
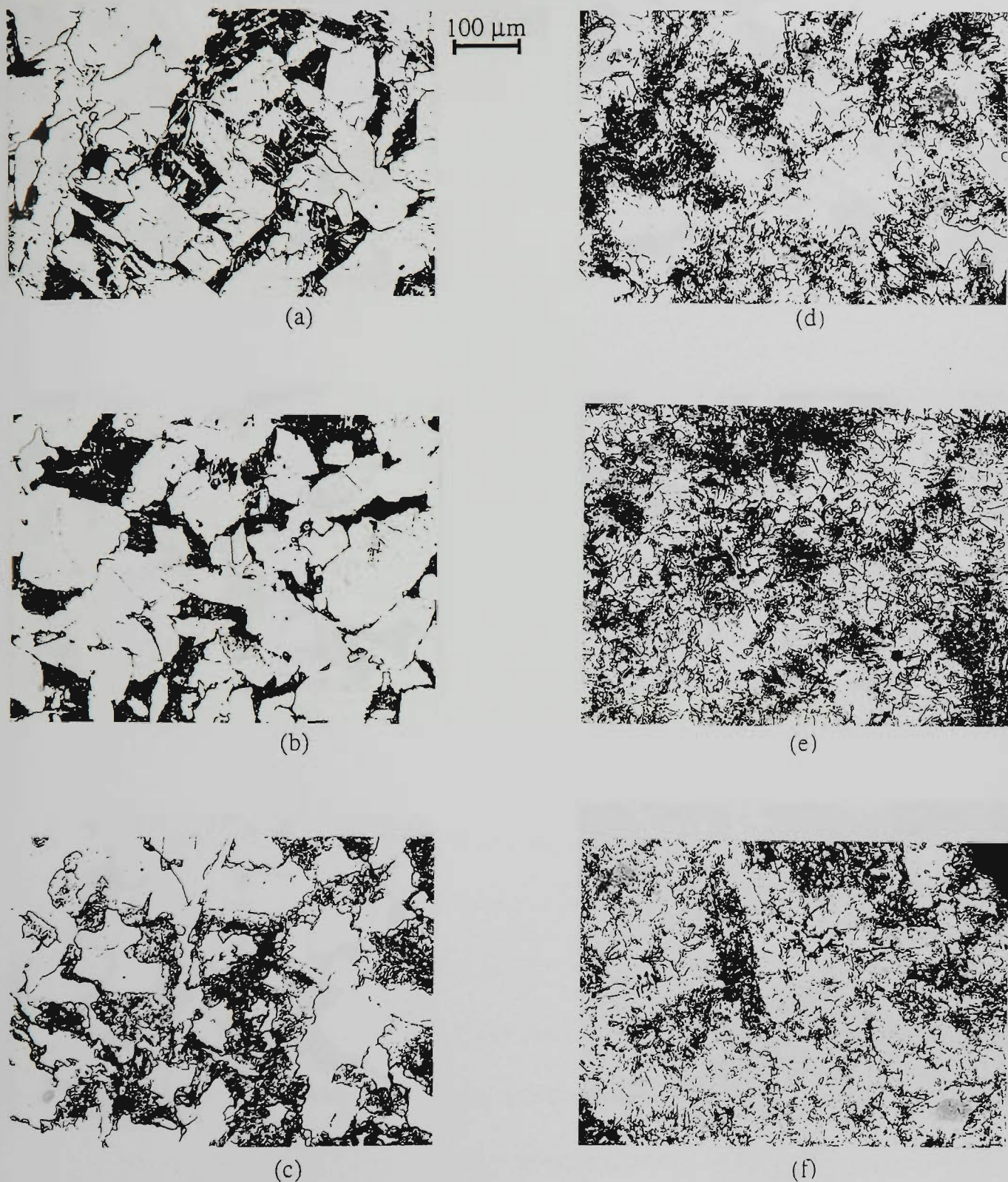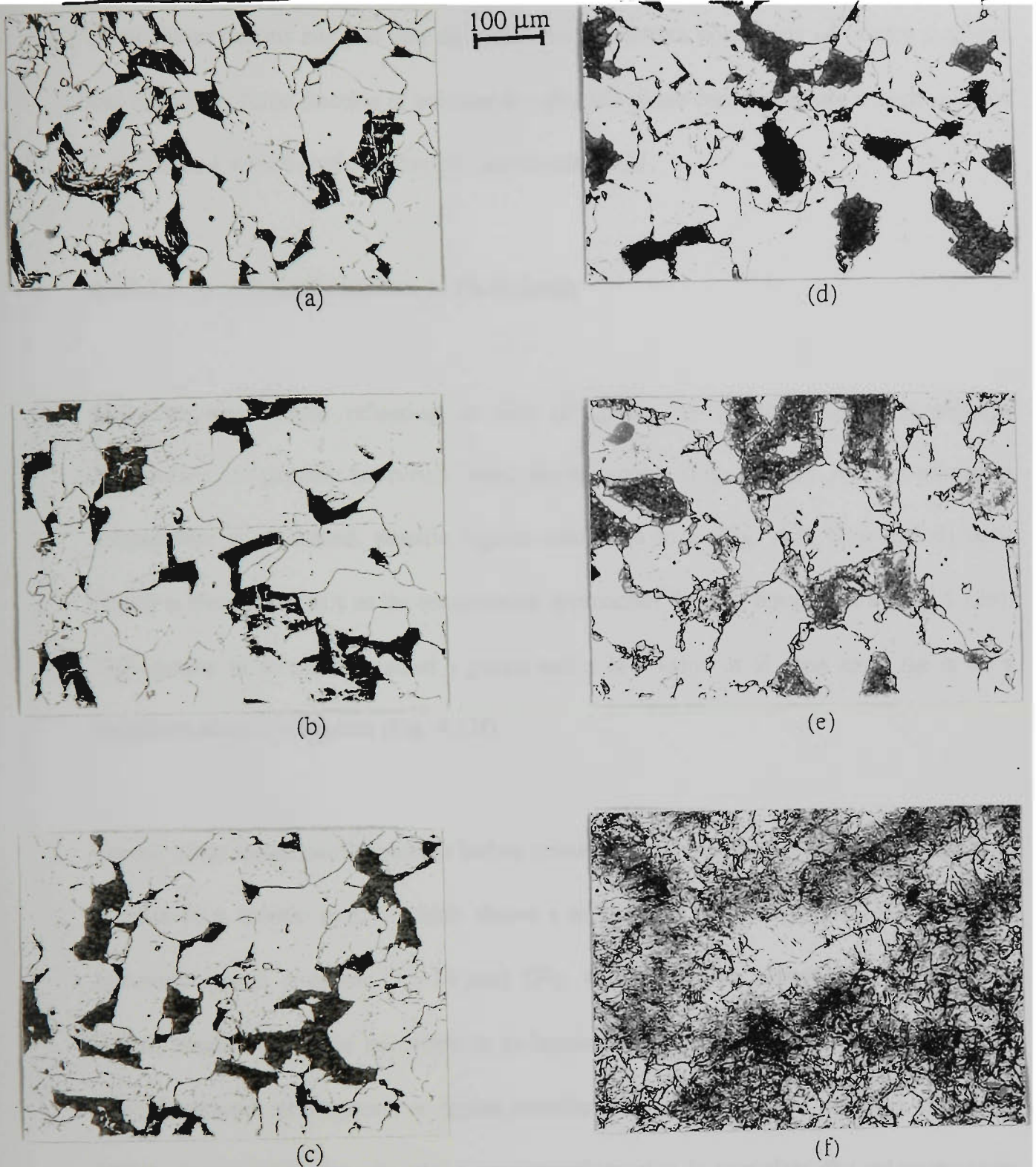
Figure 4.10: (a) Microstructure before reheating (i. e. initial microstructure) for Grade 1A (0.03% Nb, Ti-Mn-Mo) - Slab; and microstructures of samples quenched from: (b) 780 °C (just above Ac₁), (c) 830 °C, (d) 865 °C, (e) 890 °C and (f) 915 °C (just above Ac₃). Dark areas are martensite and light grains are untransformed ferrite in (b) through (e). Note in (f) the homogeneity of austenite grain sizes just after the $\alpha \rightarrow \gamma$ transformation is complete. Magnification: 100X, etching tchnique: hot saturated aqueous picric acid method.

Figure 4.11: (a) Microstructure before reheating (i. e. initial microstructure) for Grade 4 (1.1% Mn, Ti-Nb-Mo) - Slab; and microstructures of samples quenched from: (b) 760 °C (just above Ac_1), (c) 780 °C, (d) 800 °C, (e) 840 °C and (f) 910 °C (just above Ac_3). Dark areas are martensite and light grains are untransformed ferrite in (b) through (e). Note in (f) the heterogeneity of austenite grain sizes just after the $\alpha \rightarrow \gamma$ transformation is complete. Magnification: 100X, etching tchnique: hot saturated aqueous picric acid method.

These observations suggest that an initial microstructure consisting of coarse α grains and a small volume fraction of acicular α + pearlite phase could generate a high value of Z in Grade 4 which could ultimately decrease its GCT.

4.3.2.2 $\alpha \rightarrow \gamma$ Transformation in Plate Steels

Microstructure before reheating in case of Grade 1A (plate) exhibits a uniform distribution of pearlite in evenly sized ferrite grains (Fig. 4.12a). As the reheating temperature is increased, pearlite regions transform to γ (Fig. 4.12 b, c and d) until finally α transforms to γ as the temperature approaches the Ac_3 temperature (Fig. 4.12e). This results in to uniform sized γ grains and a low value of Z soon after the $\alpha \rightarrow \gamma$ transformation is complete (Fig. 4.12f).

On the other hand, microstructure before reheating in Grade 1 (Plate) exhibits bands of pearlite in a ferritic matrix which shows a mixture of extremely fine (1~2 μm) and relatively coarse α grains (12~14 μm) {Fig. 4.13a}. As the reheating temperature is raised, bands of pearlite transform in to bands of fine γ grains (Fig. 4.13 b, c and d). With increased temperature, α grains transform in to γ grains of unequal size (Fig. 4.13e). As a result, soon after the $\alpha \rightarrow \gamma$ transformation is complete, the microstructure exhibits a large variation in the γ grain size and thus a large value of Z (Fig. 4.13f).

Thus, a non-uniform distribution of pearlite (banding) and also the heterogeneity in α grain size before reheating has caused a high heterogeneity (Z) in γ grain size after the $\alpha \rightarrow \gamma$ transformation in Grade 1 (Plate).
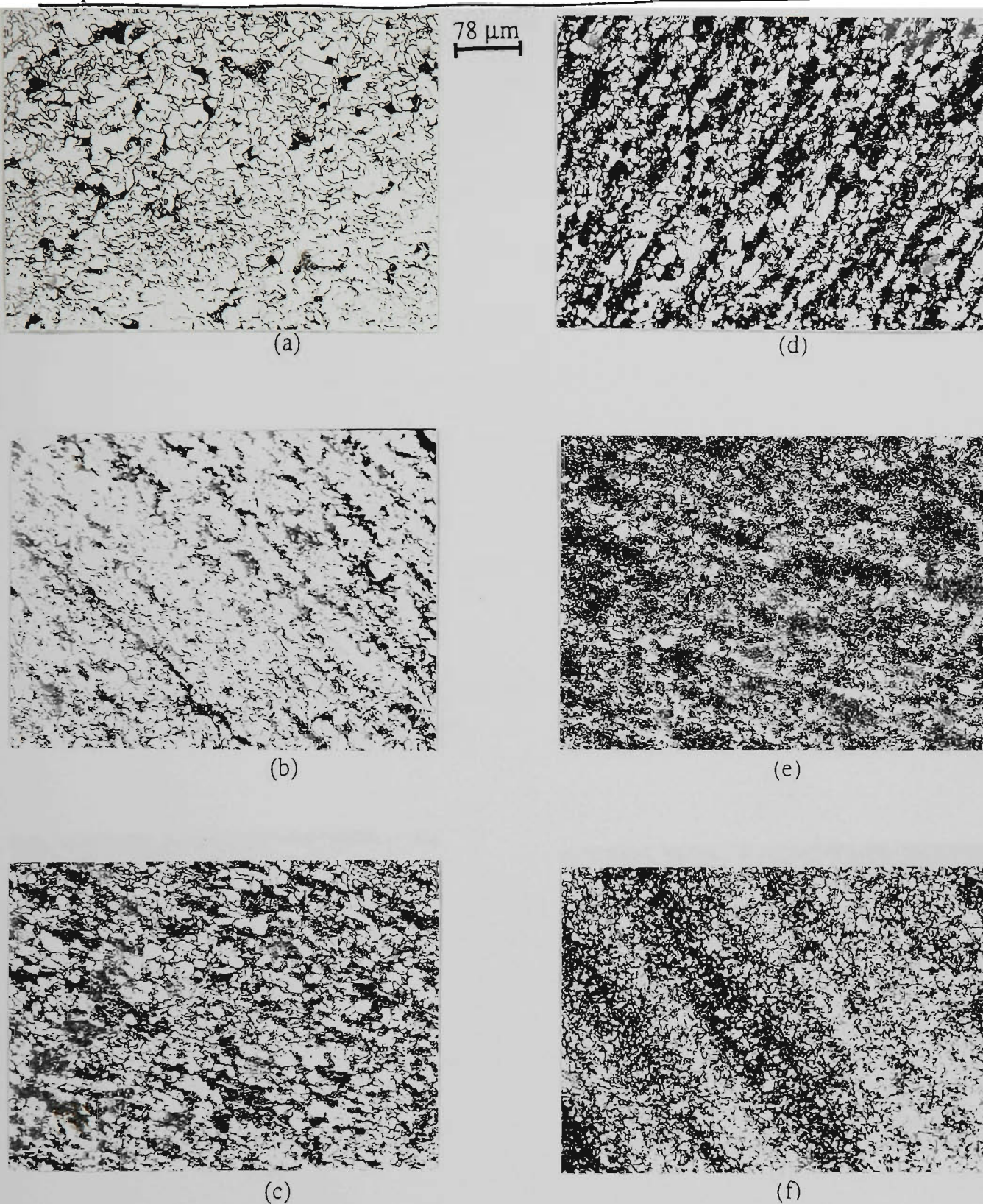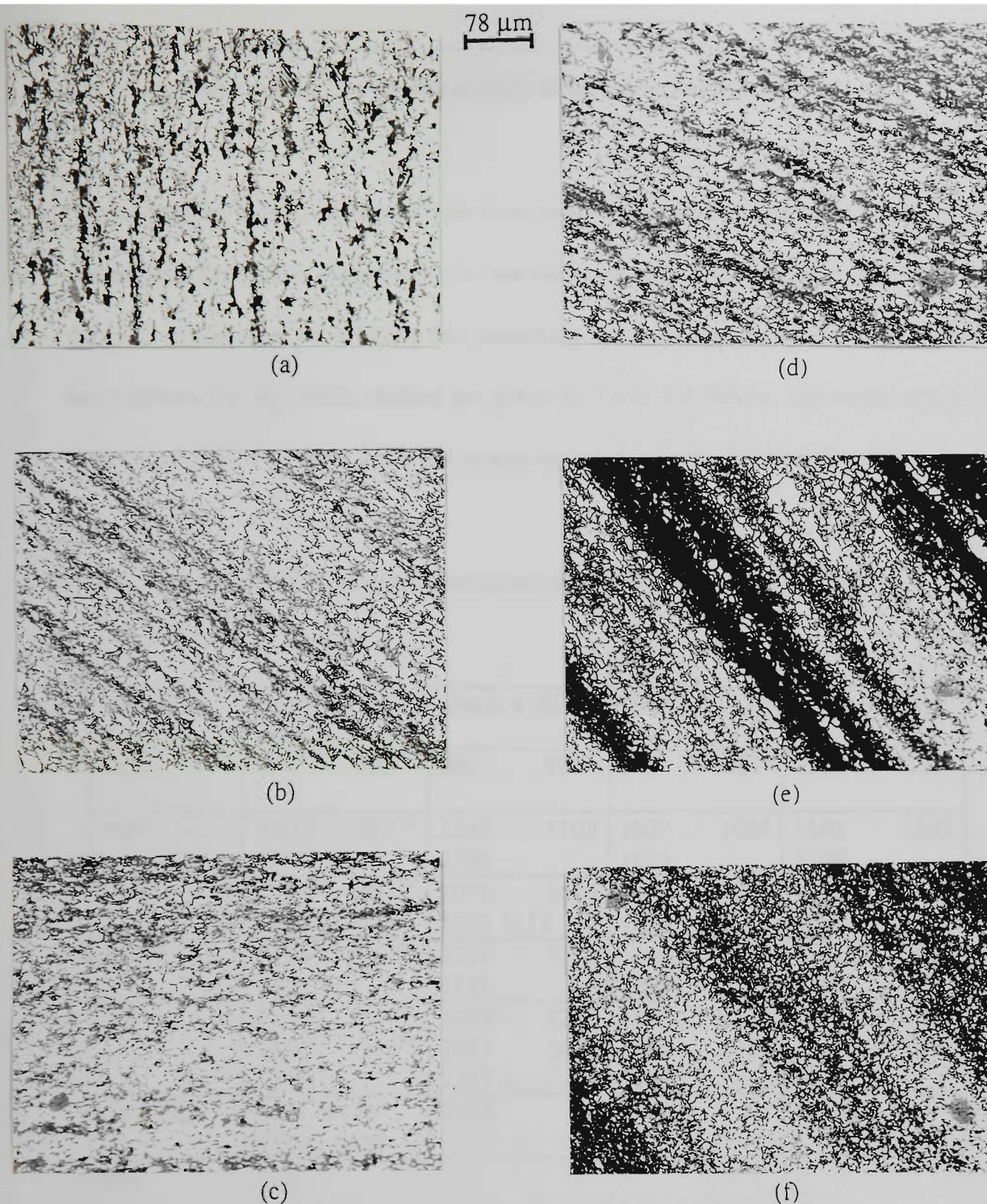
Figure 4.12: (a) Microstructure before reheating (i. e. initial microstructure) for Grade 1A (0.03% Nb, Ti-Mn-Mo) - Plate; and microstructures of samples quenched from: (b) 745 °C (just above Ac_1), (c) 780 °C, (d) 800 °C, (e) 835 °C and (f) 885 °C (just above Ac_3). Dark areas are martensite and light grains are untransformed ferrite in (b) through (e). Note in (f) the uniformity of austenite grain sizes just after the $\alpha \rightarrow \gamma$ transformation is complete. Magnification: 128X, etching tchnique: hot saturated aqueous picric acid method.

Figure 4.13: (a) Microstructure before reheating (i. e. initial microstructure) for Grade 1 (0.06% Nb, Ti-Mn-Mo) - Plate; and microstructures of samples quenched from: (b) 750 °C (just above Ac_1), (c) 770 °C, (d) 790 °C, (e) 820 °C and (f) 870 °C (just above Ac_3). Dark areas are martensite and light grains are untransformed ferrite in (b) through (e). Note in (f) the heterogeneity of austenite grain sizes just after the $\alpha \rightarrow \gamma$ transformation is complete. Magnification: 128X, etching tchnique: hot saturated aqueous picric acid method.

4.3.3 Correlation of GCT with Precipitate Dissolution Temperatures

As presented in # 1.1.5, attempts have been made in the past to correlate the GCT with precipitate dissolution temperature in microalloyed steels and other materials. It is pertinent at this stage to examine this possibility. The calculated precipitate dissolution temperatures for the steels studied are given in Table 4.2 below. The experimentally determined GCT data from Table 4.1 is also included in Table 4.2 for comparison.

Table 4.2: Calculated precipitate dissolution temperatures ($^{\circ}$C)

Precipitate Type	Grade 1A (Slab & Plate)		Grade 4 (Slab)		Grade 5 (Slab)		Grade 1(Plate)	
TiC	954^{59}	991^{60}	961	997	943	983	929	973
NbN	1002^{60} 1021^{62}	1021^{61}	1099 1105	1103	1007 1025	1024	1103 1108	1107
NbC	1033^{60} 1044^{70} 1083^{63}	1083^{62}	1072 1083 1115	1114	1050 1056 1092	1089	1072 1075 1119	1118
NbCN	1132^{59} 1106^{71}	1059^{64}	1176 1148	1129	1139 1113	1094	1181 1150	1096
TiN	1480^{65} 1295^{67} 1505^{69}	1147^{66} 1369^{68}	1639 1363 1587	1202 1438	1459 1286 1494	1139 1360	1573 1336 1553	1180 1410
GCT ($^{\circ}$C)	Slab - 1150 Plate - 1200		1050		1100		1150	

Notes:

1. Numbers in superscript indicate the references from which the precipitate dissolution equations are taken.

2. References for Columns 3, 4 and 5 are exactly the same as those given in Column 2.

The GCT of Grade 5 (Slab) corresponds well with the expected dissolution temperature for all precipitates except TiN precipitates. The type of TiN precipitates that remain undissolved at high temperatures have been classified as Type I precipitates by Liu and

Jonas [140]. It has been reported that such precipitates are formed prior to, during and immediately after solidification of the steel, but they are usually too large and too sparse to resist austenitic grain growth [135, 140, 175]. In case of Grade 4 (Slab), the GCT is about 100 °C lower than the expected dissolution temperature for NbCN precipitates. As has been explained in # 4.3.1 above, Grade 4 (Slab) exhibits the highest value of heterogeneity ratio Z which can lower its GCT. For Grade 1A (Slab), the GCT is somewhat higher than the dissolution temperature for NbCN precipitates. It has been shown in # 4.3.1 that this steel exhibits the lowest value of heterogeneity ratio Z which indicates the reduced inherent tendency for abnormal grain growth thus raising its GCT in an isochronal experiment.

From above analysis it appears that the precipitate dissolution temperature may not always correspond with the GCT because the GCT is also influenced by heterogeneity in γ grain size distribution before coarsening. Further, the expected solubility temperature for any precipitate calculated from different equations available in literature varies quite significantly, see Table 4.2 and #1.1.5 (as much as 50 to 100 °C). It is, therefore, difficult to formulate an exact mathematical relationship between the calculated precipitate dissolution temperatures and the GCT. However, the calculated precipitate dissolution temperatures may provide a useful pointer in locating the GCT.

In case of plate steels, the steels exhibit two stages of accelerated grain growth. It has been reported by Houghton et al. [79] that the controlled rolled plates exhibit different types of precipitates as shown in Table 4.3.

Table 4.3: Main precipitate types present in controlled rolled plates

Stoichiometry	Shape	Temperature of Formation (°C)	Size (nm)
$Nb_xTi_{1-x}C_yN_{1-y}$	Spheroidal	800 - 1100	2 - 50
$Ti_zNb_{1-z}N$	Cubic	1200	40 - 120

where x = 0.8 to 1.0, y = 0.55 to 1.0 and z = 0.55 to 0.65.

The low temperature grain growth (950 - 1050 °C) can be related to the coarsening and progressive dissolution of NbC and TiC precipitates (Tables 4.2 and 4.3). The high temperature accelerated grain growth can be related to the coarsening and dissolution of the more stable precipitates Ti, Nb (C, N) and the coarsening of TiN.

4.3.4 Effectiveness of the Metallographic Method Developed in Studying Austenite Grain Growth

The alternative method developed in this work which consists of measuring the mean size of the largest grain as a function of temperature is found to be much more sensitive and effective in studying the grain growth in microalloyed steels. Although the conventional method of plotting the mean grain size as a function of temperature could show the onset of abnormal grain growth in slab steels (Figs. 4.1 - 4.3) but it was not able to provide information about the termination stage of abnormal grain growth. On the other hand, the new suggested method of plotting the mean size of the largest grain v/s temperature clearly distinguishes the onset and termination stages of abnormal grain growth in slab steels.

For example, consider the grain growth behaviour of Grade 5 (Slab) shown in Fig. 4.3. Mean size of the largest grain v/s temperature curve exhibits three distinct stages of grain growth behaviour. At lower temperatures (<1100 °C), mean size of the largest grain is observed to be considerably larger (about five times) than the mean grain size. This is due to the inhomogeneity of the as-cast microstructure and retention of the grain size heterogeneity after reaustenitization. According to Hillert's size distribution theory [18], grains with radius larger than 1.8 times the mean grain radius must grow abnormally, resulting in low temperature abnormal grain growth until the grain size distribution is normalised. However, it can be seen from Fig. 4.3 that the mean size of the largest grain increases only gradually. This means that abnormal grain growth due to initial size differences is either insignificant or very sluggish in Grade 5. Similar observation can be made for other slab steels also (Figs. 4.1 and 4.2). Therefore it seems that the expected low temperature abnormal grain growth is insignificant for the microalloyed slab steels studied. Grain growth in the temperature range 900 - 1100 °C for Grade 5 can thus be considered as normal or stable grain growth.

In the temperature range of 1100 - 1200 °C, the mean size of the largest grain increases sharply and heterogeneity Z in the microstructure increases significantly (Fig. 4.8e). This behaviour is typical of abnormal grain growth and is related to the progressive dissolution and coarsening of the pinning precipitates.

At still higher temperatures (>1200 °C), the situation becomes relatively stabilised as indicated by the marginal increase in the mean size of the largest grain and the decreasing heterogeneity Z in the microstructure. This can be interpreted as normal grain growth after the termination of abnormal grain growth due to elimination of fine grains and the subsequent impingement of coarse grains. Normal grain growth proceeds at

these high temperatures when the precipitates are either dissolved or too coarsened to be effective in offering resistance for grain growth. Similar observations can be made for Grades 4 (Slab) and 1A (slab).

The conventional method of plotting mean grain size as function of temperature was unable to show the abnormal grain growth in both **plate** steels (see Figs. 4.5 and 4.6). The mean grain size is seen to increase continuously without any significant change in slope. On the other hand, the mean size of the largest grain v/s temperature curves given in Figs. 4.5 and 4.6 exhibit two stages of accelerated grain growth in plate steels. Although the abnormal grain growth in both plate steels is not as significant as that in slab steels, the new technique is able to detect the sequence of grain coarsening in plate steels quite effectively.

4.4 Conclusions

The observations regarding the grain growth behaviour of microalloyed austenite in slab and plate steels can be summarised as follows:

1. GCT of microalloyed steels is significantly influenced by heterogeneity in initial austenite grain sizes. A high value of heterogeneity ratio (Z) lowers the GCT of a more highly microalloyed steel by as much as 50 - 100 $^{\circ}$C.

2. Microstructure before reheating influences the $\alpha \rightarrow \gamma$ transformation which leads to differing values of Z in different steels. In slab steels, initial microstructure consisting of coarse ferrite and a small volume fraction of acicular ferrite + pearlite

phases generates a high value of Z. Initial microstructure consisting of coarse and fine ferrite and a non-uniform distribution of pearlite (banding) results in a high value of Z in plate steels.

3. The expected low temperature abnormal grain growth due to initial size differences is found to be either insignificant or very sluggish in all of the microalloyed steels studied. This means that grains much larger than the mean grain size (3 to 7 times larger than the mean grain size) do not spontaneously start to grow abnormally. In an isochronal experiment, the reheating temperature must be greater than the GCT for such large sized grains to grow which subsequently leads to abnormal grain growth and duplex microstructure.

4. Grain coarsening behaviour of plate steels is significantly different than that of slab steels. Plate steels exhibit two stages of abnormal grain growth as against only one stage of accelerated grain growth exhibited by slab steels. Two stage coarsening in plate steels may be related to the coarsening and dissolution of two different types of microalloy precipitates observed in plate steels. Abnormal grain growth in plate steels is not as extensive as that observed in slab steels.

5. Calculated precipitate dissolution temperature provides a useful pointer in locating the GCT. The experimentally observed GCT can be higher or lower than the calculated precipitate dissolution temperature depending on other variables such as microstructure before reheating and heterogeneity in initial austenite grain sizes.

6. Conventional method of analysing mean grain size as a function temperature was able to detect the onset of abnormal grain growth but could not detect its termination

in some cases in slab steels. Conventional method also failed to detect abnormal grain growth in both plate steels. The alternative metallographic technique developed in this work which consists of measuring the mean size of the largest grain as a function of temperature is found to be more effective and sensitive in detecting the onset and termination of abnormal grain growth in slab as well as plate steels.

Chapter 5: Development of a Mathematical Model to Predict Grain Growth of Austenite in Microalloyed Steels

5.1 Background

Sellars and Whiteman [105] analysed previously published grain growth data for low carbon - manganese steels and arrived at the following general expression for predicting the grain growth behaviour of austenite:

$$d^n - d_o^n = \{A \exp. (-Q_{gg}/RT)\} t \qquad (5.1)$$

where d is the final grain diameter, d_o is the initial grain diameter, n and A are constants which depend on material composition and processing conditions, Q_{gg} is the apparent activation energy for grain growth, R is the universal gas constant, T is the absolute temperature and t is the time for grain growth. Eq. (5.1) has been adopted by many authors to predict the grain growth behaviour of statically or metadynamically recrystallized austenite C-Mn, C-Mn-V, C-Mn-Ti and C-Mn-Nb steels. Currently available mathematical models are summarised in Table 5.1.

Another empirical approach has been presented by Nishizawa [102] and Yoshie et al. [103] to predict grain growth of austenite in as-cast C-Mn steel. Their model can be represented as follows:

$$d^2 - d_o^2 = K_2 t$$

where,

$$K_2 = \sigma V_m D_{gb}/\lambda RT$$

$$D_{gb} = D^o_{gb} \exp. (-Q/RT)$$

Here d is the final grain diameter (cm), d_o is the initial grain diameter (cm), t is the time for grain growth (s), σ is the grain boundary energy (= 800×10^{-7} J/cm^2), V_m is the molar volume of austenite (= 6.97 cm^3 /mol), D_{gb} is the diffusion coefficient at grain boundary

for iron (cm^2/s), D$^{\circ}_{gb}$ is the frequency factor (= 2.0 cm^2/s), Q is the activation energy for

diffusion (= 171544 J/mol), R is the universal gas constant (= 8.31 J/molK), T is the

absolute temperature (K) and λ is the thickness of grain boundary ($\cong$ lattice parameter of

austenite = 3.59x10^{-8} cm [237]).

Table 5.1: Summary of mathematical models describing grain growth of austenite

Ref.	Steel type	γ condi- tion	n	A	Q_{gg}	Units
[105]	C-Mn	SR	10	3.87x10^{32} for T>1273 and 5.02x10^{53} for T<1273	400000 for T>1273 and 914000 for T<1273	g.s. in µm, Q_{gg} in J/mol, R in J/molK and t in sec.
[234]	Low C-Mn	SR	2	4.27x10^{12}	66600	g.s. in µm, Q_{gg} in Kcal/mol, R in Kcal/molK and t in sec.
[235]	0.22 C - 0.9 Mn	SR	2	1.44x10^{12}	63780	g.s. in µm, Q_{gg} in Kcal/mol, R in Kcal/molK and t in sec.
[64]	C-Mn and C-Mn-V	SR or MR	7	1.45x10^{27}	400000	g.s. in µm, Q_{gg} in J/mol, R in J/molK and t in sec.
[64]	C-Mn-Ti	SR or MR	10	2.6x10^{28}	437000	g.s. in µm, Q_{gg} in J/mol, R in J/molK and t in sec.
[64, 236]	C-Mn-Nb	SR or MR	4.5	4.1x10^{23}	435000	g.s. in µm, Q_{gg} in J/mol, R in J/molK and t in sec.

SR = Statically recrystallized, MR = Metadynamically recrystallized

Assuming a hypothetical but typical value for d_o of 27 μm, t = 1800 s, and solving all of

the above models by substituting T = 1173 K (900 °C) up to T = 1523 K (1250 °C) in

steps of 50 K, the results obtained are given in Figs. 5.1 - 5.3. For comparison,

experimental grain growth data for two Ti-microalloyed steels reported by Feng et al.

[175] are included in Fig. 5.2 while data for two Nb-microalloyed steels reported by
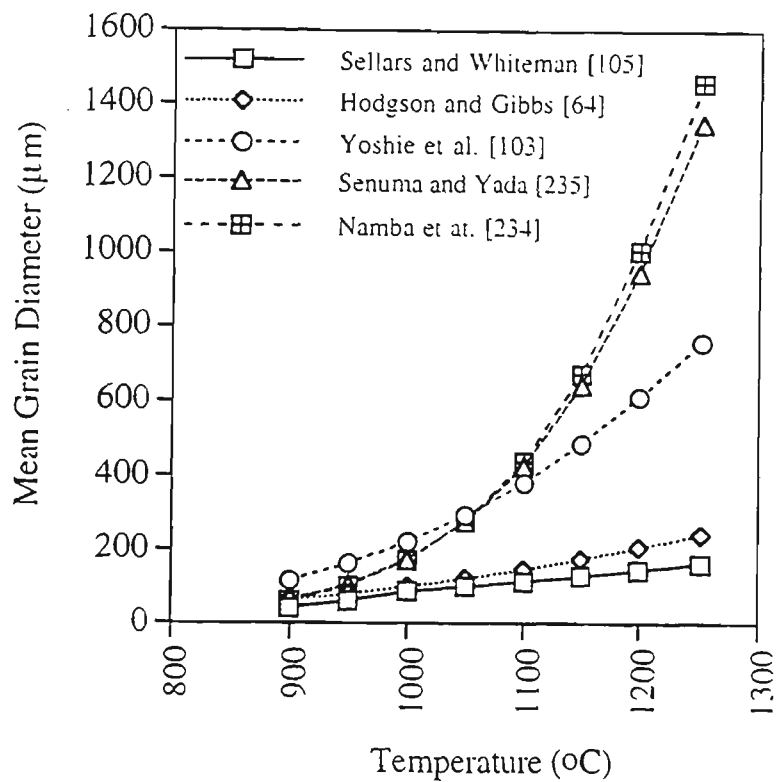
Palmiere et al. [48] are shown in Fig. 5.3.

Figure 5.1: Predicted austenite grain growth in
C-Mn steels (d_O = 27 μm, t = 1800s)
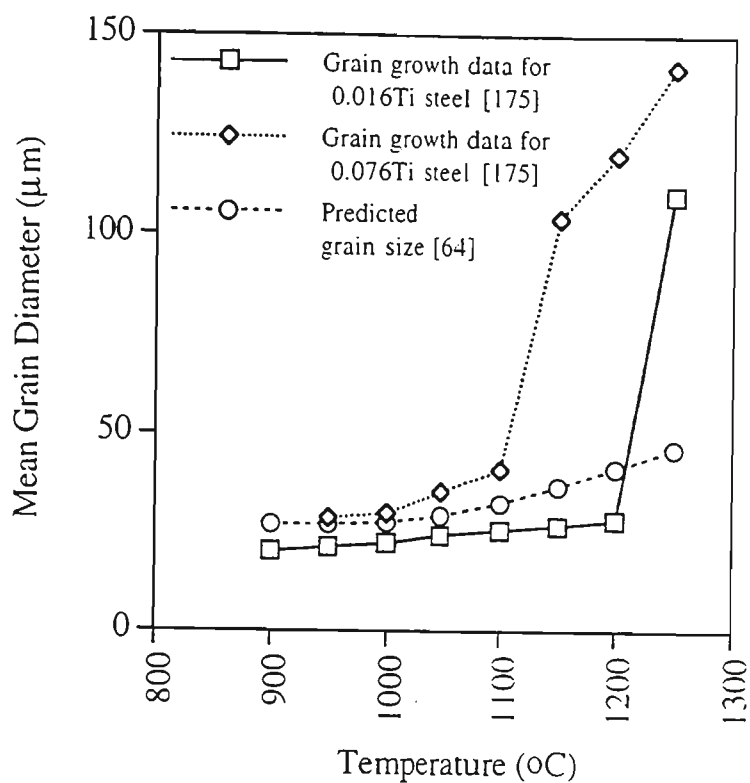
Figure 5.2: Comparison of predicted and experimental grain growth behaviour in Ti-microalloyed steels
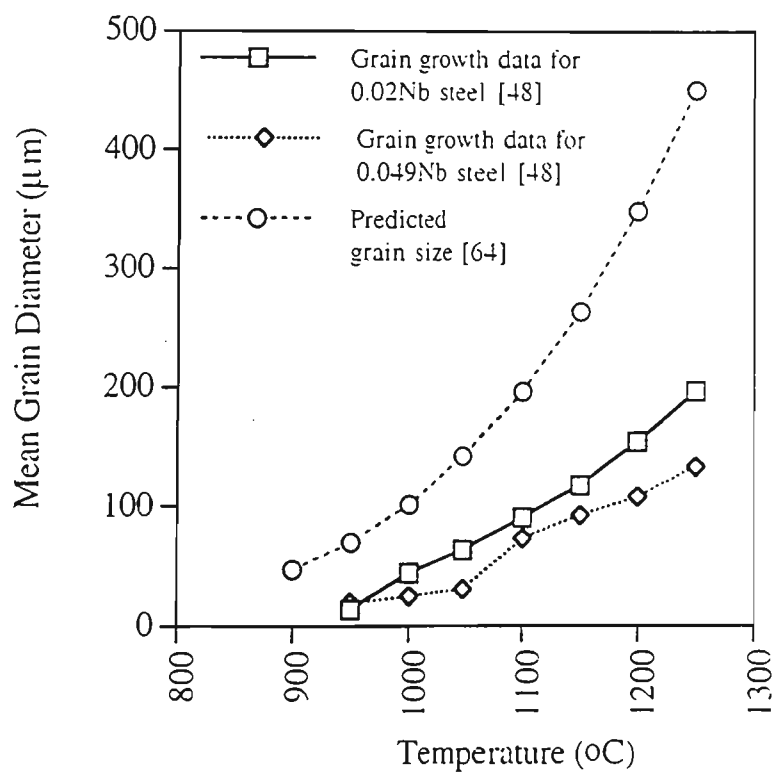
Figure 5.3: Comparison of predicted and experimental grain growth behaviour in Nb-microalloyed steels

It can be seen from Fig. 5.1 that the predictions from different models for grain growth of austenite do not match very well with each other. Also, it is evident from Fig. 5.2 that the experimentally observed grain sizes in Ti-microalloyed steels are much larger than the predicted sizes at temperatures above 1100 °C for 0.076 Ti steel and above 1200 °C for 0.016 Ti steel. This could be due to the inability of the model to account for contribution due to abnormal grain growth at higher temperatures. It can be seen from Fig. 5.3 that model for Nb-microalloyed steels overestimates the grain sizes at all temperatures. This seems probably due to the inability of the model to account for the retarding influence of second phase particles at lower temperatures and drag effect caused by dissolved Nb precipitates at higher temperatures.

An attempt was, therefore, made to develop a mathematical model which can account for abnormal grain growth in microalloyed steels and which can predict the austenite grain growth with a reasonable degree of accuracy. Development of such a model to describe the grain growth of microalloyed austenite is described in the following sections.

5.2 Basic Mathematical Relation to Predict Austenite Grain Growth

A fundamental approach in the theoretical solution of grain growth behaviour, in the presence of second phase particles (such as in microalloyed steels), centres on finding a hypothetical grain radius R_c, such that any grain with radius equal to R_c will neither grow nor shrink. Such a grain with its radius equal to R_c is considered to be thermodynamically stable because the driving pressure for grain growth is balanced by the pinning pressure exerted by the particles on the moving grain boundary. R_c is

considered as the maximum grain size up to which normal grain growth can proceed. As described in #1.3.1, Zener [20] first assigned a quantitative value for R_c as given by:

$$R_c = K\ r/f^m \qquad (1.9)$$

where K = 1.33 and m = 1 according to Zener. Hillert [18] also showed that the value of R_c corresponds to the actual mean grain size of the sample.

Modification of Eq. (1.9) due to Gladman [19] is given by:

$$R_c = \pi\ (1/4 - 1/3Z)\ r/f \qquad (1.20)$$

Gladman found that Z value between 1.41 and 2 gave excellent agreement with experimental results. Hannerz and Kazinczy [133] have chosen Z = 1.7 based on the Hillert's theory [18]. Substituting Z = 1.7 in Eq. (1.20) yields:

$$R_c = 0.17\ r/f \qquad (5.2)$$

Solution of Eq. (5.2) enables the calculation of stable austenite grain size under any combination of volume fraction and particle radius of precipitates. The dissolution and coarsening of precipitates thus have a pivotal role in deciding the stable austenite grain size. Methodology used to estimate f and r is described in # 5.3.2 and # 5.3.3 respectively.

In general, the quantities r and f depend on time, temperature, initial conditions and composition and it was believed that Eq. (1.9) could be used to predict the mean grain size in microalloyed steels. Eq. (1.9) was thus chosen as the basic relation in this work to predict the grain growth behaviour in Ti-Nb-Mn-Mo microalloyed steels. As discussed in detail in #1.3.1.2 and 1.3.1.3 previously, the derivation of Eq. (1.9) involves a number of assumptions. In particular reference to microalloyed steels, Eq. (1.9) has two main limitations: Firstly, the shape of the particles effective in restricting

the austenite grain growth is <u>cubic</u>, and not spherical as assumed in the original derivation. Secondly, Eq. (1.9) does not include any parameter which can account for the effect of initial microstructure and grain size on grain growth.

In the current work, therefore, a mathematical model is developed which is based on the logic of Zener, but which also accounts for the effect of initial size of the cubic shaped particle and the initial size of the grains on the critical grain size. The model is then applied to predict the mean austenite grain size as a function of temperature for microalloyed steels in as-cast slab as well as in controlled rolled plate conditions. It will be shown that the predicted grain size compares well with the experimental grain growth data with a reasonable degree of accuracy for both slab and plate steels.

5.3 Development of the Mathematical Model

5.3.1 Derivation of the Mathematical Model

The geometry of the particle - grain boundary interaction assumed in this derivation is given in Fig. 5.4. Based on the Zener theory, the equation for maximum pinning pressure due to all particles on the grain boundary can be written as:

$$P_z = F_z \, n_s \qquad (5.3)$$

where F_z is the maximum force exerted by one particle and n_s is the surface density of particles. n_s can be calculated by finding the number of particles within a distance "a" on either side of the grain boundary, where "a" is the cube length of the cubic shaped particles. This yields:

$$n_s = (f/a^3) \, 2a = 2f/a^2 \qquad (5.4)$$

where f is the volume fraction of particles.

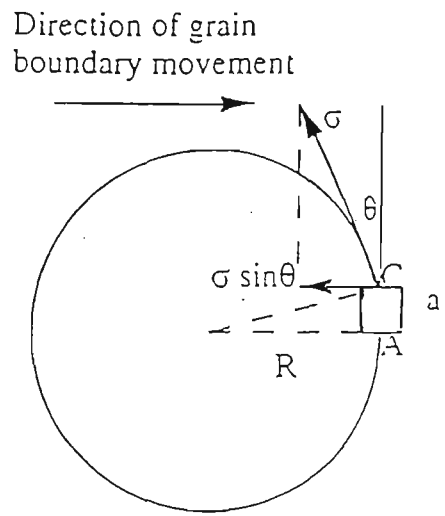Direction of grain
boundary movement

Figure 5.4: Schematic illustration of the particle - grain boundary interaction geometry assumed in the current work.

F_z can be calculated by referring to Fig. 5.4 as follows:

Pull due to one particle = (total length of the line of contact in three dimensions) X

(component of the surface tension opposing the movement

of the grain boundary)   (5.5a)

Total length of the line of contact in three dimensions = 4 Arc AC   (5.5b)

Considering the ratio of Arc AC to the perimeter of the grain as a parameter "β", one

can write:

Arc AC/ $2\pi R = \beta$, or, Arc AC = $2\pi\beta R$ (5.5c)

Incorporating Eq. (5.5c) in to Eq. (5.5b) gives:

Total length of the line of contact in three dimensions = $8\pi\beta R$ (5.5d)

Component of the surface tension opposing the movement of the grain boundary is:

$= \sigma\sin\theta$ (5.5e)

Substitution of Eq. s (5.5d) and (5.5e) in to Eq. (5.5a) yields:

Pull due to one particle = $8\pi\beta R (\sigma\sin\theta)$ (5.5f)

For maximum pull due to one particle, $\theta = 90°$, which leads to:

$$F_z = 8\pi\beta\sigma R \qquad (5.5g)$$

Inserting Eq. s (5.5g) and (5.4) in to Eq. (5.3) results in the following relation:

$$P_z = 16\pi\beta\sigma fR/a^2 \qquad (5.6)$$

Driving pressure for grain growth is given by:

$$P_g = \sigma/R \qquad (5.7)$$

At equilibrium, $P_z = P_g$; $R = R_c$; from Eq. s (5.6) and (5.7) this leads to:

$$R_c = a/7.1\sqrt{\beta f} \qquad (5.8)$$

Equations describing coarsening kinetics of cubic particles are not available at this stage while coarsening of spherical particles has been described by Lifshitz and Slyozov [110]. As first approximation, therefore, one can convert cube length "a" to the radius "r" of a spherical particle of equal volume which yields:

$$a = 1.61r \qquad (5.9)$$

Substituting Eq. (5.9) in to Eq. (5.8) leads to:

$$R_c = (1.61/7.1\sqrt{\beta}) \, (r/\sqrt{f}) \qquad (5.10)$$

Order of magnitude for the parameter β can be found by considering the initial conditions of precipitate size and the grain size for any given steel. According to Eq. (5.5c), we have:

$$\text{Arc } AC = 2\pi\beta R$$

For $R \gg a$, Arc AC can be taken as equal to "a". Therefore β can be given as:

$$\beta = a_0/2\pi R_0 \qquad (5.11)$$

where a_0 and R_0 are the values of initial particle and grain sizes. Solution of Eq. s (5.11) and (5.10) thus enables the calculation of mean austenite grain size.

5.3.2 Calculation of the Volume Fraction of Precipitates

Presence of microalloy precipitates restrict the grain growth of austenite through their pinning influence on the moving grain boundary. As the reheating temperature is increased, the precipitates start to dissolve in austenite. The dissolution reaction primarily depends on the chemical nature of the precipitates. The dissolved microalloying elements may still influence, though not as strongly as the particle pinning, the kinetics of grain growth through solute drag effect. Therefore, it is important to predict the partitioning of microalloying elements either as microalloy precipitates or as dissolved elements in austenite as a function of reheating temperature and soaking time. The mathematical treatment to predict the volume fraction of TiN precipitates as a function of temperature and time is described in the following sections.

5.3.2.1 Prediction of TiN Solubility

Choice of the equation describing solubility of TiN in austenite is very important. In the current work, TiN solubility product equation given by Matsuda and Okumura [65] has been used. Choice of this equation will be discussed in a later section.

$$\log [Ti] [N] = 0.322 - 8000/T$$

$$\therefore [Ti] [N] = \log^{-1} \{0.322 - 8000/T\}$$

where bracketed quantities indicate the amount dissolved. Multiplying both sides by [Ti]/[N] -

$$[Ti]^2 = [\log^{-1} \{0.322 - 8000/T\}] [Ti]/[N]$$

It is now assumed that the formation as well as dissolution of TiN precipitates proceeds such that stoichiometric relation of Ti : N {= 3.42 [175]} is maintained whenever the

overall Ti : N ratio in the given composition of steel is close to the stoichiometric ratio

of 3.42. Therefore, substituting [Ti]/[N] = 3.42 in the above equation enables calculation

of dissolved Ti as a function of temperature according to:

$$[Ti]^2 = [\log^{-1}\{0.322 - 8000/T\}]\, 3.42 \qquad (5.12)$$

Solution of Eq. (5.12) for different value of T yields the corresponding values of [Ti],

which is the percent Ti in solution in austenite (C^s). The amount of Ti out of solution, i.

e. in precipitated form (C^p) can be calculated according to:

$$C^p = \text{Total Ti content of the steel-} C^s \qquad (5.13)$$

5.3.2.2 Calculation of Volume Fraction of TiN Precipitates

Volume 'V' of a given mass 'm' of a material can be given as:

$$V = m\, N_a\, V_u / N_u\, A_r$$

where N_a is the Avogadro's number $\{ = 6.0222 \times 10^{23}\}$, V_u is the volume of one unit

cell of the material $\{ = (4.246 \times 10^{-8})^3 \text{ cm}^3 \text{ for TiN [174] and } (3.59 \times 10^{-8})^3 \text{ cm}^3$ for

austenite [237]$\}$, N_u is the number of atoms per unit cell $\{= 4$ for TiN and austenite$\}$ and

A_r is the atomic weight of the material $\{ = 61.91$ gms for TiN and 55.9 gms for

austenite$\}$. Substituting appropriate numerical value in the above equation gives:

$$V_{TiN} = 0.19\, m_{TiN} \text{ and}$$

$$V_{Fe} = 0.13\, m_{Fe}$$

$$m_{TiN} = m_{Ti} + m_{Fe} = m_{Ti} + (m_{Ti}/3.42) = 1.29\, m_{Ti}$$

$$m_{Fe} = 1 - m_{TiN};\ \text{and}$$

$$m_{Ti} = C^p/100$$

Volume fraction of precipitates can now be calculated according to:

$$f = V_{TiN} / (V_{TiN} + V_{Fe}) \qquad (5.14)$$

Sample calculation for predicted volume fraction of precipitates as a function of

temperature Grade 5 (Slab) is presented in Fig. 5.5.
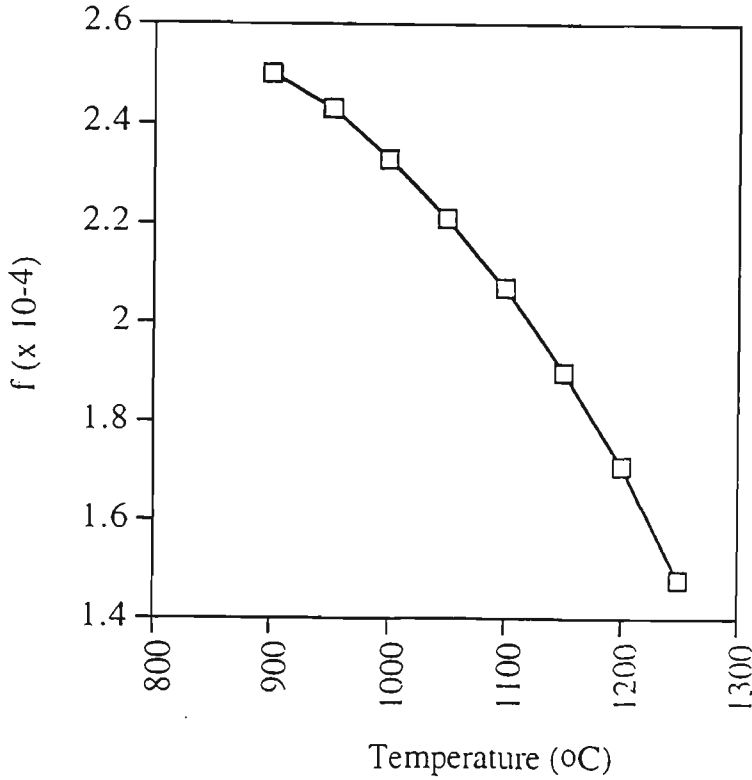
Figure 5.5: Predicted volume fraction of precipitates at
temperatures of interest in Grade 5 (Slab)

5.3.3 Calculation of Particle Coarsening

Lifshitz and Slyozov [110] have outlined principles of second phase particle coarsening

kinetics. The growth process (which follows after the nucleation stage) is considered to

begin when the grains (of second phase) have reached appreciable size and the degree of

supersaturation of the matrix has become very slight. In this situation, coalescence starts

i. e. growth of larger grains by incorporating smaller ones begins. The theory predicts

particle grain growth through the following equation:

$$r^3 - r_0^3 = [8\sigma V_m DtC^s]/9RT \tag{5.15}$$

where r is the final particle radius (cm), r_0 is the initial particle radius (typically equal to

13.5 x 10^{-7} cm), σ is the interfacial energy {= grain boundary energy = 800 x 10^{-7} J/cm^2

[133, 134]}, V_m is the molar volume of TiN {= 11.53 cm^3/mol}, D is the diffusivity of

solute in matrix {= Ti in austenite in this case, cm^2/s}, t is the time for particle coarsening

(=1800 s in the present case), C^s is the concentration of the saturated solution {=

solution of Eq. (5.12) in this case} and R and T have the usual meaning. Diffusivity of Ti

in austenite [81] has been given as:

$$D_{Ti} = 0.15 \exp. (-250000/RT) \text{ cm}^2/\text{s} \tag{5.16}$$

Solution of Eq. s (5.16) and (5.15) enables the estimation of the particle coarsening as a

function of time, temperature and composition.

Sample calculation for predicted particle coarsening with respect to temperature in

Grade 5 (Slab) is presented in Fig. 5.6.
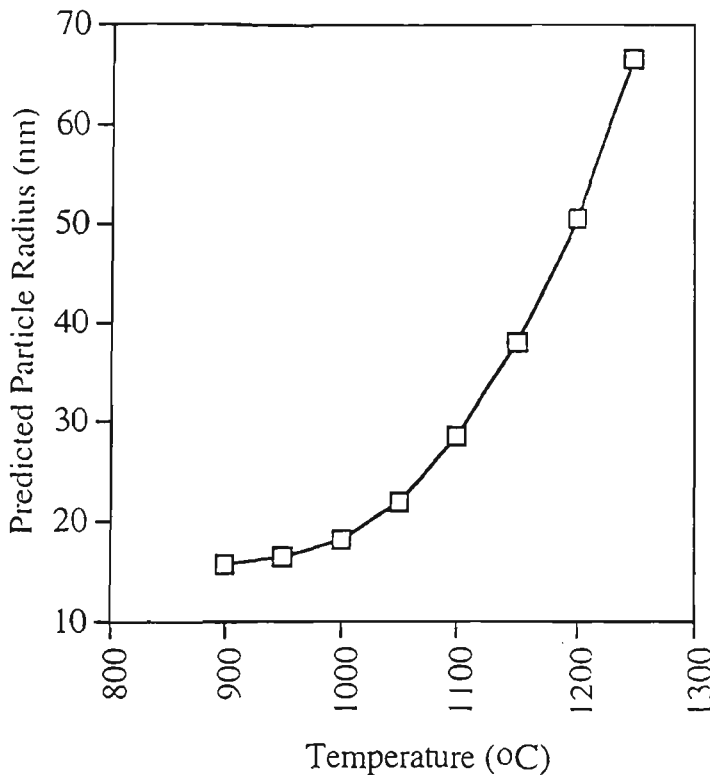
Figure 5.6: Predicted particle coarsening as a function of temperature
in Grade 5 - Slab (t= 1800s, r_0 = 15.5 nm)

5.4 Comparison of Predicted and Experimental Grain Growth of Microalloyed Austenite

Substitution of r and f values from Eqs. (5.15) and (5.14) in to Eq. (5.2) enables the prediction of grain size as function temperature based on Gladman's approach. On the other hand, considering a typical value of $a_0 = 25$ nm and inserting R_0 = mean austenite grain size soon after austenitization (i.e. at 900 °C) in to Eq. (5.11) enables estimation of the parameter β for each steel grade. Substituting the appropriate values of β, r and f in Eq. (5.10) enables the prediction of mean austenite grain size according to the new model. The predicted grain sizes according to Eq. s (5.2) and (5.10) and the experimentally determined mean grain size in Grades 5, 4 and 1A slabs steels are presented in Figs. 5.7 - 5.9 respectively. The predicted grain sizes according to Eqs. (5.2) and (5.10) and the experimentally determined mean grain size in Grades 1A and 1 (Plates) is presented in Figs. 5.10 and 5.11 respectively. It is clear from Figs. 5.7 - 5.9 that both models successfully predict the grain growth of austenite in slab steels while the new model is able to predict the grain growth of plate steels also with a reasonable degree of accuracy, see Figs. 5.10 and 5.11. However, model based on Eq. (5.2) overestimates the grain growth in plate steels.
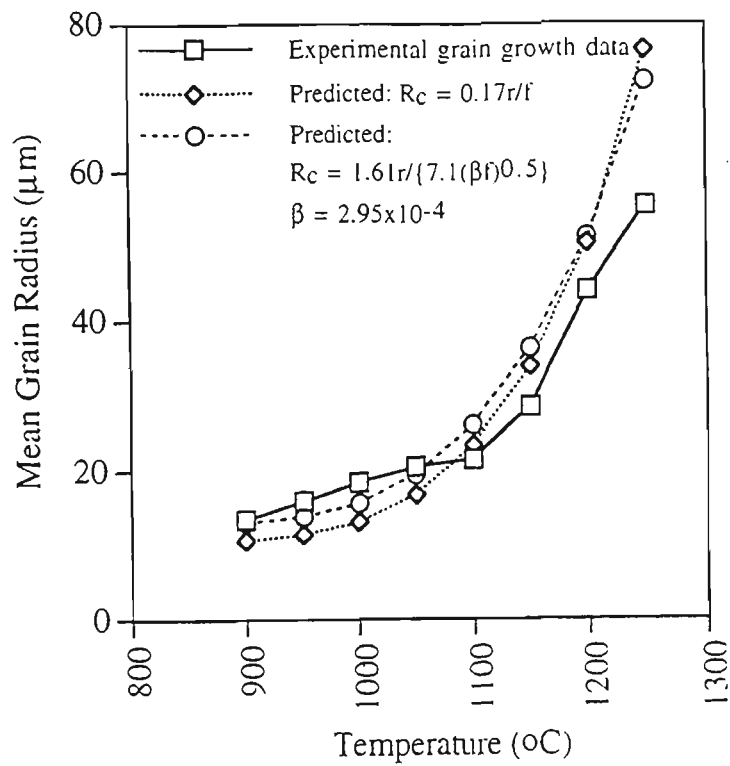
Figure 5.7: Comparison of predicted and experimental mean grain size
as a function of temperature in Grade 5 (Slab) at t = 1800s
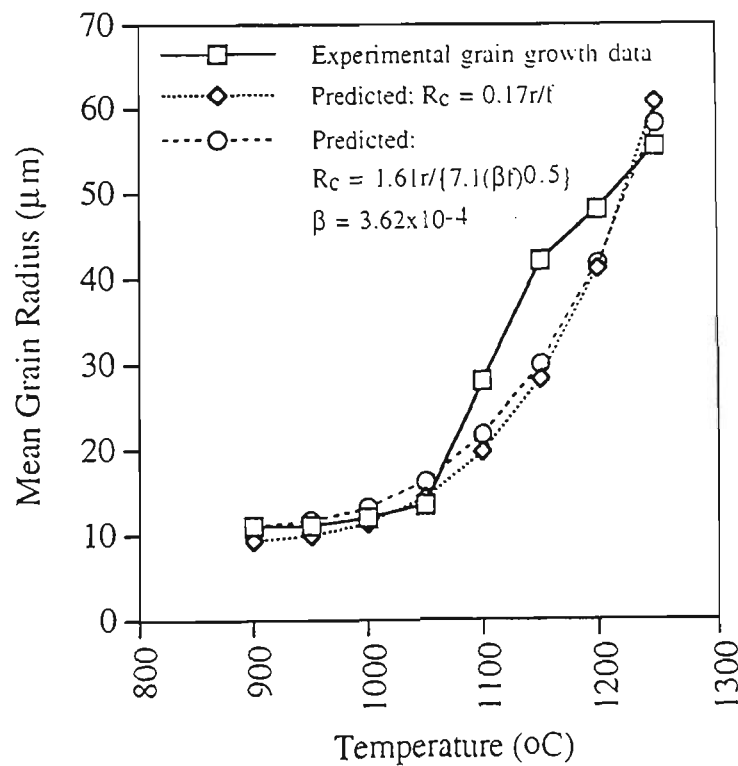
Figure 5.8: Comparison of predicted and experimental mean grain size
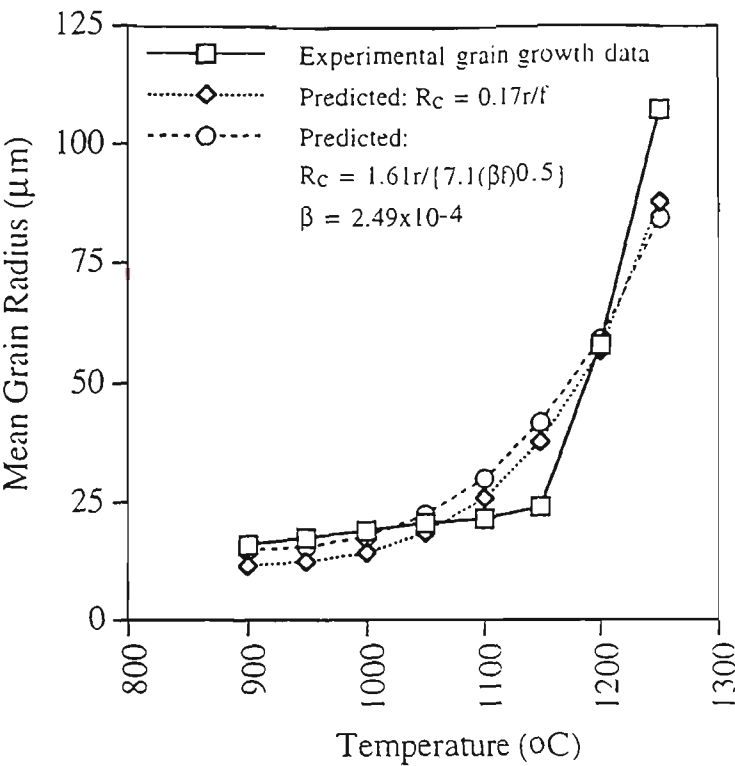as a function of temperature in Grade 4 (Slab) at t = 1800s

Figure 5.9: Comparison of predicted and experimental mean grain size
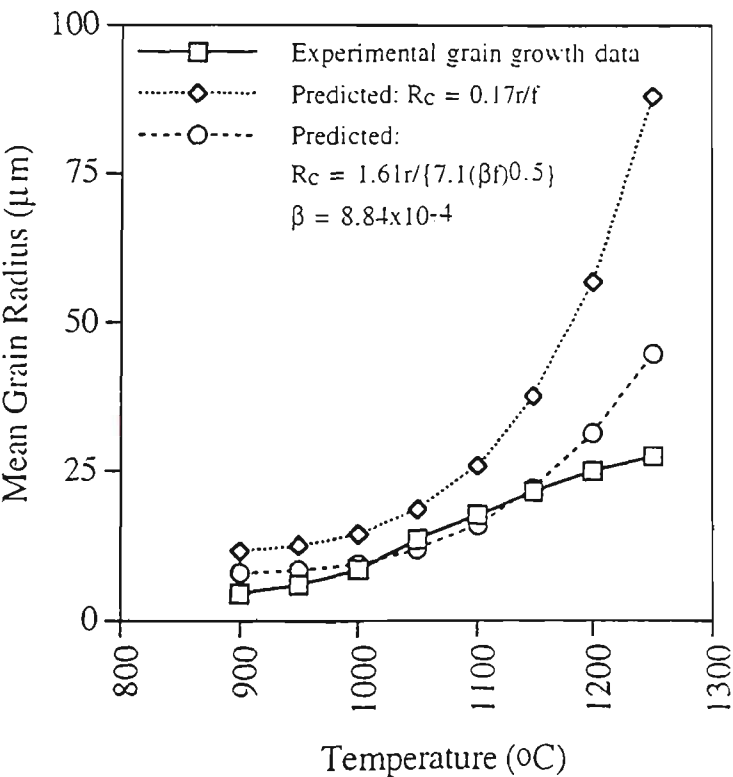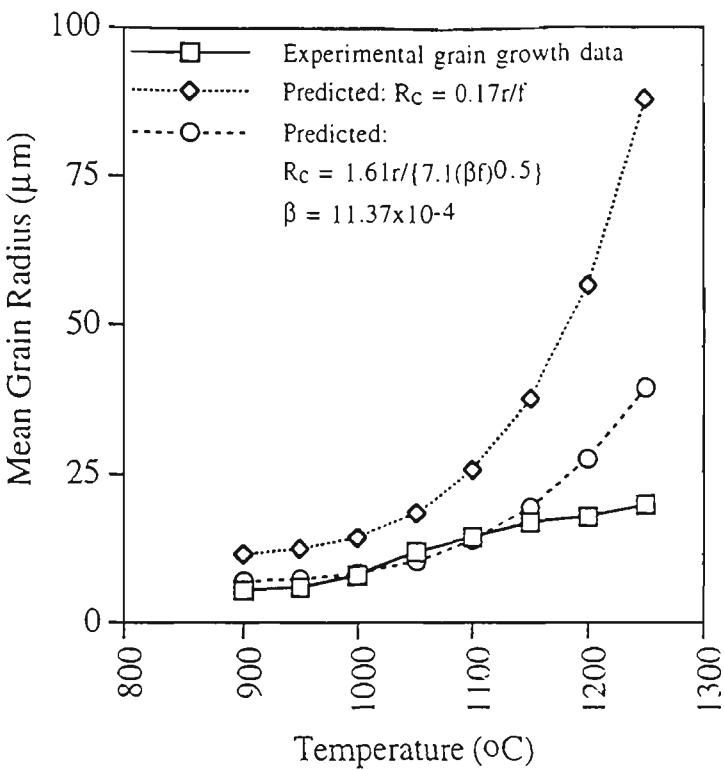as a function of temperature in Grade 1A (Slab) at t = 1800s

Figure 5.10: Comparison of predicted and experimental mean grain size
as a function of temperature in Grade 1A (Plate) at t = 1800s

Figure 5.11: Comparison of predicted and experimental mean grain size
as a function of temperature in Grade 1 (Plate) at t = 1800s

5.5 Discussion

5.5.1 Nature of the Relative Size Parameter (β)

The parameter β accounts for the effect of initial austenite grain size (R_o) relative to the initial particle size (a_o) on the predicted value of R_c. It can be seen from Eq. (5.11) that the value of β decreases as the initial austenite grain size increases or as the initial particle size decreases. The decreasing value of β in turn leads to a larger predicted R_c. This means that a material with relatively coarser initial grain size with finer particles will have a lesser tendency for abnormal grain growth because R_c would be larger in this case. On the other hand, a material with initially finer grain size with coarser particles would have a larger tendency for abnormal grain growth because R_c is small. This result is in qualitative agreement with Gladman's analysis [19].

The parameter β proposed in this work is quite different than that proposed by Hellman and Hillert [124]. The correction factor β due to Hellman and Hillert was given as $\beta = 0.125 \ln (8\rho/r)$ or $\beta = 0.125 \ln (40\rho/r)$. The choice of either equations is rather arbitrary. Further, Hellman-Hillert β factor was found to be dependent on the composition. On the other hand, in the current work, the value of β parameter is given as ratio of initial particle size to initial grain size (perimeter) according to Eq. (5.11). The value of β is evaluated by using typical values of a_0 while the values of R_0 are determined experimentally for each steel which allows for flexibility of applying the new model to steels with differing initial conditions.

The value of β has been treated as a constant during the process of grain growth. As the grains and particles coarsen, presumably at different rates, the value of β may not remain a constant. However, as long as the particles and grains grow proportionately, the value of β may not change significantly during the process of normal grain growth.

5.5.2 Effect of TiN Solubility on Predicted Grain Size

Choice of the solubility product equation for TiN precipitates is very important because partitioning of the available or total Ti as precipitates and as dissolved Ti in austenite plays a crucial role in deciding the grain growth characteristics of microalloyed austenite. Many equations are available in literature which describe dissolution of TiN in austenite [65 - 69]. Effect of choice of these equations on the predicted austenite grain size in Grade 5 (Slab) is presented in Fig. 5.12.
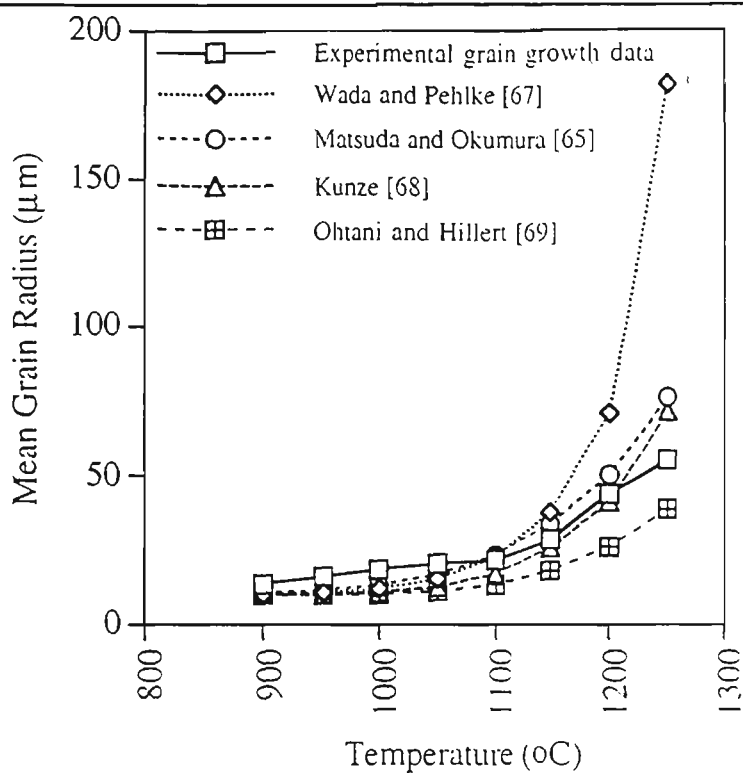
Figure 5.12: Effect of choice of TiN solubility equation
on predicted grain size in Grade 5 (Slab).
All grain size predictions are based on the
conditions:
r$_o$ = 15.5 nm, t = 1800s and R$_c$ = 0.17r/f

It is clear from Fig. 5.12 that grain growth predictions using equation by Matsuda and

Okumura [65] and Kunze [68] are much closer to the experimental data than others. In

particular, predictions based on equation due to Matsuda and Okumura [65] are better at

lower temperatures as compared to those based on the results by Kunze [68]. In

addition, several other researchers [82, 135, 238] have also found the equation by

Matsuda and Okumura [65] to be more applicable than other relations. Therefore, the

choice of Matsuda and Okumura equation made in this work seems to be reasonable.

5.5.3 Applicability of the Mathematical Models

Some assumptions involved in the original Zener equation were accounted for in the

derivation of the new model, however, some other assumptions were not covered. It is,

therefore, necessary to outline the framework within which the models would apply. The

assumption made in the derivation of the models are:

a) Particles are randomly distributed and the size distribution of the particles is ignored.

b) Influence of possible "mixed" precipitates such as Ti, Nb (C, N) on the grain growth behaviour is not accounted for.

c) Synergistic effects of other alloying elements such as Mo, Mn, Si etc. on particle dissolution and coarsening are not taken in to account.

d) The model is applicable to those steels where the overall Ti:N ratio in steel composition is less than or very close to the stoichiometric ratio of 3.42. This means that all of the available Ti forms TiN particles and the formation of low temperature dissolving precipitates such as TiC, Ti(C,S) etc. is avoided.

Notwithstanding these limitations, the models developed in this work {Eq.s (5.2) and (5.10)} are able to predict the grain growth of austenite in slabs with a fair degree of accuracy. However, the model based on Eq. (5.2) overestimates the grain growth in plate steels at all temperatures, which seems to be due to the fact that the model does not account for the effect of initial particle and grain size on the predicted R_c. The new model {Eq. (5.10)}, on the other hand, is able to predict the grain growth of plate steels up to 1100 - 1150 °C reasonably well, but overestimates the grain growth at higher temperatures. This is probably due to the inability of the model to account for solute drag effect caused by dissolved microalloying elements, especially in more highly microalloyed Grade 1, which keeps the mean grain sizes lower than the predicted values.

5.6 Conclusions

Following conclusions may be drawn based on the observations given in the preceding sections:

1. Empirical models for predicting the grain growth of austenite in C-Mn steels do not match very well with each other. Some empirical models for microalloyed steels are effective in predicting grain growth of austenite at lower temperatures, however, at higher temperatures, these models underestimate the grain sizes in Ti-microalloyed steels and overestimate the grain sizes in Nb-microalloyed steels.

2. Grain growth in slab steels can be predicted reasonably well at all temperatures using both mathematical models developed in this work. However, model based on Gladman approach ($R_c = 0.17r/f$) overestimates the grain sizes in plate steels. New model based on the equation $R_c = 1.61r/(7.1\sqrt{\beta}f)$ is found to be effective in predicting the grain growth of austenite in slab as well as plate steels.

Chapter 6:   Continuous Cooling Transformation Behaviour of Austenite in

Ti-Nb-Mn-Mo Microalloyed Steels

6.1 Introduction

This chapter reports and discusses the results obtained after laboratory simulation of industrial thermomechanical processing of Ti-Nb-Mn-Mo microalloyed steels. Laboratory simulation of TMP is carried out using quench and deformation dilatometry. The effects of Nb and Mn additions, TMP and accelerated cooling on austenite transformation critical temperature (Ar_3), continuous cooling transformation products and kinetics, CCT diagrams and microhardness are investigated. The experimental work was designed to address several issues of technological significance such as:

- providing the basis for optimisation of industrial controlled cooling process for the steel grades utilising the CCT diagrams which were to be generated in this work,

- investigating the possibility of using leaner and cost-effective compositions to achieve microstructures and properties similar to the established grades by optimising TMP variables (product development); and

- obtaining grade-specific information about the grain growth and phase transformation behaviour of the steels studied which could be used in future mathematical modelling work.

The experimental results of the response of Ti-Nb-Mn-Mo microalloyed steels to TMP and accelerated cooling are given in the following section.

6.2 Results

6.2.1 Effect of TMP, Cooling Rate and Nb and Mn Contents on Austenite Transformation Critical Temperature (Ar$_3$)

Effect of TMP and cooling rate on Ar$_3$ of Grades 1 and 1A (Plates) and Grades 1 and 4 (Slabs) is given in Fig. 6.1. It can be seen from Fig. 6.1 that TMP raises the Ar$_3$ significantly while an increase in cooling rate lowers this temperature in these steels.

Effect of Nb content on Ar$_3$ in Grade 1 (0.054% Nb) and Grade 1A (0.031% Nb) steel in plate condition is shown in Fig. 6.2. The results show that the Ar$_3$ of Grade 1 is lower than that of Grade 1A in undeformed state for all cooling rates used. However, this situation is reversed in deformed samples. In the case on TMP samples, Ar$_3$ of Grade 1 - is higher than that of Grade 1A. For example at a cooling rate of 0.3 °C/s, undeformed samples of Grades 1 and 1A exhibit Ar$_3$ to be 685 °C and 705 °C respectively whilst samples with 40% finish deformation in Grades 1 and 1A, at the same cooling rate of 0.3 °C/s, show Ar$_3$ of 790 °C and 765 °C respectively.

Effect of Mn content on Ar$_3$ in Grade 1 (1.66% Mn) and Grade 4 (1.07% Mn) in slab condition is given in Fig. 6.3. The results show that the Ar$_3$ of Grade 1 is lower than that of Grade 4 in undeformed as well as in deformed conditions for all cooling rates used.
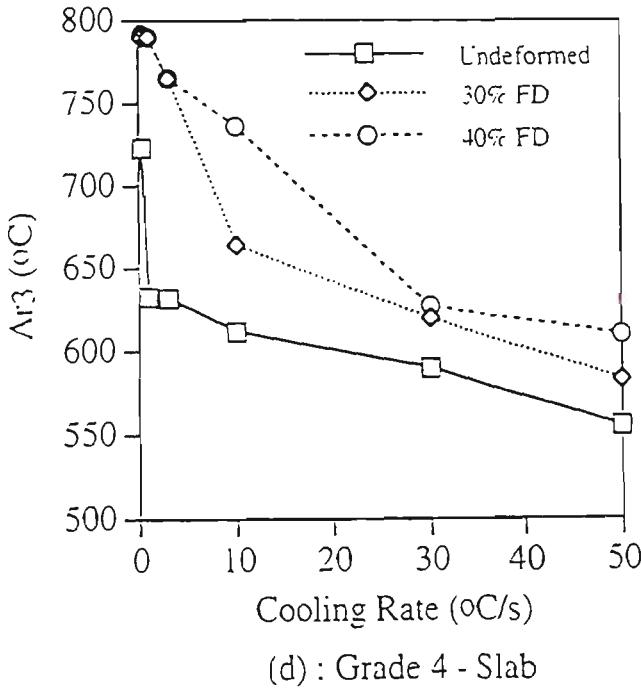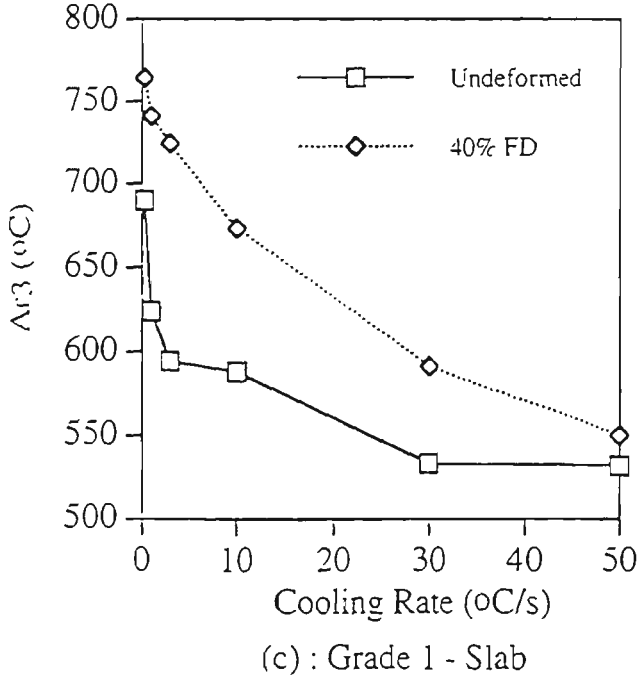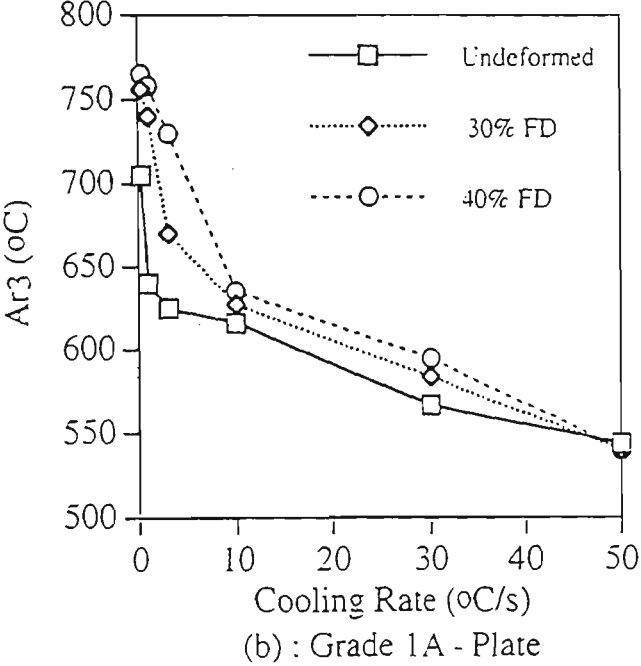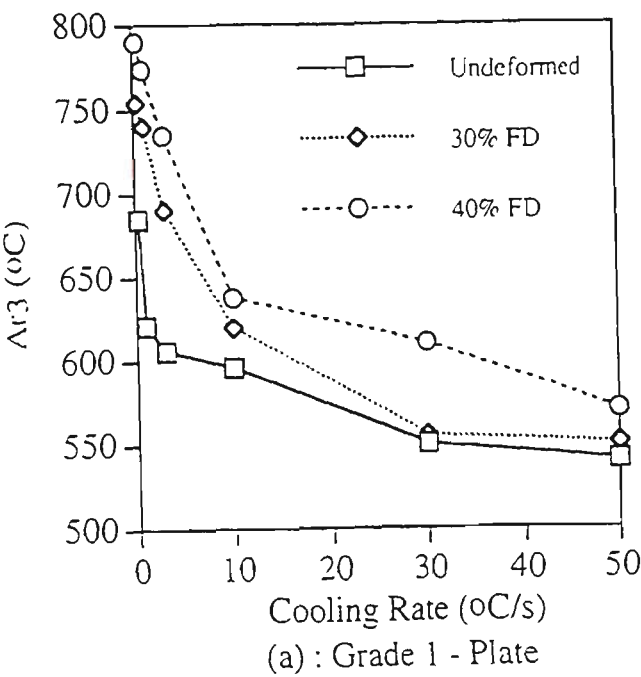
Figure 6.1: Effect of TMP and cooling rate on Ar3 of the steels studied: (a) Grade 1 - Plate, (b) Grade 1A - Plate, (c) Grade 1 - Slab and (d) Grade 4 - Slab.
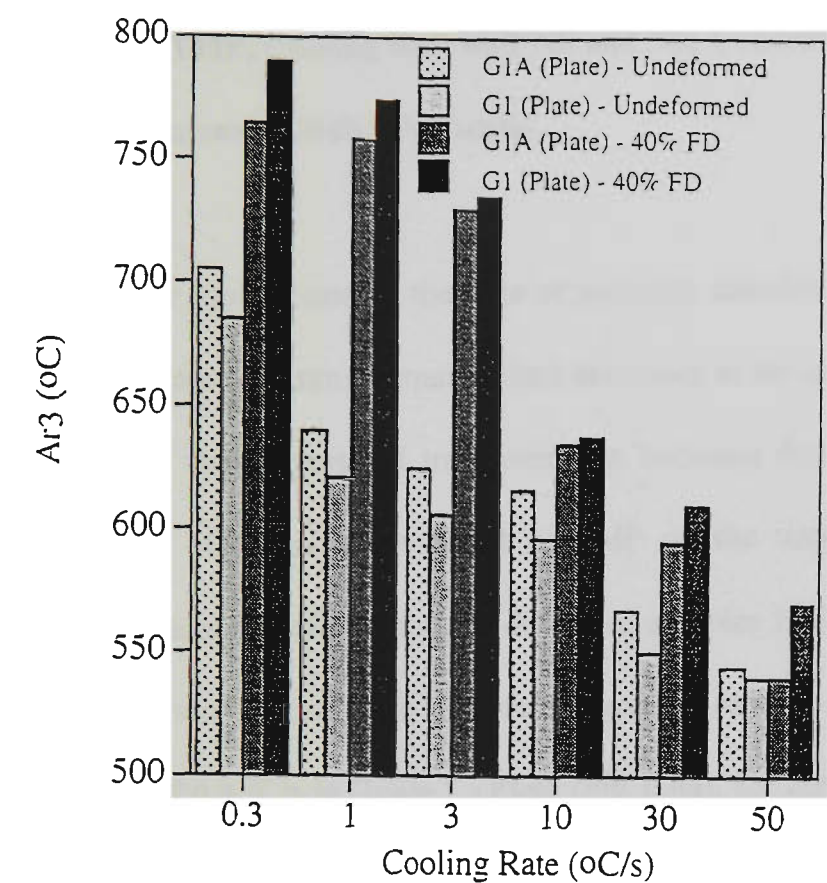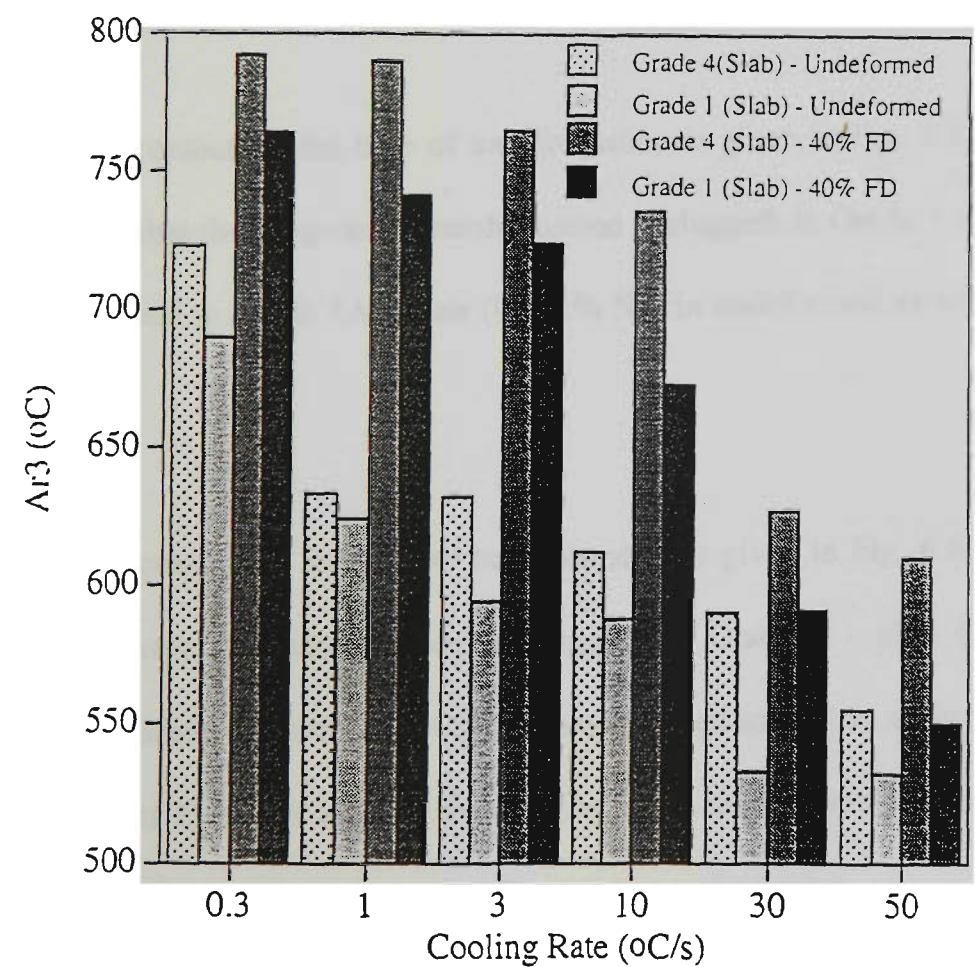
Figure 6.2: Effect of Nb content on Ar₃.

Figure 6.3: Effect of Mn content on Ar₃.

6.2.2 Influence of TMP, Cooling Rate and Nb and Mn Contents on Transformation Kinetics of Continuously Cooled Austenite

Effect of TMP and cooling rate on the time of austenite transformation is given in Fig. 6.4. The data indicate that transformation time decreases as the cooling rate is increased for all steels i. e. the progress of transformation becomes faster as the cooling rate increases. On the other hand, the effect of TMP on the time of transformation is opposite. The time of transformation for deformed samples is found to be longer than that of samples in undeformed state with similar cooling rates in all steels. For example, at a cooling rate of 0.3 °C/s in Grade 1 - Plate (Fig. 6.4a), the time of transformation for undeformed, 30% and 40% finish deformation samples are 167, 297 and 340 s respectively demonstrating that the progress of transformation is retarded by TMP.

Effect of Nb content on the time of transformation is given in Fig. 6.5. It is apparent from Fig. 6.5 that the progress of transformation is sluggish in Grade 1 - Plate (0.054% Nb) as compared to Grade 1A - Plate (0.031% Nb) in undeformed as well as deformed condition.

Effect of Mn content on the time of transformation is given in Fig. 6.6. It can be seen that the progress of transformation is sluggish in Grade 1 - slab (1.66% Mn) as compared to Grade 4 - Slab (1.07% Mn) in undeformed as well as deformed conditions. Comparison of Figs. 6.5 and 6.6 reveals that Mn is much more effective in retarding austenite transformation kinetics than Nb at higher cooling rates.
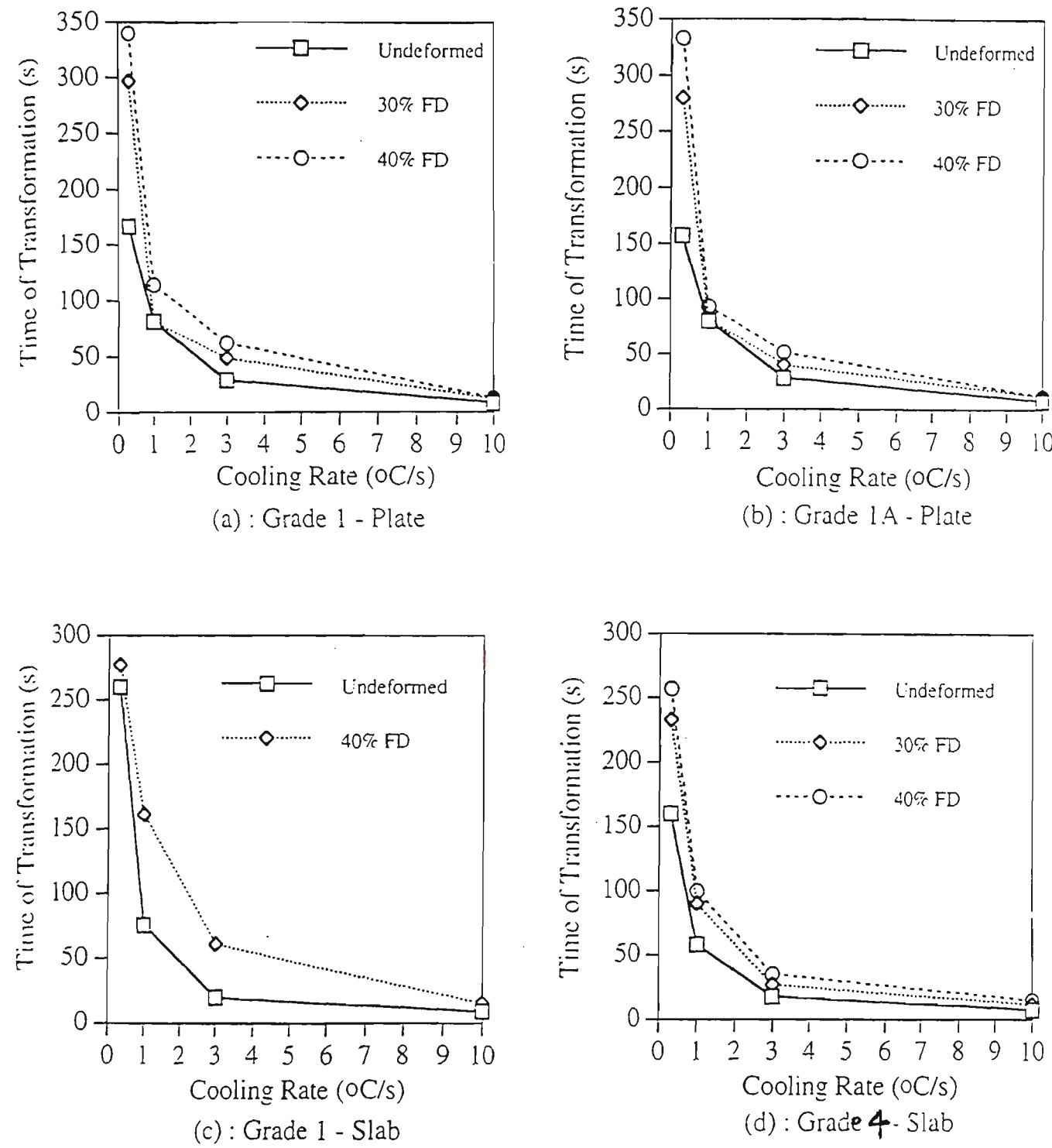
Figure 6.4: Effect of TMP and cooling rate on the time of transformation for the steels studied: (a) Grade 1 - Plate, (b) Grade 1A - Plate, (c) Grade 1 - Slab and (d) Grade 4 - Slab.
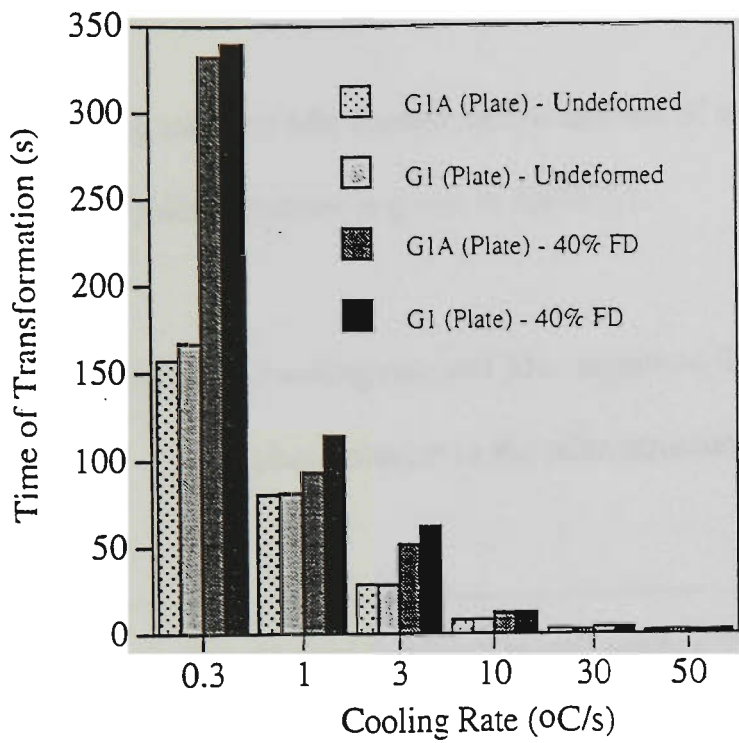
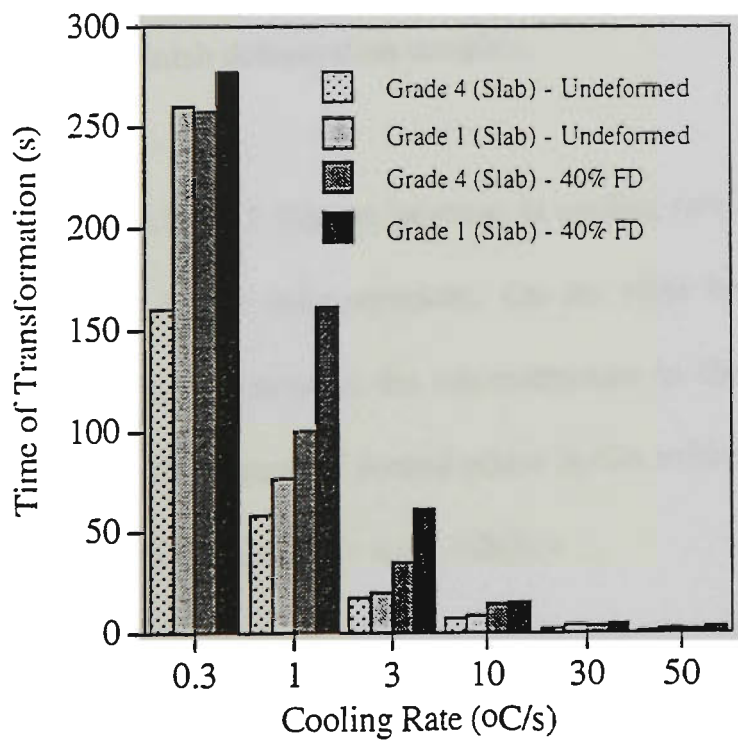Figure 6.5: Effect of Nb content on the time of transformation.

Figure 6.6: Effect of Mn content on the time of transformation.

6.2.3 Effect of TMP, Cooling Rate and Mn Content on Microstructure

Effect of TMP, cooling rate and Mn content on the amount of second phase (pearlite or bainite) present in the microstructure is given in Table 6.1.

Table 6.1: Effect of TMP, cooling rate and Mn content on the amount of second phase present in the microstructure.

CR (°C/s)	Amount of second phase (pearlite or bainite) present in the microstructure (%)											
	Grade 1 - Plate			Grade 1A - Plate			Grade 1 - Slab			Grade 4 - Slab		
	UD	30%	40%	UD	30%	40%	UD	30%	40%	UD	30%	40%
0.3	38	27.7	25.3	33	25	23.3	69	-	24.7	29	13	11.3
1	83	37	35.3	78	35	33.7	88	-	35	85.5	21.3	17
3	100	84	50.3	100	58	45.6	100	-	69	100	24	23.3
10	100	100	100	100	100	87	100	-	93.7	100	75.3	72

Notes: CR = cooling rate, UD = undeformed samples, 30% = 30% finish deformation samples, 40% = 40% finish deformation samples.

It can be seen from Table 6.1 that an increase in cooling rate increases the amount of second phase present in the microstructure. On the other hand, TMP decreases the amount of second phase present in the microstructure in these steels. Effect of Mn content in increasing the amount of second phase is also evident from the data in Table 6.1 based on the results for Grades 1 and 4 (Slabs).

Effect of TMP, cooling rate and Mn content on ferrite grain size is given in Table 6.2.

Table 6.2: Effect of TMP, cooling rate and Mn content on ferrite grain size.

CR °C/s	Ferrite grain size (µm)											
	Grade 1 - Plate			Grade 1A - Plate			Grade 1 - Slab			Grade 4 - Slab		
	UD	30%	40%	UD	30%	40%	UD	30%	40%	UD	30%	40%
0.3	22.1	7.7	6.1	22.4	8.5	8.0		NA	5.7		8.5	6.8
1		7.2	6.3		7.3	7.1		NA	5.7		8.6	7.0
3								NA			6.9	6.4

Notes: UD = undeformed samples, 30% = 30% finish deformation samples, 40% = 40% finish deformation samples, NA = not applicable, Open = difficult to measure

It can be seen from Table 6.2 that TMP refines ferrite grain size significantly in present steels and the addition of Nb and Mn also refine the ferrite grain size to some extent. An increase in cooling rate from 0.3 °C/s to 3 °C/s is found to influence the ferrite grain refinement marginally.

Optical micrographs of the undeformed and deformed samples are shown in Figs. 6.7 and 6.8 for Grade 1 (1.7% Mn) and in Figs. 6.9 and 6.10 for Grade 4 (1.1% Mn). Effect of TMP on promoting the ferrite transformation and refining the grain size of polygonal ferrite in both steels is evident by comparing the microstructures of the undeformed and deformed samples at equivalent cooling rates. As the cooling rate is increased, the nature of second phase changes progressively from Widmanstatten (B_3^P) to granular bainite (B_3^{m-a}) to upper bainite (B_2^c) and finally to lower bainite (B_1^c). It can be seen that the amount of second phase increases and the structure becomes more and more refined as the cooling rate is increased in both steels. High Mn steel (Grade 1) exhibits finer microstructure as compared to low Mn steel (Grade 4) at all cooling rates in undeformed and deformed conditions.
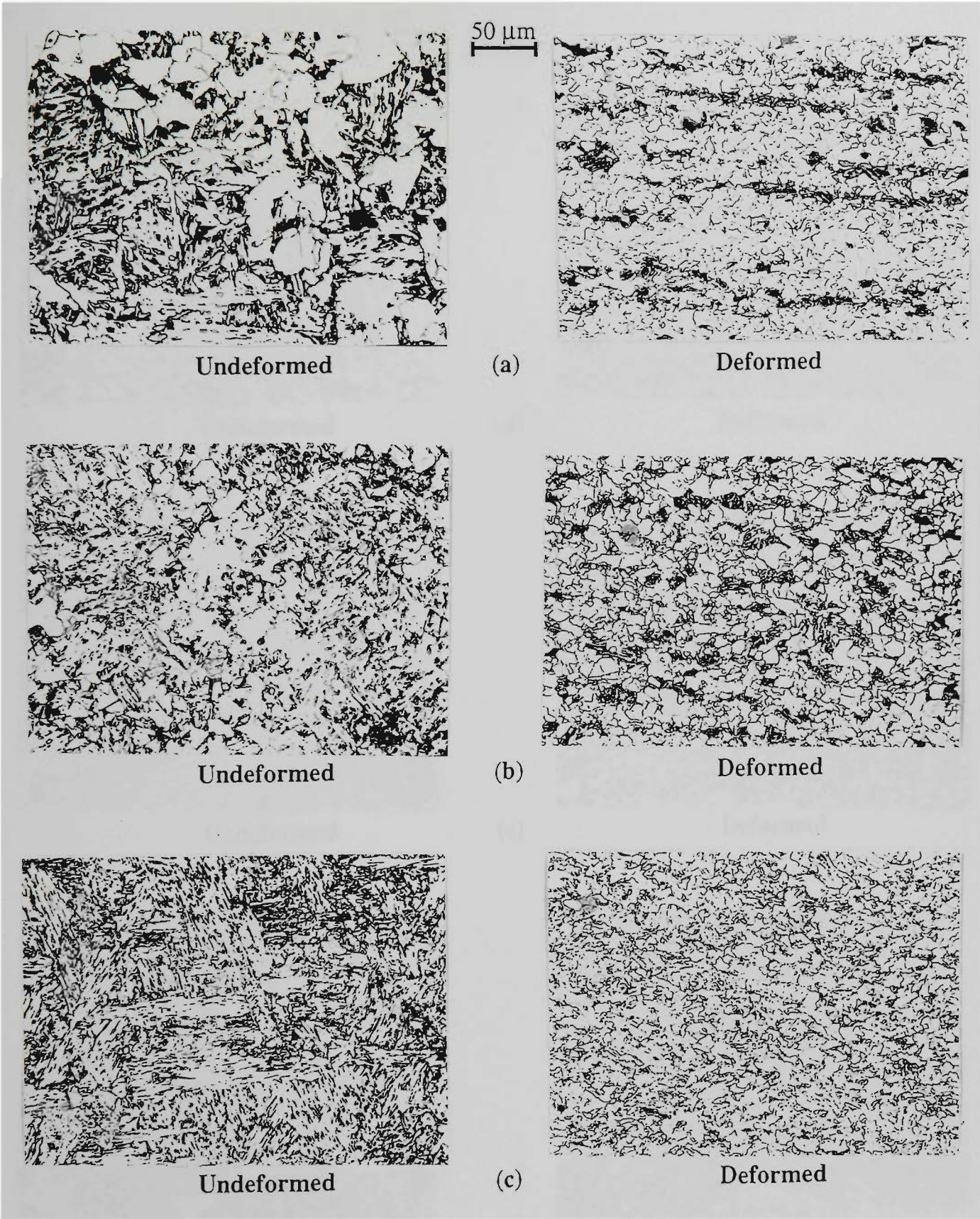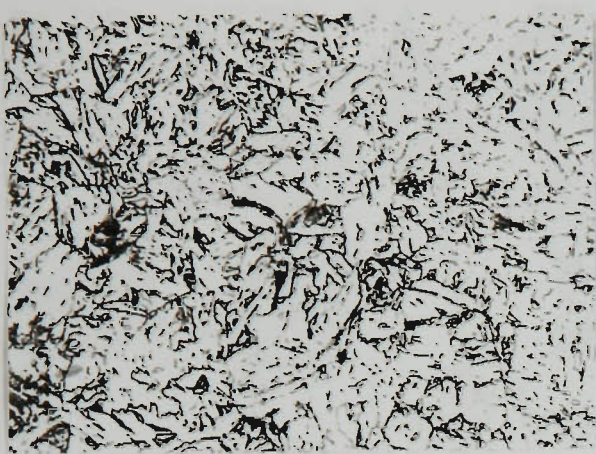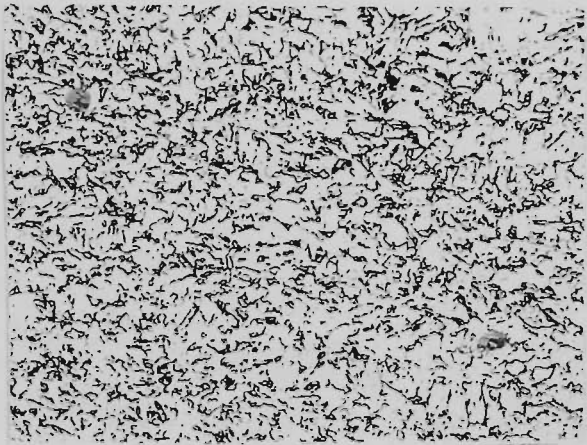
Figure 6.7: Optical microstructures of the undeformed and deformed (3*15% R + 2*20% F) samples in Grade 1 (1.7% Mn, Ti-Nb-Mo) - Slab. The samples were cooled to room temperature after TMP at: (a) 0.3 °C/s, (b) 1 °C/s, and (c) 3 °C/s. Magnification: 200X, etchant: 2.5% Nital. {Microstructures at higher cooling rates are shown in Fig. 6.8}.
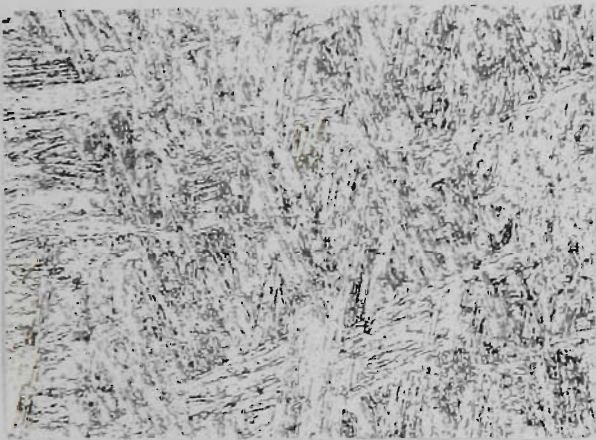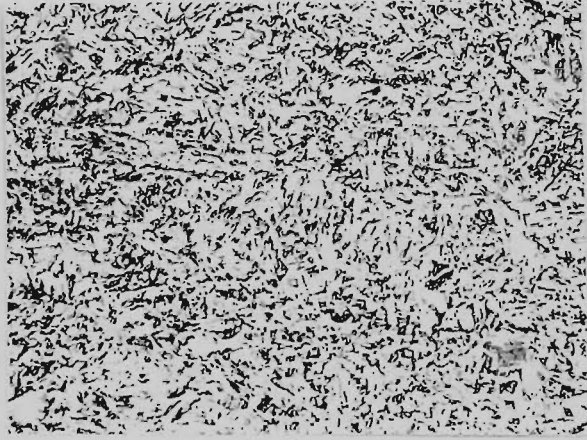
25 µm

Figure 6.8: Optical microstructures of the undeformed and deformed (3*15% R + 2*20% F) samples in Grade 1 (1.7% Mn, Ti-Nb-Mo) - Slab. The samples were cooled to room temperature after TMP at: (d) 10 °C/s, (e) 30 °C/s, and (f) 50 °C/s. Magnification: 400X, etchant: 2.5% Nital. {Continued from Fig. 6.7}.

50 µm

Undeformed   (a)   Deformed

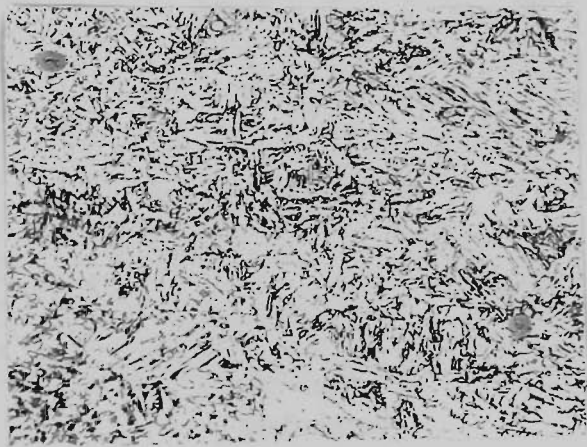Undeformed   (b)   Deformed

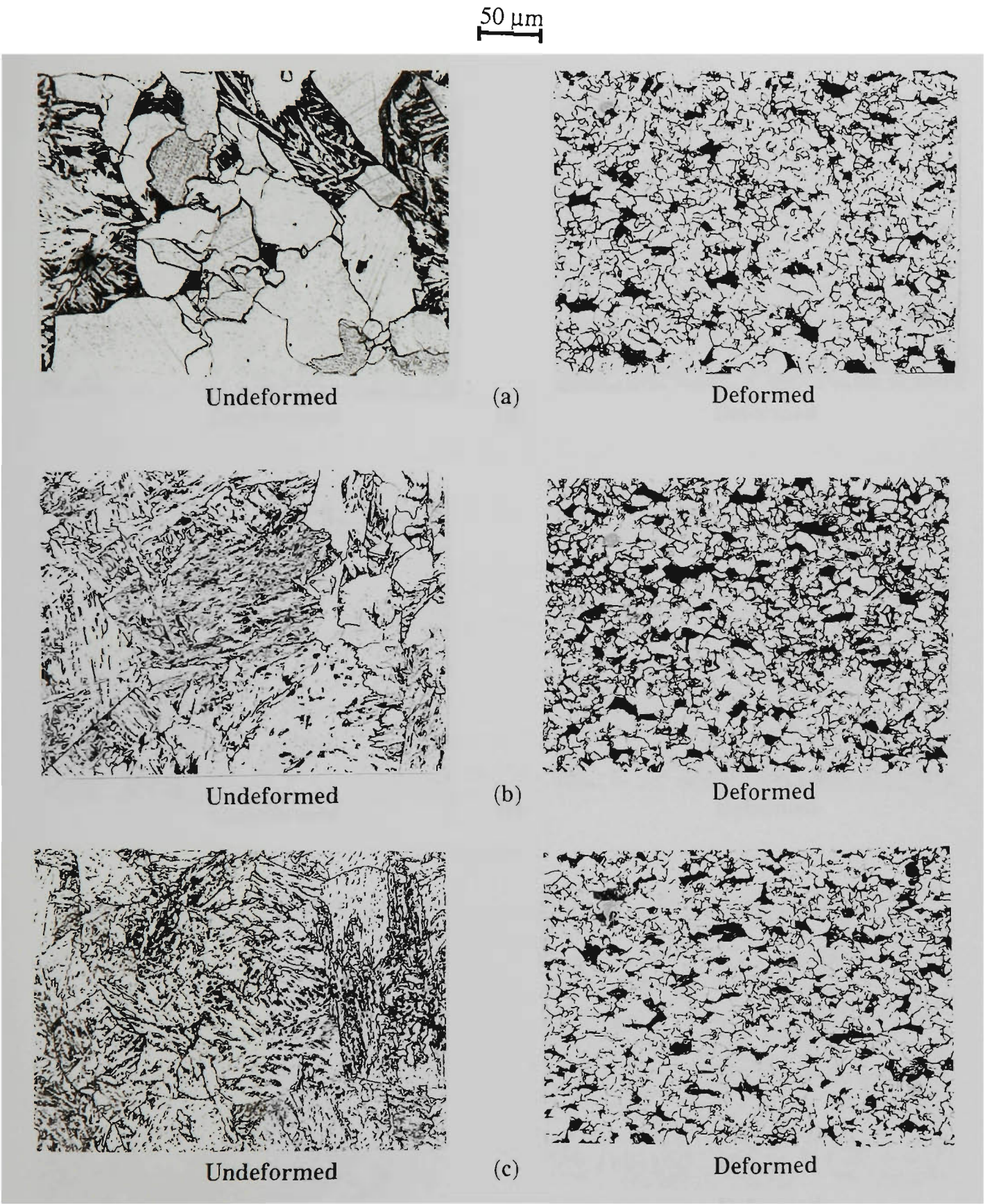Undeformed   (c)   Deformed

Figure 6.9: Optical microstructures of the undeformed and deformed (3*15% R + 2*20% F) samples in Grade 4 (1.1% Mn, Ti-Nb-Mo) - Slab. The samples were cooled to room temperature after TMP at: (a) 0.3 °C/s, (b) 1 °C/s, and (c) 3 °C/s. Magnification: 200X, etchant: 2.5% Nital. {Microstructures at higher cooling rates are shown in Fig. 6.10}.
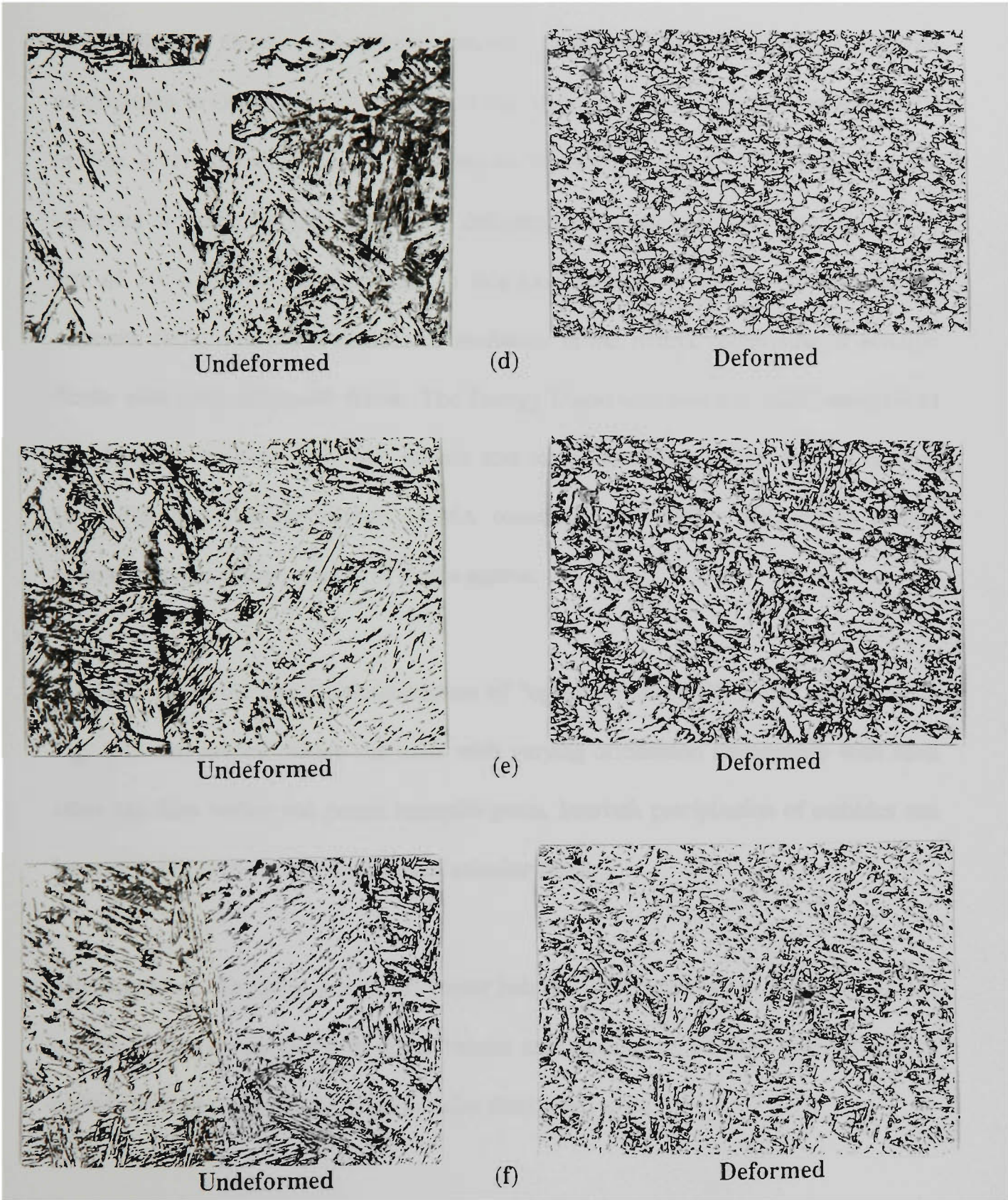
25 µm

Figure 6.10: Optical microstructures of the undeformed and deformed (3*15% R + 2*20% F) samples in Grade 4 (1.1% Mn, Ti-Nb-Mo) - Slab. The samples were cooled to room temperature after TMP at: (d) 10 °C/s, (e) 30 °C/s, and (f) 50 °C/s. Magnification: 400X, etchant: 2.5% Nital. {Continued from Fig. 6.9}.

Microstructural analysis was also carried out by using a Leica - Cambridge Stereoscan S440 scanning electron microscope attached with EDS facility. Scanning electron micrographs in Grade 1 (Slab) of some of the representative microstructures are shown in Figs. 6.11, 6.13 and 6.14. Fig. 6.11 shows "granular bainite (B_3^{m-a})" microstructure observed in Grade 1 - Slab, 40% finish deformed and cooled to room temperature at a rate of 10 °C/s. The microstructure in this case consists of islands of martensite - austenite (MA) constituent distributed randomly in the matrix comprising of acicular ferrite with some polygonal ferrite. The Energy Dispersive Spectral (EDS) analysis of the chemical composition of MA islands and matrix is shown in Fig. 6.12. It is clear from Fig. 6.12 that the islands of MA constituent are highly enriched in carbon compared to the carbon content of ferrite matrix.

Fig. 6.13 shows the typical microstructure of "upper bainite (B_2^c)". It can be seen from Fig. 6.13 that several bainite sub-units with varying orientation relationship with each other can form within one parent austenite grain. Interlath precipitation of carbides can be seen to be parallel to the lath axes of acicular ferrite.

Microstructure consisting mainly of "lower bainite (B_1^c)" is shown in Fig. 6.14. Lower bainite is finer as compared to upper bainite and consists of intralath precipitation of carbides oriented at an angle to the acicular ferrite lath axes.
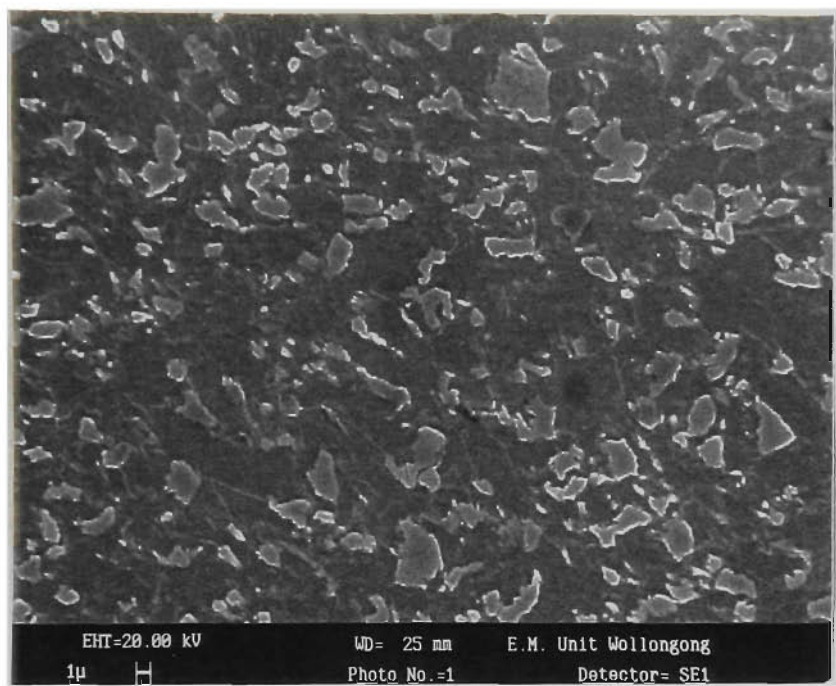
Figure 6.11: Scanning electron micrograph showing granular bainite (B_3^{m-a}) in Grade 1 - Slab, sample cooled to room temperature at 10 °C/s after finish deformed 40% at 840 °C. Islands of Martensite - Austenite (MA) constituent are distributed randomly in the matrix comprising of acicular ferrite with some polygonal ferrite.
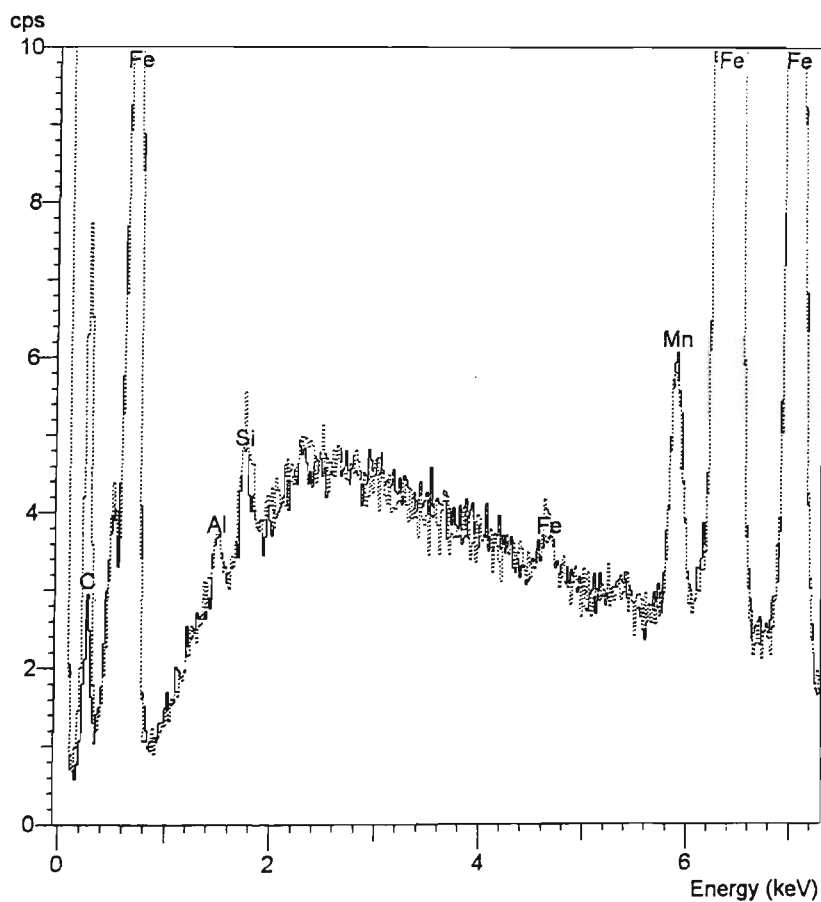

Figure 6.12: EDS analysis of composition of MA islands (dotted line) and acicular ferritic matrix (full line). Higher carbon content in MA islands compared to the ferrite matrix is clearly evident.
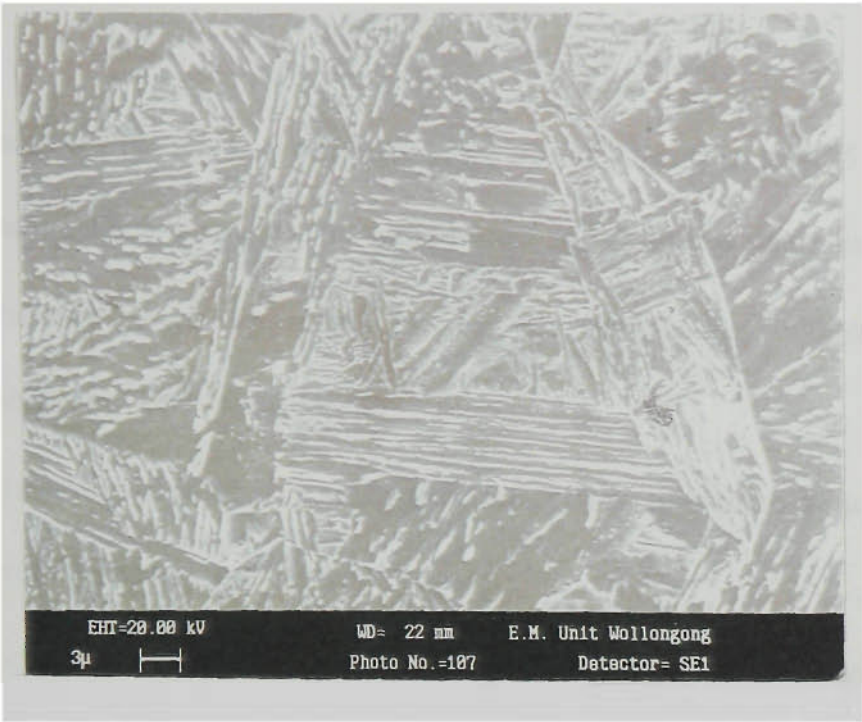
Figure 6.13: SEM micrograph showing the microstructure of upper bainite (B_2^c). Interlath precipitates of carbides are parallel to the acicular ferrite lath axes. Evidently, several sub-units of upper bainite have formed within one parent austenite grain. Sample: Grade 1 - Slab, 40% finish deformed, cooled to room temperature at 50 °C/s.
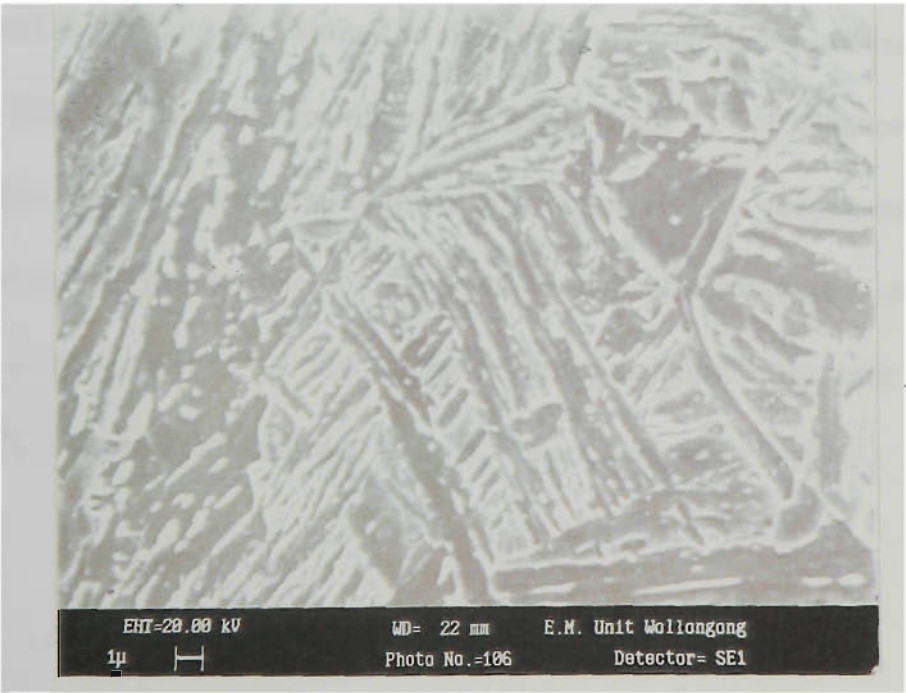

Figure 6.14: SEM image of lower bainite (B_1^c). Finely dispersed, intralath precipitates of carbides are evident at an angle to the acicular ferrite lath axes. Some upper bainite can also be seen in the microstructure. Sample: Grade 1 - Slab, undeformed, cooled to room temperature at 50 °C/s.

6.2.4 CCT Diagrams: Undeformed and Thermomechanically Processed Conditions

CCT diagrams for the steels studied are presented in Figs. 6.15 to 6.25. Comparison of CCT diagrams for any given steel in undeformed and deformed states suggests that:

a) $\gamma \rightarrow \alpha$ transformation is raised to higher temperatures indicating decreased hardenability of TMP austenite,

b) ferrite transformation nose is shifted towards left (i. e. towards faster cooling rates) in deformed samples; and

c) $\gamma \rightarrow \alpha$ occurs over a wider temperature range indicating a retarded rate of progress of transformation in TMP austenite.

Comparison of CCT diagrams for Grade 1 - Slab (1.66% Mn) and Grade 4 - Slab (1.07% Mn) given in Figs. 6.21 to 6.25 for similar deformation strains shows that the pearlite and ferrite noses are shifted to right (i. e. towards slower cooling rates) in high Mn steel (Grade 1) as compared to low Mn steel (Grade 4). For instance, in 40% finish deformation samples, Widmanstatten microstructure (B_3^P) is predominant in Grade 4 only when the cooling rate exceeds 3 °C/s while such microstructure is evident in Grade 1 even at a cooling rate of 0.3 °C/s. In the deformed samples, ferrite nose is shifted from about 30 °C/s cooling rate in Grade 4 to 10 °C/s cooling rate in Grade 1.

Figure 6.15: CCT diagram for Grade 1 - Plate in undeformed condition.

Figure 6.16: CCT diagram for Grade 1 - Plate in deformed condition (3 * 15% roughing and 1 * 30% finishing deformation).

Figure 6.17: CCT diagram for Grade 1 - Plate in deformed condition (3 * 15% roughing and 2 * 20% finishing deformation).
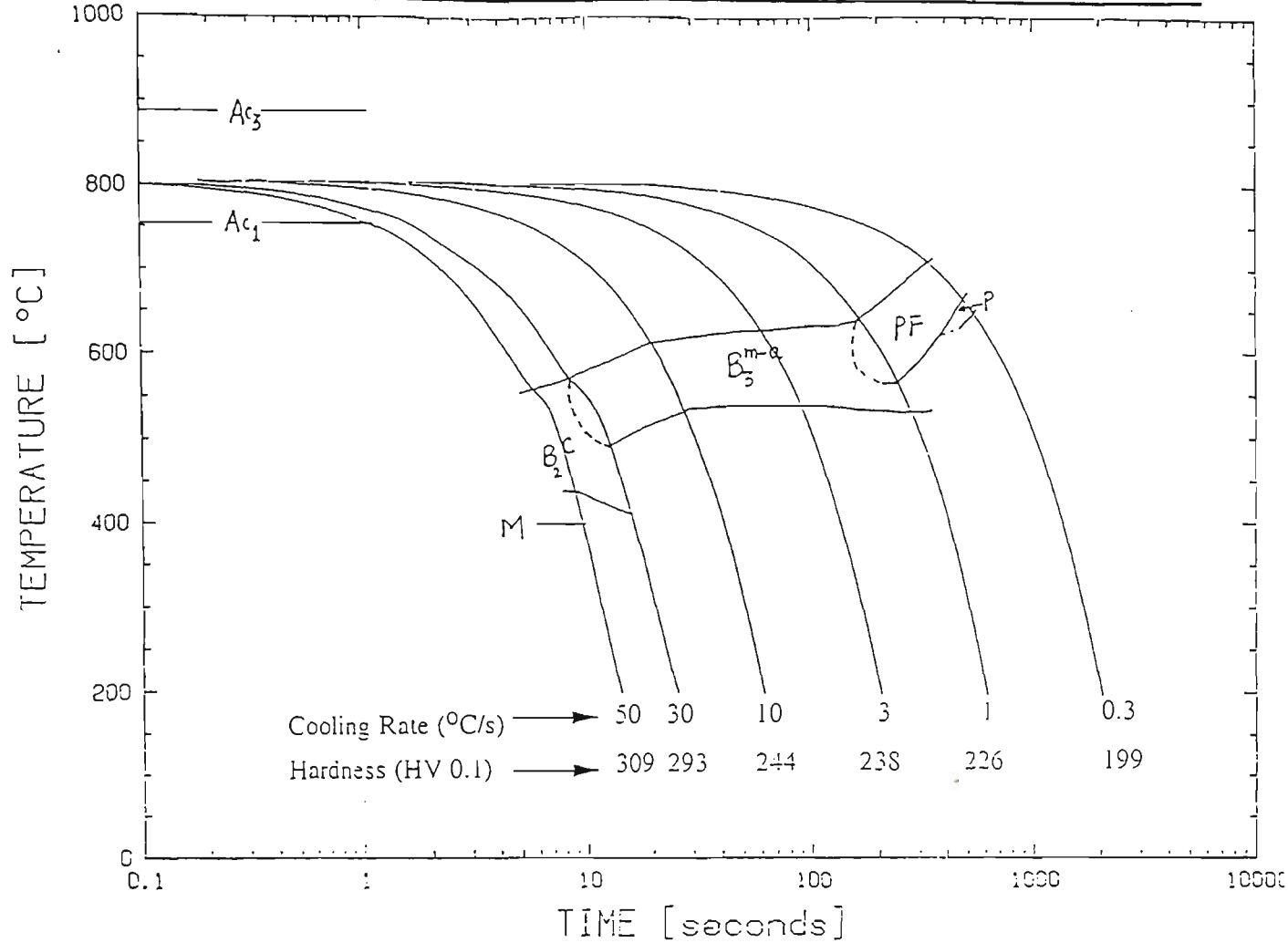
Figure 6.18: CCT diagram for Grade 1A - Plate in undeformed condition.
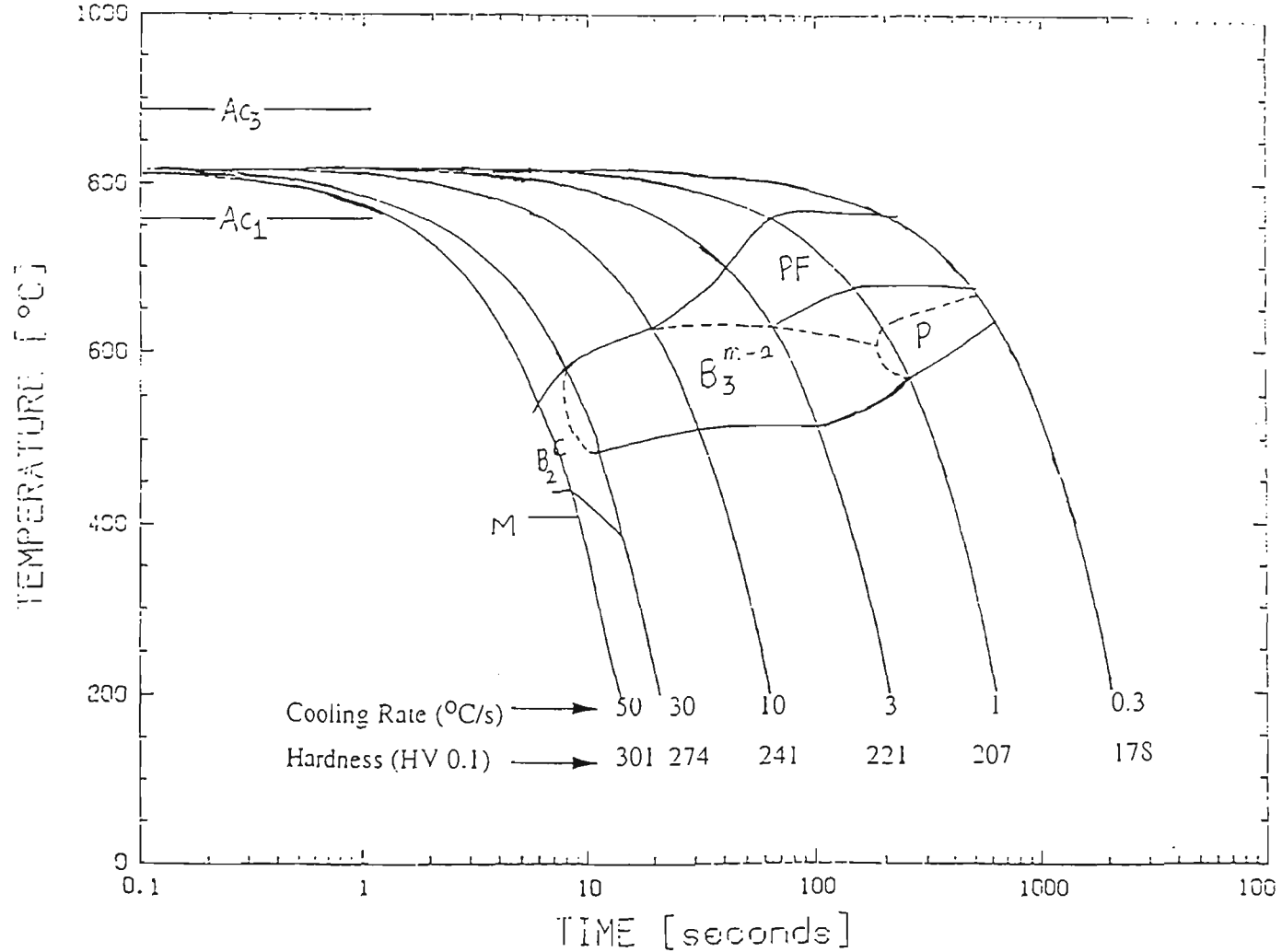
Figure 6.19: CCT diagram for Grade 1A - Plate in deformed condition (3 * 15% roughing and 1 * 30% finishing deformation).
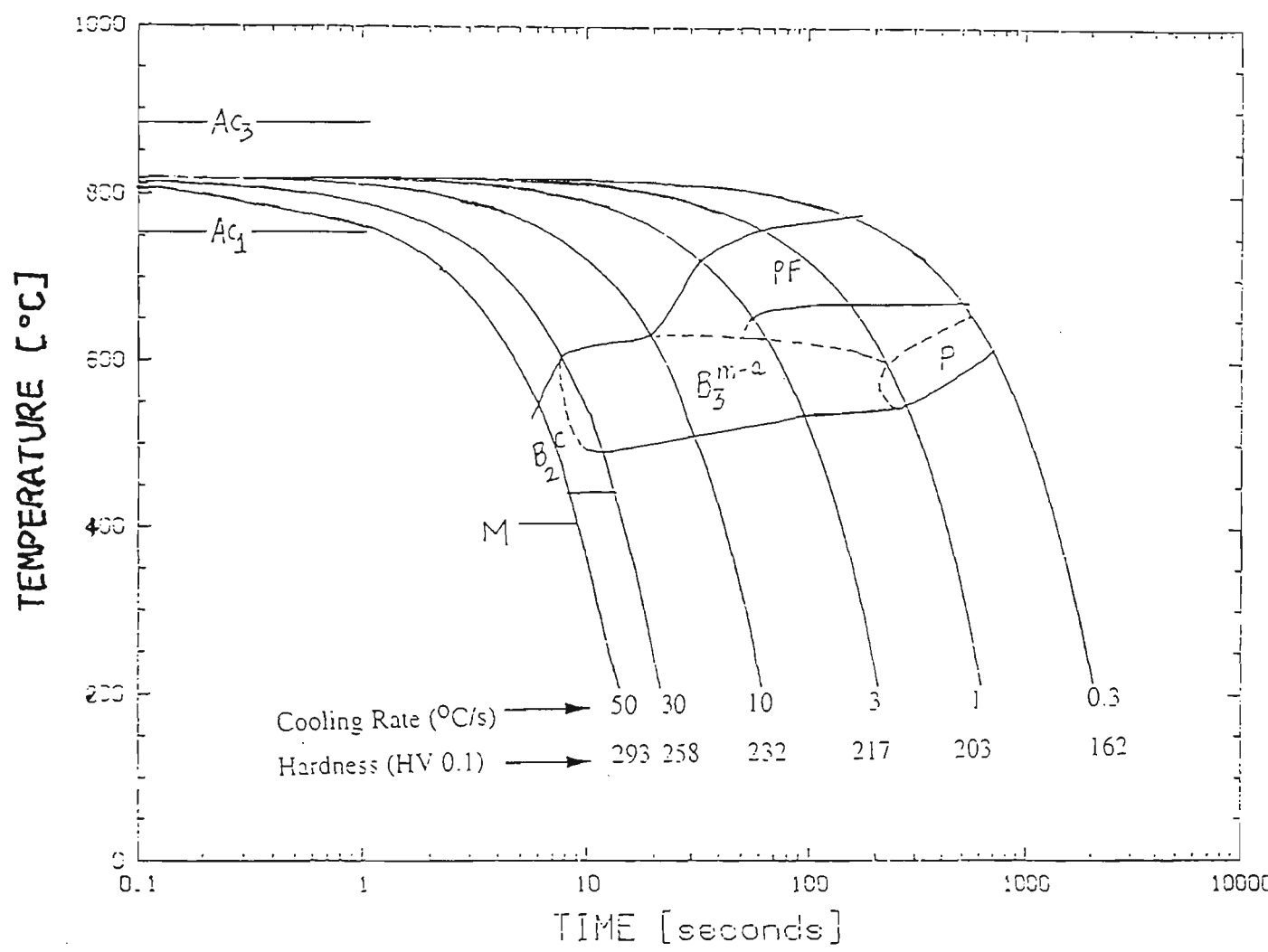
Figure 6.20: CCT diagram for Grade 1A - Plate in deformed condition (3 * 15% roughing and 2 * 20% finishing deformation).
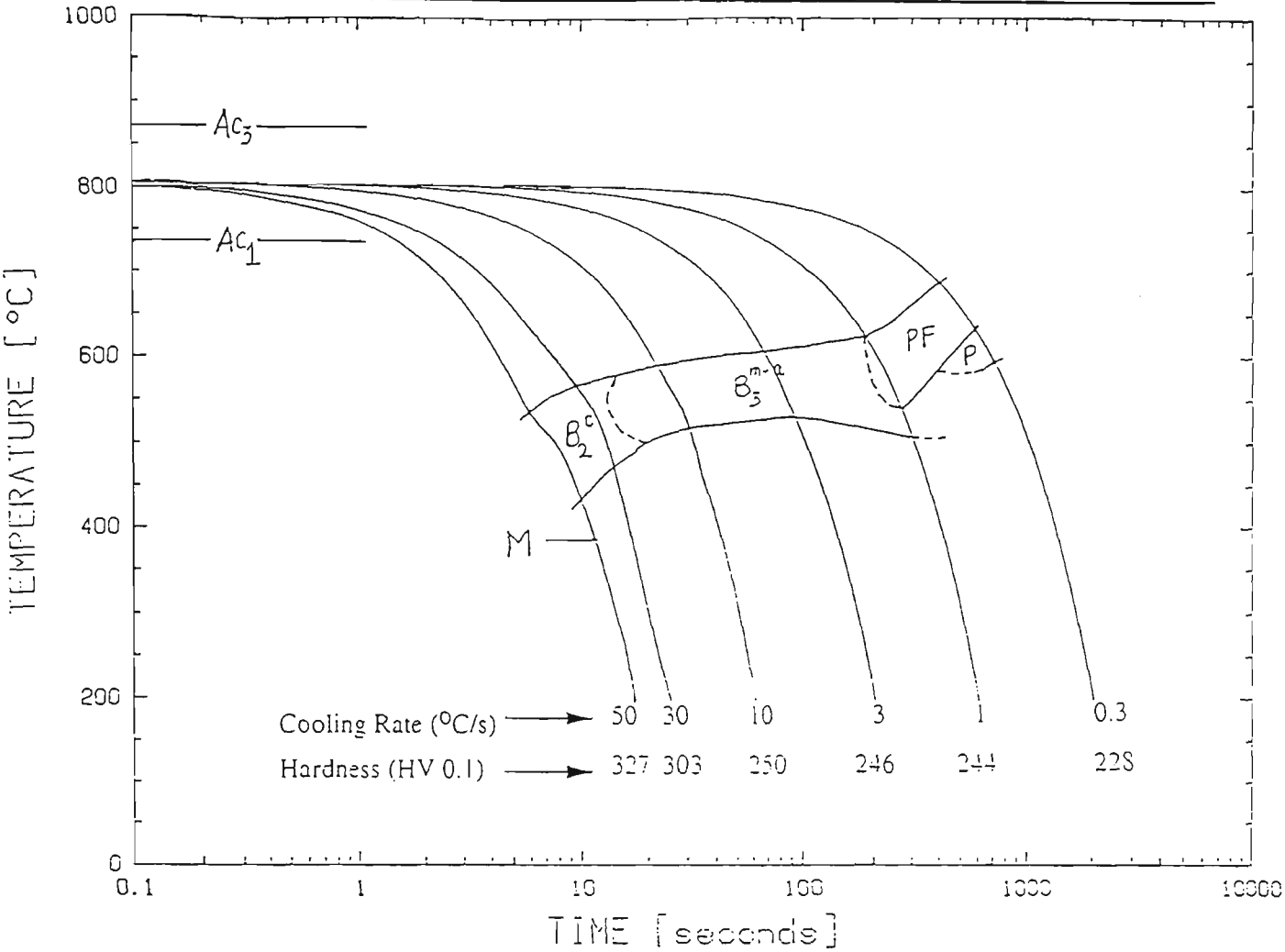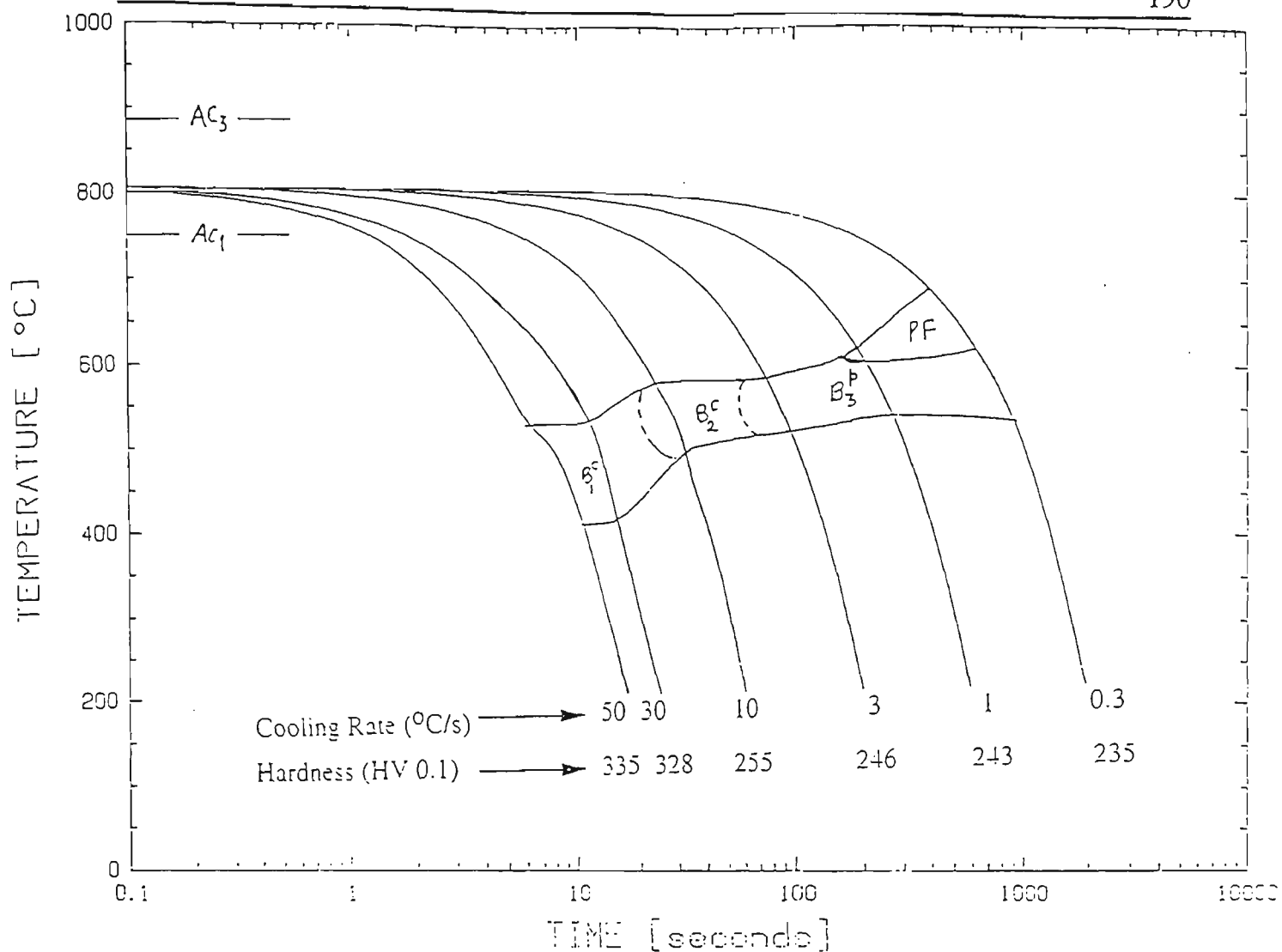
Figure 6.21: CCT diagram for Grade 1 - Slab in undeformed condition.
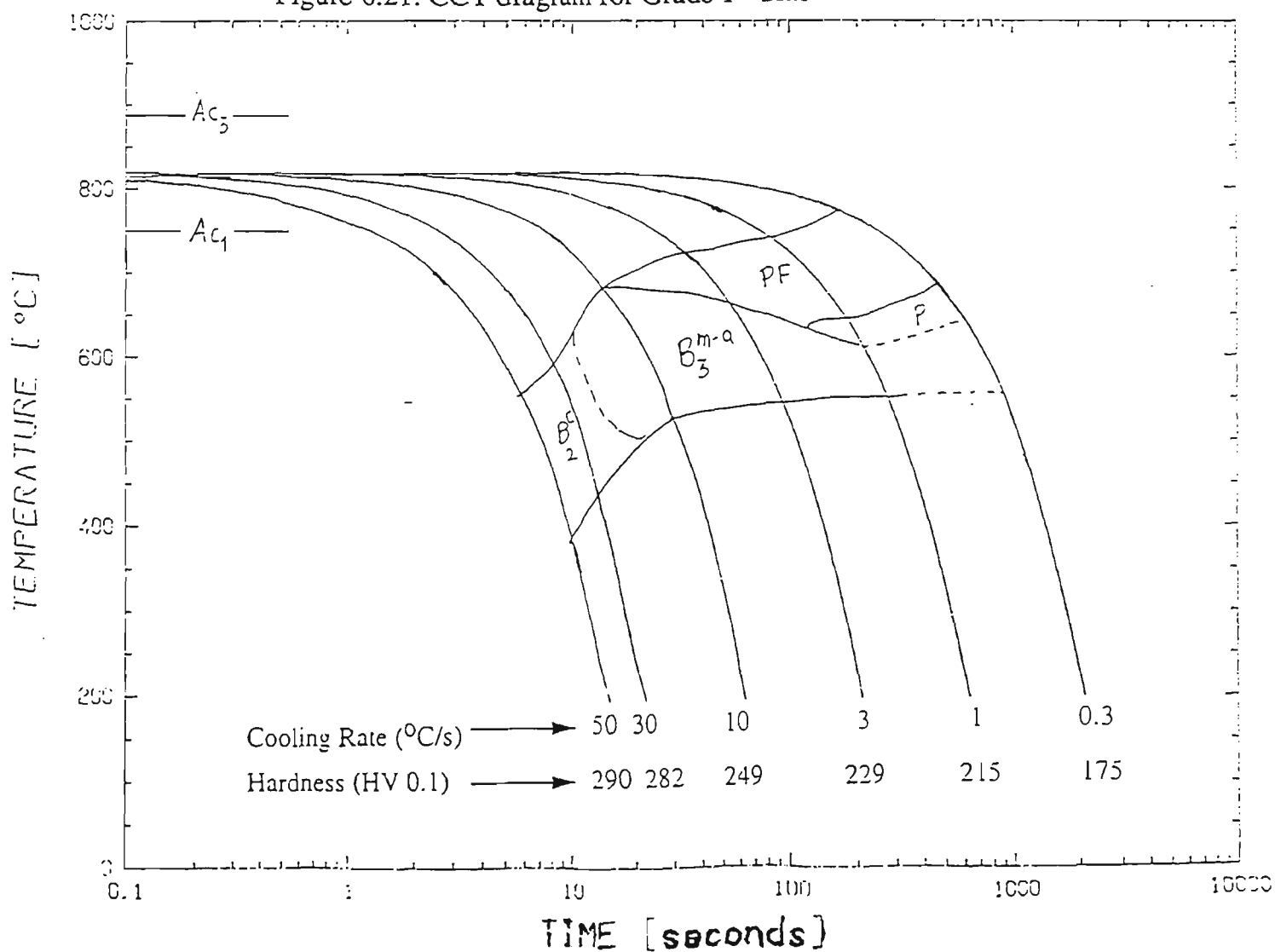
Figure 6.22: CCT diagram for Grade 1 - Slab in deformed condition (3 * 15% roughing and 2 * 20% finishing deformation).
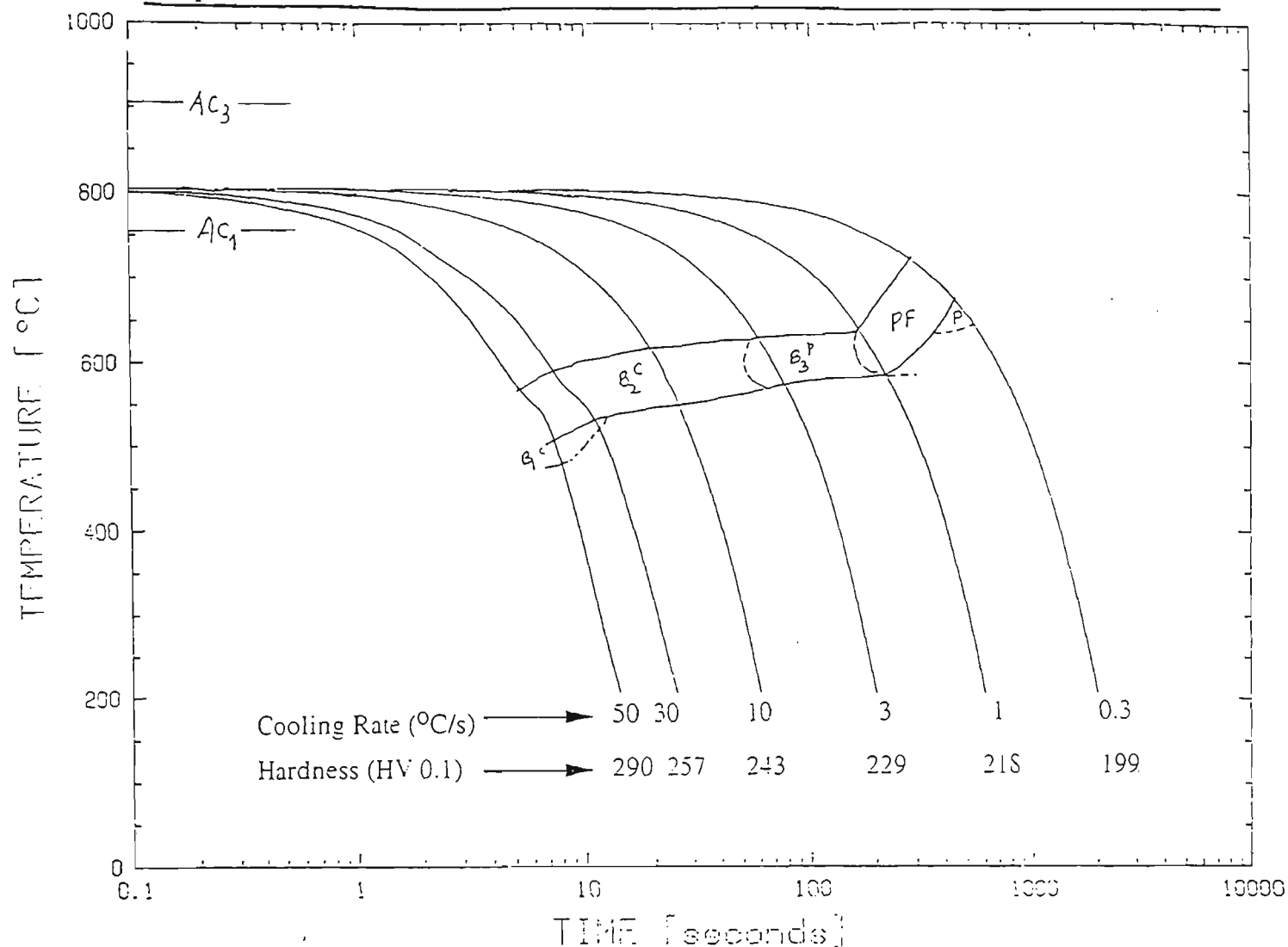
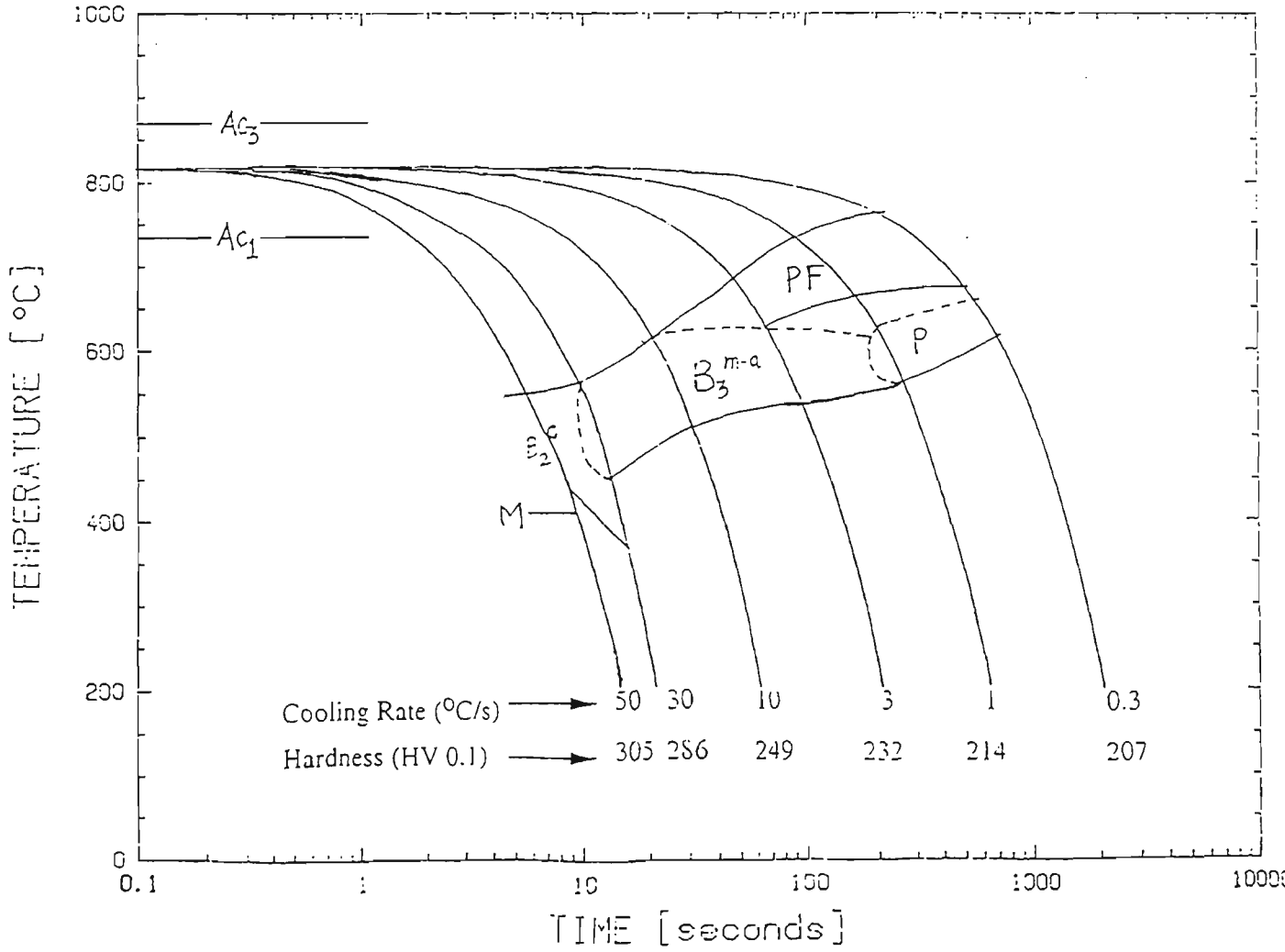Figure 6.23: CCT diagram for Grade 4 - Slab in undeformed condition.
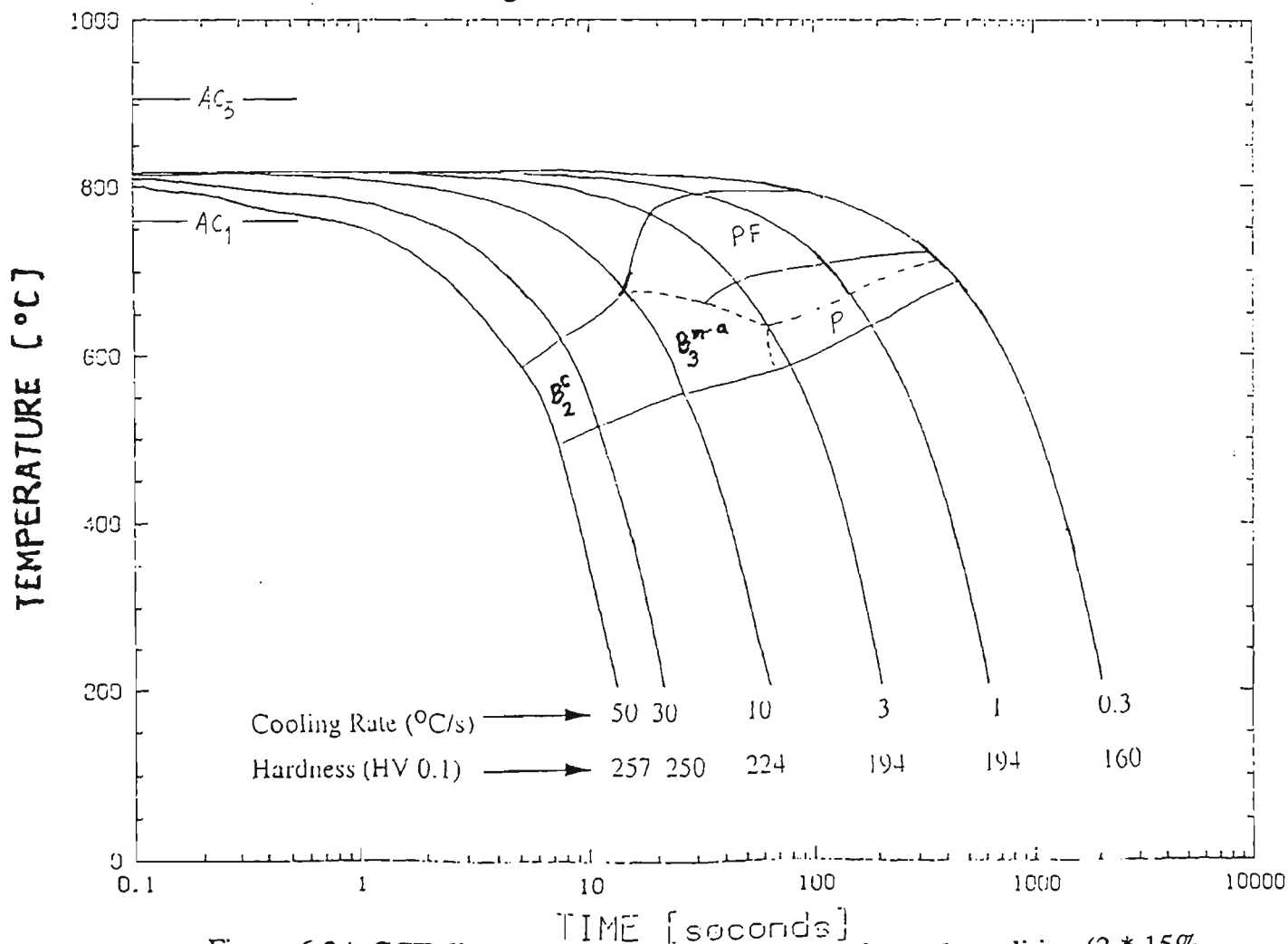
Figure 6.24: CCT diagram for Grade 4 - Slab in deformed condition (3 * 15%
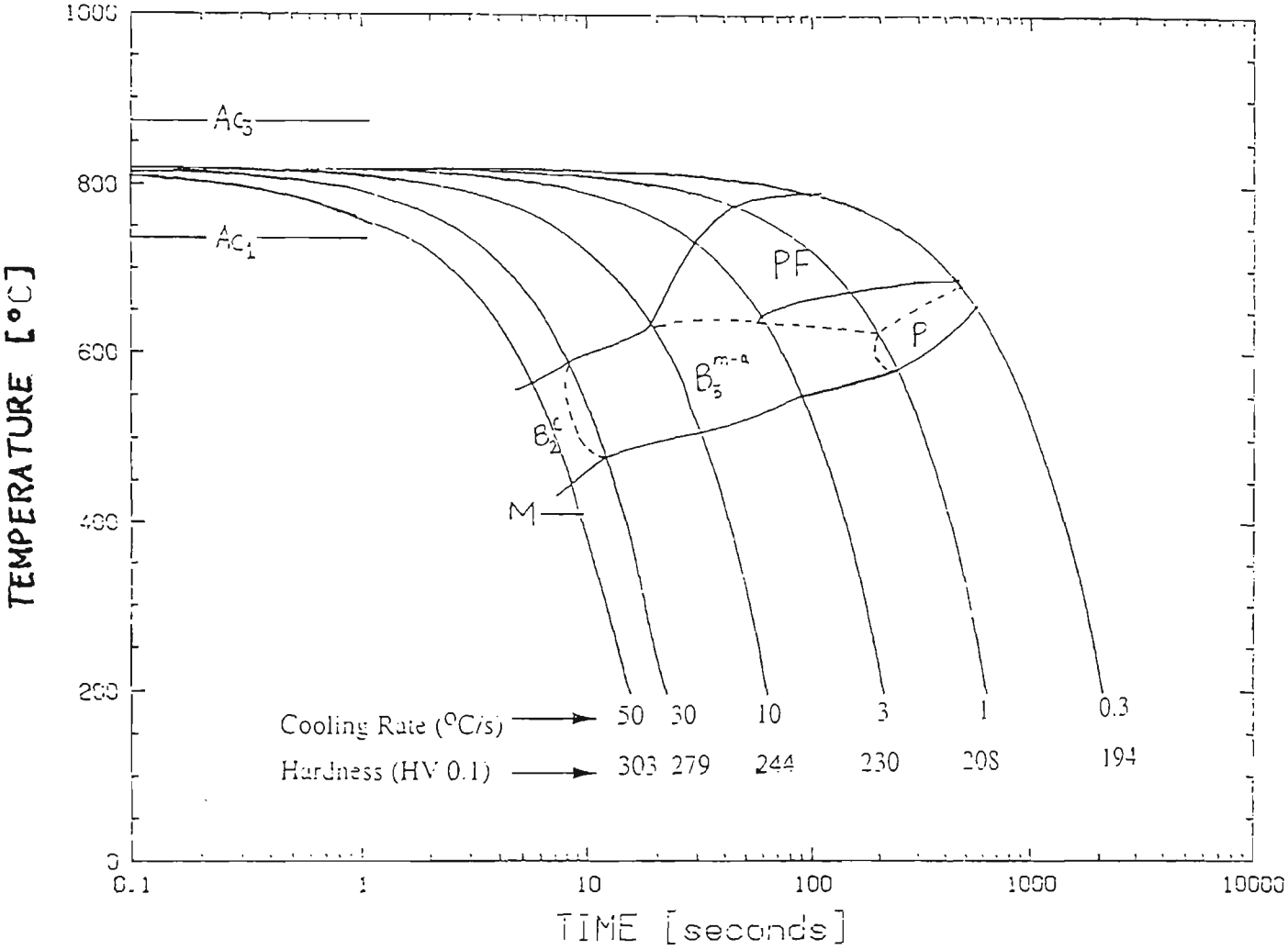roughing and 1 * 30% finishing deformation).
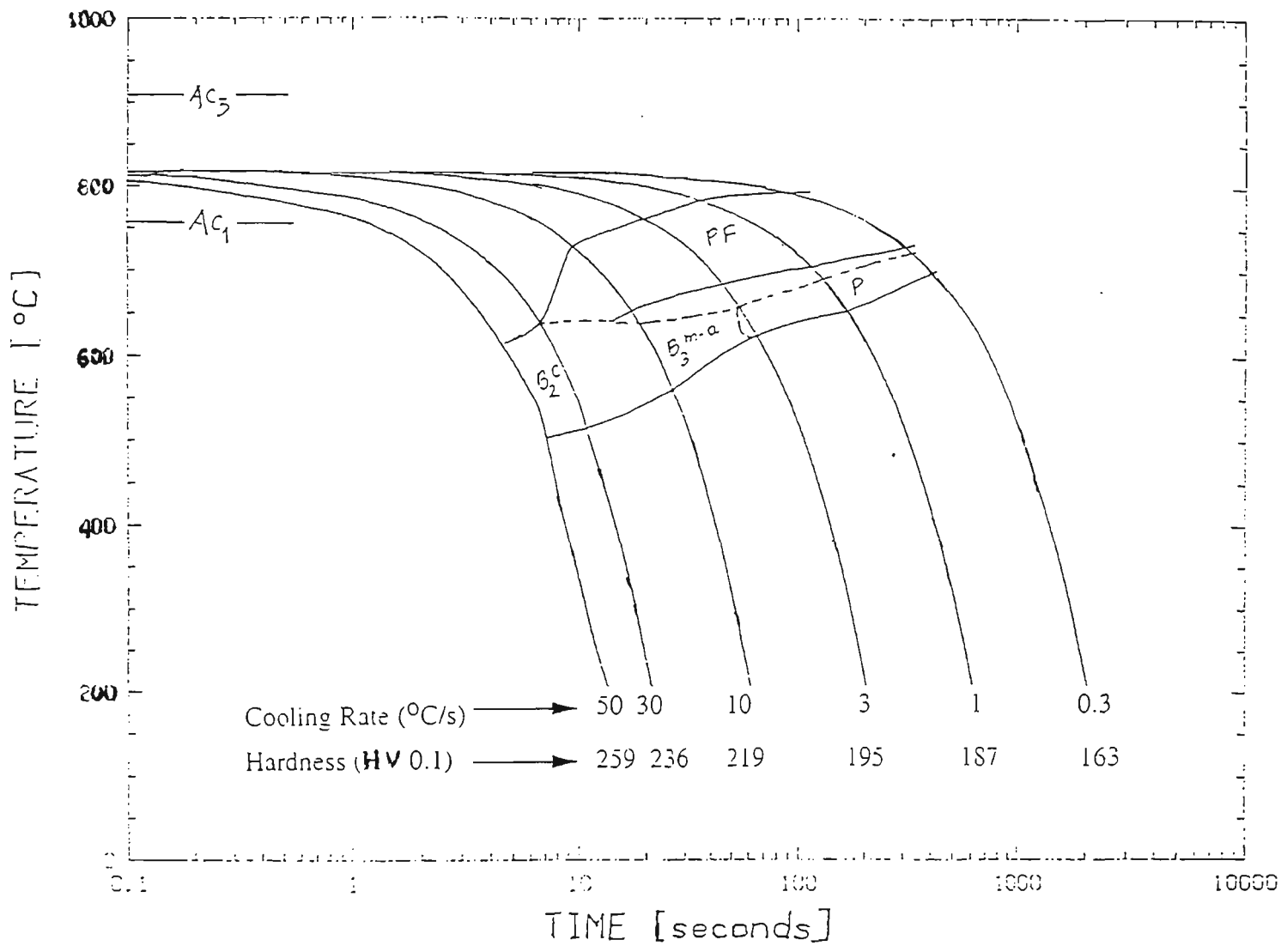
Figure 6.25: CCT diagram for Grade 4 - Slab in deformed condition (3 * 15% roughing and 2 * 20% finishing deformation).

6.2.5 Effect of TMP, Cooling Rate and Nb and Mn Contents on Microhardness

Effect of TMP and cooling rate on hardness of samples is given in Fig. 6.26.
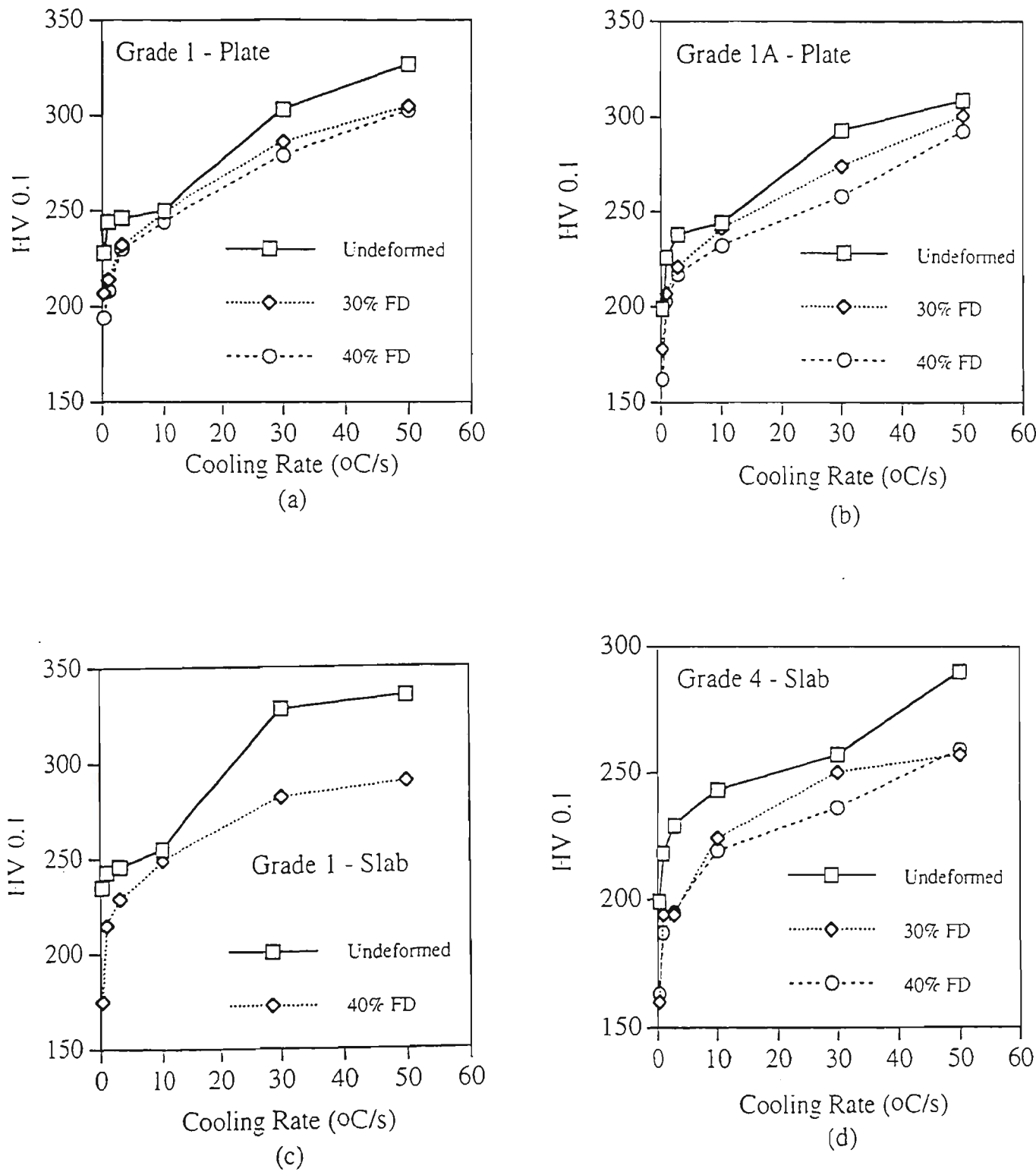
Figure 6.26: Effect of TMP and cooling rate on the hardness of samples in: Grade 1 - Plate, (b) Grade 1A - Plate, (c) Grade 1 - Slab and (d) Grade 4 - Slab.

It can be seen that an increase in cooling rate increases the hardness while the hardness of TMP samples is significantly lower than that of undeformed samples for all grades of steels. Effect of Nb and Mn contents on the hardness of samples is shown in Fig. 6.27.
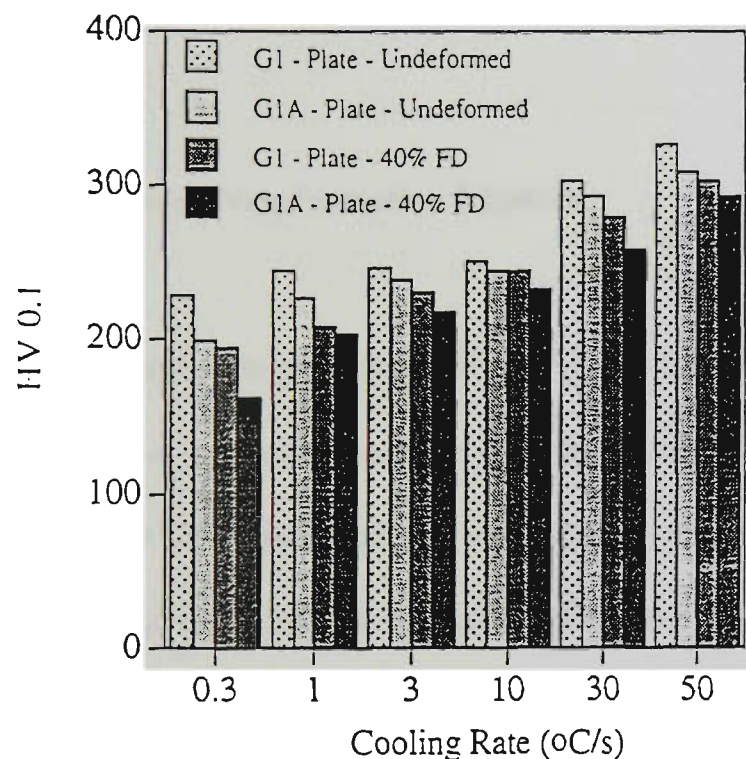
(a)
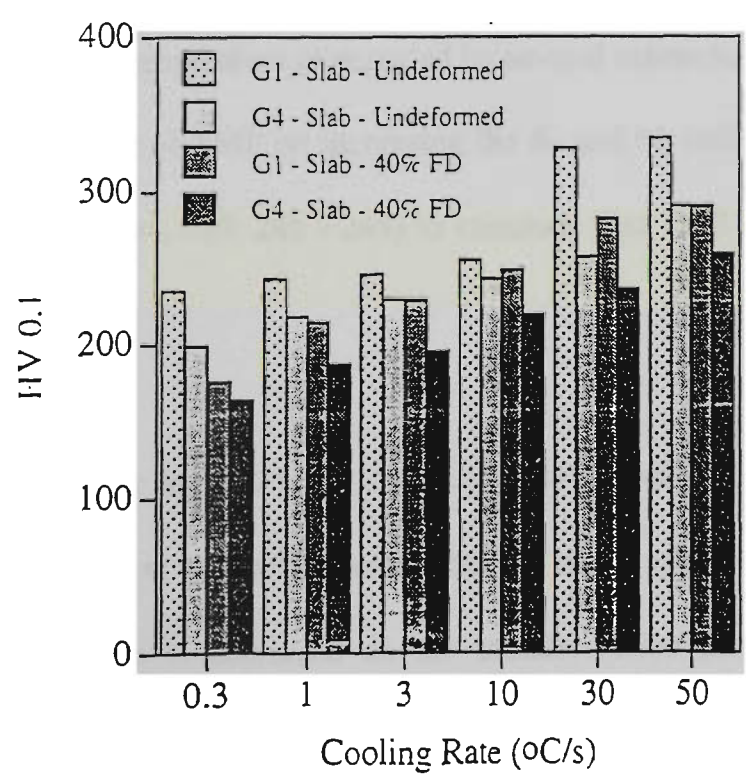
(b)

Figure 6.27: Effect of (a) Nb content and (b) Mn content on the hardness of samples.

It can be seen from Fig. 6.27 that an increase in Nb or Mn content leads to an increases in the hardness of the samples in undeformed as well as deformed condition.

6.3 Discussion

6.3.1 Effect of TMP on $\gamma \rightarrow \alpha$ Transformation Kinetics

Role of TMP in refining austenite grain size and also controlling austenite grain shape just before the onset of $\gamma \rightarrow \alpha$ transformation is well documented. Kozasu et al. [144] showed that the effective interfacial area per unit volume of austenite (S_v) and the nucleation rate (N_s) are increased by austenite grain refinement and deformation below T_{nr}. This effect has been attributed to the increased free energy of austenite and to the availability of more nucleation sites by way of substructures in the deformed austenite grains. It is, thus, expected that deformation would accelerate the $\gamma \rightarrow \alpha$ transformation and would raise the Ar_3 temperature as reported by several researchers [239, 240]. These observations of the effect of TMP on increasing the S_v and N_s leading to an increase in Ar_3 led many authors [144, 239, 241 - 244] to conclude that TMP accelerates the $\gamma \rightarrow \alpha$ transformation.

On the other hand, some authors [177, 240, 245 - 247] believe that TMP retards the $\gamma \rightarrow \alpha$ transformation. Liu et al. [240] reported that the stored energy of cold work within unrecrystallized austenite is decreased as the transformation progresses resulting in lessening of driving force for transformation. Sandberg and Roberts [245] suggested that the nucleation rate drops drastically once the favourable sites in deformed austenite are exhausted. Also, the volume of material which must transform via intragranular

nucleation is considerable and thus controlled rolled material has a lower rate of transformation as compared to the normalized (conventional hot rolled) one. Honeycombe [177] pointed out that the precipitates formed in austenite, particularly those precipitates which form at temperatures approaching the transformation, can pin the interface during transformation. Sellars [247] suggests that strain induced precipitation may retard growth rate relative to nucleation.

This situation can now be resolved by quantifying the kinetics of $\gamma \rightarrow \alpha$ transformation in terms of two parameters: a) Ar_3 - which is an index of nucleation for transformation; and b) time for transformation - which measures the rate of progress of transformation. TMP causes acceleration of the onset of $\gamma \rightarrow \alpha$ transformation leading to an increase in Ar_3 as shown in Fig. 6.1. On the other hand, progress of transformation is significantly retarded in deformed samples, see Fig. 6.4. The results of the present work thus demonstrate that TMP accelerates the onset of $\gamma \rightarrow \alpha$ transformation but retards its progress once the transformation is initiated.

The reasons why TMP retards the progress of $\gamma \rightarrow \alpha$ transformation are as follows. Firstly, the amount of ferrite formed in the TMP samples is much more than that formed in undeformed samples, see Table: 6.1. The other reason can be seen through the analysis of dilatometer data as presented in Figs. 6.28 - 6.31.
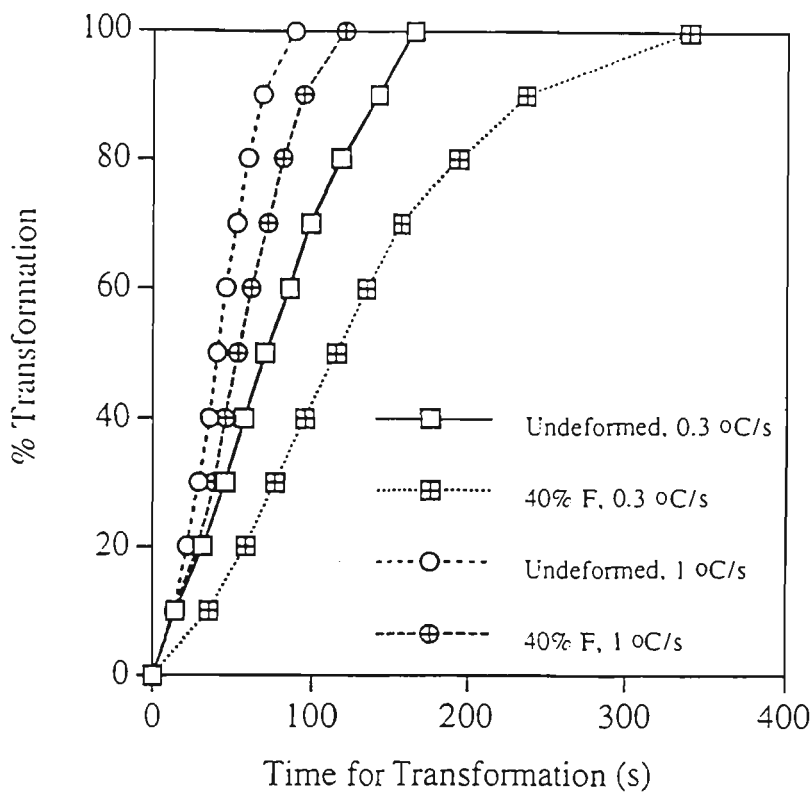
Figure 6.28: Effect of TMP on the progress of transformation in Grade 1 - Plate.
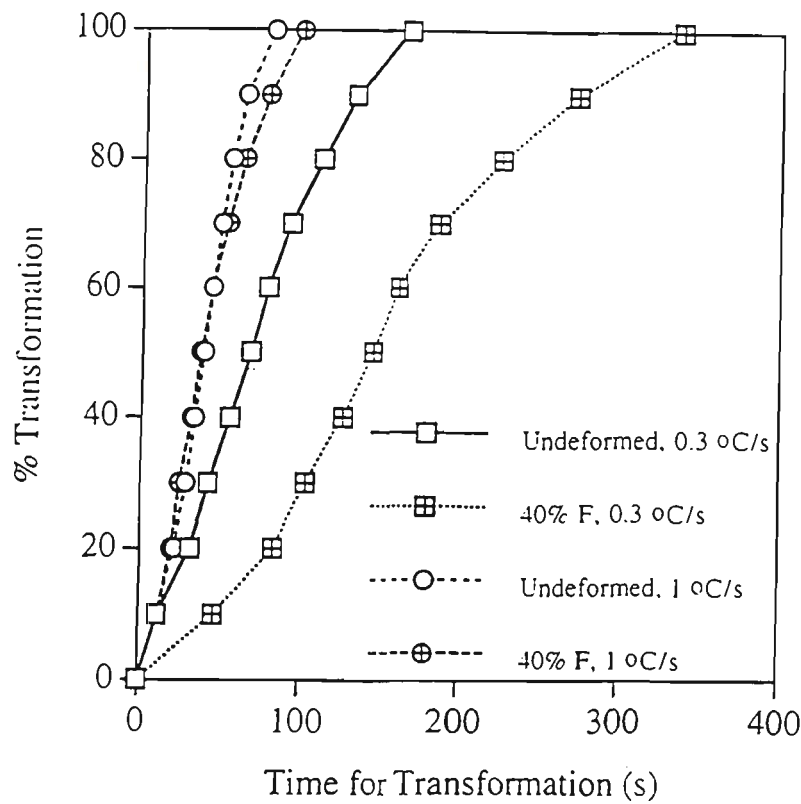
Figure 6.29: Effect of TMP on the progress of transformation in Grade 1A - Plate.
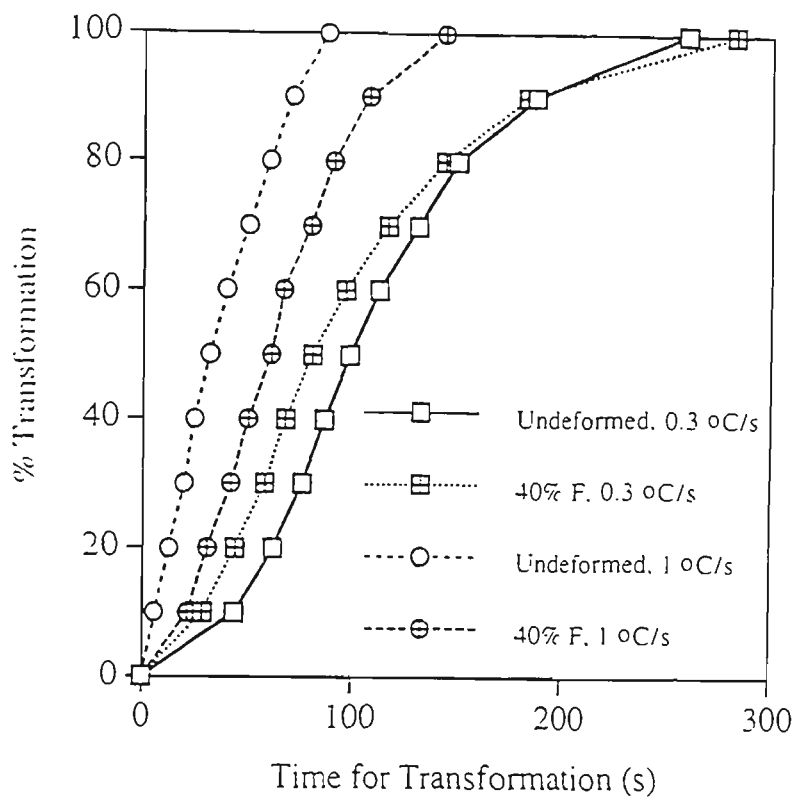
Figure 6.30: Effect of TMP on the progress of transformation in Grade 1 - Slab.
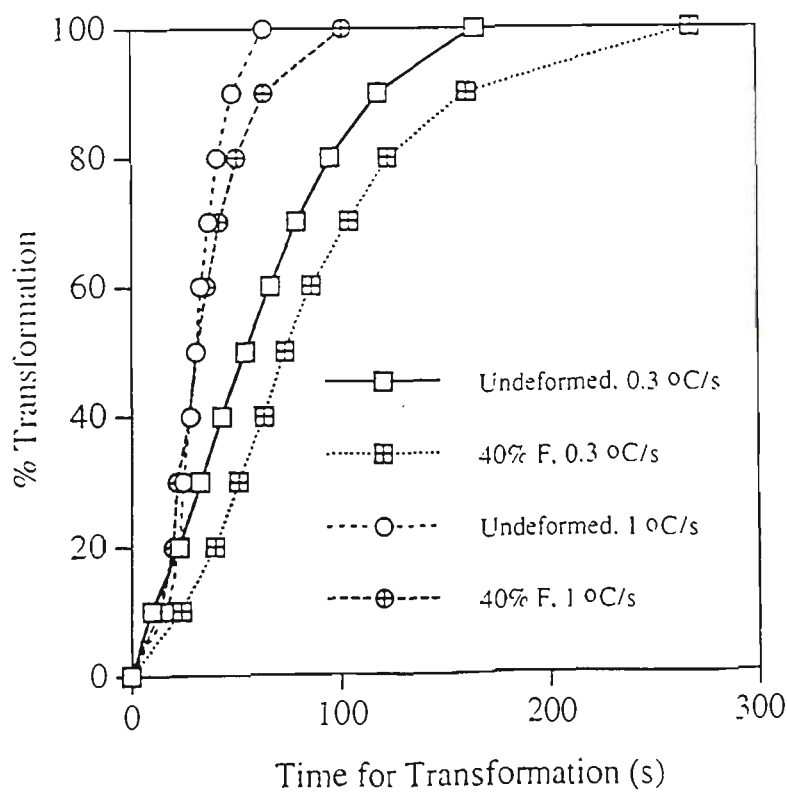
Figure 6.31: Effect of TMP on the progress of transformation in Grade 4 - Slab.

The Figs. 6.28 - 6.31 present the transformation kinetics of undeformed and deformed samples in all grades. It can be seen from Fig. 6.31 that the progress of transformation in deformed samples in Grade 4 - Slab is at least as rapid as that in undeformed samples until about 70% of the transformation is complete. However, it can be seen from Fig. 6.31 that the progress of the remaining 30% of the transformation requires considerably longer time in deformed samples as compared to undeformed ones. Similar observations can be made for other steels as shown in Figs. 6.28 - 6.30. Such direct experimental evidence lends support to the view that driving force for transformation decreases in TMP samples as the transformation progresses resulting in the net retardation of the transformation to reach completion as compared to undeformed samples.

6.3.2 Role of Increase in Nb Content on γ Transformation Kinetics

Effect of dissolved Nb on $\gamma \rightarrow \alpha$ transformation seems to be well established [155, 162, 244, 248 - 251]. Nb in solution is considered to retard the $\gamma \rightarrow \alpha$ transformation. Lee et al. [250] have suggested that solute Nb strongly segregates to γ / α phase boundary and reduces ferrite growth kinetics due to solute drag effect and thus lowers the Ar_3 temperature. However, quantitative relationship between solute Nb and the lowering of Ar_3 temperature is not in agreement. Abe et al. [248] found that Nb lowered Ar_3 at a rate of 30 °C per 0.01% dissolved Nb while Subramanian et al. [251] reported that Nb lowered Ar_3 at a rate of 10 °C per 0.01% dissolved Nb. In the present work, Ar_3 for Grade 1 - Plate (0.05% Nb) is found to be about 20 °C lower than that of Grade 1A - Plate (0.03% Nb) in undeformed samples (Fig. 6.2) suggesting that dissolved Nb lowers Ar_3 at a rate of ~ 10 °C per 0.01% solute Nb.

Role of Nb precipitates on $\gamma \rightarrow \alpha$ transformation is two fold. On one hand, precipitation of Nb in austenite can accelerate $\gamma \rightarrow \alpha$ transformation because these precipitates act as nucleation sites for $\gamma \rightarrow \alpha$ transformation and thus raise the Ar_3 temperature [155, 162, 249]. Other consequence of Nb precipitation in austenite is that less amount of Nb is left in solution, which decreases austenite hardenability and promotes the occurrence of $\gamma \rightarrow \alpha$ transformation. On the other hand, precipitation of Nb in austenite during transformation can retard the progress of transformation by pinning the interphase interface [177, 247, 251].

The data given in Fig. 6.2 indicate that Ar_3 of Grade 1 - Plate is lower than that for Grade 1A - Plate in undeformed condition, but Ar_3 for Grade 1 is higher than that for Grade 1A in deformed samples. Grade 1 contains higher Nb compared to Grade 1A and it is likely that relatively more precipitation of NbCN in Grade 1 would raise Ar_3 temperature in deformed state. Results indicate that the progress of transformation is more sluggish in Grade 1 as compared to Grade 1A in undeformed as well as in deformed condition (Fig. 6.5). As discussed earlier, whether Nb is in solution (undeformed state) or Nb is present as strain induced precipitates (deformed state) - both have the same effect of retarding the progress of $\gamma \rightarrow \alpha$ transformation. Thus, Grade 1 with its higher Nb content exhibits sluggish transformation kinetics as compared to Grade 1A once the transformation is initiated.

6.3.3 Influence of Mn Addition on $\gamma \rightarrow \alpha$ Transformation

It is well known that Mn dissolves in austenite and increases the hardenability of austenite as shown by its effect on the isothermal transformation diagrams. In the

context of microalloyed steels, it has been suggested that an increase in Mn content delays the precipitation of Ti [170] and Nb [70, 75] in austenite. Mn lowers the Ar_3 temperature [180, 252, 253] and suppresses or delays the $\gamma \rightarrow \alpha$ transformation [78, 162, 180, 254]. Results of the current work show that Mn lowers the Ar_3 temperature of microalloyed steels in undeformed as well as deformed condition (Fig. 6.3). Furthermore, it is found that the time of transformation for Grade 1 - Slab (1.66% Mn) is longer as compared to Grade 4 - Slab (1.07% Mn) in undeformed and deformed conditions which suggests that $\gamma \rightarrow \alpha$ transformation is retarded by a higher Mn content (Fig. 6.6). Mn exerts a significant influence on the CCT diagrams (Fig. 6.21 - 6.25). Polygonal ferrite and pearlite noses are shifted towards right (i. e. towards slower cooling rates) which indicates increased hardenability of microalloyed steels due to the addition of Mn. Increased hardenability of austenite results in austenite transformation to Widmanstatten (B_3^P) or granular bainitic (B_3^{m-a}) microstructures instead of ferrite - pearlite at slower cooling rates.

6.3.4 Effect of Accelerated Cooling on Austenite Transformation

Role of accelerated cooling on $\gamma \rightarrow \alpha$ transformation and ferrite grain refinement has been summarised by DeArdo [255]. Increased cooling rate decreases Ar_3 (Fig. 6.1) and accelerates the progress of transformation (Fig. 6.4). It has been suggested that increase in cooling rate increases transformation rate due to two main reasons: a) Ar_3 and temperature range for transformation is pushed towards lower temperatures, which increases undercooling ($\Delta T = Ac_3 - Ar_3$) and hence increases the nucleation rate; and b) low temperature transformation promotes intragranular nucleation [248]. Another reason could be that increased cooling rate decreases the amount of pro-eutectoid ferrite

that can form during transformation (because of suppression of growth rate of ferrite) and as a consequence the time of transformation is reduced. The data in Table 6.2 shows that increased cooling rate increases the bainite fraction (i.e. decreases the amount of ferrite content) in the microstructure in all steels as can be seen from the micrographs in Figs. 6.7 - 6.10.

6.3.5 Effect of TMP on CCT Diagrams

Comparison of CCT diagrams for undeformed and deformed samples shows that the onset of $\gamma \rightarrow \alpha$ transformation is accelerated in TMP samples. The $\gamma \rightarrow \alpha$ transformation begins at a higher temperature, progresses over a wider transformation range and occurs even at faster cooling rates (ferrite nose is shifted towards left) in deformed samples. For example, ferrite nose is shifted from 1 °C/s in undeformed samples of Grade 1 - Plate up to 10 °C/s in the deformed samples.

Various effects of TMP such as austenite grain refinement, increase in S_v, strain induced microalloy precipitation and the consequent loss of microalloying elements due to precipitation in austenite, ultimately result in promoting the $\gamma \rightarrow \alpha$ transformation and also decrease in the hardenability of TMP austenite. As a result, hardness of deformed samples is found to be lower than that of undeformed samples at similar cooling rates (Figs. 6.26 and 6.27). It seems that while the TMP has the advantage of refining the ferrite grain size resulting in tougher steels but the subsequent disadvantage could be the loss in hardness due to decreased hardenability. However, this situation can be dealt with by utilising the fact that TMP samples exhibit a wider transformation range as found in this work. Hence for a given hardenability, as decided by the steel composition

and TMP variables, it is possible to design an appropriate cooling schedule to generate multiphase microstructures. An alternative way of compensating for the loss of hardenability could be the addition of Mn. This would compensate for the loss in hardness and at the same time retain the advantage gained by ferrite grain refinement due to the TMP.

6.4 Conclusions

Effects of TMP, accelerated cooling and composition on Ar_3 temperature, transformation kinetics, CCT diagrams and microhardness can be summarised as given below:

1. TMP accelerates the onset of $\gamma \rightarrow \alpha$ transformation (raises Ar_3), but retards the progress of transformation.

2. Addition of Nb lowers the Ar_3 in undeformed state but raises it in deformed state and retards the progress of transformation in undeformed as well as deformed state.

3. Addition of Mn lowers Ar_3 and retards the progress of transformation in undeformed as well as deformed state.

4. Increase in cooling rate lowers the Ar_3 and accelerates the progress of transformation in undeformed as well as deformed state.

5. Effect of TMP on CCT diagrams of the steels studied shows that:

$\gamma \rightarrow \alpha$ transformation is raised to higher temperatures indicating decreased hardenability,

ferrite transformation nose is shifted towards faster cooling rates (towards left); and

$\gamma \rightarrow \alpha$ transformation occurs over a wider temperature range indicating retardation of the progress of transformation.

6. Addition of Mn increases the hardness of undeformed and deformed samples through its effect of increasing the hardenability of microalloyed austenite which promotes austenite transformation to Widmanstatten (B_3^P) or granular bainitic (B_3^{m-a}) microstructures instead of polygonal ferrite - pearlite microstructure.

7. TMP and the addition of Mn refines ferrite grain size significantly. While the effect of accelerated cooling of phase transformation and kinetics is substantial, its effect on ferrite grain refinement is found to be marginal in TMP samples for the range of cooling rates studied.

8. Various effects of TMP such as austenite grain refinement, increase in S_v, (strain induced) microalloy precipitation and the consequent loss of microalloying elements due to precipitation in austenite, ultimately result in promoting the $\gamma \rightarrow \alpha$ transformation and a decrease in the hardenability of TMP austenite. As a consequence, hardness of deformed samples is found to be lower than that of undeformed samples at similar cooling rates.

Chapter 7:   General Conclusions and Future Work

7.1 Introduction

In the preceding chapters grain growth during reheating and phase transformation behaviour of austenite during continuous cooling in Ti-Nb-Mn-Mo microalloyed steels in as-cast slab and as-rolled plate conditions has been reported. In the present chapter, the main conclusions from previous sections will be summarised; suggestions will then be made on future work on these alloys. This work has made contributions to overcome some of the inadequacies of the currently available methods of analysing and modelling the grain growth behaviour of austenite in microalloyed steels. CCT diagrams of the undeformed and thermomechanically processed Ti-Nb-Mn-Mo microalloyed steels have been generated for the first time. Such diagrams have several potential applications in the development of new technologies such as alloy design and product development, optimisation of the industrial controlled cooling processes, design of thermomechanical processing schedules and the development of expert systems incorporating metallurgical models.

7.2 General Conclusions

Grain Growth Behaviour of Austenite During Reheating in Ti-Nb-Mn-Mo Microalloyed Steels

The grain growth behaviour of austenite in microalloyed steels is significantly influenced not only by the composition but also the condition of microstructure before reheating. The important features can be summarised as follows:

1. GCT of microalloyed steels is significantly influenced by heterogeneity in initial austenite grain sizes. A high value of heterogeneity ratio (Z) lowers the GCT of a more highly microalloyed steel by as much as 50 - 100 °C.

2. Microstructure before reheating influences the $\alpha \rightarrow \gamma$ transformation which leads to differing values of Z in different steels. In slab steels, initial microstructure consisting of coarse ferrite and a small volume fraction of acicular ferrite + pearlite phases generates a high value of Z. Initial microstructure consisting of coarse and fine ferrite and a non-uniform distribution of pearlite (banding) results in a high value of Z in plate steels.

3. The expected low temperature abnormal grain growth due to initial size differences is found to be either insignificant or very sluggish in all of the microalloyed steels studied. This means that grains much larger than the mean grain size (3 to 7 times larger than the mean grain size) do not spontaneously start to grow abnormally. In an isochronal experiment, the reheating temperature must be greater than the GCT for such large sized grains to grow which subsequently leads to abnormal grain growth and duplex microstructure.

4. Grain coarsening behaviour of plate steels is significantly different than that of slab steels. Plate steels exhibit two stages of abnormal grain growth as against only one stage of accelerated grain growth exhibited by slab steels. Two stage coarsening in plate steels may be related to the coarsening and dissolution of two different types of microalloy precipitates observed in plate steels. Abnormal grain growth in plate steels is not as extensive as that observed in slab steels.

5. Calculated precipitate dissolution temperature provides a useful pointer in locating the GCT. The experimentally observed GCT can be higher or lower than the calculated precipitate dissolution temperature depending on other variables such as microstructure before reheating and heterogeneity in initial austenite grain sizes.

6. Although the conventional method of analysing mean grain size as a function temperature was able to detect the onset of abnormal grain growth but it could not detect the termination of abnormal grain growth in some cases in slab steels. Conventional method also failed to detect abnormal grain growth in both plate steels. The alternative metallographic technique developed in this work which consists of measuring the mean size of the largest grain as a function of temperature is found to be more effective and sensitive in detecting the onset and termination of abnormal grain growth in slab as well as plate steels.

Prediction of Grain Growth of Austenite During Reheating in Ti-Nb-Mn-Mo Microalloyed Steels

The observations regarding the mathematical modelling of grain growth of austenite in microalloyed steels can be summarised as follows:

1. Empirical models for predicting grain growth of austenite in C-Mn steels do not match very well with each other. Some empirical models for microalloyed steels are effective in predicting grain growth of austenite at lower temperatures, however, at higher temperatures, these models underestimate the grain sizes in Ti-microalloyed steels and overestimate the grain sizes in Nb-microalloyed steels.

2. Grain growth in **slab** steels can be predicted reasonably well at all temperatures using both mathematical models developed in this work. However, model based Gladman approach ($R_c = 0.17r/f$) overestimates the grain sizes in plate steels. New model based on the equation $R_c = 1.61r/(7.1\sqrt{\beta f})$ is found to be effective in predicting grain growth of austenite in slab as well as plate steels.

Effect of TMP on Transformation Behaviour of Microalloyed Austenite

1. TMP accelerates the onset of $\gamma \rightarrow \alpha$ transformation (raises Ar_3), but retards the progress of transformation.

2. Effect of TMP on CCT diagrams of the steels studied shows that:

- $\gamma \rightarrow \alpha$ transformation is raised to higher temperatures indicating decreased hardenability of austenite,

- ferrite transformation nose is shifted towards faster cooling rates (towards left); and

- $\gamma \rightarrow \alpha$ transformation occurs over a wider temperature range indicating retardation of the progress of transformation.

Influence of Composition and Accelerated Cooling on γ Transformation

1. Addition of Nb lowers the Ar_3 in undeformed state but raises it in deformed state and retards the progress of transformation in undeformed as well as deformed state.

2. Addition of Mn lowers Ar_3 and retards the progress of transformation in undeformed as well as deformed state.

3. Addition of Mn increases the hardness of undeformed and deformed samples through its effect of increasing the hardenability of microalloyed austenite which promotes austenite transformation to Widmanstatten (B_3^P) or granular bainitic microstructures (B_3^{m-a}) instead of polygonal ferrite - pearlite microstructure. On the other hand, increase in Nb content from 0.03% up to 0.06% is found to have no significant effect on the location of transformation noses in the CCT diagrams. Addition of Nb increases the hardness of undeformed and deformed austenite but its influence on hardness is not as significant as that of Mn addition.

4. Increase in cooling rate lowers the Ar_3 and accelerates the progress of transformation in undeformed as well as deformed state.

Combined Effects of TMP, Composition and Accelerated Cooling on γTransformation

1. TMP and the addition of Mn refines ferrite grain size significantly. While the effect of accelerated cooling of phase transformation and kinetics is substantial, its effect on ferrite grain refinement is found to be marginal in TMP samples.

2. Various effects of TMP such as austenite grain refinement, increase in S_v, (strain induced) microalloy precipitation and the consequent loss of microalloying elements due to precipitation in austenite, ultimately result in promoting the $\gamma \rightarrow \alpha$ transformation and a decrease in the hardenability of TMP austenite. As a

consequence, hardness of deformed samples is found to be lower than that of undeformed samples at similar cooling rates. Thus, while the TMP has the advantage of refining the ferrite grain size resulting in tougher steels, the consequent disadvantage could be the loss in hardness due to decreased hardenability. However, this situation can be dealt with by utilising the fact that TMP samples exhibit a wider transformation range. Thus, for given conditions of hardenability, as decided by the steel composition and TMP variables, it is possible to design an appropriate cooling schedule to generate multiphase microstructures. An alternative way of compensating for the loss of hardenability could be the addition of Mn in conjunction with accelerated cooling. This would compensate for the loss in hardness and at the same time retain the advantage gained by ferrite grain refinement due to the TMP.

7.3 Suggestions for Future Work

1. Experimental data on grain boundary mobility are scarce at the present time. Isothermal experiments at different temperatures could be carried out to find the effect of Nb and Mn contents on grain boundary mobility. Such data would be very useful in developing more precise mathematical models to predict the normal and abnormal grain growth of microalloyed austenite.

2. Quantitative electron microscopic analysis of microalloy precipitates at different reheating temperatures in plate steels may be conducted to investigate in more detail the two stage grain coarsening behaviour observed in plate steels.

3. While the effect of deformation on Ar_3 temperature is substantial, its effect on B_s and M_s temperatures appears to be less significant. Effect of strain on bainite transformation kinetics may be investigated further by systematic experimentation using deformation dilatometer. However, before this research is undertaken, it is important to identify clearly the specific type of bainite transformation product to be researched because several types of bainites may form during accelerated continuous cooling in high Mn microalloyed steel.

4. Other types of thermomechanical process simulations such as weld-thermal cycles, strip rolling etc. for these alloys may be undertaken to investigate the effects of higher rates of heating, cooling and straining on Ar_3 temperature, transformation products and kinetics, and CCT diagrams.

5. Effect of interrupted accelerated cooling on austenite transformation may be investigated with an objective of optimising the strip coiling process parameters.

6. The austenite transformation kinetics data generated in this work could be utilised for developing austenite transformation models in Ti-Nb-Mn-Mo microalloyed steels during continuous cooling conditions.

Appendix I

Relation Between G_o and M_o

Burke and Turnbull [13] postulated that the progress of normal grain growth is controlled by a parameter 'G' which is the linear rate of grain growth given by:

$$D = G (t-\tau) \tag{1}$$

where D is the grain diameter, t is total time for grain growth and τ is the incubation period before grain growth begins. In case of normal grain growth, all grains participate in the process and therefore nucleation period is unimportant. Further, $t \gg \tau$. Thus τ can be ignored.

$$\therefore D = Gt \tag{2}$$

Burke and Turnbull assumed further that 'G' to be independent of 't' and therefore G can represent the instantaneous rate of grain growth given by:

$$G = dD/ dt \tag{3}$$

Burke and Turnbull then postulated that 'G' depends on the temperature and composition of the material according to:

$$G = G_o \exp. (-Q/RT) \tag{4}$$

where Q is the activation energy for grain growth. Burke and Turnbull applied the reaction rate theory developed earlier by Mott [101] to arrive at:

$$G = \{2.72(kT/h)(2\lambda/RT)\exp. (\Delta S/R)\}(\sigma V_m/\rho) \exp. (-Q/RT) \tag{5}$$

Comparing Eq.s (4) and (5) -

$$G_o = \{2.72(kT/h)(2\lambda/RT) \exp. (\Delta S/R)\}(\sigma V_m/\rho)$$

Considering K" = $\{2.72(kT/h)(2\lambda/RT)\exp. (\Delta S/R)\}$ -

$$G_o = K" (\sigma V_m/\rho)$$

$$\therefore K" = \rho G_o / \sigma V_m \qquad (6)$$

Inserting K" in Eq.(5) and eliminating G from Eq. s (3) and (5) gives:

$$dD/dt = K" (\sigma V_m / \rho) \exp. (-Q/RT) \qquad (7)$$

Considering $\rho \cong D$, integrating Eq. (7) and rearranging the terms -

$$D^2 - D_o^2 = (2K"\sigma V_m) \{\exp. (-Q/RT)\} t \qquad (8)$$

Derivation of isothermal grain growth law using grain boundary mobility approach gives

the result after rearranging the terms:

$$D^2 - D_o^2 = [4\sigma M_o] \{\exp. (-Q/RT)\} t \qquad (9)$$

Comparing RHS of Eq.s (8) and (9) and substituting the value of K" from Eq. (6) -

$$4\sigma M_o = 2K"\sigma V_m = (2\sigma V_m)(\rho G_o / \sigma V_m)$$

$$\therefore M_o = \rho G_o / 2\sigma \cong D \quad G_o / 2\sigma \qquad (10)$$

This derived relationship was used to convert the G_o data reported by Burke and

Turnbull [13] to the values of M_o after substituting the appropriate values of the grain

diameters given in their report and taking the value of σ to be equal to 0.324 J/m^2 in the

case of Al [108] and 0.6 J/m^2 in case of α - brasses.

References

1. E. O. Hall: Proc. Phys. Soc. - Series B, 64, (1951), 747.

2. N. J. Petch: JISI, 174, (1953), 25.

3. F. B. Pickering: Physical Metallurgy and the Design of Steels, 1st ed., Applied Science Publishers Ltd., London, (1978), 16.

4. D. J. Blickwede: Met. Trans. ASM, 61, (1968), 653.

5. C. A. Siebert, D. V. Doane and D. H. Breen: The Hardenability of Steels - Concepts, Metallurgical Influences and Industrial Applications, ASM, (1977), 66.

6. R. W. Cahn and P. Haasen (ed.): Physical Metallurgy, 4th ed., vol. 3, North-Holland Publishing Co., Amsterdam, (1996), 1991.

7. V. L. Barnwell, J. R. Myers and R. K. Saxer: Corrosion, 22, (1966), 261.

8. B. C. Woodfine: JISI, 173, (1953), 240.

9. J. M. Capus: JISI, 200, (1962), 922.

10. Metals Handbook: Vol. 1, 10th ed., Properties and Selection: Irons, Steels and High-Performance Alloys, ASM, (1990), 681.

11. F. J. Humphreys and M. Hatherly: Recrystallization and Related Annealing Phenomena, 1st ed., Elsevier Science Ltd., Oxford, UK, (1995), 408.

12. C. S. Pande and S. P. Marsh: J. of Mat., 44, No. 9, (1992), 25.

13. J. E. Burke and D. Turnbull: Progress in Metal Physics, 3, (1954), 220.

14. O. Hunderi and N. Ryum: Acta Metall., 30, (1982), 739.

15. S. K. Kurtz and F. M. A. Carpay: J. Appl. Phys., 51, (1980), 5725.

16. D. Harker and E. R. Parker: Trans. ASM, 34, (1945), 156.

17. O. O. Miller: Trans. ASM, 43, (1951), 260.

18. M. Hillert: Acta Metall., 13, (1965), 227.

19. T. Gladman: Proc. Royal Soc., London, A294, (1966), 298.

20. C. Zener: as quoted by C. S. Smith, Trans. AIME, 175, (1948), 15.

21. C. G. Dunn and P. K. Koh: Trans. Met. Soc. AIME, 206, (1956), 1017.

22. G. T. Higgins: Metal Sci. J., 8, (1974), 143.

23. P. A. Beck, J. C. Kremer, L. J. Demer and M. L. Holzworth: Trans. Met. Soc. AIME, 175, (1948), 372.

24. J. E. Palmer, C. V. Thompson and H. J. Smith: J. Appl. Phys., 62, (1987), 2492.

25. T. Tanaka, T. Funakoshi, M. Ueda, J. Tsuboi, T. Yasuda and C. Utahashi: Proc. of Int. Symp. on Microalloying '75, Union Carbide Corp., Washington D. C., (1975), 399.

26. L. J. Cuddy: Met. Trans. ASM, 15A, (1984), 87.

27. F. J. Humphreys and M. Hatherly: Recrystallization and Related Annealing Phenomena, 1st ed., Elsevier Science Ltd., Oxford, UK, (1995), 283.

28. Z. Jeffries: Trans. Met. Soc. AIME, 56, (1916), 571.

29. C. G. Dunn and J. L. Walter: Recrystallization, Grain Growth and Textures, ASM, Ohio, (1966), 461.

30. R. W. Cahn and P. Haasen (ed.): Physical Metallurgy, 4th ed., vol. 3, North Holland Publishing Co., Amsterdam, (1996), 2482.

31. M. Avrami: J. Chem. Phys., 7, (1939), 1103.

32. F. D. Rosi, B. H. Alexander and C. A. Dube: Trans. Met. Soc. AIME, 194, (1952), 189.

33. D. J. Srolovitz, G. S. Grest and M. P. Anderson, Acta Metall., 33, (1985), 2233.

34. C. V. Thompson, H. J. Frost and F. Spaepen: Acta Metall., 35, (1987), 887.

35. T. Gladman: J. of Mater., 44, No. 2, (1992), 21.

36. V. Y. Novikov: Scripta Metall., 34, (1996), 685.

37. ASTM E: 112 - 88, Annual Book of ASTM Standards, vol. 03.01, (1993), 318.

38. Metals Handbook: Vol. 9, 9th ed., Metallography and Microstructures, ASM, (1985), 170.

39. R. Riedl: Metallography, 14, (1981), 119.

40. W. C. Leslie: The Physical Metallurgy of Steels, 1st ed., McGraw Hill, London, (1981), 251.

41. A. Brownrigg, P. Curcio and R. Boelen: Metallography, 8, (1975), 529.

42. G. H. Akbari, C. M. Sellars and J. A. Whiteman: Mater. Sci. Technol., 11, (1995), 1261.

43. M. J. Godden, L. E. Collins and J. D. Boyd: Proc. of Int. Conf. on HSLA Steels, ed. by D. P. Dunne and T. Chandra, Wollongong, Australia, (1984), 113.

44. P. A. Manohar, D. P. Dunne and T. Chandra: Proc. of 4th Japan Int. SAMPE Symp., ed. by Z. Maekawa et al., Tokyo, (1995), 1431.

45. P. A. Manohar, T. Chandra and D. P. Dunne: Proc. 3rd Int. Conf. on Recrystallization and Related Phenomena, "ReX 96", Oct. 21 - 24, 1996, Monterey, California, ed. by T. R. McNelly, 445.

46. T. Gladman and F. B. Pickering: JISI, 205, (1967), 653.

47. P. R. Rios: Acta Metall., 40, (1992), 649.

48. E. J. Palmiere, C. I. Garcia and A. J. DeArdo: Met. Trans. ASM, 25A, (1994), 277.

49. T. George and J. J. Irani: J. Aust. Inst. of Metals, 13, (1968), 94.

50. B. Feng: Ph. D. Thesis, University of Wollongong, 1990.

51. T. Gladman: Iron Making and Steel Making, 16, (1989), 241.

52. T. Gladman, I. D. McIver and F. B. Pickering: JISI, 209, (1971), 380.

53. L. Erasmus: JISI, 202, (1964), 32.

54. L. Erasmus: JISI, 202, (1964), 128.

55. D. Webster and G. B. Allen: JISI, 200, (1962), 520.

56. T. Siwecki, S. Zajac and G. Engberg: Proc. of 37th Mechanical Working and Steel Processing Conf., vol. XXXIII, ISS, Hamilton, Canada, (1995), 635.

57. G. Sheard and J. Nutting: Metal Sci. J., (1979), 131.

58. H. Tamehiro and H. Nakasugi: Trans. ISIJ, 25, (1985), 311.

59. K. J. Irvine, F. B. Pickering and T. Gladman: JISI, 205, (1967), 161.

60. K. Narita: Trans. ISIJ, 15, (1975), 145.

61. K. Balasubramanian and J. S. Kirkaldy: Can. Met. Quart., 28, (1989), 301.

62. H. Nordberg and B. Aronsson: JISI, 206, (1968), 1263.

63. V. K. Lakshmanan and J. S. Kirkaldy: Met. Trans. ASM, 15A, (1984), 541.

64. P. D. Hodgson and R. K. Gibbs: ISIJ Int., 32, (1992), 1329.

65. S. Matsuda and N. Okumura: Trans. ISIJ, 18, (1978), 198.

66. W. Roberts: Proc. Int. Conf. on HSLA Steels: Technology and Applications, ASM, (1983), 33.

67. H. Wada and B. Pehlke: Met. Trans. B, 16B, (1985), 815.

68. J. Kunze: Metal Sci. J., 16, (1982), 217.

69. H. Ohtani and M. Hillert: CALPHAD, 15, (1991), 25.

70. M. G. Akben, I. Weiss and J. J. Jonas: Acta Metall., 29, (1981), 111.

71. P. R. Rios: Mater. Sci. Technol., 4, (1988), 324.

72. B. Dutta and C. M. Sellars: Mater. Sci. Technol., 3, (1987), 197.

73. R. A. Swalin: Thermodynamics of Solids, 2nd ed., John Wiley & Sons, New York, (1972), 180.

74. S. S. Hansen, J. B. Vander Sande and M. Cohen: Met. Trans. ASM, 11A, (1980), 387.

75. L. Xiuqiu and C. Wenxuan: Proc. Int. Conf. on HSLA Steels: Metallurgy and Applications, ed. by J. M. Gray et al., Beijing, (1985), 235.

76. S. Koyama: J. Japan Inst. of Metals, 52, (1972), 1090.

77. B. Bacroix, M. G. Akben and J. J. Jonas: Proc. Int. Conf. on Thermomechanical Processing of Microalloyed Austenite, ed. by A. J. DeArdo et al., Pittsburgh, TMS, (1981), 293.

78. T. G. Oakwood, A. P. Coldren and K. Miyano: Proc. Int. Conf. on HSLA Steels: Metallurgy and Applications, ed. by J. M. Gray et al., Beijing, (1985), 715.

79. D. C. Houghton, G. C. Weatherly and J. D. Embury: Proc. Int. Conf. on Thermomechanical Processing of Microalloyed Austenite, ed. by A. J. DeArdo et al., Pittsburgh, TMS, (1981), 267.

80. A. Guth, L. Kaun, A. Kothe, D. Muller and J. Richter: Scripta Met., 21, (1987), 163.

81. S. Suzuki, G. C. Weatherly and D. C. Houghton: Acta Metall., 35, (1987), 341.

82. R. C. Peterson: Ph. D. Thesis, Monash University, Clayton, Victoria, Australia, (1994), 46.

83. C. S. Smith: Metal Interfaces, ASM, (1952), 65.

84. O. Hunderi and N. Ryum: J. Mater. Sci., 15, (1980), 1104.

85. H. V. Atkinson: Acta Metall., 36, (1988), 469.

86. P. Peltham: Acta Metall., 5, (1957), 97.

87. N. P. Louat: Acta Metall., 22, (1974), 721.

88. F. N. Rhines and K. R. Craig: Met. Trans. ASM, 5, (1974), 413.

89. K. Lucke, G. Abruzzese and I. Hecklemann: Proc. of Int. Conf. on Recrystallization '90, ed. by T. Chandra, TMS, Wollongong, Australia, (1990), 37.

90. V. Y. Novikov: Acta Metall., 26, (1978), 1739.

91. E. A. Ceppi and O. B. Nasello: Scripta Met., 18, (1984), 1221.

92. D. Weaire and J. P. Kermode: Phil. Mag., B48, (1983), 245.

93. M. P. Anderson, G. S. Grest, D. J. Srolovitz and P. S. Sahni: Acta Metall., 32, (1984), 783.

94. H. Telley, Th. M. Liebling and A. Mocellin: Proc. of 7th Int. Riso Symp. on Metallurgy and Materials Science, Riso, Roskilde, Denmark, (1986), 573.

95. F. J. Humphreys and M. Hatherly: Recrystallization and Related Annealing Phenomena, 1st ed., Elsevier Science Ltd., Oxford, UK, (1995), 298.

96. J. E. Burke: Trans. Met. Soc. AIME, 180, (1949), 73.

97. F. J. Humphreys and M. Hatherly: Recrystallization and Related Annealing Phenomena, 1st ed., Elsevier Sci. Ltd., Oxford, UK, (1995), 286.

98. ibid., 299.

99. P. A. Manohar and T. Chandra: ISIJ Int., 37, (1997), 726.

100. D. Turnbull: Trans. AIME, 191, (1951), 661.

101. N. F. Mott: Proc. Phys. Soc., 60, (1948), 391.

102. T. Nishizawa: Tetsu-to-Hagane, 70, (1984), 1984.

103. A. Yoshie, M. Fujioka, Y. Watanabe, K. Nishioka and H. Morikawa: ISIJ Int., 32, (1992), 395.

104. S. Bjorklund and M. Hillert: Metal Sci. J., 9, (1975), 127.

105. C. M. Sellars and J. A. Whiteman: Metal Sci. J., 13, (1979), 187.

106. F. J. Humphreys and M. Hatherly: Recrystallization and Related Annealing Phenomena, 1st ed., Elsevier Sci. Ltd., Oxford, UK, (1995), 96.

107. J. E. Burke: J. Appl. Phys., 18, (1947), 1028.

108. F. J. Humphreys and M. Hatherly: Recrystallization and Related Annealing Phenomena, 1st ed., Elsevier Sci. Ltd., Oxford, UK, (1995), 92.

109. M. P. Anderson and O. Grong: Acta Mater., 43, (1995), 2673.

110. I. M. Lifshitz and V. V. Slyozov: J. Phys. Chem. Solids, 19, (1961), 35.

111. R. E. Reed-Hill and R. Abbaschian: Physical Metallurgy Principles, 3rd ed., PWS-Kent Publishing Co., USA, (1992), 262.

112. E. Nes, N. Ryum and O. Hunderi: Acta Metall., 33, (1985), 11.

113. M. F. Ashby, J. Harper and J. Lewis: Trans. Met. Soc. AIME, 245, (1969), 413.

114. R. D. Doherty: Metal Sci. J., 16, (1982), 1.

115. N. Ryum, O. Hunderi and E. Nes: Scripta Met., 17, (1983), 1281.

116. S. P. Ringer, W. B. Li and K. E. Easterling: Acta Metall., 37, (1989), 831.

117. N. A. Haroun and D. W. Budworth: J. Matls. Sci., 3, (1968), 326.

118. R. L. Fullman: Metal Interfaces, ASM, (1952), 179.

119. K. G. Wold and F. M. Chambers: J. Aust. Inst. of Metals, 13, (1968), 79.

120. P. M. Hazzledine, P. B. Hirsch and N. Louat: Proc. 1st Int. Symp. on Metallurgy and Materials Science, "Recrystallization and Grain Growth of Multi-Phase and Particle Containing Materials", ed. by N. Hansen et al., Riso National Lab, Riso, Roskilde, Denmark, (1980), 159.

121. O. Hunderi, E. Nes and N. Ryum: Acta Metall., 37, (1989), 129.

122. N. Louat: Acta Metall., 30, (1982), 1291.

123. H. M. Chan and F. J. Humphreys: Acta Metall., 32, (1984), 235.

124. P. Hellman and M. Hillert: Scand. J. Metals, 4, (1975), 211.

125. B. R. Patterson and Y. Liu: Met. Trans. ASM, 23A, (1992), 2481.

126. J-H Han and D-Y Kim: Acta Metall., 43, (1995), 3185.

127. R. Elst, J. Van Humbeeck and L. Delaey: Acta Metall., 36, (1988), 1723.

128. C. J. Tweed, N. Hansen and B. Ralph: Met. Trans. ASM, 14A, (1983) 2235.

129. L. Anand and J. Gurland: Met. Trans. ASM, 6A, (1975), 928.

130. J. D. L'Ecuyer and G. L'Esperance: Acta Metall., 37, (1989), 1023.

131. P. P. Sinha, K. Sreekumar, A. Natarajan and K. V. Nagarajan: J. Mater. Sci., 26, (1991), 4155.

132. R. H. Palma, V. Martinez and J. J. Urcola: Powder Met., 32, No. 4, (1989), 291.

133. N. E. Hannerz and F. de Kazinczy: JISI, 208, (1970), 475.

134. Y. Saito and M. Enomoto: ISIJ Int., 32, (1992), 267.

135. W. J. Liu and J. J. Jonas: Proc. Int. Symp. on Physical Metallurgy and Thermomechanical Processing of Steels and Other Metals, "Thermec '88", ed. by I. Tamura, ISIJ, Tokyo, (1988), 90.

136. T. Gladman: Heat Treatment of Metals, 1994.1, (1994), 11.

137. G. T. Grewal and J. Ankem: Acta Metall., 38, (1990), 1607.

138. C. H. Worner and P. M. Hazzledine: J. of Metals, 44, No. 2, (1992), 16.

139. P. R. Rios: Acta Metall., 35, (1987), 2805.

140. W. J. Liu and J. J. Jonas: Proc. Int. Symp. on Processing, Microstructure and Properties of HSLA Steels, ed. by A. J. DeArdo, Pittsburgh, TMS, (1987), 39.

141. A. J. DeArdo: Proc. of Int. Conf. on Microalloying '95, ed. by M. Korchynsky et al., ISS, Pittsburgh, (1995), 15.

142. M. Korchynsky: Proc. of Int. Conf. on Processing, Microstructure and Properties of HSLA Steels, ed. by A. J. DeArdo, TMS, Pittsburgh, (1987), 169.

143. E. E. Underwood: Quantitative Stereology, Addison - Wesley Publishing Co., Massachusetts, (1970), 30.

144. I. Kozasu, C. Ouchi, T. Sampei and T. Okita: Proc. of Int. Symp. on Microalloying '75, Union Carbide Corp., Washington D. C., (1975), 120.

145. L. J. Cuddy, J. J. Bauwin and J. C. Raley: Met. Trans. ASM, 11A, (1980), 381.

146. A. J. DeArdo: Proc. of Int. Conf. on HSLA Steels '95, ed. by L. Guoxun et al., CSM, Beijing, China, (1995), 99.

147. T. Siwecki, B. Hutchinson and S. Zajac: Proc. of Int. Conf. on Microalloying '95, ed. by M. Korchynsky et al., ISS, Pittsburgh, (1995), 197.

148. E. V. Pereloma and J. D. Boyd: Mater. Sci. Technol., 12, (1996), 808.

149. Y. Matsumura and H. Yada: Trans. ISIJ, 27, (1987), 492.

150. M. K. Graf, H. -G. Hillenbrand and P. A. Peters: Proc. of Int. Symp. on Accelerated Cooling of Steel, ed. by P. D. Southwick, Pittsburgh, (1987), 165.

151. W. Mueschenborn, K. -P. Imlau, L. Meyer and U. Schriver: Proc. of Int. Conf. on Microalloying '95, ed. by M. Korchynsky et al., ISS, Pittsburgh, (1995), 35.

152. O. Kwon and A. J. DeArdo: Proc. of Int. Conf. on Processing, Microstructure and Properties of HSLA Steels, ed. by A. J. DeArdo, TMS, Pittsburgh, (1987), 63.

153. A. A. Zadeh and D. P. Dunne: Proc. of Int. Conf. on HSLA Steels '95, ed. by L. Guoxun et al., CSM, Beijing, China, (1995), 157.

154. H. Tamehiro, R. Habu, N. Yamada, H. Matsuda and M. Nagumo: Proc. of Int. Symp. on Accelerated Cooling of Steel, ed. by P. D. Southwick, Pittsburgh, (1987), 401.

155. L. Meyer, C. Straßburger and C. Schneider: Proc. of Int. Conf. on HSLA Steels: Metallurgy and Applications, ed. by J. M. Gray et al., CSM, Beijing, China, (1985), 29.

156. P. S. Mitchell, P. H. M. Hart and W. B. Morrison: Proc. of Int. Conf. on Microalloying '95, ed. by M. Korchynsky et al., ISS, Pittsburgh, (1995), 149.

157. J. L. Albarran, B. Campillo, F. Estevez and L. Martinez: Scripta Met., 23, (1989), 1099.

158. M. Korchynsky: Proc. of Int. Conf. on Microalloying '95, ed. by M. Korchynsky et al., ISS, Pittsburgh, (1995), 3.

159. S. H. Park, K. S. Ro and O. Kwon: Proc. of Int. Symp. on Low Carbon Steels for the 90's, ed. by R. Asfahani and G. Tither, TMS, Pittsburgh, (1993), 355.

160. J. L. Lee and Y. T. Pan: Mater. Sci. Technol., 8, (1992), 236.

161. C. Ouchi: Proc. of Int. Conf. on HSLA Steels, ed. by D. P. Dunne and T. Chandra, Wollongong, Australia, (1984), 17.

162. L. Meyer, F. Heisterkamp and W. Muescenborn: Proc. of Int. Symp. on Microalloying '75, Union Carbide Corp., Washington D. C., (1975), 153.

163. S. Kurokawa, J. E. Ruzzante, A. M. Hey and T. Dyment: Metal Sci. J., 17, (1983), 433.

164. J. G. Williams, C. R. Killmore, F. J. Barbaro, A. Meta and L. Fletcher: Proc. of Int. Conf. on Microalloying '95, ed. by M. Korchynsky et al., ISS, Pittsburgh, (1995), 117.

165. S. F. Medina and J. E. Mancilla: ISIJ Int., 36, (1996), 1070.

166. J. G. Speer and S. S. Hansen: Met. Trans. ASM, 20A, (1989), 25.

167. D. Q. Bai, S. Yue, W. P. Sun and J. J. Jonas: Met. Trans. ASM, 24A, (1993), 2151.

168. R. W. K. Honeycombe: Trans. ISIJ, 20, (1980), 139.

169. M. Djahazi, X. L. He, J. J. Jonas and W. P. Sun: Met. Trans. ASM, 23A, (1992), 2111.

170. Z. Hongtao: Proc. of Int. Conf. on Microalloying '95, ed. by M. Korchynsky et al., ISS, Pittsburgh, (1995), 61.

171. S. F. Medina and J. E. Mancilla: Scripta Met., 30, (1994), 73.

172. S. F. Medina and J. E. Mancilla: ISIJ Int., 36, (1996), 1063.

173. T. V. Floros, A. A. Macchione and M. G. Akben: Proc. of Int. Conf. on HSLA Steels, ed. by D. P. Dunne and T. Chandra, Wollongong, Australia, (1984), 92.

174. W. B. Pearson: Handbook of Lattice Spacings and Structures of Metals and Alloys, Vol. 2, Pergmon Press, Oxford, England, (1967), 455.

175. B. Feng, T. Chandra and D. P. Dunne: Materials Forum, 13, (1989), 139.

176. J. J. Jonas and I. Weiss: Metal Sci. J., 13, (1979), 238.

177. R. W. K. Honeycombe: Proc. of Int. Conf. on HSLA Steels: Metallurgy and Applications, ed. by J. M. Gray et al., CSM, Beijing, China, (1985), 243.

178. I. Weiss and J. J. Jonas: Met. Trans. ASM, 11A, (1980), 403.

179. E. Valdes and C. M. Sellars: Mater. Sci. Technol., 7, (1991), 622.

180. R. W. K. Honeycombe: Proc. of Int. Conf. on Processing, Microstructure and Properties of HSLA Steels, ed. by A. J. DeArdo, TMS, Pittsburgh, (1987), 1.

181. I. Weiss and J. J. Jonas: Met. Trans. ASM, 10A, (1979), 831.

182. R. Smith, D. Dunne and T. Chandra: Proc. Int. Symp. on Physical Metallurgy and Thermomechanical Processing of Steels and Other Metals, "Thermec '88", ed. by I. Tamura, ISIJ, Tokyo, (1988), 275.

183. E. J. Palmiere: Proc. of Int. Conf. on Microalloying '95, ed. by M. Korchynsky et al., ISS, Pittsburgh, (1995), 307.

184. S. Okaguchi and T. Hashimoto: ISIJ Int., 32, (1992), 283.

185. N. L. Zou and J. S. Kirkaldy: Met. Trans. ASM, 22A, (1991), 1511.

186. C. Roucoules, S. Yue and J. J. Jonas: Met. Trans. ASM, 26A, (1995), 181.

187. W. J. Liu and J. J. Jonas: Met. Trans. ASM, 20A, (1989), 689.

188. O. Kwon and A. J. DeArdo: Acta Metall., 39, (1991), 529.

189. L. J. Cuddy: Proc. of Int. Conf. on Thermomechanical Processing of Microalloyed Austenite, ed. by A. J. DeArdo et al., AIME, (1982), 129.

190. L. J. Cuddy: Met. Trans. ASM, 12A, (1981), 1313.

191. J. G. Speer, J. R. Michael and S. S. Hansen: Met. Trans. ASM, 18A, (1987), 211.

192. D. Q. Bai, S. Yue, T. Maccagno and J. J. Jonas: ISIJ Int., 36, (1996), 1084.

193. X. Liu, J. K. Solberg, R. Gjengedal and A. O. Kluken: Mater. Sci. Technol., 11, (1995), 469.

194. M. J. Luton, R. Dorvel and R. A. Petkovic: Met. Trans. ASM, 11A, (1980), 411.

195. S. F. Medina: Scripta Met., 32, (1995), 43.

196. R. Barbosa, F. Boratto, S. Yue and J. J. Jonas: Proc. of Int. Conf. on Processing, Microstructure and Properties of HSLA Steels, ed. by A. J. DeArdo, TMS, Pittsburgh, (1987), 51.

197. T. M. Maccagno, J. J. Jonas, S. Yue, B. J. McCrady, R. Slobodian and D. Deeks: ISIJ Int., 34, (1994), 917.

198. J. Majta, J. G. Lenard and M. Pietrzyk: ISIJ Int., 36, (1996), 1094.

199. S. F. Medina and J. E. Mancilla: ISIJ Int., 36, (1996), 1077.

200. F. G. Arieta and C. M. Sellars: Proc. of Int. Symp. on Low Carbon Steels for the 90's, ed. by R. Asfahani and G. Tither, TMS, Pittsburgh, (1993), 101.

201. E. J. Palmiere, C. I. Garcia and A. J. DeArdo: Met. Trans. ASM, 27A, (1996), 951.

202. J. S. Kirkaldy, B. A. Thomson and E. A. Baganis: Proc. of Int. Symp. on Hardenability Concepts with Applications to Steels, ed. by D. V. Doane and J. S. Kirkaldy, Met. Soc. AIME, Chicago, (1978), 82.

203. C. Fossaert, G. Rees, T. Maurickx and H. K. D. H. Bhadeshia: Met. Trans. ASM, 26A, (1995), 21.

204. B. Garbarz and F. B. Pickering: Mater. Sci. Technol., 4, (1988), 967.

205. O. Kwon, K. J. Lee, J. K. Lee, K. B. Kang, J. K. Kim, J. D. Lee and J. Kim: Proc. of Int. Conf. on HSLA Steels '95, ed. by L. Guoxun et al., CSM, Beijing, China, (1995), 82.

206. J. R. Bradley and H. I. Aaronson: Met. Trans. ASM, 12A, (1981), 1729.

207. M. Enomoto, N. Nojiri, and Y. Sato: Mater. Trans. JIM, 35, (1994), 859.

208. E. A. Simielli, S. Yue and J. J. Jonas: Met. Trans. ASM, 23A, (1992), 597.

209. I. Kozasu: Proc. of Int. Conf. on Microalloying '95, ed. by M. Korchynsky et al., ISS, Pittsburgh, (1995), 95.

210. C. M. Sellars: Proc. of Int. Conf. on HSLA Steels: Metallurgy and Applications, ed. by J. M. Gray et al., CSM, Beijing, China, (1985), 73.

211. I. Tamura: Trans. ISIJ, 27, (1987), 763.

212. M. Umemoto, Z. H. Guo and I. Tamura: Mater. Sci. Technol., 3, (1987), 249.

213. M. Umemoto, I. Tamura and Z. H. Guo: Proc. of Int. Conf. on HSLA Steels: Metallurgy and Applications, ed. by J. M. Gray et al., CSM, Beijing, China, (1985), 97.

214. C. I. Garcia: Proc. of Int. Conf. on Microalloying '95, ed. by M. Korchynsky et al., ISS, Pittsburgh, (1995), 365.

215. G. Krauss and S. W. Thompson: ISIJ Int., 35, (1995), 937.

216. H. I. Aaronson and H. J. Lee: Scripta Met., 21, (1987), 1011.

217. W. T. Reynolds, Jr., H. I. Aaronson and G. Spanos: Mater. Trans. JIM, 32, (1991), 737.

218. B. L. Bramfitt and J. G. Speer: Met. Trans. ASM, 21A, (1990), 817.

219. S. W. Thompson, D. J. Colvin and G. Krauss: Scripta Met., 22, (1988), 1069.

220. T. Araki and K. Shibata: Proc. of Int. Conf. on HSLA Steels '95, ed. by L. Guoxun et al., CSM, Beijing, China, (1995), 13.

221. T. Araki, M. Enomoto and K. Shibata: Mater. Trans. JIM, 32, (1991), 729.

222. J. L. Lee and M. H. Hon: Scripta Met., 21, (1987), 521.

223. Z. Bojarski and T. Bold: Acta Metall., 22, (1974), 1223.

224. P. H. Shipway and H. K. D. H. Bhadeshia: Mater. Sci. Technol., 11, (1995), 1116.

225. S. B. Singh and H. K. D. H. Bhadeshia: Mater. Sci. Technol., 12, (1996), 610.

226. K. Fujiwara, S. Okaguchi and H. Ohtani: ISIJ Int., 35, (1995), 1006.

227. S. Yamamoto, H. Yokoyama, K. Yamada and M. Niikura: ISIJ Int., 35, (1995), 1020.

228. S. K. Liu and J. Zhang: Met. Trans. ASM, 21A, (1990), 1517.

229. S. K. Liu and J. Zhang: Met. Trans. ASM, 21A, (1990), 1509.

230. M. Umemoto, A. Hiramatsu, A. Moriya, T. Watanabe, S. Namba, N. Nakajima, G. Anan and Y. Higo: ISIJ Int., 32, (1992), 306.

231. M. Korchynsky: Proc. of Int. Symp. on Accelerated Cooling of Steel, ed. by P. D. Southwick, Pittsburgh, (1987), 3.

232. L. J. Cuddy: Proc. of Int. Symp. on Accelerated Cooling of Steel, ed. by P. D. Southwick, Pittsburgh, (1987), 235.

233. G. Bognin, V. M. Contursi, G. Tanzi, A. Aprile, G. DeFlorio, A. Liguori, P. Borsi and M. Ghersi: Proc. of Int. Symp. on Accelerated Cooling of Steel, ed. by P. D. Southwick, Pittsburgh, (1987), 69.

234. S. Namba, M. Kitamura, M. Shimada, M. Katsumata, T. Inoue, H. Imamura, Y. Maeda and S. Hattori: ISIJ Int., 32, (1992), 377.

235. T. Senuma and H. Yada: Proc. 7th Riso Int. Symp. on Metallurgy and Materials Science, "Annealing Processes - Recovery, Recrystallization and Grain Growth", ed. by N. Hansen et al., Riso, Denmark, (1986), 547.

236. J. H. Beynon and C. M. Sellars: ISIJ Int., 32, (1992), 359.

237. D. R. Askeland: The Science and Engineering of Materials, Chapman and Hall Publishers, 2nd SI ed., London, England, (1990), 861.

238. S. C. Wang: J. Matls. Sci., 24, (1989), 105.

239. M. Umemoto and I. Tamura: Proc. of Int. Conf. on HSLA Steels: Metallurgy and Applications, ed. by J. M. Gray et al., CSM, Beijing, China, (1985), 373.

240. X. Liu, J. K. Solberg and R. Gjengedal: Proc. of Int. Conf. on HSLA Steels '95, ed. by L. Guoxun et al., CSM, Beijing, China, (1995), 253.

241. Y. E. Smith and C. A. Siebert: ASTM STP 480, (1969), 131.

242. Y. E. Smith and C. A. Siebert: Met. Trans. ASM, 2A, (1971), 1711.

243. J. A. Straatmann, D. V. Doane and Y. Jin Park: Proc. of Int. Conf. on Processing, Microstructure and Properties of HSLA Steels, ed. by A. J. DeArdo, TMS, Pittsburgh, (1987), 287.

244. R. K. Amin and F. B. Pickering: Proc. of Int. Conf. on Thermomechanical Processing of Microalloyed Austenite, ed. by A. J. DeArdo et al., AIME, (1982), 377.

245. A. Sandberg and W. Roberts: Proc. of Int. Conf. on Thermomechanical Processing of Microalloyed Austenite, ed. by A. J. DeArdo et al., AIME, (1982), 405.

246. R. Kaspar, A. Streißelberger and O. Pawelski: Proc. of Int. Conf. on Thermomechanical Processing of Microalloyed Austenite, ed. by A. J. DeArdo et al., AIME, (1982), 555.

247. C. M. Sellars: Proc. of Int. Conf. on HSLA Steels: Metallurgy and Applications, ed. by J. M. Gray et al., CSM, Beijing, China, (1985), 73.

248. T. Abe, K. Tsukada and I. Kozasu: Proc. of Int. Conf. on HSLA Steels: Metallurgy and Applications, ed. by J. M. Gray et al., CSM, Beijing, China, (1985), 103.

249. T. M. Hoogendoorn: Proc. of Int. Symp. on Microalloying '75, Union Carbide Corp., Washington D. C., (1975), 75.

250. K. J. Lee, K. B. Kang, J. K. Lee, O. Kwon and R. W. Chang: Proc. Int. Conf. on Mathematical Modelling of Hot Rolling of Steels, ed. by S. Yue, Hamilton, Canada, ISS, (1990), 435.

251. S. V. Subramanian, X. Zeng, L. E. Collins, M. Bucholtz and M. Kostic: Proc. of Int. Symp. on Low Carbon Steels for the 90's, ed. by R. Asfahani and G. Tither, TMS, Pittsburgh, (1993), 313.

252. C. Ouchi, T. Sampei and I. Kozasu: Trans. ISIJ, 22, (1982), 214.

253. M. Cohen and S. S. Hansen: Proc. of Int. Conf. on HSLA Steels: Metallurgy and Applications, ed. by J. M. Gray et al., CSM, Beijing, China, (1985), 61.

254. R. Priestner and M. S. Biring: Metal Sci. J., 7, (1973), 60.

255. A. J. DeArdo: Proc. of Int. Symp. on Accelerated Cooling of Steel, ed. by P. D. Southwick, Pittsburgh, (1987), 97.

256. O. Hunderi and N. Ryum: Acta Metall., 30, (1982), 739.

257. P. R. Rios: Acta Metall., 35, (1987), 2805.

258. R. D. Doherty, D. J. Srolovitz, A. D. Rollet and M. P. Anderson: Scripta Metall., 21, (1987), 675.

259. M. Hillert: Acta Metall., 36, (1988), 3177.

260. Y. Liu and B. R. Patterson: Scripta Metall., 27, (1992), 539.

261. C. J. Tweed, N. Hansen and B. Ralph: Met. Trans. ASM, 14A, (1983), 2235.

262. P. A. Manohar, D. P. Dunne and T. Chandra: ISIJ Int., 36, (1996), 194.

263. P. R. Rios: Scripta Mater., 34, (1996), 1185.

264. ASTM E: 1181 - 87, Annual Book of ASTM Standards, vol. 03.01, (1997), 739.

265. ASTM E: 930 - 92, Annual Book of ASTM Standards, vol. 03.01, (1997), 675.

List of Relevant Publications

Journal Papers:

1. P. A. Manohar and T. Chandra: 'Continuous Cooling Transformation Behaviour of High Strength Microalloyed Steels for Linepipe Applications", ISIJ International, Vol. 38, No. 7, (1998), pp. 766 - 774.

2. P. A. Manohar and T. Chandra: "Dimensions of Grain Boundary Mobility", ISIJ International, Vol. 37, No. 7, (1997), pp. 726 - 728.

3. P. A. Manohar, T. Chandra and C. R. Killmore: "Continuous Cooling Transformation Behaviour of Microalloyed Steels Containing Ti, Nb, Mn and Mo", ISIJ International, Vol. 36, No. 12, (1996), pp. 1486 - 1493.

4. P. A. Manohar, D. P. Dunne, T. Chandra and C. R. Killmore: "Grain Growth Predictions in Microalloyed Steels", ISIJ International, Vol. 36, No. 2, (1996), pp. 194 - 200.

5. P. A. Manohar, M. Ferry and T. Chandra: "Overview: Five Decades of the Zener Equation", ISIJ International, (in press).

Conference Papers:

1. P. A. Manohar and T. Chandra: "Application of Relative Rate Model to Predict Abnormal Grain Growth in Microalloyed Steels", paper presented at "Australasia Pacific Forum on Intelligent Processing and Manufacturing of Materials - (IPMM '97)", July 14 - 17, 1997, Gold Coast, Queensland, Australia, published in the conference proceedings, ed. by T. Chandra et al., pp. 1200 - 1206.

2. P. A. Manohar and T. Chandra: "Effect of TMP and Mn Content on the CCT Behaviour of Ti-Nb-Mo Microalloyed Steels", paper presented at the international conference "Thermomechanical Processing of Steels and Other Materials (THERMEC '97)", July 7 - 11, 1997, Wollongong, Australia, published in the conference proceedings, ed. by T. Chandra and T. Sakai, pp. 749 - 755.

3. P. A. Manohar, T. Chandra and D. P. Dunne: "Grain Coarsening Behaviour of Microalloyed Steels Containing Ti, Nb, Mn and Mo", paper presented at the 3rd international conference on Recrystallization and Related Phenomena, "ReX '96", Oct. 21 - 24, 1996, Monterey, California, USA, published in the conference proceedings, ed. by T. R. McNelley, pp. 445 - 451.

4. A. Manohar, D. P. Dunne and T. Chandra: "Grain Coarsening Behaviour of a Microalloyed Steel Containing Ti, Nb and Mo", paper presented at the 4th Japan International SAMPE Symposium, Tokyo, Sept. 25 - 28, 1995, published in the conference proceedings, ed. by Z. Maekawa et al., pp. 1431 - 1436.